

A Thesis Submitted for the Degree of PhD at the University of Warwick

Permanent WRAP URL:

<http://wrap.warwick.ac.uk/78797>

Copyright and reuse:

This thesis is made available online and is protected by original copyright.

Please scroll down to view the document itself.

Please refer to the repository record for this item for information to help you to cite it.

Our policy information is available from the repository home page.

For more information, please contact the WRAP Team at: wrap@warwick.ac.uk

Development of Polymers for Nanoreactors and Enzyme Stabilisation

Katherine Farrance

THE UNIVERSITY OF
WARWICK

Department of Chemistry

Submitted for the degree of Doctor of Philosophy

2016

...For Mathew Smith

Contents

List of Figures, Schemes and Tables.....	IX
Acknowledgements	XXVII
Declaration of Authorship.....	XXVIII
Summary of Thesis	XXIX
List of Abbreviations.....	XXX
1 Introduction.....	1
1.1 Enzyme structures	2
1.1.1 Primary Structure	2
1.1.2 Secondary structure.....	3
1.1.3 Tertiary structure.....	5
1.1.4 Quaternary structure.....	6
1.1.5 Assembly and aggregation of proteins.....	7
1.2 Characterisation of protein structures.....	9
1.2.1 Circular Dichroism.....	9
1.2.2 Small Angle X-Ray Scattering.....	12
1.3 Enzyme stabilisation.....	14
1.3.1 Enzymes and additives.....	16
1.3.2 Enzyme immobilisation	18
1.3.3 Non-Covalent adsorption	22
1.3.4 Characterisation of enzyme stabilisation	23

1.4	Enzyme mimics	25
1.5	Guanidine catalysts.....	27
1.6	Self-assembly of amphiphilic block copolymers	30
1.7	Polymerisation techniques.....	33
1.7.1	NMP	34
1.7.2	ATRP	38
1.7.3	RAFT Polymerisation	39
1.8	Concluding remarks	43
1.9	References	44
2	Immobilisation of 1,5,7-triazabicyclo[4.4.0]dec-5-ene onto an amphiphilic block copolymer for the assembly of catalytic nanoreactors.	57
2.1	Abstract	58
2.2	Introduction	58
2.2.1	Immobilisation of triazabicyclodec-5-ene.....	58
2.3	Results and Discussion.....	62
2.3.1	Synthesis of the StTBD (2.1)	62
2.3.2	Polymer synthesis <i>via</i> RAFT	65
2.3.3	Polymer synthesis using NMP	82
2.3.4	Micelle assembly.....	95
2.4	Conclusions	102
2.5	Experimental	103
2.5.1	Materials.....	103

2.5.2	Instrumentation	103
2.5.3	Synthesis of StTBD 2.1	104
2.5.4	Synthesis of 2-(dodecylthiocarbonothioylthio)-2-methylpropionic acid (DDMAT) 2.2. ²⁵	105
2.5.5	RAFT polymerisation of St and BzCl, P2.1.....	105
2.5.6	TBD substitution on to the polymer, P2.2.....	106
2.5.7	RAFT polymerisation of DMA, P2.3.....	106
2.5.8	Chain extension to afford P2.4.....	107
2.5.9	End group removal P2.5.....	108
2.5.10	TBD Substitution of P2.5.....	108
2.5.11	Synthesis of the Universal alkoxyamine initiator. ³⁴	109
2.5.12	A general polymerisation <i>via</i> NMP of DMA.....	111
2.5.13	Chain extension of P2.7b to afford P2.8b	112
2.5.14	TBD substitution onto P2.8b to produce P2.9b	113
2.5.15	Micellar assembly	114
2.5.16	TEM Sample preparation	114
2.6	References	116
3	Catalysis in aqueous environments using TBD-loaded nanoreactors	120
3.1	Abstract	121
3.2	Introduction	121
3.2.1	TBD Catalysis	121
3.2.2	Transesterification.....	123

3.2.3	Amidations	125
3.2.4	Michael addition.....	126
3.3	Results and discussion.....	129
3.3.1	Michael addition on solution.....	129
3.3.2	Micellar Michael additions	134
3.3.3	Altering core loading.....	142
3.3.4	Blended Micelles.....	150
3.4	Conclusions	157
3.5	Experimental	159
3.5.1	Materials and Methods.....	159
3.5.2	Micellar assembly	160
3.5.3	TEM sample preparation.....	160
3.5.4	Michael addition reaction to afford 3.1 and 3.2.....	160
3.5.5	Michael addition reactions in micelles.....	161
3.6	References	163
4	Stabilisation of Lipases from <i>Thermomyces lanuginosus</i> , in Polymer Solutions	166
4.1	Abstract	167
4.2	Introduction	167
4.2.1	Lipase	170
4.3	Results and Discussion.....	174
4.3.1	Comparison of TLL and Lipex	174

4.3.2	Polymer lipase solutions	186
4.3.3	PDMA Polymers with Lipolase and Lipex	201
4.3.4	Synthesis of water soluble copolymers	206
4.3.5	The effects of immobilised TBD on the structure of Lipolase and Lipex 209	
4.4	Conclusions	212
4.5	Materials and Methods	214
4.5.1	Synthesis of PSt-co-PBzCl.....	214
4.5.2	Synthesis of PDMA	215
4.5.3	Synthesis of P4.6.....	216
4.5.4	Synthesis of P4.7.....	216
4.5.5	Assays	217
4.5.6	Stain Tests	217
4.5.7	Tergo Tests.....	218
4.5.8	Circular Dichroism.....	218
4.5.9	SAXS	219
4.6	References	221
5	Stabilisation of Lipases from <i>Thermomyces lanuginosus</i> , in Polymer Solutions 226	
5.1	Abstract	227
5.2	Introduction	227
5.2.1	Mechanism of protein folding and stability	227

5.2.2	Protein unfolding.....	230
5.3	Results and discussion.....	232
5.3.1	Lipolase and Lipex temperature stability.....	232
5.3.2	Polymer lipase stability with PDMA	237
5.3.3	Polymer lipase stability with P4.7.....	248
5.3.4	Activity studies of the polymer-lipase solutions.....	251
5.4	Conclusions	262
5.5	Outlook.....	263
5.6	Experimental	265
5.6.1	Circular dichroism.....	265
5.6.2	SAXS	265
5.6.3	Stain Testing	266
5.6.4	Activity studies	266
5.6.5	Lipase Assay	266
5.7	References	267
6	Conclusions and future work	270

List of Figures, Schemes and Tables

Figures

Figure 1.1: The generic structure of L- α -amino acids, where R represents the side chain.	3
Figure 1.2: Cartoon representation of the helical structure of the α -helix, using PDB file 1U00 (taken from the PyMOL Molecular Graphics System, Version 1.5.0.4 Schrödinger, LLC). ¹² The dotted line indicates the hydrogen bonding in the peptide backbone and the R groups are facing outward.	4
Figure 1.3: Structure of antiparallel (left) and parallel (right) β -sheets, where the dashed lines represent hydrogen bonding.	5
Figure 1.4: Cartoon representation of the quaternary structure of the dimeric protein lipase from <i>Thermomyces lanuginosus</i> , using structure 4GWL (taken from the PyMOL Molecular Graphics System, Version 1.5.0.4 Schrödinger, LLC). ¹² The red cartoon represents the secondary structure and the blue represents the tertiary structure.	7
Figure 1.5: Energy curve of protein folding. Reprinted with permission from Dobson <i>et al.</i> ¹⁴ License Number: 3807041295335.	8
Figure 1.6: Formation of circularly polarised light (a) blue and green lines are 90° out of phase, the red line is polarised in the horizontal direction. (b) shows the combination of the 2 planes of light when they are 90° out of phase resulting in circularly polarised light purple line. (c) green right handed polarised light and red left handed polarised light, purple is the resultant image seen down the z-axis after right handed light has been absorbed. In this case more left handed light has been absorbed.	10

Figure 1.7: CD spectrum: full line- α -helix, long dash-anti-parallel β -sheet, dots-type I β -turn, and dots and short dashes-random coil, reprinted with permissions from Price <i>et al.</i> ³¹ License number: 3807050868173. Observable transitions present in enzymes and their wavelengths.....	11
Figure 1.8: Schematic representation of the SAXS experimental set up.	12
Figure 1.9: SAXS model of I vs q for a spherical particle, taken from O'Reilly <i>et al.</i> ³⁶ License number: 3807051208924.	14
Figure 1.10: The structure of Trehalose.....	16
Figure 1.11: The “grafting to” approach using epoxide functional groups, adapted from Bhushan <i>et al.</i> ⁶⁸	20
Figure 1.12: The polymerisation of PQA from the ATRP-functionalised chymotrypsin, adapted from Russell <i>et al.</i> ⁷⁶	22
Figure 1.13: A schematic representation of the adsorption of Lipase onto hydrophobic surfaces, reproduced with permission from Magner <i>et al.</i> ⁵⁶ Licence number: 3807051388538.	23
Figure 1.14: Kinetic deactivation curve where the gradient is equal to $-k$	24
Figure 1.15: A schematic representation of the catalytic cavity formation using a MIP, Reprinted with permission from Molecularly Imprinted Hydrogels Exhibit Chymotrypsin-like Activity. <i>Macromolecules</i> 1996, 29 (4), 1366-1368. Copyright (1996) American Chemical Society. ⁸⁹	26
Figure 1.16: The structures of guanidine-containing organocatalysts TBD, MTBD, TMG, TMO and ARG.....	28
Figure 1.17: The structure of Acyl-TBD (ATBD) in the twisted intermediate and the Acyl-TBO in the planar intermediate, reprinted with permission from Cyclic Guanidine Organic Catalysts: What Is Magic About Triazabicyclodecene? <i>J. Org.</i>	

Chem., 2009, 74 (24), 9490-9496. Copyright (2009) American Chemical Society.¹¹⁴

.....30

Figure 1.18: Self-assembled structures formed by amphiphilic block copolymers and assignment of packing parameters, ρ , Reprinted with permission from Ryan *et al.*¹¹⁷ license number 3807060606613.32

Figure 1.19: An illustration of a micelle assembly and the unimer exchange into the solution of the polymeric chains.33

Figure 1.20: The structure of the nitroxides TEMPO, TIPNO and SG1.36

Figure 1.21: Structure of the NMP universal initiator.38

Figure 1.22: ATRP equilibrium mechanism.¹⁴⁹ P_n-X is the halide capped polymer chain, Mt^m/L is the transition metal at an oxidation state m , and L is the ligand. M represents the monomers, and P_n the polymer chain, and k the rate constants for activation (act), deactivation (deact), propagation (p) and termination (t).38

Figure 1.23: A schematic of the RAFT mechanism. Reproduced from Moad *et al.*¹⁵⁴40

Figure 1.24: The generic structure of a RAFT agent, adapted from O'Reilly *et al.*¹⁶¹41

Figure 1.25: Guidelines for selecting which RAFT agent to use, here S = styrenes, MA = methacrylates, AA = acrylic acid, AM =acrylamide, AN = acrylonitrile, MMA = methyl methacrylate and Vac = vinyl acetate. The dotted lines indicate that there is partial control over the polymerisation, adapted from a Moad *et al.*¹⁵⁴42

Figure 2.1: Structure of TBD, MTBD and immobilised TBD.59

Figure 2.2: A schematic representation of the immobilisation of TBD for catalysis in water.61

Figure 2.3: ^1H NMR spectrum showing the overlaid spectra of purified 2.1 StTBD (black) and BzCl (blue) in CDCl_3 at 400 MHz.	64
Figure 2.4: ^{13}C NMR spectrum for purified 2.1, StTBD, in CDCl_3 at 400 MHz.	64
Figure 2.5: ^1H NMR spectrum of purified 2.2, DDMAT, in CDCl_3 at 400 MHz.	66
Figure 2.6: Conversion ^1H NMR spectrum for P2.1, in CDCl_3 at 400 MHz.	68
Figure 2.7: Long acquisition ^1H NMR spectrum for P2.1, in CDCl_3 at 400 MHz. ...	69
Figure 2.8: Overlay of the normalised SEC data in CHCl_3 (PSt standards) for the RI trace (blue) and the UV absorbance (red) for P2.1 as a function of differential weight fraction against molecular weight.	70
Figure 2.9: ^1H NMR spectrum for P2.2 (black) overlaid with P2.1 (blue), in CDCl_3 at 400 MHz.	71
Figure 2.10: DOSY NMR spectrum for P2.2, in CDCl_3 at 500 MHz.	72
Figure 2.11: Overlay of the SEC traces in CHCl_3 (PSt standards), Left: RI trace of P2.1 (solid blue) and P2.2 (blue dashed) as a function of normalised differential weight fraction against molecular weight. Right: RI (solid red) and UV (red dashed) trace for P2.2 as a function of response to molecular weight.	73
Figure 2.12: Long acquisition ^1H NMR spectrum of P2.3, in CDCl_3 at 400 MHz.	75
Figure 2.13: Overlay of the normalised SEC data in CHCl_3 (PSt standards) for the RI trace (blue) and the UV absorbance (red) for P2.3 as a function of differential weight fraction against molecular weight.	76
Figure 2.14: Long acquisition ^1H NMR spectrum of P2.4, in CDCl_3 at 400 MHz.	77
Figure 2.15: Overlay of the normalised SEC data in CHCl_3 (PSt standards) for the RI trace (blue) and the UV absorbance (red) for P2.4 as a function of normalised differential weight fraction against molecular weight.	77
Figure 2.16: Long acquisition ^1H NMR spectrum of P2.5, in CDCl_3 at 400 MHz.	79

Figure 2.17: Overlay of the SEC traces in CHCl ₃ (PSt standards), for P2.4 (blue), P2.5 (red). A: RI traces as a function of normalised differential weight fraction against molecular weight. B: 309 nm traces as a function of normalised response to molecular weight.....	80
Figure 2.18: Long acquisition ¹ H NMR spectrum of P2.6, in CDCl ₃ at 400 MHz....	81
Figure 2.19: Overlay of the SEC traces in CHCl ₃ , for P2.3 (blue), P2.4 (red), P2.5 (green), P2.6 (purple) Left: 309 nm traces as a function of response to molecular weight. Right: RI traces as a function of differential weight fraction against molecular weight.....	82
Figure 2.20: ¹ H NMR spectrum of 2.3, in CDCl ₃ at 300 MHz.....	84
Figure 2.21: ¹³ C NMR spectrum of 2.3, in CDCl ₃ at 300 MHz.....	84
Figure 2.22: ¹ H NMR spectrum of 2.5, in CDCl ₃ at 400 MHz.....	87
Figure 2.23: COSY NMR spectrum of 2.5, in CDCl ₃ at 400 MHz, the red line highlights the coupling of e' to d' and the blue line highlights the coupling of e to d.	88
Figure 2.24: Conversion ¹ H NMR spectrum of P2.7b, in CDCl ₃ at 400 MHz.	90
Figure 2.25: Long acquisition ¹ H NMR spectrum of P2.7b, in CDCl ₃ at 400 MHz..	91
Figure 2.26: Long acquisition ¹ H NMR spectrum of P2.8b, in CDCl ₃ at 400 MHz..	92
Figure 2.27: Long acquisition ¹ H NMR spectrum of P2.8b (blue) and P2.9b (black), in CDCl ₃ at 400 MHz.....	93
Figure 2.28: Overlay of the SEC data, for the RI traces of P2.7b (blue), P2.8b (red), P2.9b (green) as a function of normalised differential weight fraction against molecular weight in CHCl ₃ (PSt standards).....	94
Figure 2.29: Schematic representation of the formation of M2.9a-c using the solvent switch method.	96

Figure 2.30: DLS data Left: Representation of the size distribution of M2.9a-c in water at 0.1 mg mL ⁻¹ obtained at 20 °C, by intensity (blue), volume (red) and number (green).Right: the correlation function for M2.9a-c plotted against time (μs).	97
Figure 2.31: Left: TEM images of M2.9a-c at 0.1 mg mL ⁻¹ scale bar = 100 nm Right: Histograms of the data obtained <i>via</i> TEM for M2.9a-c on GO. Images obtained by Dr Helen Wilcock.	99
Figure 2.32: Left: TEM images of M2.9a-c at 0.1 mg mL ⁻¹ scale bar (100 nm) Right: Histograms of the data obtained <i>via</i> TEM for M2.9a-c after staining with phosphotungstic acid. Images obtained by Dr Yan Kang.	100
Figure 3.1: An illustrative representation of catalytic TBD tethered to the core of a micelle for the Michael addition within the core.	128
Figure 3.2: Isomers formed by the Michael addition with MTBD and TBD.	130
Figure 3.3: ¹ H NMR spectrum of purified 3.1, in CDCl ₃ at 400 MHz.	130
Figure 3.4: ¹ H NMR spectrum of 3.2, in CDCl ₃ at 400 MHz.	131
Figure 3.5: A computational model demonstrating the positions of protons j in 3.2, using ChemBio3D version 14.	132
Figure 3.6: The formation of micelles from P2.9a to M2.9a.	134
Figure 3.7: Schematic of the micellar catalysis work-up.	135
Figure 3.8: ¹ H NMR spectrum of the worked up reaction (black) overlaid with expected product 3.1 synthesised <i>via</i> conventional synthesis shown in Paragraph 3.3.1 (green), <i>trans</i> -chalcone (red) and dimethyl malonate (blue), in CDCl ₃ at 400 MHz.	136
Figure 3.9: Percentage conversion for the Michael addition reaction <i>vs</i> time (h) with 5 mol% TBD catalyst in M2.9a in triplicate, monitored <i>via</i> HPLC (95:5 water: methanol gradient to 5:95 water: methanol for 16 min, flow rate: 2 mL min ⁻¹) using a	

UV detector at 280 nm and 254 nm: error bars represent standard deviation from averaged multiple measurements.	137
Figure 3.10: The formation of M2.8a from P2.8a.....	138
Figure 3.11: Particle size analysis of M2.8a. (A1) Histogram of particle size as determined by PA-stained TEM images at 0.1 mg mL ⁻¹ . (A2) PA-stained TEM image at 0.1 mg mL ⁻¹ (scale bar – 100 nm). (B1) Size distribution, in water at 0.1 mg mL ⁻¹ obtained by DLS: by intensity (blue), volume (red) and number (green) at 20 °C. (B2) DLS correlation function. TEM Images obtained by Dr Yan Kang.....	139
Figure 3.12: Altering the mol% catalyst vs substrate through changing the concentration of the substrate solution added. This schematic is not to scale.	141
Figure 3.13: Percentage conversion for the Michael addition reaction vs time (h) with 1 mol% (diamonds), 5 mol% (squares) and 10 mol% catalyst (triangles) vs substrate. Monitored <i>via</i> HPLC (95:5 water: methanol gradient to 5:95 water: methanol for 16 min, flow rate: 2 mL min ⁻¹) using a UV detector at 280 nm and 254 nm.....	142
Figure 3.14: Altering the catalyst loading; red represents the hydrophobic block, blue the hydrophilic block, and the green represents the catalyst, and subsequently assembled to M2.9a-c.....	143
Figure 3.15: Zimm plot for M2.9a (blue), M2.9b (red) and M2.9c (green) at a concentration of 1 mg mL ⁻¹	145
Figure 3.16: Preparation of catalytic solutions with 5mol% catalyst concentration with respect to the reaction mixture using micelles of different core loadings. (A) Addition of different concentrations of substrates ensuring the same reaction volume and number of micelles. (B) Changing the number of micelles added yet maintaining a constant volume and concentration of substrate. These schematics are not to scale.	147

Figure 3.17: The percentage conversion for the Michael addition against time, with (A) M2.9b and (B) M2.9c in triplicate, before dilution (method A, red) and after dilution (method B, blue), in triplicate: error bars represent standard deviation from averaged multiple measurements.	148
Figure 3.18: The percentage conversion for the Michael addition reaction with different catalyst core loadings, with M2.9a (blue diamonds, 1% core loading) M2.9b (red squares, 6% core loading) and M2.9c (green triangles, 11% core loading) against time with 5 mol% catalyst loading, in triplicate: error bars represent standard deviation from averaged triplicate measurements.....	149
Figure 3.19: Assembly of blended micelles with 6% loading.	151
Figure 3.20: Particle size analysis of M2.9m. (A1) Histogram of particle size as determined by PA stained TEM analysis at 0.1 mg mL ⁻¹ . (A2) PA stained TEM image at 0.1 mg mL ⁻¹ (scale bar 100 nm). (B1) Size distribution by intensity (blue), number (red) and green (volume), in water at 0.1 mg mL ⁻¹ obtained by DLS at 20 °C. (B2) DLS correlation function.	152
Figure 3.21: The aggregation numbers, determined by SLS, against percentage core loading for the pure systems (blue diamonds) and the mixed system M2.9m (red square). SLS data obtained by Mr Lewis Blackman.....	153
Figure 3.22: Mixing of the pre-assembled micelles M2.9a and M2.9c to yield a 6% loading.....	155
Figure 3.23: The percentage conversion for the Michael addition of dibenzyl malonate and <i>trans</i> -chalcone against time (hours) for M2.9b (blue diamonds), M2.9m (red squares) and the pre-assembled micelles mixed system (green triangles). In triplicate, and monitored <i>via</i> HPLC.....	156

Figure 4.1: The general structure of a triglyceride and the formation of glycerol and fatty acid chains.....	170
Figure 4.2: Active site of TLL from 1DU4 (The PyMOL Molecular Graphics System, Version 1.5.0.4 Schrödinger, LLC). ²¹	171
Figure 4.3: Crystal structure of TLL in the closed 1DU4 (a) and open 1EIN (b) positions, with the active site shown in blue. (i) The secondary structure. (ii) The surface structure (The PyMOL Molecular Graphics System, Version 1.5.0.4 Schrödinger, LLC). ²¹	172
Figure 4.4: Kyte-Doolittle plot of TLL (A), Lipolase (B) and Lipex (C) were the highlighted boxes represent were a change in the hydrophobicity is observed, with thanks to Dietmar Lang, Unilever.....	175
Figure 4.5 Crystal structure of TLL, the known arginine mutations in Lipex and the observed mutations for residues 51-58 are highlighted in green, the lid is pink with the orange residues representing the active site. (The PyMOL Molecular Graphics System, Version 1.5.0.4 Schrödinger, LLC). ²¹	176
Figure 4.6: Far-UV CD spectra of Lipolase and Lipex as molar circular dichroism ($\Delta\epsilon$) as a function of wavelength. Run at 20 °C. The spectra were averaged over three runs and three accumulations, buffer was subtracted.....	177
Figure 4.7: Experimental set up for stain testing.	182
Figure 4.8 A bar chart representing the Δ SRI for the beef fat stain when subtracted from the blank surfactant for Lipex and Lipolase in Blackbull formulation. Each stain test was repeated four times over four plates and averaged.	183
Figure 4.9: A bar chart representing the Δ SRI of beef fat stain when subtracted from the blank surfactant for Lipex and Lipolase in Ecoboost and Blackbull formulations. Each stain test was repeated four times over four plates and averaged.	184

Figure 4.10: Green represents the mutated residues on TLL, (PDB: 1EIN) at T231R and N233R, Active site (pink), hydrophobic residues (red), and hydrophilic residues (blue). ²² (A) The mutated TLL with ARG mutations found in Lipex (B) stabilisation of Lipex at the core corona interface of surfactant micelles. (The PyMOL Molecular Graphics System, Version 1.5.0.4 Schrödinger, LLC). ²¹	185
Figure 4.11: Long acquisition ¹ H NMR spectrum of P4.1, in CDCl ₃ at 400 MHz..	187
Figure 4.12: Structures of P4.1-P4.2.....	188
Figure 4.13: ΔSRI at pH 8.5 and pH 7 for P4.1 and P4.2 and Lipex with beef fat stain.	189
Figure 4.14: ΔSRI at pH 8.5 and pH 7 for P4.1 and P4.2 and Lipex with lard stain.	190
Figure 4.15: Long acquisition ¹ H NMR spectrum of P4.3, in CDCl ₃ at 400 MHz..	192
Figure 4.16: ΔSRI at pH 8.5 and pH 7 for P4.3 and P4.4 and Lipex with beef fat stain.	193
Figure 4.17: ΔSRI at pH 8.5 and pH 7 for P4.3 and P4.4 and Lipex with lard stain.	193
Figure 4.18: Comparison of the SRI observed with cooking oil at 30 °C and 250 rpm with Blackbull formulation (blue) and formulation with Lipex (red) at different concentrations. The calculated ΔSRI for Lipex (triangles).....	196
Figure 4.19: Experimental set up for TERGO tests.	197
Figure: 4.20 Far-UV CD spectra of P4.3 (A), P4.4 (B), P4.5 (C), Lipex (1) and Lipolase (2) as molar circular dichroism (Δε) as a function of wavelength. Run at 20 °C. The spectra were averaged over three runs and three accumulations, buffer was subtracted.	202

Figure 4.21: Guinier-Porod plots of P4.4 and Lipolase (A1) and P4.5 and Lipolase (B1) of I plotted against q . A Kratky plot of Iq^2 plotted against q for P4.4 (A2) P4.5 (B2) and P4.4 and Lipolase (A3) and P4.457 and Lipolase (B3).	204
Figure 4.22: Long acquisition ^1H NMR spectrum of P4.6, in CDCl_3 at 400 MHz..	207
Figure 4.23: Structures of P4.6 and P4.7.	208
Figure 4.24: Far-UV CD spectra of (A1) P4.6 (no TBD) and Lipex. (A2) P4.6 and Lipolase. (B1) P4.7 (TBD containing polymer) with Lipex. (B2) P4.7 with Lipolase. Plotted as molar circular dichroism ($\Delta\epsilon$) as a function of wavelength. Run at 20 °C. The spectra were averaged over 3 runs and 3 accumulations, buffer was subtracted.	210
Figure 4.25: Kratky plots of Iq^2 against q for P4.7 and Lipolase at different molar ratios of Lipolase to P4.7 (C1 = 50:1, C2 = 12.5:1, C3 =4:1, C4 =3:1, C5 =2.5:1 and C6 =2:1)	211
Figure 5.1: A schematic of the equilibrium of a protein in its native and unfolded state, where K_u is the rate of unfolding and K_f is the rate of folding.	228
Figure 5.2: Thermal unfolding curve obtained <i>via</i> CD spectroscopy.	229
Figure 5.3: Far-UV CD spectra of (A1) Lipolase and (B1) Lipex as molar circular dichroism ($\Delta\epsilon$) as a function of wavelength. Run at 20 °C before and after heating. CD analysis at $\Delta\epsilon_{222}$ of Lipolase (A2) and Lipex (B2) as a function of temperature (°C).....	233
Figure 5.4: A thermal unfolding curve comparing the fraction unfolded against temperature (°C) of Lipolase and Lipex.	234
Figure 5.5: A; Kratky plot of Iq^2 plotted against q . B; Porod plot of Lipolase at 25-65 °C as $\ln I$ against $\ln q$ at different temperatures, all SAXS data was collected and fitted by Dr Anaís Pitto-Barry.	236

Figure 5.6: Far-UV CD spectra of (A1) P4.5 and Lipolase and (B1) P4.5 and Lipex as molar circular dichroism ($\Delta\epsilon$) as a function of wavelength. Run at 20 °C before and after heating. CD spectroscopy analysis at $\Delta\epsilon_{222}$ of P4.5 and Lipolase (A2) and P4.5 and Lipex (B2) as a function of temperature (°C).	239
Figure 5.7: A comparison of the fraction unfolded of (A) Lipolase and Lipolase with P4.5, and (B) Lipex and Lipex with P4.5 against temperature (°C).	240
Figure 5.8: Far-UV CD spectra of (A1) P4.4 and Lipolase and (B1) P4.4 and Lipex as molar circular dichroism ($\Delta\epsilon$) as a function of wavelength. Run at 20 °C before and after heating. CD spectroscopic analysis at $\Delta\epsilon_{222}$ of P4.4 and Lipolase (A2) and P4.4 and Lipex (B2) as a function of temperature (°C).	242
Figure 5.9: (A) An overlay of Lipolase and P4.4 CD spectra before heating, after heating and at 80 °C. (B) A comparison of the fraction unfolded plotted against temperature for Lipex and Lipex with P4.4.	243
Figure 5.10: A Porod plot at 25-65 °C of $\ln I$ vs $\ln q$ for P4.4 with Lipolase (A) and P4.5 with Lipolase (B).	247
Figure 5.11: Structure of P4.7.	248
Figure 5.12: Far-UV CD spectra of (A1) P4.7 and Lipolase and (B1) P4.7 and Lipex as molar circular dichroism ($\Delta\epsilon$) as a function of wavelength compared to Lipolase and Lipex (20 °C). Run at 20 °C before and after heating. CD spectroscopy analysis at $\Delta\epsilon_{222}$ of P4.4 and Lipolase (A2) and P4.4 and Lipex (B2) as a function of temperature (°C).	249
Figure 5.13: A Porod plot at 25-65 °C of $\ln I$ vs $\ln q$ for P4.7 with Lipolase.	250
Figure 5.14: PDMA polymers of different molecular weights stored in solution with a 10 times molar excess to Lipolase to monitor their effects on Lipolase stabilisation.	252

Figure 5.15: A plot of absorbance vs [PNP] (M) to give the extinction coefficient of the substrate PNP of $14676 \text{ M}^{-1}\text{cm}^{-1}$	253
Figure 5.16: Bar chart of the velocity of Lipolase, and Lipolase with P4.3, P4.4 and P4.5 after storage at time intervals 0 h, 10 h and 1 week. Each set of data is shown as an average over five data sets with standard deviation.....	254
Figure 5.17: The velocity of P4.3, P4.4 and P4.5. Each set of data is shown as an average over 5 data sets with standard deviation as error.....	256
Figure 5.18: The ΔSRI for additive-free Lipolase, and Lipolase with P4.5 after storage at time intervals 0 h and 1 week, in 0.8 g L^{-1} Blackbull formulation. Each set of data is shown as an average over ten data sets with standard deviation as error.	257
Figure 5.19: A Porod plot before and after one week storage with $\ln I$ plotted vs $\ln q$ for P4.5 and P4.5 with Lipolase.....	258
Figure 5.20: The velocity of Lipolase, and Lipolase with P4.7, P4.5 and MTBD. Each set of data is shown as an average over five data sets with standard deviation.	259
Figure 5.21: The percentage of original activity for Lipolase, and Lipolase with P4.7, P4.5 and MTBD after storage at $75 \text{ }^\circ\text{C}$ overnight. Each set of data is shown as an average over three data sets with standard deviation as error.....	260
Figure 5.22: The velocity of P4.7, P4.5 and MTBD. Each set of data is shown as an average over three data sets with standard deviation.....	260
Figure 5.23: Schematic of the deamidation and hydrolysis of Asn and Asp (top) and the hydrolysis of the peptide backbone from an Asp residue (bottom). ^{17, 18}	263

Schemes

Scheme 1.1: Schematic representation of the conjugation of thiol end group coupled to a thiol reactive glycopolymer.....	19
--	----

Scheme 1.2: A schematic representation of site specific modification of Myoglobin with PLP. Adapted from Gilmore <i>et al.</i> ⁷²	20
Scheme 1.3: Mechanism of the ring opening polymerisation of L-lactide catalysed by TBD, in THF at 1 mol% catalyst loading, this polymerisation was observed for 40 minutes reaching 99% conversion.	29
Scheme 1.4: The simplified mechanism of NMP. Adapted from Nicolas <i>et al.</i> ¹²⁸ M = monomer, k_d = rate of decomposition, k_c = rate of recombination, k_t = rate of termination.	35
Scheme 2.1: Formation of MCM-41 or SBA-15-TBD. ¹⁰	59
Scheme 2.2: Conditions initially explored for the synthesis of StTBD.	62
Scheme 2.3: Synthesis of monomer 2.1, StTBD using BzCl, TBD and KOH.	63
Scheme 2.4: The synthesis of DDMAT, 2.2.	66
Scheme 2.5: Schematic representation of the copolymerisation of St with BzCl to form a RAFT polymeric scaffold P2.1	67
Scheme 2.6: Schematic of the substitution of TBD onto the polymer scaffold P2.1 to form P2.2.....	70
Scheme 2.7: Stepwise synthesis of the amphiphilic block copolymer with TBD functionality embedded into the hydrophobic domain.....	74
Scheme 2.8: Schematic of the proposed mechanism for end group removal using AIBN and LPO, proposed by Rizzardo <i>et al.</i> ³¹	78
Scheme 2.9: Synthesis of the universal initiator 2.5.	83
Scheme 2.10: Schematic representation of the formation of 2.5.	85
Scheme 2.11: Schematic representations of the formation of the amphiphilic block copolymers containing the catalyst TBD by NMP.	89

Scheme 3.1: The TBD-catalysed aldol reaction of a keto-aldehyde resulting in the formation of a cyclic aldol product. Reproduced from Baati <i>et al.</i> ²	122
Scheme 3.2: Example of the Wittig reaction between methyltriphenylphosphonium bromide and 4-nitrobenzaldehyde in the presence of TBD, to form 4-nitrostyrene.	124
Scheme 3.3: A schematic representation of the Horner-Wadsworth-Emmons Wittig reaction. Reproduced from Clayden <i>et al.</i> ¹⁶	124
Scheme 3.4: Amidation of vinyl acetate with <i>n</i> -butylamine.....	125
Scheme 3.5: Schematic representation of the Michael addition of dimethyl malonate and 2-cyclopenten-1-one, catalysed by TBD in toluene.	126
Scheme 3.6: Michael addition reactions for the formation of 3.1 and 3.2 in bulk...	129
Scheme 3.7: The activated species formed for the Michael addition with TBD (left) and MTBD (right).	134
Scheme 4.1: Schematic of the PNP-assay for lipases.	179
Scheme 4.2: Synthesis of P4.3 and P4.4.	191
Scheme 4.3: The substitution of TBD onto the polymeric backbone of P4.6 to afford P4.7.	207
Scheme 5.1: Lumry-Eyring framework describing protein aggregation/inactivation where K_a is the rate of aggregation.	231
Scheme 5.2: Formation of PNP and Stearic acid from the hydrolysis of PNP-Stearate in the presence of lipase.	252

Tables

Table 1.1: The pK_a values for TBD, MTBD, TMG and ARG. *Predicted values from Leito <i>et al.</i> ¹¹⁰	29
Table 2.1: Characterisation data of polymers P2.7a-P2.9c by ¹ H NMR spectroscopy (CDCl ₃ , 400 MHz) and SEC analysis (CHCl ₃ , PSt standards), n represents the DP of	

St and BzCl, x is the fraction of St in the hydrophobic block and m is the DP of DMA.	95
Table 2.2: SLS data of polymers M2.9a-c, determining hydrodynamic radius and aggregation number obtained by Lewis Blackman.	98
Table 2.3: Characterisation data of the spherical micelles; ^a DLS (1 mg mL ⁻¹), ^b SLS analysis (1 mg mL ⁻¹), ^c TEM GO (0.1 mg mL ⁻¹) and ^d TEM stained (0.1 mg mL ⁻¹).	101
Table 3.1: The percentage product formation (3.1 and 3.2) with catalysts TBD and MTBD at 5 mol% catalyst loading in different solvents, monitored via HPLC (95:5 water: methanol gradient to 5:95 water: methanol for 16 min, flow rate: 2 ml min ⁻¹) using a UV detector at 280 nm at 7 hours and 24 hours.	133
Table 3.2: Comparison of the Michael addition reaction for MTBD in THF, and micellar solution M2.8a, to M2.9a and P2.9a in THF after 1 hour and 24 hours with 5 mol% catalyst loading.	140
Table 3.3: A summary of the number of nanoparticles in the reaction solution for M2.9a, M2.9b and M2.9c.	146
Table 3.4: A summary of the number of nanoparticles in the reaction solution for the diluted and non-diluted micelles (M2.9b and M2.9c) in triplicate.	148
Table 3.5: The number of micelles in the reaction solution, calculated using N_{agg} as determined by SLS. Percentage conversion for the Michael addition of <i>trans</i> -chalcone and dibenzyl malonate to afford 3.2 with catalysts M2.9a-c and M2.9m, after 24 hours, calculated by HPLC (analysis in triplicate).	153
Table 4.1: The secondary structure content of Lipolase and Lipex determined by CD spectroscopy and interpreted using DICROWEB using CONTIN/LL analysis	

programme and reference set 4. Normalised root-mean-square deviation (NRMSD) gives the deviation of the data set to the model used. ^{28, 30}	178
Table 4.2: Activity of lipase, measured using PNP-caprylate as a substrate, observed at 405 nm with six repeats.....	180
Table 4.3 Characteristics of polymers P4.1-4.2, ^a determined by ¹ H NMR spectroscopy (400 MHz, CDCl ₃), ^b determined by SEC (CHCl ₃ , PSt standards)....	188
Table 4.4 The properties of polymers P4.3-4.4, ^a determined by ¹ H NMR spectroscopy (400 MHz, CDCl ₃), ^b determined by SEC (CHCl ₃ , PSt standards).....	192
Table 4.5: The ΔSRI of P4.3 and P4. 4 when compared to a blank standard on stains beef fat and cooking oil with Lipex at pH 8.5.....	195
Table 4.6: The ΔSRI and SRI of P4.3 and P4.4 on beef fat stain with Lipex at pH 8.5, when compared to a white cotton fabric control.....	198
Table 4.7: The ΔSRI and SRI of P4.3 and P4.4 on lard stain with Lipex at pH 8.5, when compared to a white cotton fabric control.....	199
Table 4.8: The ΔSRI and SRI of P4.3 and P4.4 on cooking oil stain with Lipex at pH 8.5, when compared to a white cotton fabric control.....	199
Table 4.9: The ΔSRI of P4.5 with stains beef fat and cooking oil with Lipex at pH 8.5 when compared to a blank standard.....	201
Table 4.10: The properties of the polymers P4.6 and 4.7, determined by ^a ¹ H NMR spectroscopy, ^b SEC (CHCl ₃ , PSt callibration).....	208
Table 4.11: The ΔSRI of P4.6 and P4.7 with Lipex at pH 8.5, when compared to a blank standard on stains beef fat and cooking oil	209
Table 5.1: The secondary structure content of Lipolase and Lipex determined by CD spectroscopy and interpreted using DICROWEB, using CONTIN/LL analysis	

programme and reference set 4. Normalised root-mean-square deviation (NRMSD) gives the deviation of the data set from the model used. ^{21, 23}	235
Table 5.2: The estimated particle size radius of gyration (R_g) and the dimension parameter (s) for Lipolase at 25-65 °C.....	237
Table 5.3 The properties of polymers P4.4-4.5, ^a determined by ¹ H NMR spectroscopy (400 MHz, CDCl ₃), ^b determined by SEC analysis (CHCl ₃ , PSt standards).	238
Table 5.4: The secondary structure content of P4.5 with Lipolase and Lipex determined by CD spectroscopy and interpreted using DICROWEB analysis programme and using CONTIN/LL reference set 4 and 7 (for P4.5 after heating). ^{21, 23}	241
Table 5.5: The secondary structure content of P4.4 with Lipolase and Lipex determined by CD spectroscopy and interpreted using DICROWEB analysis programme and using CONTIN/LL reference set 4. ^{21, 23}	245
Table 5.6: The percentage change in secondary structure content of Lipolase and Lipex both with and without P4.5 and P4.4 after heating, determined by CD spectroscopy and interpreted using DICROWEB, using CONTIN/LL analysis programme and reference set 4. ^{21, 23} T_m Calculated at $\Delta\epsilon_{222}$	246
Table 5.7: The estimated particle size radius of gyration (R_g) and the dimension parameter (s) for P4.4 and Lipolase at 25-65 °C.....	248
Table 5.8: Estimated particle size radius of gyration (R_g) and the dimension parameter (s) for P4.7 and Lipolase at 25-65 °C.....	251
Table 5.9: The percentage activity retained for Lipolase and Lipolase with polymers P4.3, P4.4 and P4.5. An average from 5 replicates, and compared to the original activity observed at 0 hour.	255

Acknowledgements

I would like to firstly thank Rachel O'Reilly for the opportunity to study for my PhD within her group; more importantly, if it wasn't for her sound advice and encouragement my PhD would not have been possible. Rachel has instilled a positive working mentality, which is reflected within the group and I hope this work ethic stays with me throughout my career.

I would like to thank the University of Warwick and Unilever for providing funding for me to carry out my studies; especially my industrial collaborators Ezat Koshdel, who has been a constant support throughout my academic career, and Dietmar Lang, for providing sound scientific advice and excellent discussion. A special thanks to Andrew Cook, Ilaria Samba, Sukriti Singh and Jessica Lee for providing excellent training and a welcoming environment for during my long visits to Unilever.

I would also like to thank the members of the O'Reilly group both past and present particularly Helen, Becky, Marianne, Dafni and Anais for proof reading my thesis. Thank you to my training buddies who encouraged me to start training every morning before 7:30 am, I am not a morning person. A special thanks to Dafni for physically getting me to the lab each day! Finally, to members of bay awesome, I don't think I have ever laughed so much.

Thank you to Mathew Smith who moved to a new area to allow me to carry out this research and supported me throughout. Not forgetting to mention my family for providing the foundations and supporting me throughout my undergraduate degree and their continued support through my postgraduate studies.

Declaration of Authorship

This thesis is submitted to the University of Warwick in support for the degree of Doctor of Philosophy. I hereby declare all of the work discussed in this thesis was carried out by the author unless otherwise stated. Any experiments or data analysis carried out by other persons is clearly stated within each chapter. Any work carried by an alternative author is highlighted below:

- TEM images were collected with the supervision of Dr Helen Willcock (formerly University of Warwick), and stained images were collected by Dr Yan Kang (University of Warwick).
- In Chapters 2 and 3 the SLS data was collected and analysed by Lewis Blackman.
- All SAXS data was collected and analysed by Dr Anaïs Pitto-Barry (University of Warwick).
- Micelle schematics have been modified from a micelle template provided by Dr Dafni Moatsou.

Summary of Thesis

This thesis explores the use of polymer nanoreactors in catalysis as well as the use of water-soluble polymers in enzyme stabilisation.

Chapter 1: An introduction to the literature currently covering the research topics relevant to the techniques used within this thesis, providing further background on the fundamental enzyme theory that is to be explored

Chapter 2: This looks at the techniques available for tethering the catalyst triazabicyclodec-5-ene to the hydrophobic block of an amphiphilic block copolymer, synthesised by nitroxide mediated polymerisation and the assembly of these polymers.

Chapter 3: The previously synthesised nanoreactors were used to catalyse Michael additions with varied loadings within the core of the micelles.

Chapter 4: Looks into the effect of using water soluble polymers of varying molecule weights on the activity of Lipases Circular dichroism spectroscopy and stain tests were used as tools to indicate changes to the native structure and activity.

Chapter 5: Thermostability of lipase was investigated, and the use of the water-soluble polymers to extend the lifetime of the enzyme in solution was investigated through monitoring changes in the melting temperatures as well as stability studies.

List of Abbreviations

$^3J_{\text{H-H}}$	Vicinal proton coupling constant
AIBN	2,2'-azobis(2-methylpropionitrile)
Arg	Arginine
Asp	Aspartic acid
ATRP	Atom transfer radical polymerisation
BzCl	Vinyl benzyl chloride
<i>c</i>	Concentration
CD	Circular Dichroism
COSY	Correlation spectroscopy
CTA	Chain transfer agent
Cys	Cysteine
d	Doublet
Da	Dalton
D_{ave}	Average diameter
D_{h}	Hydrodynamic diameter
DLS	Dynamic light scattering
\bar{D}_{M}	Molecular weight distribution ($M_{\text{w}}/M_{\text{n}}$)
DMA	<i>N,N</i> -dimethyl acrylamide

DMF	<i>N,N</i> -dimethylformamide
dn/dc	Refractive index
DOSY	Diffusion-ordered spectroscopy
DP	Degree of polymerisation
DSC	Differential scanning calorimetry
ESI-MS	Electrospray ionisation mass spectroscopy
ϵ	Molar Extinction coefficient
FAEA	Ferulic acid esterase
FH	French Hard
f_u	Fraction unfolded
GO	Graphene oxide
His	Histidine
HPLC	High performance liquid chromatography
I	Scattering intensity
K	Contrast factor
k_{act}	Rate of activation
k_{add}	Rate of addition
k_{deact}	Rate of deactivation
K_m	Michaelis constant

k_p	Rate of propagation
k_t	Rate of termination
K_u	Unfolded equilibrium constant
l	Path length
LPO	Lauryl peroxide
m	Multiplet
M_n	Number-average molecular weight distribution
MRW	Mean residue weight
MS	Mass spectrometry
MTBD	7-methyl-1,5,7-triazabicyclo[4.4.0]dec-5-ene
M_w	Weight-average molecular weight distribution
N_A	Avogadro's constant
N_{agg}	Aggregation number
NMP	Nitroxide-mediated polymerisation
NMR	Nuclear magnetic resonance
NRMSD	Normalised root-mean-square deviation
PA	Phosphotungstic acid
PDB	Protein databank
PDMA	Poly(<i>N,N</i> -dimethyl acrylamide)

PNP	Para-nitrophenol
ppm	Parts per million
PSt	Polystyrene
q	Wave vector
RAFT	Reversible addition-fragmentation chain transfer
RDRP	Reversible deactivation radical polymerisation
R_f	Retardation factor
R_g	Radius of gyration
R_h	Hydrodynamic radius
RI	Refractive index
ROP	Ring-opening polymerisation
rpm	Revolutions per minute
R_θ	Rayleigh ratio
s	Singlet, when referring to NMR spectroscopy
s	Dimension parameter, when referring to SAXS
SAXS	Small angle X-ray Scattering
SEC	Size exclusion chromatography
Ser	Serine
SLS	Static light scattering

SRI	Stain removal index
St	Styrene
<i>t</i>	Triplet
TBD	1,5,7-Triazabicyclo[4.4.0]dec-5-ene
TEM	Transmission electron microscopy
TERGO	Tergotometer
T_g	Glass transition temperature
THF	Tetrahydrofuran
TIPNO	Trimethyl-4-phenyl-3-azahexane-3-nitroxide
TLL	Lipases from <i>Thermomyces lanuginosus</i>
T_m	Melting temperature
TMB	1,2,4-trimethoxybenzene
TMG	1,1,3,3-tetramethyl guanidine
TMO	1,4,6-triazabicyclo-[3.3.0]oct-4-ene
TON	Turn over number
™	Trade mark
UV	Ultra violet
UV-Vis	Ultraviolet - visible
ν	Rate

V_{\max}	Maximum velocity
wt. %	Weight percentage
δ	Chemical shift
ΔA	Change in absorbance
ΔE	Change in colour
$\Delta \epsilon$	Molar ellipticity
ΔG_{N-U}	Gibbs free energy of protein folding
ΔSRI	Change in stain removal index
Δt	Change in time
θ	Ellipticity, in context of CD
θ	Angle, with respect to light scattering data
λ	Wavelength
ρ	Packing parameter

1 Introduction

1.1 Enzyme structures

Enzymes, often described as Nature's catalysts, are found in biological systems where they accelerate reactions up to a million times faster than un-catalysed reactions.^{1, 2} These catalysts operate in specific conditions allowing for catalysis of defined substrates, this is achieved through evolution of the structure enabling finely tuned folding.^{3, 4} These biocatalysts are a class of proteins whose macromolecular structure is formed from a peptide sequence, while their catalytic activity is reliant on the specific folding of the peptide.⁵ This highly specific structure enables the formation of active site cavities for substrate recognition.⁶ Non-covalent bonding is crucial for stabilisation of the proteins, where numerous interactions such as hydrogen bonding, hydrophobic interactions, electrostatic interactions and dispersion forces cooperatively enhance protein folding and stability.⁷ There are four levels of organisation within a protein structure: the primary, secondary, tertiary, and quaternary structures. At each of these levels the complexity of the structural organisation increases forming tailored catalysts with specific reproducible folding.⁸

1.1.1 Primary Structure

The primary structure of a protein consists of a linear sequence of amino acids reported from the N-terminus (terminal amine group) to the C-terminus (terminal carboxylic acid group).⁵ In Nature the peptide sequence namely consists of L- α -amino acids (Figure 1.1), of which there are 20 naturally occurring varieties. This varied selection of amino acids allows for a diverse array of catalytic functions and enzymatic structures.⁵

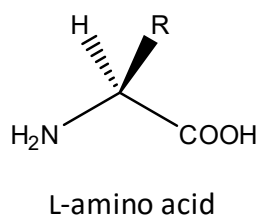


Figure 1.1: The generic structure of L- α -amino acids, where R represents the side chain.

In many cases the active site of an enzyme is formed by amino acids that are not adjacent in the peptide sequence. For instance Lipase, from *Thermomyces lanuginosus* (TLL), contains the active residues Serine, Histidine and Aspartic acid at positions 146, 258 and 201 in the sequence, yet the complex folding of the peptide backbone brings these residues into close proximity enabling creation of a catalytically active site.^{9, 10}

1.1.2 Secondary structure

The secondary structure involves between 10 and 20 amino acids in a sequence. This sequence of amino acids folds *via* hydrogen-bonding of the peptide backbone, through coordination of the available lone pair on the carbonyl group and the N-H functionality.^{1, 5} There are three main types of organised structures: α -helices, β -sheets and β -turns.

1.1.2.1 α -helix

The C=O and N-H hydrogen bond form a right handed helix (like DNA), in which the side chains point outwards. It is estimated that each turn contains 3.6 residues (Figure 1.2).⁵ Owing to the hydrogen-bonded nature of the structure, α -helices are

said to be more stable in the absence of water, hence are commonly found buried within the core of the protein structure.⁵ The amino acids methionine, alanine, leucine, uncharged glutamic acid and lysine are widely found within the α -helix, due to their flexible structures and small side chains. In contrast, the amino acids proline and glycine are not commonly found in the helical structure due to the alkylated N_{α} (eliminating H-bonding) in proline and absence of flexibility in the side chains (glycine).¹¹

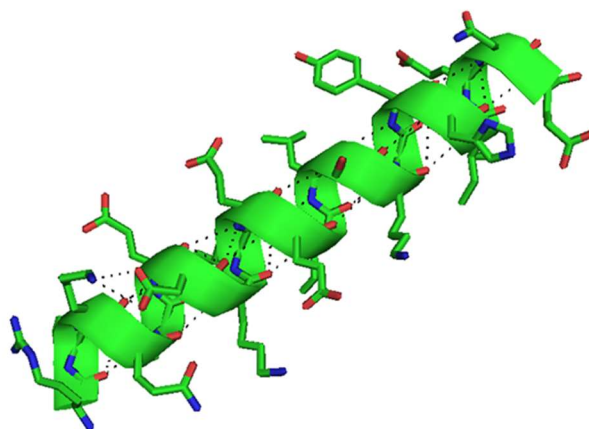


Figure 1.2: Cartoon representation of the helical structure of the α -helix, using PDB file 1UO0 (taken from the PyMOL Molecular Graphics System, Version 1.5.0.4 Schrödinger, LLC).¹² The dotted line indicates the hydrogen bonding in the peptide backbone and the R groups are facing outward.

1.1.2.2 β -Sheets

Another widely encountered secondary structure within proteins is the β -sheet. These sheets are assigned as parallel (N-C terminal of the chains facing in the same direction) or antiparallel (N-C terminal of the chains in opposite directions) (Figure 1.3) where typically β -sheets can have up to 15 strands.⁵

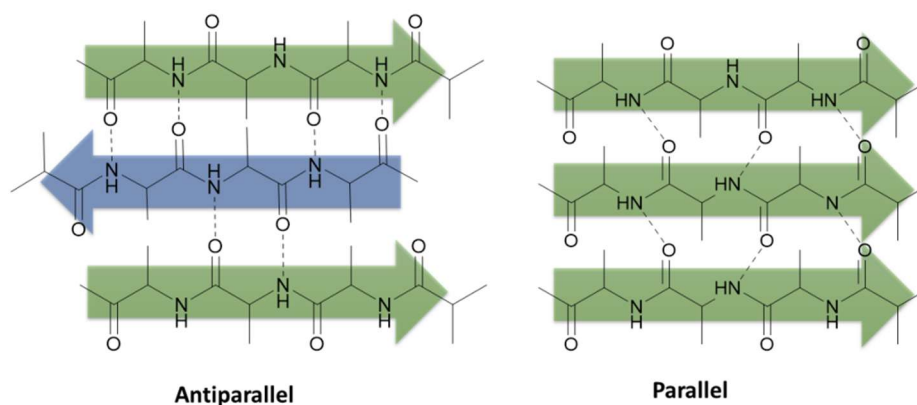


Figure 1.3: Structure of antiparallel (left) and parallel (right) β -sheets, where the dashed lines represent hydrogen bonding.

When the strands are antiparallel the hydrogen bonding is perpendicular to the strand, whereas parallel sheets have distorted hydrogen bonding, hence it is commonly agreed that the antiparallel β -sheets often have higher stability.¹

1.1.2.3 β -turns

This class of secondary structure (β -turns) are only encountered next to β -sheets, however they constitute their own family as they play an important role in enabling protein folding and thus protein functionality. They achieve this by changing the direction of the sheet by 180° .¹ These turns typically involve four amino acids where the second residue is commonly proline.⁵

1.1.3 Tertiary structure

The tertiary structure of a protein is the formation of a higher order structure through the arrangement of polar amino acids on the surface, allowing to the protein to assume a globular shape.⁸ Much like surfactants, proteins are arranged in such a

manner that the hydrophobic functional groups are primarily found in the interior. As a result of the tertiary structure formation, the hydrophobic residues are embedded within the core providing additional stability to the, hydrophobic, secondary structures.⁸ This allows for hydrophilic interactions through the surface with the surrounding aqueous environment, leading to an overall lowering of the total free energy. The formation of the tertiary structure assembly is entropically driven by the release of water upon the formation of hydrophobic interactions.⁵ Covalent bonding can also stabilise the tertiary structure through the formation of disulfide bridges which form as a result of bonding through cysteine side chains.⁵

1.1.4 Quaternary structure

The quaternary structure is a more complex higher ordered structure than the tertiary structure and is formed through protein-protein interactions (*i.e.* concerning two or more peptide sequences) which effectively further stabilise the protein structure through the oligomer assembly (Figure 1.4).⁵ It is well-documented that upon the formation of these interactions, hydrophobic domains on the surface of the proteins can form β -sheets through protein-protein interactions, resulting in the formation of protein aggregates.⁵

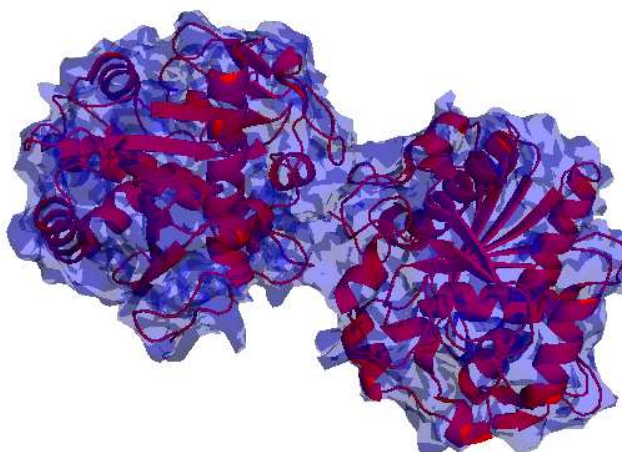


Figure 1.4: Cartoon representation of the quaternary structure of the dimeric protein lipase from *Thermomyces lanuginosus*, using structure 4GWL (taken from the PyMOL Molecular Graphics System, Version 1.5.0.4 Schrödinger, LLC).¹² The red cartoon represents the secondary structure and the blue represents the tertiary structure.

1.1.5 Assembly and aggregation of proteins

When the protein assembles into the structure with the lowest energy configuration it is described as being in its native state (Figure 1.5).^{13, 14} It was highlighted by Levinthal's paradox that proteins containing just 100 amino acids can adopt 10^{70} conformations, assuming all configurations are adopted this can take $\sim 10^{52}$ years to achieve the native state.^{15, 16} Proteins spontaneously fold into their native states in nanoseconds, hence it is agreed that folding takes place through several pathways prior to assuming the lowest energy configuration.¹⁵⁻¹⁸

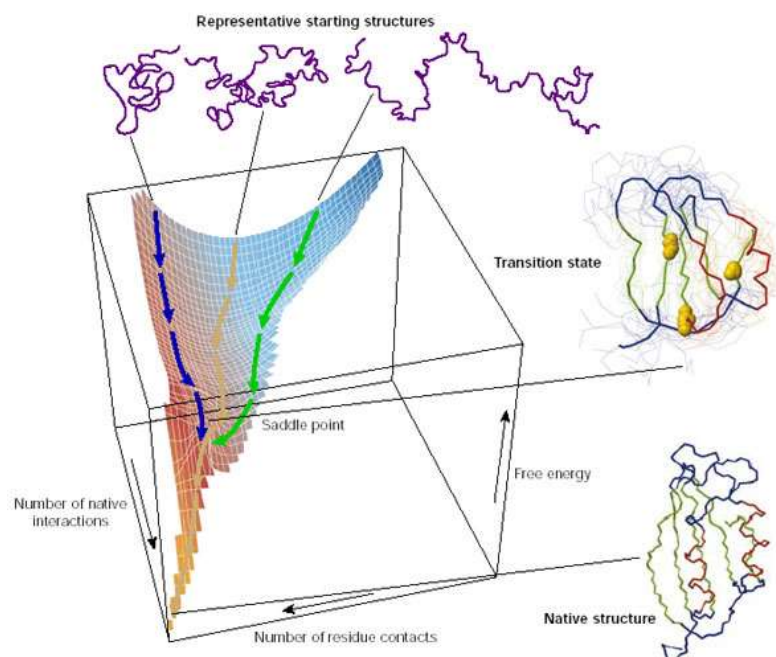


Figure 1.5: Energy curve of protein folding. Reprinted with permission from Dobson *et al.*¹⁴ License Number: 3807041295335.

Although the pathway of protein folding is not yet fully understood, two pathways have been suggested: folding through hierarchical assembly *via* local interactions, and folding through tertiary nucleation, where the tertiary structure assembles and the secondary structures form as a result of folding.^{11, 14, 19, 20} Based on these predictions, Dill and co-workers have developed a mechanistic model which predicts the kinetics of folding for a protein based on its amino acids sequence.²¹ The premise of this model relies on a two-state model where the formation of the secondary structures is in rapid equilibrium with the coiled unfolded structure. These secondary structures gradually become stabilised by the formation of adjacent secondary structures leading to tertiary interactions. For smaller proteins there is good correlation between the model and reality, yet it is highly size-dependent. Larger proteins, which rely heavily on tertiary interactions, are not modelled equally well, therefore other models are required for the prediction of their secondary structure.²¹

1.2 Characterisation of protein structures

Several techniques have been developed to identify the structures of proteins: matrix-assisted laser desorption/ionisation (MALDI) mass spectrometry and Edman degradations are used for identifying the primary structure.^{22, 23} Circular dichroism (CD) spectroscopy, and Fourier transform infrared (FTIR) spectroscopy are employed to identify secondary structures,^{24, 25} while hydrogen/deuterium exchange nuclear magnetic resonance (NMR) spectroscopy, and small angle X-ray scattering (SAXS) are used to study the tertiary structure.^{26, 27}

Perhaps the most commonly used technique for protein characterisation is X-ray crystallography; a technique that was developed by Kendrew *et al.* for resolving the 3-D structure of proteins, for which they were awarded a Nobel prize in Chemistry in 1962.²⁸ Since the initial development, the crystal structures of over 90% of known proteins have since been resolved and are openly available *via* the protein databank, allowing for better understanding of their macromolecular structures.^{29, 30}

1.2.1 Circular Dichroism

A common technique for exploring the secondary structure of a protein is circular dichroism (CD) spectroscopy, which is achieved by examining the far ultra violet (UV) spectrum of the protein solution.³¹ CD spectroscopy is defined as the difference in right and left handed polarised transmitted light which oscillates in the single plane (Figure 1.6, *a*). Circularly polarised light is generated by slowing down one of the linear phases of polarised light by a quarter of a wavelength (90°) (Figure 1.6 *a*, green line). Looking down the z-axis, a rotating helical structure is seen (Figure 1.6 *b*, purple line) that is circularly polarised. In a CD instrument left and

right handed light is pulsed and optically active compounds interfere with the signal. When right-handed polarised light is absorbed by the protein a negative response is detected. The data is reported in terms of ellipticity (Equation 1.1), derived from the varying contributions of polarised light (E_R and E_L , Figure 1.6 c). The angle is calculated using vectors **a** and **b** from Figure 1.6 c.

Equation 1.1: Calculation of ellipticity (θ).

$$\theta = \tan^{-1}(b/a)$$

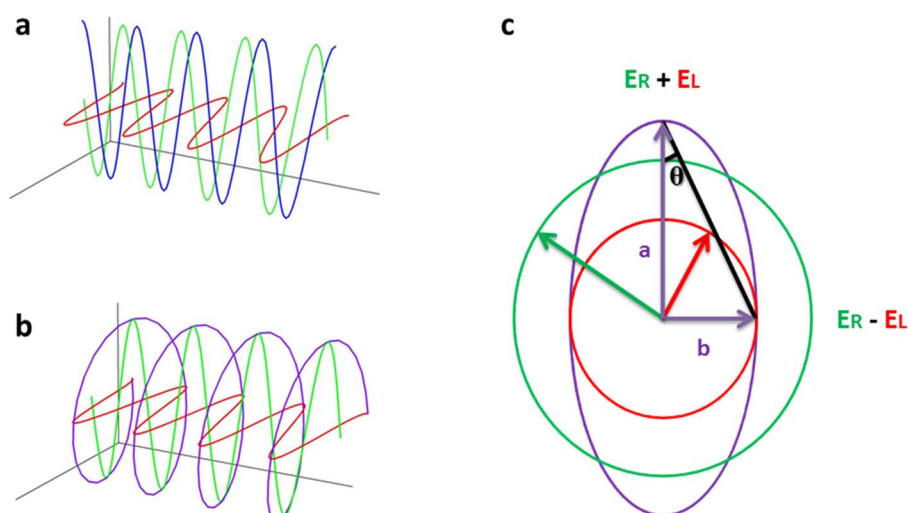


Figure 1.6: Formation of circularly polarised light (a) blue and green lines are 90° out of phase, the red line is polarised in the horizontal direction. (b) shows the combination of the 2 planes of light when they are 90° out of phase resulting in circularly polarised light purple line. (c) green right handed polarised light and red left handed polarised light, purple is the resultant image seen down the z-axis after right handed light has been absorbed. In this case more left handed light has been absorbed.

In biological molecules the average absorption is in the range of ten millidegrees (mdeg), where the ellipticity is the degree of polarisation. The secondary structures of proteins can be observed in the far UV wavelength range (180-250 nm); specifically, the $\pi \rightarrow \pi^*$ and $n \rightarrow \pi^*$ transitions from the amide groups can be observed.³² These transitions change depending on the surrounding environment.

Figure 1.7 shows the typical CD spectrum for the secondary structures of an α -helix, a β -sheet, a β -turn and a random coil. Many proteins contain all three structures giving an average in the CD spectrum. Whilst it is possible to monitor changes in the secondary structure through changes in the spectrum, work has been carried out towards the theoretical deconvolution of these spectra to give the fractions of each secondary structure.³²⁻³⁴

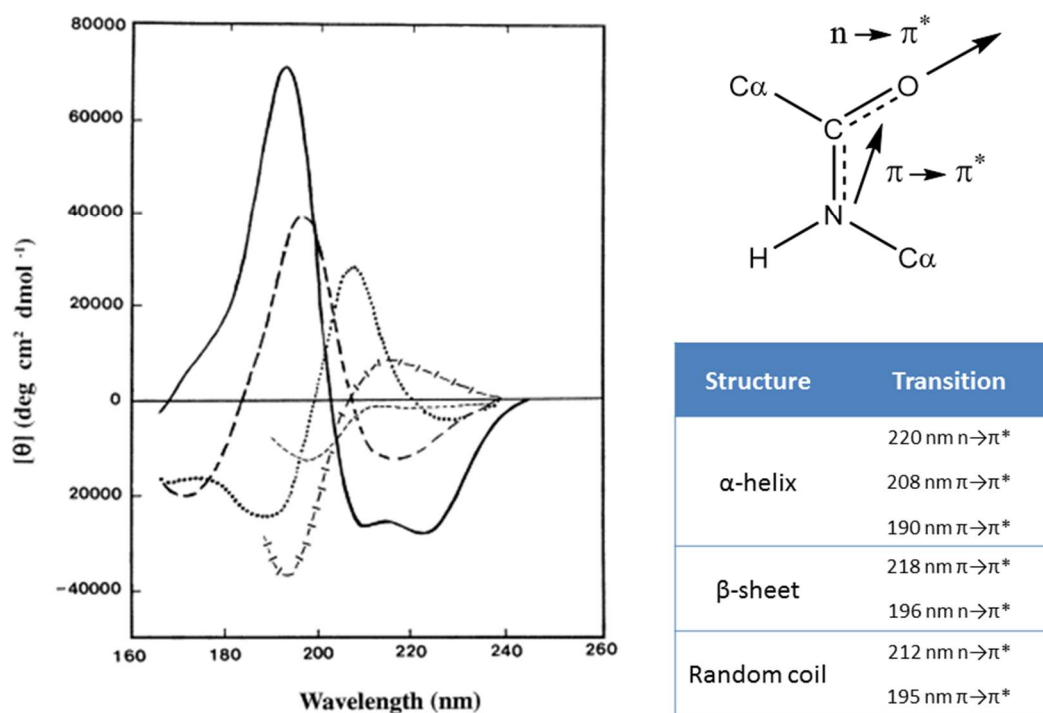


Figure 1.7: CD spectrum: full line- α -helix, long dash-anti-parallel β -sheet, dots-type I β -turn, and dots and short dashes-random coil, reprinted with permissions from Price *et al.*³¹ License number: 3807050868173. Observable transitions present in enzymes and their wavelengths.

The online data analysis software DICHROWEB provides a web-based server for prediction of the secondary structure which is calculated using popular algorithms.³⁴

The software can also be used as a tool to predict changes in the secondary structure upon applying an external stimuli.

1.2.2 Small Angle X-Ray Scattering

Small angle X-ray scattering (SAXS) is a common technique for the analysis of soft materials such as synthetic nanoparticles or biological macromolecules. This technique allows the study of the three dimensional structure of materials. Owing to the short wavelength of X-rays ($\sim 1 \text{ \AA}$) they can be used to probe environmental details about the structure.³⁵⁻³⁷ Following emission from an X-ray source the rays are collimated to yield uniform and parallel waves. These are passed through the sample (as shown in Figure 1.8) and a signal is detected when the X-rays are scattered by the electron cloud of the sample material, while the intensity of this signal is directly proportional to the size of the element and its concentration. Hence, heavier elements provide a higher scattering.³⁶

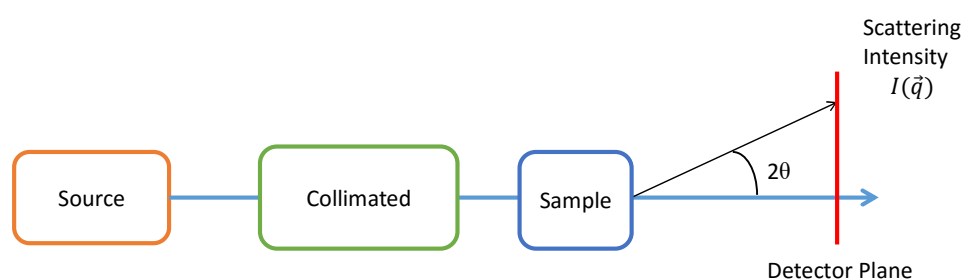


Figure 1.8: Schematic representation of the SAXS experimental set up.

The analysis of the data commonly requires a linear fit such as those obtained from Guinier or Porod plots (Figure 1.9), which enables estimation of particle size and

shape.^{36, 38} The Guinier region takes into account the scattering of the whole particle (hence the radius of gyration, R_g , can be determined), whereas the Porod region provides information on the slope of the scattering curve and depending on this value it is possible to determine the aggregates in solution which can be represented by the dimension parameter. For this reason, SAXS can be used to predict the morphology of assembled soft nanostructures. For instance, a dimension parameter (s) of $s = 1$ is characteristic of a rigid rod. As s increases the aggregates are representative of swollen chains ($s = 1-2$), chains ($s = 2$), “mass fractals” (such as gels) ($s = 2-3$), rough surfaces ($s = 3-4$) and smooth surfaces ($s = 4$). When the dimension parameter is less than 1, a spherical structure is present. For biomolecules such as proteins, radius of gyration will include the hydration shell.³⁹ This is because the water molecules will be more closely packed on the surface of a protein, owing to the hydrophobic moieties embedded on the protein surface, therefore changing the R_g .³⁹ Kratky plots derived from SAXS data ($q^2I(q)$ vs q) enable probing of the globular nature of a protein.^{39, 40} If a random coil is observed then this plot will exhibit a linear increase. However, in the presence of a tightly packed structure, such as a globular folded protein, a bell shaped curve will be observed. These plots are a useful tool to determine if a protein is becoming partially denatured when changing the external environment, through temperature or the addition of a chemical stimulus.

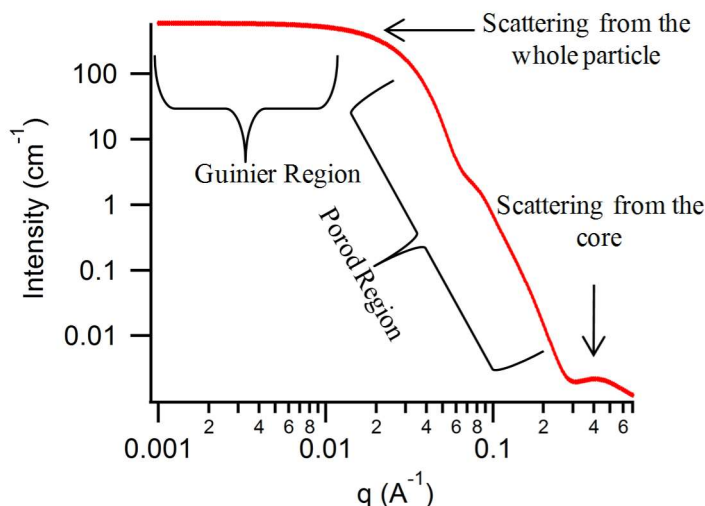


Figure 1.9: SAXS model of I vs q for a spherical particle, taken from O'Reilly *et al.*³⁶ License number: 3807051208924.

1.3 Enzyme stabilisation

Owing to their high activity, specificity and applicability for aqueous catalysis, there is much industrial interest focussed on utilising enzymes, for example in detergents, biocatalysts and in the drugs, food and paper industries.^{41, 42} Although the idea of using an enzyme like a chemical catalyst seems simple in principle, enzymes have the tendency to denature once removed from their optimum conditions, hindering their applicability.⁴³ For example enzymes used in detergents can be used for cleaning specific stains, such as the use of lipase for the transesterification of fat stains, here the fat will be hydrolysed, thus removing the stain.⁴⁴ However upon storage it is often found that using enzymes in detergent formulations resulted in a loss in enzyme activity, likely due to numerous factors such as the presence of high surfactant concentrations (disrupting the native structure) and prolonged storage (from the factory to consumer use, leading to potential unfolding and aggregations).⁴⁵ Hence enhancing the stability of these enzymes within formulations is essential in order to provide to the consumer the intended enzyme benefits.

Another example of using lipases industrially is in the biofuel industry; although enzymes are expensive in contrast to their chemical counterparts (*e.g.* sodium hydroxide 69 £/kg as opposed to lipase 270 £/kg), prolonging the shelf life/stability of these enzymes will dramatically reduce the production costs of biofuels, increasing the viability of enzyme useage.⁴⁶

Nature has provided a vast array of enzymes designed to operate in a range of environments, including a group called extremophiles.⁴⁷ A way to circumvent the problematic stability of typical enzymes is the use of extremophiles that are inherently more stable. These enzymes are known to operate under extreme conditions such as pH > 9 (alkaliphiles), pH < 2-3 (acidophiles), > 60-80 °C (thermophiles), > 80 °C (hyperthermophiles), < 15°C (psychrophiles), high salt concentrations of 2-5 M sodium chloride (halophiles) and up to 130 MPa (piezophiles).⁴⁸ One of the most attractive class of extremophiles is that of Thermophiles (including Hyperthermophiles) as they allow for catalysis at higher temperatures and offer higher stability, through an increased surface charge and higher core hydrophobicity and rigidity.^{48, 49} This rigidity comes at a cost as these enzymes can be inactive at lower temperatures. To overcome this, chemical denaturants (*e.g.* guanidinium hydrochloride) can be used to activate the enzymes at these lower temperatures.⁴⁹

Psychrophiles operate at low temperatures and are ideal for lowering operating temperatures (*i.e.* for laundry products used in cold water). They are more flexible than their thermophilic counterparts because a higher flexibility is required to lower the activation enthalpy (ΔH) for enzymatic catalysis.^{3, 48} As a consequence, the number of interactions between the enzyme active site and the substrate are reduced. It is due to this increased flexibility that these enzymes have relatively low stability

(e.g. alkaline phosphatase has a half-life of 6 minutes at 40 °C) hence a lower shelf life is observed.⁵⁰

Due to the storage difficulties and the monetary cost of enzymes, methods have been explored to stabilise protein structures, including the addition of additives, covalent immobilisation of the enzyme, and non-covalent absorption onto supports.⁵¹⁻⁵⁸

1.3.1 Enzymes and additives

Additives have been widely explored for the stabilisation of enzymes in solution, including small molecules such as surfactants, polyols, and polymers.^{51, 59-62} One of the most investigated polyols is trehalose (Figure 1.10).^{59-61, 63} Inspired by Nature, the stability behaviour of trehalose was initially explored as it is found in high concentrations in organisms which can recover biological activity after dehydration.⁶¹ Full activity of the enzyme type II restriction endonuclease, PstI, was retained after 98 days of dehydration whereas with other sugars, such as sucrose, only partial activity was retained after 14 days dehydration (25-50%). The Bhat group compared the influence of surface tension of various polyols on enzyme stability finding that the presence of these small molecules increases the surface tension of water and therefore the thermostability of the enzyme.⁵¹

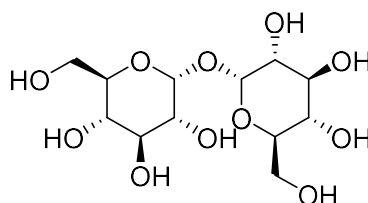


Figure 1.10: The structure of Trehalose.

Much work has been carried out utilising polymers as stabilisers. More recently work from the Maynard group has explored polytrehalose, where trehalose was immobilised onto a styrenic monomer and subsequently polymerised, with additional stability observed after lyophilisation of the horseradish peroxidase-polymer solution.^{58, 60} This increase in stability resulted from the hydrogen bonding network formed between the polyol and the enzyme, horseradish peroxidase (HRP), which keeps the protein in the hydrated state after freeze drying.⁶⁰ Various other polymers explored for stabilisation include poly(vinylpyrrolidone) (PVP), polyethyleneimine (PEI) and poly(ethylene glycol) (PEG).⁶⁴⁻⁶⁶

Ulmer and co-workers also utilised the polymer PVP in a copolymer with polyvinyl acetate (PVAc), PVP-*co*-PVAc, to stabilise glucose oxidase at elevated temperatures.⁶⁴ After 4 hours at 50 °C glucose oxidase exhibited double the activity of the polymer-free solution when in the presence of PVP-PVAc. This stabilisation is achieved through the inhibition of the kinetic pathway for the deactivation of the enzyme. However, at higher temperatures (above 60 °C) no stabilisation was observed, due to disassociation of the enzyme cofactor leading to a loss in activity.⁶⁴

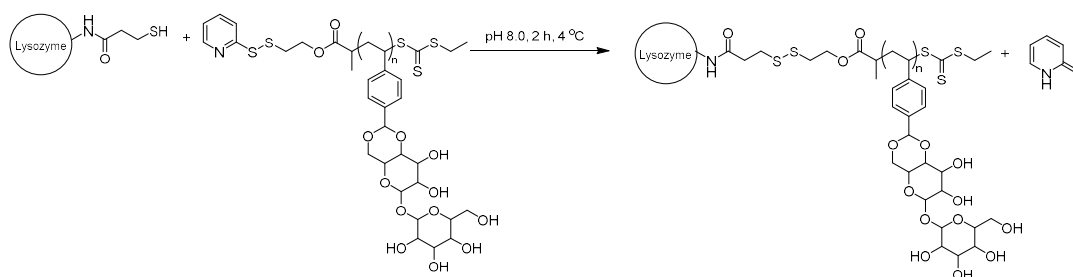
It has been shown that PEI can protect lactate dehydrogenase (LDH) from inactivation, increasing the shelf life of the enzyme.⁶⁵ One of the main mechanisms for enzyme degradation is oxidation of the sulfhydryl group. Upon storage of LDH in solution with Cu²⁺ ions (to trigger oxidation) PEI prevented precipitation enabling activity retention.⁶⁵

1.3.2 Enzyme immobilisation

One of the first examples of covalently binding polymers to enzymes was reported in 1977 by the Davis group, where PEG was bound to Bovine Liver Catalase (BLC).⁶⁶ A decrease in activity was observed due to shielding of the catalytic site; however, no immune response was detected after five injections into mice. Hence, it was proposed that covalently bound PEG could be used for enzyme therapy.⁶⁶ These positive side effects have led to an increased interest in protein immobilisation. Widely explored, there are two main techniques for immobilisation: “grafting to” and “grafting from” the protein.^{54, 67}

1.3.2.1 *Grafting to*

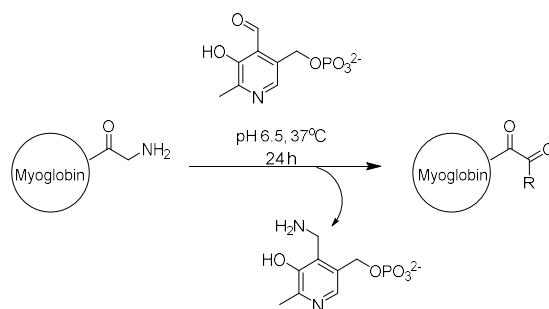
The “grafting to” approach utilises a pre-synthesised polymer chain containing one or more reactive functionalities, allowing for good control over the polymeric properties.⁶⁸⁻⁷⁰ The main limitations of “grafting to” is grafting density, as a consequence of unfavourable conjugation of two macromolecular species leading to inefficient bioconjugation.⁷¹ As an example of “grafting to” a trehalose containing monomer was polymerised *via* Reversible Addition-Fragmentation Chain Transfer (RAFT) polymerisation, this polymer contained thiol reactive pyridyl disulphide on the end group. The protein lysozyme from egg white was functionalised with *N*-succinimidyl-S-acetylthio propionate forming thiolated lysozyme which was then conjugated to the end group of a polymer through the displacement of the thiol group as shown in Scheme 1.1.⁵⁸



Scheme 1.1: Schematic representation of the conjugation of thiol end group coupled to a thiol reactive glycopolymer.

This enabled stabilisation of the dehydrated lysozyme through the free hydroxyl groups on the trehalose disaccharide. These hydroxyl groups surround the protein *via* H-bonding, stabilising the protein from its surrounding environment.⁵⁸

Gilmore and co-workers have targeted the N-terminal of a protein by exploiting the lower pK_a of the amino-group.^{72, 73} This allowed for specific binding of the N-terminal group over the lysine (-NH₂) functionalities on the surface. Here the N-terminus of myoglobin was modified with pyridoxal-5-phosphate (PLP) to afford ketone functionality at the N-terminus, subsequently PEG-alkoxyamine was grafted to the end group resulting in 69% conversion at 37 °C at pH 6.5 as shown in Scheme 1.2.⁷² Only one conjugation product was obtained as a result of site-specific grafting demonstrating the robustness of this technique.



Scheme 1.2: A schematic representation of site specific modification of Myoglobin with PLP. Adapted from Gilmore *et al.*⁷²

Indeed, proteins have multiple functionalities on their surface, such as lysine residues, that can react with the reactive functional groups leading to the formation of a covalently bound protein-polymer complex (Figure 1.11).⁵⁶ Work from Bhushan and co-workers showed the immobilisation of lipase from *Arthrobacter sp.* onto synthetic polymer beads with porosity greater than 0.2 cm³ g⁻¹.⁶⁸

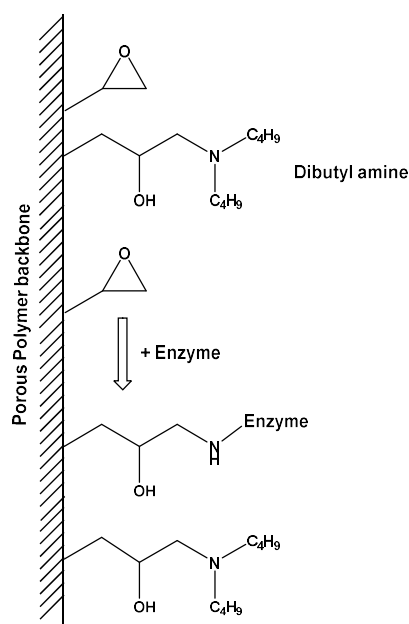


Figure 1.11: The "grafting to" approach using epoxide functional groups, adapted from Bhushan *et al.*⁶⁸

These polymer beads were synthesised from glycidyl methacrylate, (GMA), ethylene glycol dimethyl acrylate (EGDM) and dibutyl amine. Immobilisation resulted in enhanced thermostability, where 20% residual activity was retained after heating at 60 °C; in contrast the native lipase had no activity. It is thought that this stability is due to the introduction of covalent bonds, increasing the rigidity of the enzyme thus increasing melt temperature (T_m).⁶⁸

1.3.2.2 *Grafting from*

The “grafting from” approach features a polymer chain which is grown from a protein. Commonly, the protein is functionalised with an initiating group such as those suitable for atom transfer radical polymerisation (ATRP) or chain transfer species (for RAFT polymerisation) prior to growing the polymer chain. One disadvantage of this technique is that some polymerisations require harsh conditions and this can be detrimental to the enzyme stability.⁵⁶ Despite this, the literature shows numerous examples of this approach, with both macro-ATRP initiators and macro-RAFT agents synthesised.^{54, 55, 74, 75} The Russell group has successfully immobilised an ATRP initiator onto the surface of the protease chymotrypsin where methacryloethyl-trimethyl ammonium bromide (a quaternary amine, QA) was polymerised from the enzyme surface to afford poly(quaternary ammonium) (PQA) as shown in Figure 1.12.⁷⁶ The activity of chymotrypsin was improved at low pH (5-6) when conjugated, attributed to the increased stabilisation of the active site. Here it was proposed that the presence of PQA lowered the pK_a of the catalytic histidine residue enhancing activity at lower pH values.⁷⁶

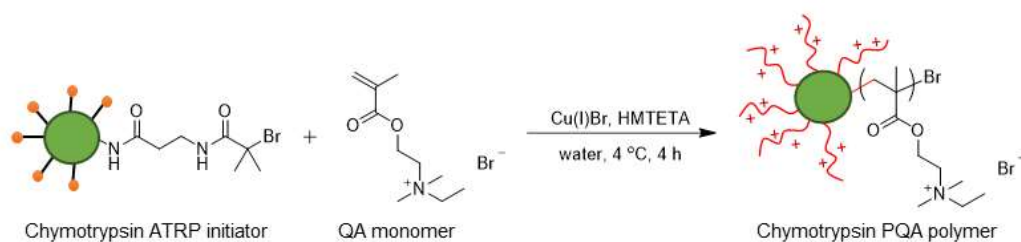


Figure 1.12: The polymerisation of PQA from the ATRP-functionalised chymotrypsin, adapted from Russell *et al.*⁷⁶

Another example from Sumerlin *et al.* used this approach to create a poly(*N*-isopropylacrylamide) (PNIPAM)-containing block copolymer, by conjugation of lysozyme (*via* the lysine residues) to a RAFT end group (R group).⁵⁴ The polymerisation took place in aqueous conditions at 25 °C, decreasing the detrimental effects of organic solvents and elevated temperature on the protein. The polymerisation was monitored by sodium dodecyl sulfate polyacrylamide gel electrophoresis, commonly referred to as SDS-PAGE, and demonstrated a considerable amount of control of the polymer characteristics.⁵⁴

1.3.3 Non-Covalent adsorption

Another frequently exploited method involves the non-covalent immobilisation technique; this has advantages over other methods as the enzyme is not chemically modified thus preventing any premature degradation of the enzyme. However, as the immobilisation is through weak Van der Waals interactions, leaching can take place.⁵⁶ For instance, lipases have been widely used for immobilisation *via* non-covalent adsorption.

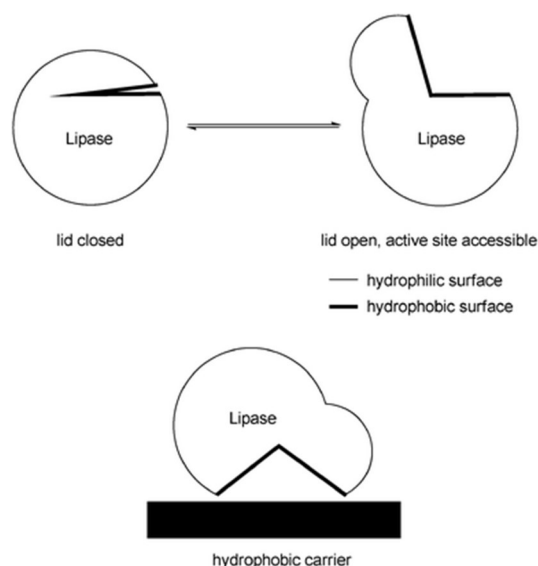


Figure 1.13: A schematic representation of the adsorption of Lipase onto hydrophobic surfaces, reproduced with permission from Magner *et al.*⁵⁶ Licence number: 3807051388538.

Monduzz and co-workers demonstrated this immobilisation technique for a lipase from *Mucor javanicus*, which was adsorbed on to a polypropylene mesoporous 1004 powder. An increased activity was observed upon immobilisation which was accounted for by the immobilisation of the enzyme rendering the enzyme permanently in an open conformation and thus active.⁷⁷ One of the most striking characteristics of lipases is that they are encountered in two configurations: the “open” active conformation or the “closed” inactive conformation.⁷⁸ In its open conformation, hydrophobic residues are exposed, thus enabling immobilisation onto hydrophobic supports. This process is entropically driven allowing for the displacement of water molecules on the hydrophobic surface (Figure 1.13).^{56,77}

1.3.4 Characterisation of enzyme stabilisation

Once the enzymes have been immobilised, it is important to be able to monitor and characterise the stability of the enzyme to determine whether any additional stability

has been imparted. It is possible to monitor the stability of a biocatalyst utilising CD spectroscopy (to obtain a thermal unfolding curve) and to record the melting temperatures (T_m) of these enzymes. An alternative technique is differential scanning calorimetry (DSC) from which it is possible to calculate ΔH , T_m , and the change in Gibbs free energy when the protein is transitioning from the folded (active) to unfolded (inactive) state.⁷⁹

Although the enzyme activity is related to its structure, it is not possible to quantify the residual activity by quantifying the degree of folding,⁷⁹ Therefore residual activity is directly calculated using enzyme assays. This is usually done through the use of absorbance/fluorescence spectroscopic techniques to detect the rate at which the enzyme catalyses a reaction, which can be used to calculate a kinetic deactivation curve (Figure 1.14). By plotting the natural logarithm (ln) of residual activity *versus* time, it is possible to produce a straight line, the gradient of which equates to the rate of deactivation constant ($-k$). This is the rate at which a loss in enzymatic activity is observed in respect to time. An enzyme half-life ($\tau_{1/2}$) can then be calculated, where $\tau_{1/2} = \ln(2/k)$.^{79, 80}

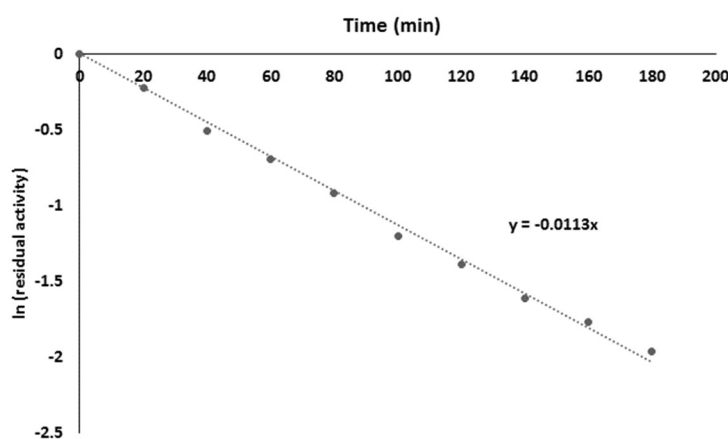


Figure 1.14: Kinetic deactivation curve where the gradient is equal to $-k$.

1.4 Enzyme mimics

Enzymes have evolved to provide Nature with some of the most efficient catalysts, which are finely tuned for catalysis in different environmental conditions.³ This is achieved through specific protein folding creating specific active sites for substrate recognition. Whilst enzymes have the major advantage of being able to carry out catalysis in water, one of the main drawbacks is the loss of activity due to denaturation once the enzymes are isolated as mentioned in Paragraph 1.3. Stabilisation of enzymes is a complex process due to differences in structures and reaction conditions for enzymes. Another disadvantage of enzymes is that they are unable to catalyse all chemical reactions such as the Kemp reaction and the Diels-Alder reactions.⁸¹ As a result, many chemists have explored alternative routes using enzyme-inspired properties of small molecules to mimic the catalytic site of enzymes.⁸²⁻⁸⁶

One technique for the formation of enzyme-like catalysts is the use of molecularly imprinted polymers (MIP). For example, Mashelkar *et al.* have imprinted the amino acids found within the chymotrypsin active site into hydrogels.⁸⁷ The synthesis of these gels relies on the coordination of metals to the monomer species prior to polymerisation, thus creating a three dimensional cavity for catalysis (Figure 1.15)⁸⁸.⁸⁹ The work by Mashelkar involved the polymerisation of three amino acids (serine, aspartic acid, and histidine), in which a cooperative triad was formed. This triad mimicked the active site of the chymotrypsin active site and was shown to hydrolyse an ester bond.^{89, 90}

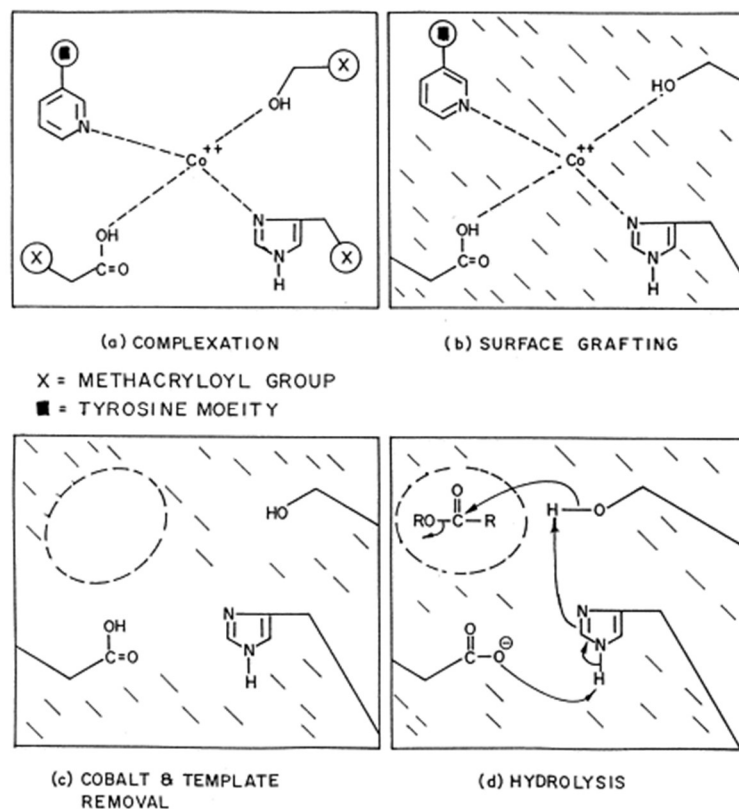


Figure 1.15: A schematic representation of the catalytic cavity formation using a MIP, Reprinted with permission from *Molecularly Imprinted Hydrogels Exhibit Chymotrypsin-like Activity*. *Macromolecules* 1996, 29 (4), 1366-1368. Copyright (1996) American Chemical Society.⁸⁹

Fréchet and Hawker have explored dendrimers for acylation reactions utilising the catalyst 4-(dialkylamino)pyridine (DAP).⁹¹ It is proposed that creating this hydrophobic pocket is similar to the active site found within enzymes. Upon catalysis in nonpolar solvents, the polar substrates preferentially accumulated in the dendrimer cavity, leading to high conversions and accelerated reaction times. This is now referred to as the “concentrator effect”, where the substrates and catalyst are brought into close proximity resulting in the acceleration of the reaction.^{91, 92}

Spherical morphologies formed by amphiphilic block copolymers are of significant interest, as the central hydrophobic block is protected by the hydrophilic corona and can be used as a central domain for sequestration and encapsulation.^{93, 94} The

immobilisation of catalysts onto the hydrophobic domain of an amphiphilic block copolymer has been widely explored.⁹⁵⁻⁹⁸ Work with organic catalysts such as L-proline showed that immobilisation of this catalyst into the core of a nanoreactor enabled the aldol reaction to take place in aqueous conditions giving similar rates to the catalysis in organic media.^{99, 100} Other examples, such as the catalyst 4-dimethylaminopyridine (DMAP), showed specificity towards more hydrophobic substrates, with the introduction of hydrophobic substrates in water resulting in higher conversions.¹⁰¹ All of these nanoreactors utilised the concentrator effect, in which the substrates preferentially diffuse into the core of the nanoparticle, and both substrates and catalysts are brought into close proximity accelerating the reaction.⁹¹ Additionally, the use of such a nanoreactor enables organic reactions to take place within aqueous media through diffusion of reactants into the hydrophobic core, this will be further discussed in Chapter 3.

1.5 Guanidine catalysts

Nature has produced a sublime array of catalysts (enzymes), utilising the functionality provided by amino acids to create specific binding sites and three-dimensional structures for substrate recognition.⁹⁴ Moreover, the specificity of these enzymes enables turnover numbers (conversion of substrate per second) far superior to the ones obtained from most synthetic organocatalysts. However, one of the main disadvantages of enzymes is they are expensive and can denature readily, losing activity upon changing pH, solvent, temperature and/or pressure, thus organocatalysts provide an alternative route for catalysis.¹⁰²

Guanidines have been shown to catalyse many organic reactions.¹⁰³⁻¹⁰⁵ The defining feature of this group is the central imine surrounded by two additional nitrogen groups. Guanidines are some of the strongest neutral organic bases, with the ability to accept a proton and delocalise this charge over two nitrogen atoms.¹⁰⁶ This functionality is found in Nature on the amino acid side chain of arginine. The presence of arginine (L96) in the antibody 43C9 (a protein produced by the immune system) enables transition-state stabilisation for both amide and ester hydrolysis.^{1, 107} There are a wide range of guanidine-containing organocatalysts such as 1,5,7-triazabicyclo[4.4.0]dec-5-ene (TBD), 7-methyl-1,5,7-triazabicyclo[4.4.0]dec-5-ene (MTBD), 1,1,3,3-tetramethyl guanidine (TMG), 1,4,6-triazabicyclo-[3.3.0]oct-4-ene (TBO) and arginine (ARG) (Figure 1.16).

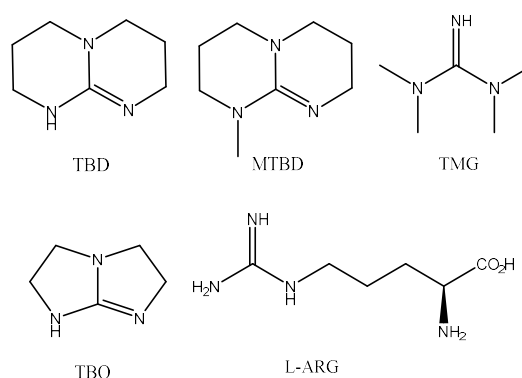
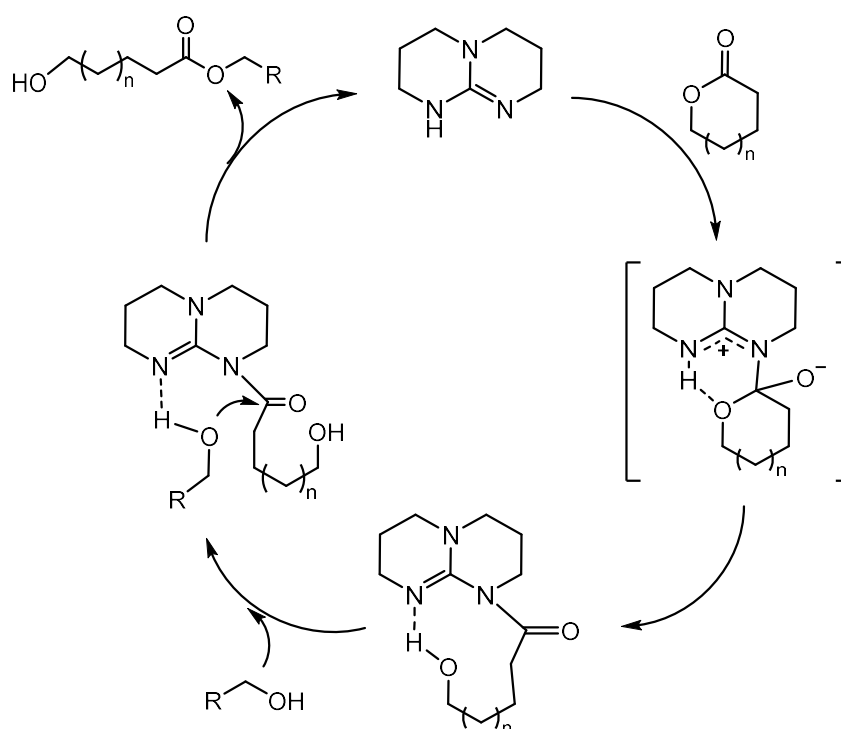


Figure 1.16: The structures of guanidine-containing organocatalysts TBD, MTBD, TMG, TMO and ARG.

Despite having relatively similar pK_a values (Table 1.1) it is often found that TBD can carry out reactions more efficiently than its methylated analogue, MTBD. This was shown by Waymouth *et al.* in the ring-opening polymerisations (ROP) of L-lactide, where TBD catalysed the ROP at much lower catalytic loadings and at faster rates in comparison to MTBD.^{108, 109}

Table 1.1: The pK_a values for TBD, MTBD, TMG and ARG. *Predicted values from Leito *et al.*¹¹⁰

Guanidine	pK_a (Acetonitrile)	pK_a (Water)	pK_a (THF)
TBD	26.0 ¹¹¹	15.2 ± 1.0 ^{*110}	21 ¹¹¹
MTBD	25.5 ¹¹¹	15.0 ± 1.0 ^{*110}	17.9 ¹¹¹
TMG	23.7 ¹⁰⁵	13.0 ± 1.0 ^{*110}	14.0 ¹¹¹
ARG	-	12.5 ⁵	-



Scheme 1.3: Mechanism of the ring opening polymerisation of L-lactide catalysed by TBD, in THF at 1 mol% catalyst loading, this polymerisation was observed for 40 minutes reaching 99% conversion.

The catalytic mechanism of this reaction has been widely discussed, and it is suggested that TBD acts as a bi-functional acylation catalyst during ROP (Figure 1.13).^{104, 112} Nucleophilic attack of the imine nitrogen on the carbonyl group forms an intermediate with a protonated nitrogen in a fixed position enabling proton transfer, and resulting in the formation of a TBD-amide species.^{112, 113} This species is able to hydrogen bond with an alcohol functionality and results in the release of an

ester and regeneration of the TBD catalyst. Whilst this mechanism is still debated, it has been suggested that TBD can act as a bi-functional transesterification catalyst where initial formation of the acyl intermediate is followed by hydrogen bonding stabilising the intermediated formed.^{108, 112, 114}

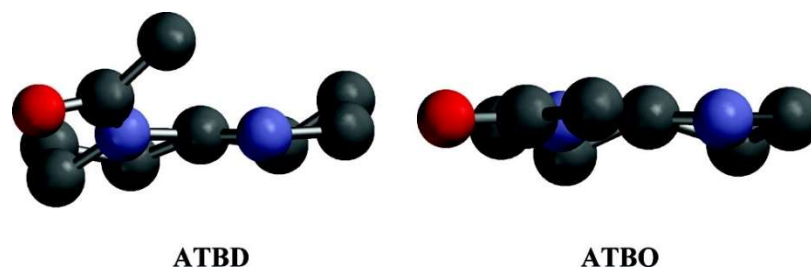


Figure 1.17: The structure of Acyl-TBD (ATBD) in the twisted intermediate and the Acyl-TBO in the planar intermediate, reprinted with permission from *Cyclic Guanidine Organic Catalysts: What Is Magic About Triazabicyclodecene?* *J. Org. Chem.*, 2009, 74 (24), 9490-9496. Copyright (2009) American Chemical Society.¹¹⁴

Another example demonstrating the efficiency of TBD as a catalyst is the comparative investigation of TBD and TBO as acylation catalysts. This theoretical study was carried out by Waymouth *et al.* who determined that the specific amide-TBD intermediate creates a higher energy twisted intermediate, rather than a planar intermediate (as seen with the Acyl-TBO), enabling the reaction to proceed (Figure 1.17).¹¹⁴ Indeed, these studies demonstrate how the structural components of TBD account for the observed higher activity over other similar catalysts.

1.6 Self-assembly of amphiphilic block copolymers

The formation of higher ordered structures, such as the aforementioned spherical morphologies which exploit the concentrator effect, can be achieved by tuning the ratio of hydrophobic and hydrophilic block lengths of an amphiphilic block

copolymer. Reversible deactivation radical polymerisations techniques (*e.g.* RAFT) have enabled the formation of copolymers with a range of functionalities located within the polymer microstructure. Indeed, well-defined block copolymers can be used to form specific self-assembled nanostructures through exploitation of selective solubility and interactions. This phenomenon occurs through the reorganisation of the polymer in solution to increase the interactions of the soluble block with the solvent, thus minimising unfavourable solvent interactions with the insoluble block.^{115, 116} These blocks are covalently bound, thus preventing phase-separation taking place and resulting in the formation of higher-order nanostructures. A wide range of specific structures can be targeted through manipulation of the packing parameter, ρ , as defined in Equation 1.2, by altering the polymeric block lengths.^{117, 118} When $\rho \leq \frac{1}{3}$ spherical micelles are formed, $\frac{1}{3} \leq \rho \leq \frac{1}{2}$ cylindrical micelles are formed and at $\frac{1}{2} \leq \rho \leq 1$ vesicles form (Figure 1.18).

$$\rho = \frac{v}{a_0 l_c}$$

Equation 1.2: Packing parameter, ρ , where v is the volume of the hydrophobic chains, a_0 is the optimal area of the head group (hydrophilic group) and l_c is the length of the fully extended hydrophobic tail.

As a general rule it can be said that for spherical micelle formation (in water), the volume fraction of the hydrophilic block must be greater than that of the hydrophobic block.

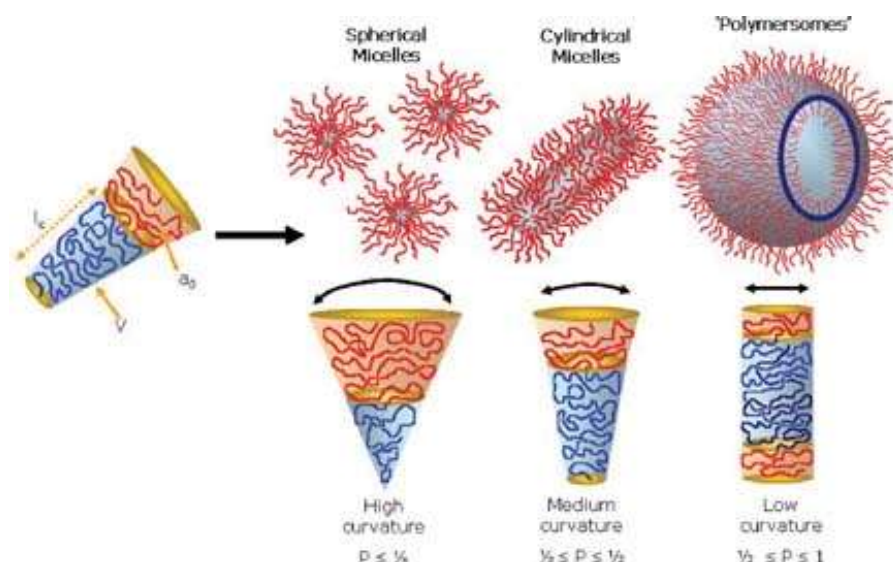


Figure 1.18: Self-assembled structures formed by amphiphilic block copolymers and assignment of packing parameters, p , Reprinted with permission from Ryan *et al.*¹¹⁷ license number 3807060606613.

There are three common techniques for the preparation of micelles: solvent-switch, thin film method, or direct dissolution techniques. Block copolymers with a high glass transition temperature (T_g) are generally considered to form “frozen” nanoparticles, meaning there is little unimer exchange between the aggregates and the solution (Figure 1.19).^{119, 120} The solvent switch method is commonly used for such high T_g polymers as it initially enables unimer exchange therefore enabling the formation of stable aggregates. A well-studied example is the assembly of micelles with poly(styrene)-*b*-poly(acrylic acid) (PSt-*b*-PAA).¹²¹ Here, *N,N*-dimethylformamide (DMF) initially solvates both blocks, and as water, a selective solvent for PAA, is slowly added the DMF decreases the free energy between the styrenic block and water. As a critical water fraction is reached, these micelles become kinetically frozen consisting of a PSt core with a PAA corona.¹¹⁵ Residual DMF is subsequently removed by dialysis.

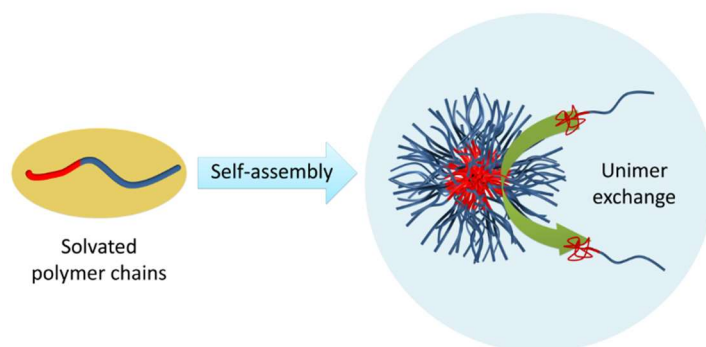


Figure 1.19: An illustration of a micelle assembly and the unimer exchange into the solution of the polymeric chains.

Interestingly, the morphology of the aggregates formed can be influenced by the solvent used. For instance, work from Eisenberg *et al.* has shown that switching the solvent from either DMF, tetrahydrofuran (THF), or 1,4-dioxane can lead to different morphologies of PSt-*b*-PAA nanostructures.^{115, 122} In this example the solubility parameter of styrene closely matched that of THF and 1,4-dioxane increasing the chain swelling and effectively producing larger core aggregates. THF and 1,4-dioxane also have lower dielectric constants and a combination of both these factors results in the formation of multiple morphologies ranging from spherical micelles, rods, vesicles, and large compound micelles.

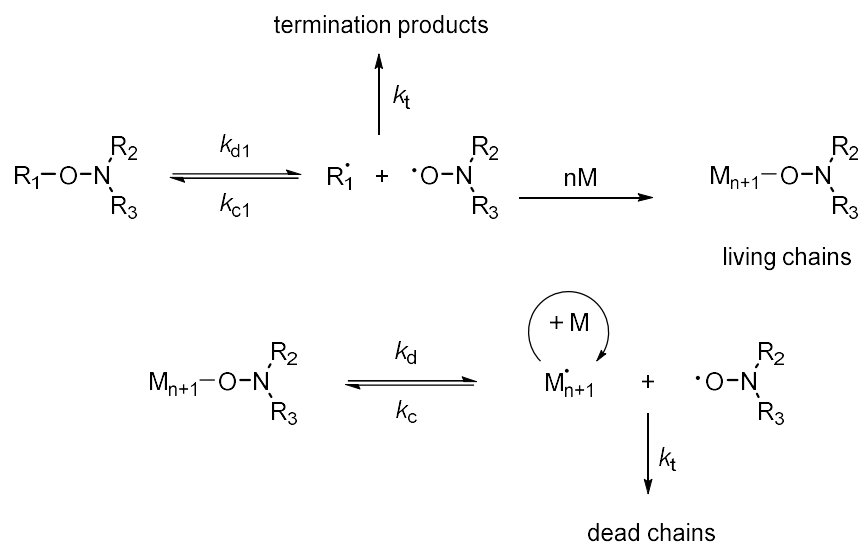
1.7 Polymerisation techniques

To enable synthesis of well-defined amphiphilic block copolymers required for the production of these self-assemblies, a range of polymerisation techniques can be used. A commonly used technique is a reversible deactivation radical polymerisation (RDRP), like ring opening polymerisations and anionic polymerisations they provide control over the molecular weight and afford polymers with relatively narrow

dispersities.^{123, 124} Since the initial development of these polymerisation methods, around 20 years ago, advances in RDRP have greatly improved.¹²⁵ The main advantages of RDRP techniques over other methods is they require simple sample preparation and often use commercially available starting materials.¹²⁴ Ideally, these polymerisations should show a linear increase of molecular weight with monomer consumption, as well as the ability to chain extend/ reinitiate the polymerisation, with linear evolution with time.¹²⁶⁻¹²⁸ RDRP polymerisation techniques include: Nitroxide Mediated Polymerisation (NMP), Atom Transfer Radical Polymerisation (ATRP) and Reversible Addition-Fragmentation Chain Transfer (RAFT) Polymerisation.^{129, 130}

1.7.1 NMP

One of the first RDRP techniques, NMP, was first shown by the Commonwealth Scientific and Industrial Research Organisation (CSIRO) group in 1982 in which 2,2,6,6-tetramethylpiperidiny-1-oxyl (TEMPO) was used as an end capping group.¹³¹ In 1985 the CSIRO group patented this technique, whereby a nitroxide was used to control radical polymerisations.¹³² This technique utilised a thermally stable nitroxide radical which contained the N-O• functionality.^{133, 134} The mechanism of this polymerisation can be simplified (Scheme 1.4), however Johnson *et al.* have described a three stage polymerisation scheme.¹³⁵⁻¹³⁷



Scheme 1.4: The simplified mechanism of NMP. Adapted from Nicolas *et al.*¹²⁸ M = monomer, k_d = rate of decomposition, k_c = rate of recombination, k_t = rate of termination.

In the initiation step, the rate constant of dissociation (initiator homolysis) needs to be greater than radical association to ensure a high level of stable radical species. This leads to a greater level of control over the polymerisation.^{128, 135, 138} As the alkoxyamine species can readily decay, termination products reduce the number of radical species available within the solution, however upon addition of a nitroxide scavenger acceleration, such as TEMPO, increased rates of the homolysis of the alkoxyamine species is observed.¹³⁵ This increases the number of nitroxide end-capped propagating polymer species allowing greater control over the growing polymer chain.¹³⁹

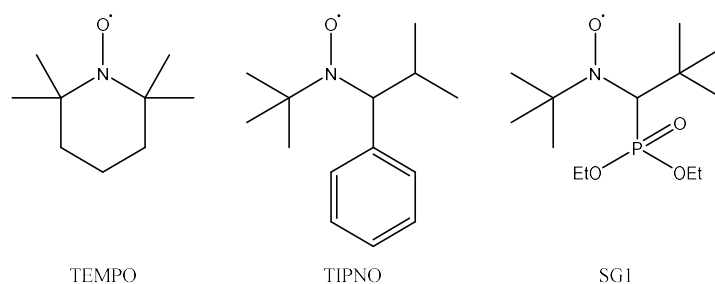


Figure 1.20: The structure of the nitroxides TEMPO, TIPNO and SG1.

NMP polymerisations were initially carried out using the nitroxide TEMPO (Figure 1.20). During the polymerisation TEMPO caps the propagating polymer chain reversibly allowing for control over the chain growth.¹³³ This technique was initially utilised for the polymerisation of styrene where it was found that control over high molecular weights gave relatively low dispersities of 1.3 in comparison to a reaction in the absence of the nitroxide species, where dispersities of 4.3 were obtained.¹³³ Attempts to modify the reactive radical species were carried out by Hawker *et al.*; here a benzoyloxy species capped the TEMPO radical forming an alkoxyamine species. This initiator was heated to 130 °C with styrene where the stable radical species and the initiating radical species form. This allowed for control over the molecular weight and produced well-defined polymers (dispersities \sim 1.06) with retention of the end group functionality.¹²⁶

Limitations of the NMP initiator TEMPO, was poor compatibility with a range of vinyl monomers, as the polymerisation is primarily limited to styrenic monomers.^{140,}¹⁴¹ This is because of the lower rate constants for the initiation step when polymerising acrylates (k). Indeed Lacroix-Desmazes *et al.* have investigated the rate constants of styrene and butyl acrylate with the nitroxide initiator *N-tert*-butyl-1-diethylphosphono-2,2-dimethylpropyl nitroxide (SG1, Figure 1.20). The rate

constant with styrene was $6.1 \times 10^{-9} \text{ mol L}^{-1}$ whereas it was calculated as $9.2 \times 10^{-11} \text{ mol L}^{-1}$ for the polymerisation of butyl acrylate, almost two orders of magnitude slower.¹⁴²⁻¹⁴⁴ This lower rate constant indicated the need for longer reaction times increasing the likelihood of termination within the reaction. In order to reduce the formation of termination products it is necessary to use a greater excess of the free nitroxide to maintain the persistent radical effect. This will both increase the rate of the reaction and the formation of termination products allowing for the polymerisation of a wider variety of monomers (such as styrene's, acrylates and acrylamides).¹⁴⁵

The structure of the nitroxide is critical for control over the polymerisation. Hawker *et al.* have developed numerous alkoxyamine initiators aiming to develop a universal initiator which can allow control of the polymerisation of a vast array of monomers.¹⁴⁶ Their work focused on the synthesis of alkoxyamines containing an α -hydrogen species, chosen as they have lower stability and hence can be used for polymerisations with less active monomer species such as acrylamides.¹⁴⁰ The alkoxyamine 2,2,5-trimethyl-3-(1-phenylethoxy)-4-phenyl-3-azahexane (Figure 1.21) showed control over a wide variety of monomers including acrylamides, acrylates, and styrenes affording polymers with narrow dispersities.¹⁴⁰ This initiator enables both the copolymerisation and incorporation of different functionalities into the polymer backbone and hence it is now known as the universal initiator for NMP.

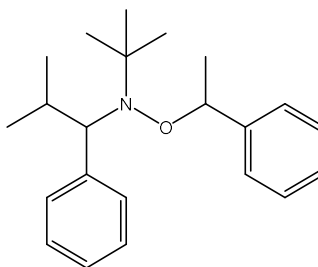


Figure 1.21: Structure of the NMP universal initiator.

1.7.2 ATRP

The first examples of ATRP were demonstrated in 1995 by both Sawamoto and Matyjaszewski, who demonstrated control over the polymerisation of methacrylates and styrene using transition metal complexes.^{147, 148} ATRP requires an alkyl halide to initiate the polymerisation; the halide bond reversibly endcaps the polymer species allowing for equilibrium between the active (growing) species and the dormant species (Figure 1.22). The halide coordinates with the transition metal increasing its oxidation state. This polymerisation technique can be used with an array of monomers allowing for the synthesis of multiblock polymers as well as complex architectures.¹⁴⁹

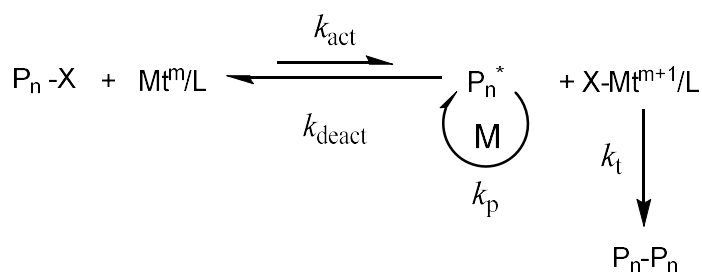


Figure 1.22: ATRP equilibrium mechanism.¹⁴⁹ P_n-X is the halide capped polymer chain, Mt^m/L is the transition metal at an oxidation state m, and L is the ligand. M represents the monomers, and P_n the polymer chain, and *k* the rate constants for activation (act), deactivation (deact), propagation (p) and termination (t).

1.7.3 RAFT Polymerisation

RAFT polymerisation was first demonstrated in 1998 by Rizzardo and Moad from the CSIRO in Australia.^{150, 151} However, it should be noted that six months prior to this Rhodia Chimie *et al.* reported the technique MADIX (Macromolecular Design *via* Interchange of Xanthates). This technique is a specific RAFT technique using xanthate chain transfer agents (CTAs) for the polymerisation of less active monomers such as vinyl acetate.¹⁵² Many advantages are gained with RAFT polymerisation as it is a versatile technique and can be used to polymerise a range of functional monomers in a range of solvents, and it provides resultant polymers with low dispersities.^{124, 153} The RAFT mechanism is shown in Figure 1.23. It is apparent that no radicals are formed or destroyed in the degenerative transfer steps (Figure 1.23, *reversible chain transfer*) which impart polymerisation control, thus radical initiators are required from an external source. Widely used initiator species are azo compounds, such as azobisisobutyronitrile (AIBN), which initiate *via* thermal decomposition with a half-life of 10 hours at 65 °C.¹²⁷ This initiating radical will react with the monomer to form propagating radicals (Figure 1.23, *initiation*). The propagating radical then undergoes an addition to the thiocarbonylthio compound forming an intermediate radical (Figure 1.23, *reversible chain transfer/propagation*). The weak S-R bond breaks as the R-group is a good leaving group in comparison to the monomer, causing the formation of an R• radical and a polymeric thiocarbonylthio compound.^{154, 155} The R• radical goes on to form new propagating radicals (Figure 1.23, *reinitiation*). Due to an equal probability of the radicals reacting with thiocarbonylthio compounds reducing the formation of dead chains, the process enables the formation of polymers with narrow dispersities.¹⁵⁵ Most of the polymer chains contain the thiocarbonylthio end group once the reaction is

quenched. There are two factors that determine the molecular weight (M_n) of the resultant polymer, the RAFT agent consumption and the initiator decomposition. Initiator concentration needs to be kept low and constant in an RDRP, increasing the initiator concentration leads to a decrease in M_n and an increased dispersities (D_M) at higher conversions.¹⁵⁶

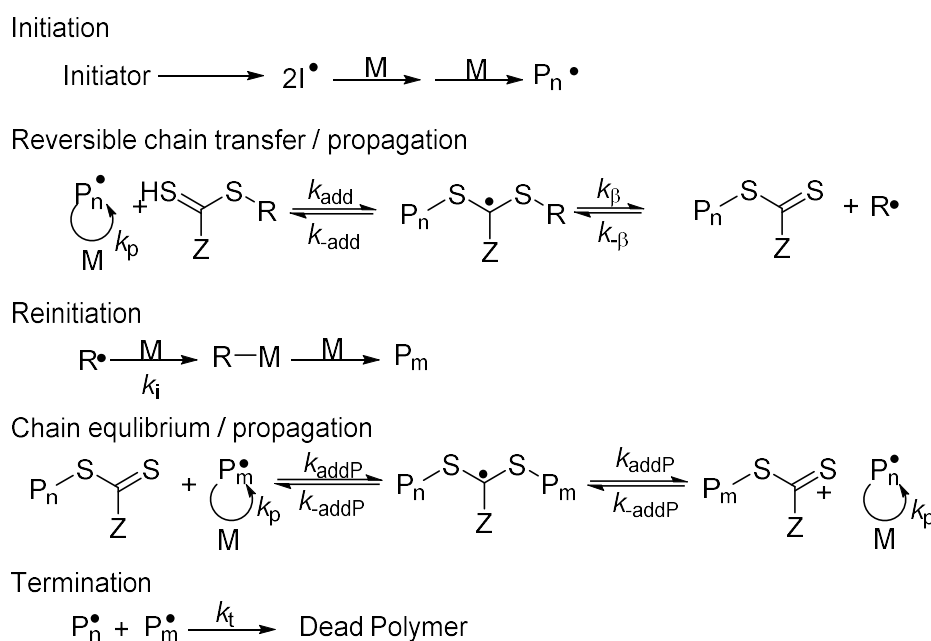
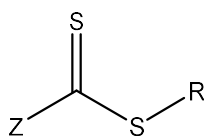


Figure 1.23: A schematic of the RAFT mechanism. Reproduced from Moad *et al.*¹⁵⁴

The mechanism above is a simplified version of the RAFT mechanism.¹⁵⁴ Inhibition and retardation are frequently observed during RAFT reactions and many modelling strategies have tried to rationalise these observations with regard to the mechanism.¹⁵⁷ Inhibition can be observed when no polymerisation of the monomers takes place upon the formation of a radical species, whereas rate retardation is dependent on the re-initiation of dormant chains which can be due to poor choice in “R” group, initiators or impurities. The intermediate radical termination model (stationary state)

suggested by Monteiro *et al.* has been shown to influence retardation. This is as a result of slow re-initiation of the dormant chains with R• radical.^{156, 158}

A wide variety of different architectures is accessible through RAFT polymerisation methods, such as stars, hyper-branched structures, combs, micelles and micro gels.^{151, 159} Good control over the polymerisation is achieved by a careful choice of RAFT agent (a.k.a. the CTA), initiator, monomer and solvent system.¹⁶⁰ Figure 1.24 shows the generic structure of a RAFT agent, of which there are four main categories: trithiocarbonates, dithioesters, dithiocarbamates, and xanthates.



1. Z = SR, Trithiocarbonate
2. Z = alkyl or aryl, Dithioester
3. Z = NR₂, Dithiocarbamate
4. Z = O-alkyl, Xanthate

R = alkyl or H

Figure 1.24: The generic structure of a RAFT agent, adapted from O'Reilly *et al.*¹⁶¹

There is a wide variety of RAFT agents available both commercially and also through the application of simple chemistries.¹⁶² Choosing the correct RAFT agent is primarily dependent on the choice of monomer being polymerised, and this is controlled by the R and Z groups present in the CTA. As a generic rule, the R group needs to be a good leaving group in comparison to the growing polymer chain, as well as good at re-initiating the polymerisation.¹³⁰ When choosing an R group, steric bulk and polarity need to be considered, as a poor choice will result in slow fragmentation occurring, leading to consumption of the radical CTA species.¹⁶³ The

role of the Z group is to activate or deactivate the C=S double bond. It is possible to change the addition rate coefficient, k_{add} , by five orders of magnitude through simply changing the Z group.¹⁶³ The transfer constant is enhanced by electron withdrawing groups which lead to higher chain transfer coefficients, although this can cause side reactions to take place. Another role of the Z group is to stabilise the intermediate radical formed.¹⁵⁵ Extensive work has been carried out by the CSIRO group to determine the rate constants for specific RAFT agents as well as finding a universal RAFT agent for a controlled polymerisation over all monomer species, through modulation of the pH of the polymerisation mixture.¹⁵⁴ Nevertheless, the correct selection of both the R and Z groups is critical to ensure the desired outcome of the polymerisation, here Figure 1.25, summarises the preferred R and Z groups for a range of different monomer species.¹⁶³

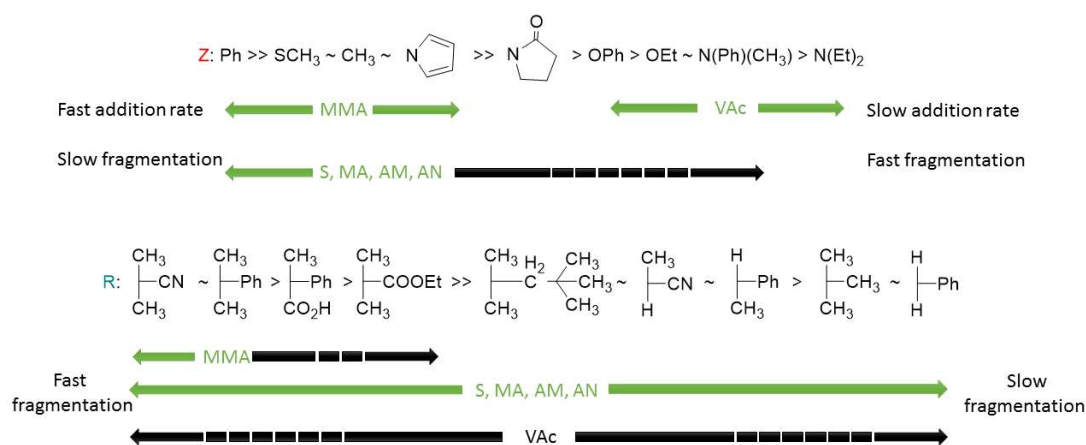


Figure 1.25: Guidelines for selecting which RAFT agent to use, here S = styrenes, MA = methacrylates, AA = acrylic acid, AM = acrylamide, AN = acrylonitrile, MMA = methyl methacrylate and Vac = vinyl acetate. The dotted lines indicate that there is partial control over the polymerisation, adapted from a Moad *et al.*¹⁵⁴

1.8 Concluding remarks

Nature has developed natural biocatalysts which are found to be most active when they are folded into their specific conformations and operating in their optimum conditions. Owing to their instability outside of these parameters, various techniques have been explored to stabilise enzymes and increase their resistance to their surroundings. Additives, covalent and non-covalent bonding of enzymes are promising techniques to provide stabilisation without loss of activity, monitored through examining changes in the secondary structure.

Enzyme mimics are explored as stable alternatives of enzymes, such as self-assembled structures, these rely on well-defined polymers, and can be readily synthesised *via* controlled polymerisations. The literature has provided excellent examples where tethering catalysts to the hydrophobic core of a micellar nanoreactor enables higher specificity and activity enhancing the activity of organic catalysts. These nanoreactors have facilitated the catalysis of organic reactions in water with substrates specificity, protecting the catalytic core.

1.9 References

1. T. Bugg, *Introduction to enzyme and coenzyme chemistry*, Wiley, Hoboken, New Jersey, Third edn., 2012.
2. T. C. Bruice, *Acc. Chem. Res.*, 2002, **35**, 139-148.
3. K. S. Siddiqui and R. Cavicchioli, *Annu. Rev. Biochem.*, 2006, **75**, 403-433.
4. P. A. Fields, Y. Dong, X. Meng and G. N. Somero, *J. Expt. Biol.*, 2015, **218**, 1801-1811.
5. R. Horton, L. Moran, G. Scrimgeour, M. Perry and D. Rawn, *Principles of Biochemistry*, Pearson International Edition, New Jersey, Fourth edn., 2006.
6. L. Mandrich, L. Merone, M. Pezzullo, L. Cipolla, F. Nicotra, M. Rossi and G. Manco, *J. Mol. Biol.*, 2005, **345**, 501-512.
7. G. E. Schulz and R. H. Schirmer, *Principles of protein structure*, Springer Science & Business Media, 2013.
8. B. Alberts, D. Bray, J. Lewis, M. Raff, K. Roberts and J. Watson, *Mol. Biol. Cell*, 1989, **2**, 87-134.
9. L. Brady, A. M. Brzozowski, Z. S. Derewenda, E. Dodson, G. Dodson, S. Tolley, J. P. Turkenburg, L. Christiansen, B. Huge-Jensen, L. Norskov, L. Thim and U. Menge, *Nature*, 1990, **343**, 767-770.
10. Y. Cajal, A. Svendsen, V. Girona, S. A. Patkar and M. A. Alsina, *Biochemistry*, 1999, **39**, 413-423.
11. R. Aurora, T. P. Creamer, R. Srinivasan and G. D. Rose, *J. Biol. Chem.*, 1997, **272**, 1413-1416.

12. L. Schrodinger, *Journal*, 2010.
13. K. A. Dill and H. S. Chan, *Nat. Struct. Biol.*, 1997, **4**, 10-19.
14. C. M. Dobson, *Nature*, 2003, **426**, 884-890.
15. M. Karplus, *Fold. Des.*, 1997, **2**, **Supplement 1**, S69-S75.
16. C. Levinthal, *J. Chim. Phys. Phys. Chim. Biol.*, 1968, **65**, 44-45.
17. B. Honig, *J. Mol. Biol.*, 1999, **293**, 283-293.
18. R. Zwanzig, A. Szabo and B. Bagchi, *Proc. Natl. Acad. Sci. U.S.A.*, 1992, **89**, 20-22.
19. R. L. Baldwin and G. D. Rose, *Trends Biochem. Sci*, 1999, **24**, 26-33.
20. R. L. Baldwin and G. D. Rose, *Trends Biochem. Sci*, 1999, **24**, 77-83.
21. G. C. Rollins and K. A. Dill, *J. Am. Chem. Soc.*, 2014, **136**, 11420-11427.
22. P. Edman and G. Begg, *Eur. J. Biochem.*, 1967, **1**, 80-91.
23. S. A. Trauger, W. Webb and G. Siuzdak, *Spectroscopy*, 2002, **16**.
24. S. M. Kelly and N. C. Price, *Curr. Protein Pept. Sci.*, 2000, **1**, 349-384.
25. A. Barth, *Biochim. Biophys. Acta -Bioenergetics*, 2007, **1767**, 1073-1101.
26. K. Wüthrich, *J. Biol. Chem.*, 1990, **265**, 22059-22062.
27. L. L. Hyland, M. B. Taraban and Y. B. Yu, *Soft Matter*, 2013, **9**, 10218-10228.
28. J. C. Kendrew, G. Bodo, H. M. Dintzis, R. G. Parrish, H. Wyckoff and D. C. Phillips, *Nature*, 1958, **181**, 662-666.

29. H. M. Berman, J. Westbrook, Z. Feng, G. Gilliland, T. Bhat, H. Weissig, I. N. Shindyalov and P. E. Bourne, *Nucleic Acids Res.*, 2000, **28**, 235-242.
30. H. Berman, K. Henrick and H. Nakamura, *Nat. Struct. Mol. Biol.*, 2003, **10**, 980-980.
31. S. M. Kelly, T. J. Jess and N. C. Price, *Biochim. Biophys. Acta*, 2005, **1751**, 119-139.
32. L. Whitmore and B. A. Wallace, *Biopolymers*, 2008, **89**, 392-400.
33. N. Sreerama, S. Y. U. Venyaminov and R. W. Woody, *Protein Sci.*, 1999, **8**, 370-380.
34. L. Whitmore and B. A. Wallace, *Nucleic Acids Res.*, 2004, **32**, W668-W673.
35. R. J. Roe, *Methods of X-ray and neutron scattering in polymer science*, Oxford University Press, New York, first edn., 2000.
36. J. P. Patterson, M. P. Robin, C. Chassenieux, O. Colombani and R. K. O'Reilly, *Chem. Soc. Rev.*, 2014, **43**, 2412-2425.
37. B. Chu and B. S. Hsiao, *Chem. Rev.*, 2001, **101**, 1727-1762.
38. B. Hammouda, *J. Appl. Crystallogr.*, 2010, **43**, 716-719.
39. S. Doniach, *Chem. Rev.*, 2001, **101**, 1763-1778.
40. O. Glatter and O. Kratky, *Small angle x-ray scattering*, Academic Press, London, First edn., 1982.
41. A. Salis, M. Monduzzi and V. Solinas, in *Industrial Enzymes*, Springer Netherlands, 2007.

42. O. Kirk, T. V. Borchert and C. C. Fuglsang, *Curr. Opin. Biotechnol.*, 2002, **13**, 345-351.
43. E. Chi, S. Krishnan, T. Randolph and J. Carpenter, *Pharm. Res.*, 2003, **20**, 1325-1336.
44. F. Hasan, A. A. Shah, S. Javed and A. Hameed, *Afr. J. Biotechnol.*, 2010, **9**, 4836-4844.
45. Jan H. Van Ee, O. Misset and E. J. Baas, *Enzymes in detergency*, Marcel Dekker, New York, 1997.
46. R. Sharma, Y. Chisti and U. C. Banerjee, *Biotechnol. Adv.*, 2001, **19**, 627-662.
47. G. D. Haki and S. K. Rakshit, *Bioresour. Technol.*, 2003, **89**, 17-34.
48. B. van den Burg, *Curr. Opin. Microbiol.*, 2003, **6**, 213-218.
49. C. Vieille and G. J. Zeikus, *Microbiol. Mol. Biol. Rev.*, 2001, **65**, 1-43.
50. R. Cavicchioli, K. S. Siddiqui, D. Andrews and K. R. Sowers, *Curr. Opin. Biotechnol.*, 2002, **13**, 253-261.
51. J. K. Kaushik and R. Bhat, *J. Phys. Chem. B*, 1998, **102**, 7058-7066.
52. S. A. Costa, T. Tzanov, A. Filipa Carneiro, A. Paar, G. M. Gübitz and A. Cavaco-Paulo, *Enzyme Microb. Technol.*, 2002, **30**, 387-391.
53. J. N. Talbert, L.-S. Wang, B. Duncan, Y. Jeong, S. M. Andler, V. M. Rotello and J. M. Goddard, *Biomacromolecules*, 2014, **15**, 3915-3922.
54. H. Li, M. Li, X. Yu, A. P. Bapat and B. S. Sumerlin, *Polym. Chem.*, 2011, **2**, 1531-1535.

55. H. Li, A. P. Bapat, M. Li and B. S. Sumerlin, *Polym. Chem.*, 2011, **2**, 323-327.
56. U. Hanefeld, L. Gardossi and E. Magner, *Chem. Soc. Rev.*, 2009, **38**, 453-468.
57. K. L. Heredia, D. Bontempo, T. Ly, J. T. Byers, S. Halstenberg and H. D. Maynard, *J. Am. Chem. Soc.*, 2005, **127**, 16955-16960.
58. R. J. Mancini, J. Lee and H. D. Maynard, *J. Am. Chem. Soc.*, 2012, **134**, 8474-8479.
59. C. Ó'Fágáin, *Enzyme Microb. Technol.*, 2003, **33**, 137-149.
60. J. Lee, E.-W. Lin, U. Y. Lau, J. L. Hedrick, E. Bat and H. D. Maynard, *Biomacromolecules*, 2013, **14**, 2561-2569.
61. C. Colaco, S. Sen, M. Thangavelu, S. Pinder and B. Roser, *Nat. Biotechnol.*, 1992, **10**, 1007-1011.
62. N. Spreti, P. Di Profio, L. Marte, S. Bufali, L. Brinchi and G. Savelli, *Eur. J. Biochem.*, 2001, **268**, 6491-6497.
63. M. A. Singer and S. Lindquist, *Mol. Cell*, 1998, **1**, 639-648.
64. J. J. O'Malley and R. W. Ulmer, *Biotechnol. Bioeng.*, 1973, **15**, 917-925.
65. M. M. Andersson and R. Hatti-Kaul, *J. Biotechnol.*, 1999, **72**, 21-31.
66. A. Abuchowski, J. R. McCoy, N. C. Palczuk, T. van Es and F. F. Davis, *J. Biol. Chem.*, 1977, **252**, 3582-3586.
67. Z. P. Tolstyka and H. D. Maynard, *9.17: Protein–Polymer Conjugates*, Elsevier, Amsterdam, 2012.

68. I. Bhushan, R. Parshad, G. N. Qazi, G. Ingavle, C. R. Rajan, S. Ponrathnam and V. K. Gupta, *Process Biochem.*, 2008, **43**, 321-330.
69. E. Baslé, N. Joubert and M. Pucheault, *Chem. Biol.*, 2010, **17**, 213-227.
70. S.-H. Choi, K.-P. Lee and H.-D. Kang, *J. Appl. Polym. Sci.*, 2003, **88**, 1153-1161.
71. J. D. Wallat, K. A. Rose and J. K. Pokorski, *Polym. Chem.*, 2014, **5**, 1545-1558.
72. J. M. Gilmore, R. A. Scheck, A. P. Esser-Kahn, N. S. Joshi and M. B. Francis, *Angew. Chem. Int. Ed.*, 2006, **45**, 5307-5311.
73. H. B. F. Dixon, *J. Protein Chem.*, 1984, **3**, 99-108.
74. D. Bontempo and H. D. Maynard, *J. Am. Chem. Soc.*, 2005, **127**, 6508-6509.
75. B. Le Droumaguet and K. Velonia, *Angew. Chem. Int. Ed.*, 2008, **120**, 6359-6362.
76. H. Murata, C. S. Cummings, R. R. Koepsel and A. J. Russell, *Biomacromolecules*, 2014, **15**, 2817-2823.
77. A. Salis, E. Sanjust, V. Solinas and M. Monduzzi, *J. Mol. Catal. B: Enzym.*, 2003, **24-25**, 75-82.
78. A. M. Brzozowski, H. Savage, C. S. Verma, J. P. Turkenburg, D. M. Lawson, A. Svendsen and S. Patkar, *Biochemistry*, 2000, **39**, 15071-15082.
79. K. M. Polizzi, A. S. Bommarius, J. M. Broering and J. F. Chaparro-Riggers, *Curr. Opin. Chem. Biol.*, 2007, **11**, 220-225.

80. A. S. Bommarius, J. M. Broering, J. F. Chaparro-Riggers and K. M. Polizzi, *Curr. Opin. Biotechnol.*, 2006, **17**, 606-610.
81. F. Mirata and M. Resmini, in *Molecularly Imprinted Polymers in Biotechnology*, eds. B. Mattiasson and L. Ye, Springer International Publishing, Cham, 2015, DOI: 10.1007/10_2015_319, pp. 107-129.
82. M. Raynal, P. Ballester, A. Vidal-Ferran and P. W. N. M. van Leeuwen, *Chem. Soc. Rev.*, 2014, **43**, 1734-1787.
83. G. Wulff, *Chem. Rev.*, 2001, **102**, 1-28.
84. Z. Dong, Q. Luo and J. Liu, *Chem. Soc. Rev.*, 2012, **41**, 7890-7908.
85. D. Carboni, K. Flavin, A. Servant, V. Gouverneur and M. Resmini, *Chem. Eur. J.*, 2008, **14**, 7059-7065.
86. P. Pasetto, S. C. Maddock and M. Resmini, *Anal. Chim. Acta*, 2005, **542**, 66-75.
87. R. N. Karmalkar, M. G. Kulkarni and R. A. Mashelkar, *Macromolecules*, 1996, **29**, 1366-1368.
88. M. Resmini, *Anal. Bioanal. Chem.*, 2012, **402**, 3021-3026.
89. B. S. Lele, M. G. Kulkarni and R. A. Mashelkar, *React. Funct. Polym.*, 1999, **39**, 37-52.
90. B. S. Lele, M. G. Kulkarni and R. A. Mashelkar, *Polymer*, 1999, **40**, 4063-4070.
91. B. Helms, C. O. Liang, C. J. Hawker and J. M. J. Fréchet, *Macromolecules*, 2005, **38**, 5411-5415.

92. C. Liang and J. M. J. Fréchet, *Prog. Polym. Sci.*, 2005, **30**, 385-402.
93. J. Du and R. K. O'Reilly, *Soft Matter*, 2009, **5**, 3544-3561.
94. Z. Dong, W. Yongguo, Y. Yin and J. Liu, *Curr. Opin. Colloid Interface Sci.*, 2011, **16**, 451-458.
95. A. Lu and R. K. O'Reilly, *Curr. Opin. Biotechnol.*, 2013, **24**, 639-645.
96. B. M. Rossbach, K. Leopold and R. Weberskirch, *Angew. Chem. Int. Ed.*, 2006, **45**, 1309-1312.
97. Z. Ge, D. Xie, D. Chen, X. Jiang, Y. Zhang, H. Liu and S. Liu, *Macromolecules*, 2007, **40**, 3538-3546.
98. J. P. Patterson, P. Cotanda, E. G. Kelley, A. O. Moughton, A. Lu, T. H. Epps III and R. K. O'Reilly, *Polym. Chem.*, 2013, **4**, 2033-2039.
99. H. A. Zayas, A. Lu, D. Valade, F. Amir, Z. Jia, R. K. O'Reilly and M. J. Monteiro, *ACS Macro Lett.*, 2013, **2**, 327-331.
100. A. C. Evans, A. Lu, C. Ondeck, D. A. Longbottom and R. K. O'Reilly, *Macromolecules*, 2010, **43**, 6374-6380.
101. P. Cotanda and R. K. O'Reilly, *Chem. Commun.*, 2012, **48**, 10280-10282.
102. M. Benaglia, A. Puglisi and F. Cozzi, *Chem. Rev.*, 2003, **103**, 3401-3430.
103. A. Barbarini, R. Maggi, A. Mazzacani, G. Mori, G. Sartori and R. Sartorio, *Tetrahedron Lett.*, 2003, **44**, 2931-2934.
104. L. Zhang, R. C. Pratt, F. Nederberg, H. W. Horn, J. E. Rice, R. M. Waymouth, C. G. Wade and J. L. Hedrick, *Macromolecules*, 2010, **43**, 1660-1664.

105. C. Ghobril, C. Sabot, C. Mioskowski and R. Baati, *Eur. J. Org. Chem.*, 2008, **2008**, 4104-4108.
106. J. E. Taylor, S. D. Bull and J. M. J. Williams, *Chem. Soc. Rev.*, 2012, **41**, 2109-2121.
107. M. M. Thayer, E. H. Olender, A. S. Arvai, C. K. Koike, I. L. Canestrelli, J. D. Stewart, S. J. Benkovic, E. D. Getzoff and V. A. Roberts, *J. Mol. Biol.*, 1999, **291**, 329-345.
108. R. C. Pratt, B. G. G. Lohmeijer, D. A. Long, R. M. Waymouth and J. L. Hedrick, *J. Am. Chem. Soc.*, 2006, **128**, 4556-4557.
109. B. G. G. Lohmeijer, R. C. Pratt, F. Leibfarth, J. W. Logan, D. A. Long, A. P. Dove, F. Nederberg, J. Choi, C. Wade, R. M. Waymouth and J. L. Hedrick, *Macromolecules*, 2006, **39**, 8574-8583.
110. K. Kaupmees, A. Trummal and I. Leito, *Croat. Chem. Acta*, 2014, **87**, 385-395.
111. I. Kaljurand, A. Kütt, L. Sooväli, T. Rodima, V. Mäemets, I. Leito and I. A. Koppel, *J. Org. Chem.*, 2005, **70**, 1019-1028.
112. L. Simón and J. M. Goodman, *J. Org. Chem.*, 2007, **72**, 9656-9662.
113. X. Fu and C.-H. Tan, *Chem. Commun.*, 2011, **47**, 8210-8222.
114. M. K. Kiesewetter, M. D. Scholten, N. Kirn, R. L. Weber, J. L. Hedrick and R. M. Waymouth, *J. Org. Chem.*, 2009, **74**, 9490-9496.
115. A. Choucair and A. Eisenberg, *Eur. Phys. J. E*, 2003, **10**, 37-44.

116. N. S. Cameron, M. K. Corbierre and A. Eisenberg, *Can. J. Chem.*, 1999, **77**, 1311-1326.
117. A. Blanz, S. P. Armes and A. J. Ryan, *Macromol. Rapid Commun.*, 2009, **30**, 267-277.
118. E. B. Zhulina and O. V. Borisov, *Macromolecules*, 2012, DOI: 10.1021/ma300195n.
119. R. Nagarajan, in *Nanoparticles: Synthesis, Stabilization, Passivation, and Functionalization*, American Chemical Society, First edn., 2008, vol. 996, ch. 24.
120. T. Nicolai, O. Colombani and C. Chassenieux, *Soft Matter*, 2010, **6**, 3111-3118.
121. Y. Mai and A. Eisenberg, *Chem. Soc. Rev.*, 2012, **41**, 5969-5985.
122. Y. Yu and A. Eisenberg, *J. Am. Chem. Soc.*, 1997, **119**, 8383-8384.
123. A. D. Jenkins, R. G. Jones and G. Moad, *Pure Appl. Chem.*, 2009, **82**, 483-491.
124. J. Chiefari, Y. K. Chong, F. Ercole, J. Krstina, J. Jeffery, T. P. T. Le, R. T. A. Mayadunne, G. F. Meijs, C. L. Moad, G. Moad, E. Rizzardo and S. H. Thang, *Macromolecules*, 1998, **31**, 5559-5562.
125. A. B. Lowe and C. L. McCormick, *Prog. Polym. Sci.*, 2007, **32**, 283-351.
126. C. J. Hawker, *J. Am. Chem. Soc.*, 1994, **116**, 11185-11186.
127. G. Moad and D. H. Solomon, *9: Living Radical Polymerization*, Elsevier Science Ltd, Amsterdam, Second edn., 2005.

128. J. Nicolas, Y. Guillaneuf, C. Lefay, D. Bertin, D. Gigmes and B. Charleux, *Prog. Polym. Sci.*, 2013, **38**, 63-235.
129. J. Zhu, X. Zhu, Z. Cheng, F. Liu and J. Lu, *Polymer*, 2002, **43**, 7037-7042.
130. S. Perrier and P. Takolpuckdee, *J. Polym. Sci., Part A: Polym. Chem.*, 2005, **43**, 5347-5393.
131. G. Moad, E. Rizzardo and D. H. Solomon, *Macromolecules*, 1982, **15**, 909-914.
132. *Australia Pat.*, 4,581,429, 1986.
133. M. K. Georges, R. P. N. Veregin, P. M. Kazmaier and G. K. Hamer, *Macromolecules*, 1993, **26**, 2987-2988.
134. M. K. Georges, R. P. N. Veregin, P. M. Kazmaier, G. K. Hamer and M. Saban, *Macromolecules*, 1994, **27**, 7228-7229.
135. D. Bertin, D. Gigmes, S. R. A. Marque and P. Tordo, *Chem. Soc. Rev.*, 2011, **40**, 2189-2198.
136. T. Fukuda, T. Terauchi, A. Goto, K. Ohno, Y. Tsujii, T. Miyamoto, S. Kobatake and B. Yamada, *Macromolecules*, 1996, **29**, 6393-6398.
137. T. Fukuda, A. Goto and K. Ohno, *Macromol. Rapid Commun.*, 2000, **21**, 151-165.
138. G. Moad and E. Rizzardo, *Macromolecules*, 1995, **28**, 8722-8728.
139. A. Goto and T. Fukuda, *Macromolecules*, 1997, **30**, 4272-4277.
140. D. Benoit, V. Chaplinski, R. Braslau and C. J. Hawker, *J. Am. Chem. Soc.*, 1999, **121**, 3904-3920.

141. N. A. Listigovers, M. K. Georges, P. G. Odell and B. Keoshkerian, *Macromolecules*, 1996, **29**, 8992-8993.
142. P. Lacroix-Desmazes, J.-F. Lutz and B. Boutevin, *Macromol. Chem. Phys.*, 2000, **201**, 662-669.
143. J.-F. Lutz, P. Lacroix-Desmazes and B. Boutevin, *Macromol. Rapid Commun.*, 2001, **22**, 189-193.
144. P. Lacroix-Desmazes, J.-F. Lutz, F. Chauvin, R. Severac and B. Boutevin, *Macromolecules*, 2001, **34**, 8866-8871.
145. H. Fischer, *Macromolecules*, 1997, **30**, 5666-5672.
146. H. Benoit, J. F. Joanny, G. Hadziioannou and B. Hammouda, *Macromolecules*, 1993, **26**, 5790-5795.
147. M. Kato, M. Kamigaito, M. Sawamoto and T. Higashimura, *Macromolecules*, 1995, **28**, 1721-1723.
148. J.-S. Wang and K. Matyjaszewski, *J. Am. Chem. Soc.*, 1995, **117**, 5614-5615.
149. K. Matyjaszewski, *Macromolecules*, 2012, **45**, 4015-4039.
150. A. J. Convertine, B. S. Lokitz, Y. Vasileva, L. J. Myrick, C. W. Scales, A. B. Lowe and C. L. McCormick, *Macromolecules*, 2006, **39**, 1724-1730.
151. G. Moad, *Aust. J. Chem.*, 2006, **59**, 661-662.
152. D. Charmot, P. Corpart, H. Adam, S. Z. Zard, T. Biadatti and G. Bouhadir, *Macromol. Symp.*, 2000, **150**, 23-32.
153. J. Zhu, D. Zhou, X. Zhu and G. Chen, *J. Polym. Sci., Part A: Polym. Chem.*, 2004, **42**, 2558-2565.

154. G. Moad, E. Rizzardo and S. H. Thang, *Aust. J. Chem.*, 2005, **58**, 379-410.
155. E. Rizzardo, M. Chen, B. Chong, G. Moad, M. Skidmore and S. H. Thang, *Macromol. Symp.*, 2007, **248**, 104-116.
156. M. J. Monteiro, *J. Polym. Sci., Part A: Polym. Chem.*, 2005, **43**, 3189-3204.
157. M. Drache, G. Schmidt-Naake, M. Buback and P. Vana, *Polymer*, 2005, **46**, 8483-8493.
158. G. Moad, *Macromol. Chem. Phys.*, 2014, **215**, 9-26.
159. Y. K. Chong, G. Moad, E. Rizzardo and S. H. Thang, *Macromolecules*, 2007, **40**, 4446-4455.
160. J. Skey and R. K. O'Reilly, *Chem. Commun.*, 2008, 4183-4185.
161. H. Willcock and R. K. O'Reilly, *Polym. Chem.*, 2010, **1**, 149-157.
162. G. Moad, E. Rizzardo and S. H. Thang, *Aust. J. Chem.*, 2006, **59**, 669-692.
163. D. J. Keddie, G. Moad, E. Rizzardo and S. H. Thang, *Macromolecules*, 2012, **45**, 5321-5342.

2 Immobilisation of 1,5,7-triazabicyclo[4.4.0]dec-5-ene onto an amphiphilic block copolymer for the assembly of catalytic nanoreactors.

2.1 Abstract

In this Chapter the synthesis of a new triazabicyclodec-5-ene (TBD) containing monomer was shown. Its polymerisation was explored *via* Reversible Addition-Fragmentation Chain Transfer (RAFT) polymerisation, in an effort to target a TBD-functionalised polymer. As a result of incompatibility of TBD with RAFT chemistry, post-polymerisation modification of polymeric scaffolds obtained by Nitroxide Mediated Polymerisation (NMP) was performed. The TBD catalyst was tethered to the hydrophobic domain of amphiphilic block copolymers, resulting in well-defined polymers. These polymers successfully assembled in water due to their amphiphilic character, giving targeted micellar nanostructures with TBD functionalised cores.

2.2 Introduction

2.2.1 Immobilisation of triazabicyclodec-5-ene

The organocatalyst triazabicyclodec-5-ene (TBD) is a widely used catalyst for numerous reactions such as Michael additions, aldol reactions, amidations and ring opening polymerisations (ROP).¹⁻⁴ The immobilisation of catalysts onto polymeric supports allows for easy product separation and catalyst regeneration.⁵ There are many examples of the immobilisation of TBD onto polymeric supports; however, immobilisation is through the catalytic functionality, and as a result, the catalytic site is more hindered.⁶⁻¹⁰ Thus, the supported catalysts can be directly compared to the more hindered less active methyl-TBD (MTBD) (Figure 2.1). Methylation of the TBD reduces the pK_a from 21 to 19.9 (in THF), this is known to affect the catalytic efficiency.¹¹

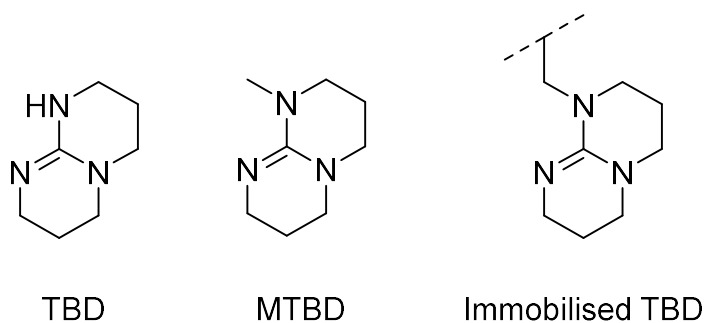
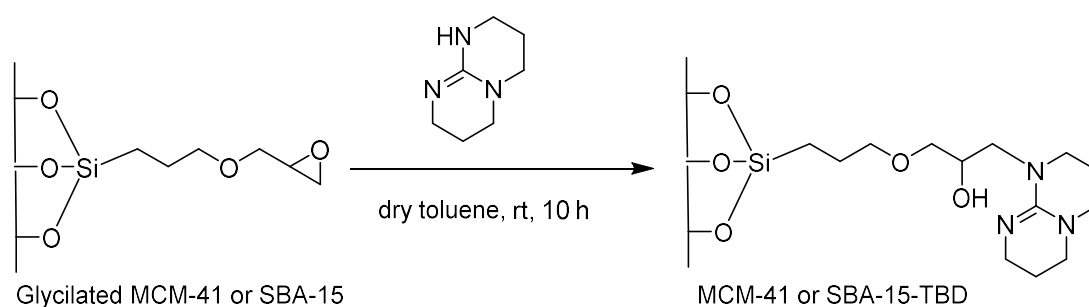


Figure 2.1: Structure of TBD, MTBD and immobilised TBD.

Kalita *et al.* immobilised TBD onto mesoporous silica (both MCM-41 and SBA-15) for the single step Michael addition of diethyl malonate and β -nitrostyrene.¹⁰ The surface was initially functionalised with 3-glycidoxy propyl trimethoxy silane and TBD immobilised through a subsequent nucleophilic substitution onto the epoxide (Scheme 2.1).¹⁰ A higher activity was observed for SBA-15-TBD when compared to MCM-41-TBD (75% and 67% respectively, after 9 hours) which was attributed to the larger pore size of SBA-15-TBD.¹⁰ These reactions required elevated temperatures of 100 °C for 9 hours with 10 wt.% catalyst to achieve high conversions.



Scheme 2.1: Formation of MCM-41 or SBA-15-TBD.¹⁰

In 2005 the Gelbard group demonstrated the use of guanidine derivatives in the transesterification of vegetable oils.¹² This led to the tethering of TBD onto a styrenic polymer backbone to enable recovery of the catalyst. These polymers were prepared utilising chloromethylated polystyrene and potassium iodide for a nucleophilic substitution with TBD.¹³ The hydrolysis of rapeseed oil was monitored; at 5 mol% polymer loading, and refluxing at 70 °C in methanol, 97% conversion was observed after 4 hours, which was comparable to the conversion observed for MTBD with 3 mol% loading.

Work from the Vaccaro group demonstrated the immobilisation of TBD onto RASTA resin, which formed a styrenic core with linear TBD-methane chains. This catalyst was used for the Michael addition of dimethyl malonate to α,β -unsaturated ketones producing high conversions after 15 hours, with 20 mol% catalyst loading in bulk conditions at 60 °C utilising a continuous flow reactor.⁶ Whilst the immobilisation of the catalyst TBD has been widely explored, one of the limitations is that these polymers are unable to catalyse reactions in aqueous conditions, and frequently require high catalytic loadings and high temperatures (60-80 °C). These are excellent examples of tethering TBD to a solid support, however many advantages can be gained from embedding the catalyst within the core of a micellar structure, as discussed in Chapter 1.4.¹⁴⁻¹⁶ This is as a consequence of the “concentrator effect” where the substrates preferentially diffuse into the core of a nanoreactor.¹⁷ This technique for immobilisation has not previously been explored with TBD, hence this has provided an excellent opportunity for further expansion of TBD catalysis.

Due to the versatile nature of TBD, we aim to immobilise this catalyst within the hydrophobic core of a polymer. We hypothesise that this hydrophobic pocket will act like an enzyme mimic, accelerating the rate of reactions in water (Figure 2.2) of the Michael addition reaction.

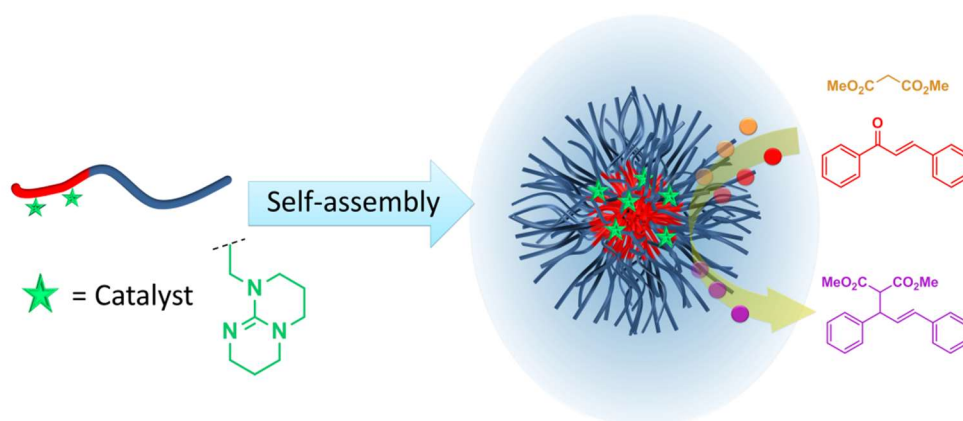
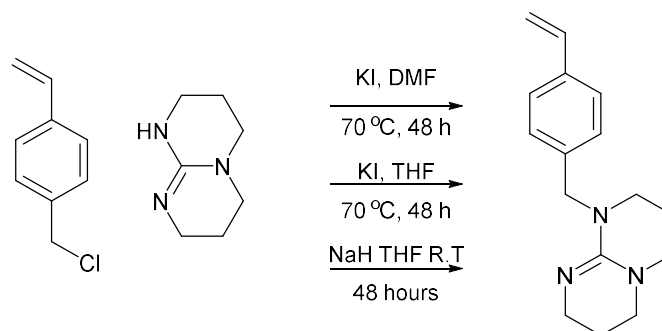


Figure 2.2: A schematic representation of the immobilisation of TBD for catalysis in water.

2.3 Results and Discussion

2.3.1 Synthesis of the StTBD (2.1)

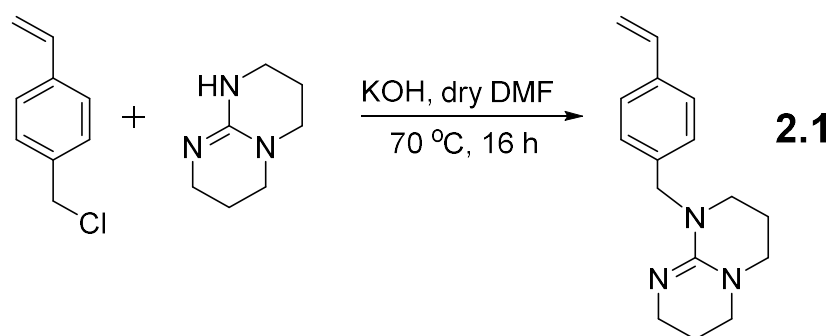
Styrene is commonly used as the core block in micellar structures as it can form kinetically frozen micelles.¹⁸ Through the incorporation of the catalyst onto the hydrophobic block the catalyst will subsequently be immobilised within the micellar core. Several techniques were explored to synthesise a TBD-containing vinyl monomer (Scheme 2.2) with limited success. Analysis of the products by ¹H NMR spectroscopy gave low conversion and the presence of unidentified by-products, as reported by Genski *et al.*¹⁹ Harsh reaction conditions and liberation of hydrochloric acid (HCl) are thought to be the cause of the low yield through by-product formation, as HCl can potentially poison the base and quaternise the amine.



Scheme 2.2: Conditions initially explored for the synthesis of StTBD.

To overcome the liberation of HCl, the nucleophilic substitution of TBD to form the monomer StTBD **2.1**, was carried out using the commercially available reagents vinyl benzyl chloride (BzCl) (1.1 equivalents), potassium hydroxide (1 eq.), and TBD (1.2 eq.). This procedure was modified from a previous approach used to synthesise 1-(4-vinylbenzyl) thymine (Scheme 2.3).²⁰ TBD was initially stirred with

potassium hydroxide in water forming the deprotonated TBD species, the water subsequently removed *via* lyophilisation prior to the addition of dry *N,N*-dimethylformamide (DMF) and BzCl.



Scheme 2.3: Synthesis of monomer **2.1**, StTBD using BzCl, TBD and KOH.

The reaction was monitored by ¹H NMR spectroscopy *via* the downfield shift of the methylene signal (4.6 ppm to 4.7 ppm). This reaction follows a S_N2 mechanism where the chlorine is substituted by the strong nucleophile, TBD. To isolate **2.1** a range of eluent conditions were tested however poor separation was observed using column chromatography; hence the product was extracted with diethyl ether. Due to the surfactant-like nature of **2.1**, some product was lost in the aqueous phase. However, combination of the washings provided **2.1** as a yellow oil, with a yield of 20%. Both ¹H NMR and ¹³C NMR spectroscopy (Figure 2.3 and Figure 2.4) were used, together with high resolution-MS where [M+1] was 256.1807 Da to confirm the formation of **2.1**.

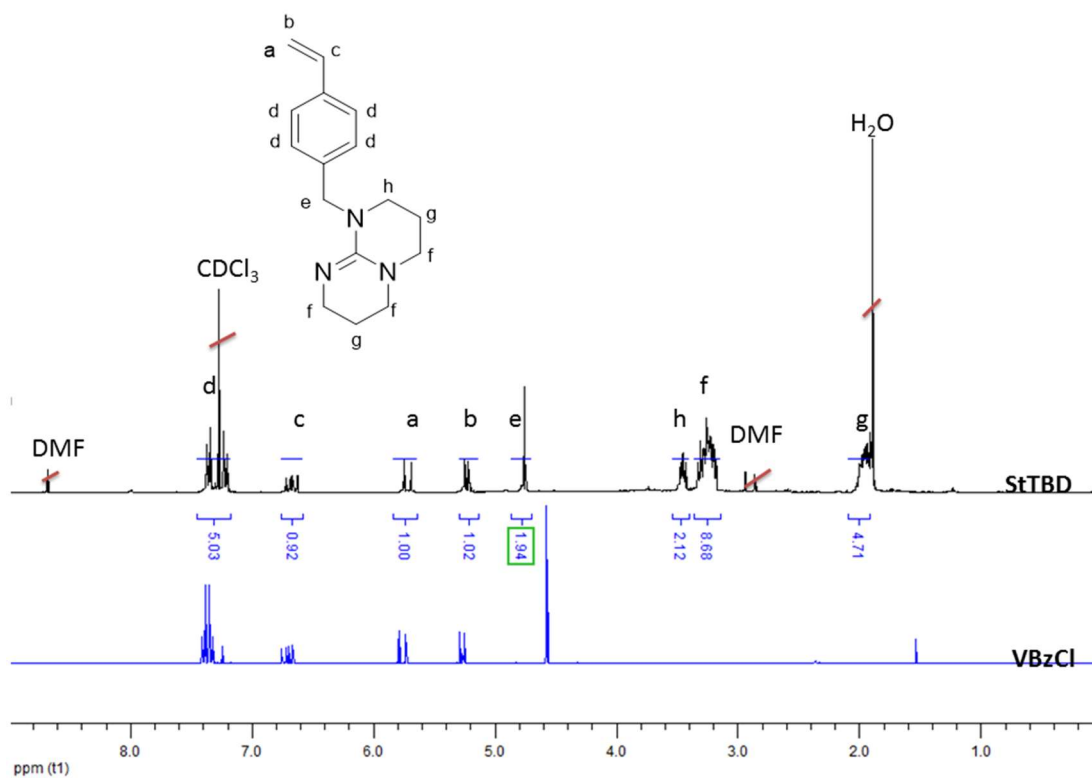


Figure 2.3: ^1H NMR spectrum showing the overlaid spectra of purified 2.1 StTBd (black) and BzCl (blue) in CDCl_3 at 400 MHz.

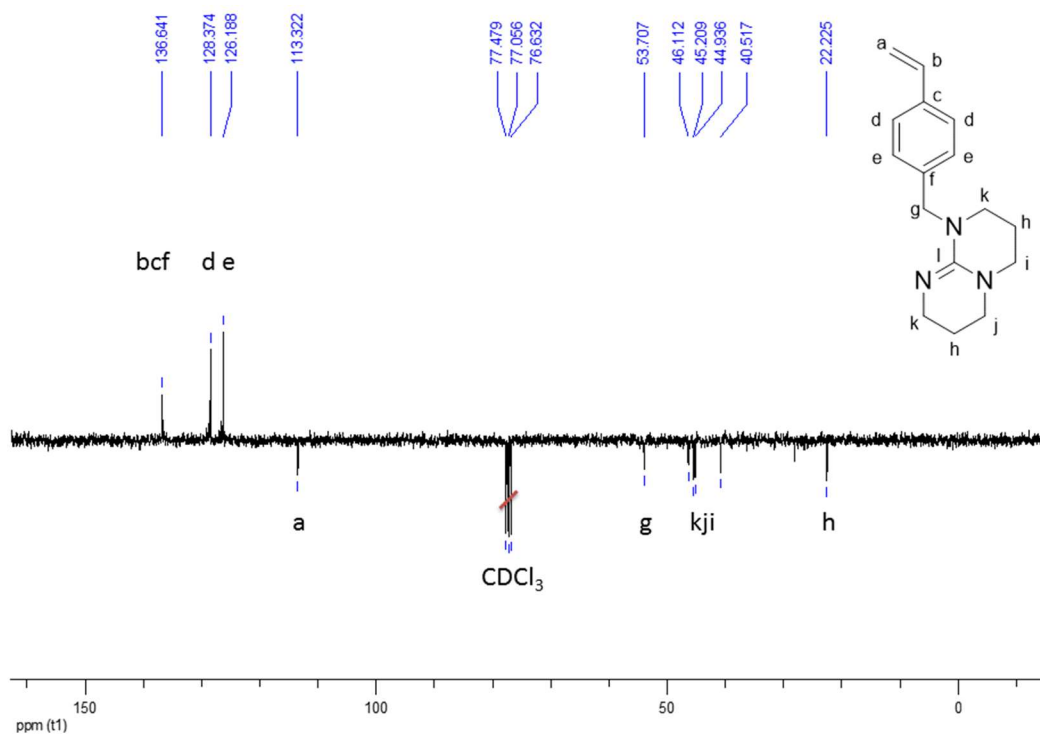


Figure 2.4: ^{13}C NMR spectrum for purified 2.1, StTBd, in CDCl_3 at 400 MHz.

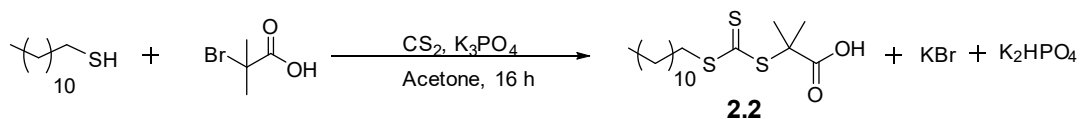
2.3.2 Polymer synthesis *via* RAFT

A polymerisation of the monomer **2.1** using reversible addition-fragmentation chain transfer (RAFT) was attempted. To a dried ampoule, equipped with a stirrer bar, the chain transfer agent (CTA) 2-(dodecylthiocarbonothioylthio)-2-methylpropionic acid and **2.1** were added in dioxane. The reaction mixture was subjected to three freeze pump thaw cycles and heated to 110 °C for 24 hours. The reaction was monitored by ¹H NMR spectroscopy, however the polymerisation was unsuccessful. We hypothesise the CTA underwent aminolysis due to the presence of the **2.1** monomer (100 eq.), as it is known that excess amines can react with a thiocarbonylthio group generating thiols.²¹ As a result of this an alternative technique was explored for the immobilisation of TBD, through the post-polymerisation modification of a polymer scaffold.

2.3.2.1 *Synthesis of 2-(dodecylthiocarbonothioylthio)-2-methylpropionic acid (DDMAT) 2.2*

When synthesising block copolymers utilising RAFT polymerisation it is important to select a CTA that can control the polymerisation of both blocks (Styrene (St), BzCl and *N,N*-dimethyl acrylamide (DMA)).^{22, 23} For this reason the CTA 2-(dodecylthiocarbonothioylthio)-2-methylpropionic acid (DDMAT) was synthesised (Scheme 2.4). This CTA is compatible with a variety of monomers such as acrylates, styrenes and acrylamides.²⁴ Following the general procedure described by O'Reilly *et al.* a solution of potassium phosphate was stirred with dodecane thiol with bromoisobutyric acid (25 eq.) with carbon disulphide and stirred for 16 hours.²⁵ Upon the addition of carbon disulfide a colour change was observed from white to

yellow, with this colour change indicating the formation of the trithiocarbonate which has an absorbance at 309 nm.²⁵



Scheme 2.4: The synthesis of DDMAT, **2.2**.

The product was purified by extracting the mixture with dichloromethane to remove the acid. The solvent was removed and **2.2** was further purified using flash column chromatography with ethyl acetate (EtOAc). The solvent was removed to give **2.2** as a yellow solid with a 53% yield. The formation of **2.2** was confirmed by ¹H NMR spectroscopy (Figure 2.5) in good agreement with the literature values.²⁵

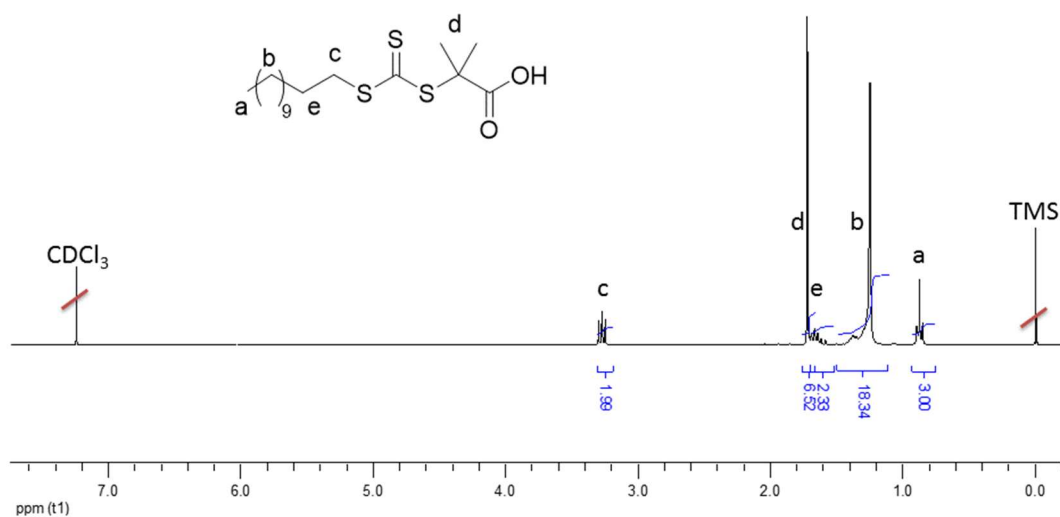
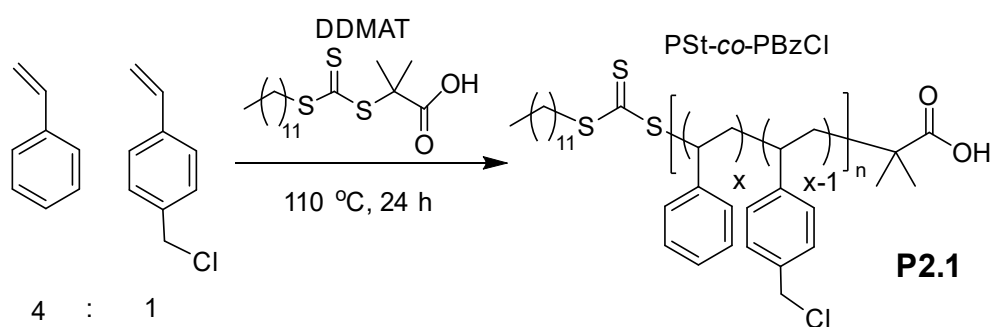


Figure 2.5: ¹H NMR spectrum of purified **2.2**, DDMAT, in CDCl₃ at 400 MHz.

2.3.2.2 Polymer synthesis

The polymer scaffold, **P2.1**, was synthesised through the copolymerisation of St and BzCl with **2.2** as shown in Scheme 2.5, where a 20% incorporation of BzCl was targeted. The monomer BzCl was used as the pendent chlorine functionality allows for further modification with TBD. These monomers are well-known to copolymerise and have relatively similar reactivity ratios producing a random copolymer.^{26, 27}



Scheme 2.5: Schematic representation of the copolymerisation of St with BzCl to form a RAFT polymeric scaffold P2.1.

To a dried ampoule, St, BzCl, and **2.2** were added. The reaction went through three freeze pump thaw cycles and was placed under nitrogen prior to heating at 110 °C for 24 hours. The conversion was calculated using ¹H NMR spectroscopy (Figure 2.6), through a comparison of the vinyl peaks at 5.2 ppm to the aryl peak at 4.5 ppm for BzCl, and the aromatic polymer peaks (6.2-7.6 ppm) and the BzCl conversion for styrene. The conversion is calculated as shown in Equation 2.3.

$$\% \text{ Conversion BzCl} = \frac{H_{PBzCl}}{(H_{PBzCl} + H_{BzCl})} \times 100$$

$$\% \text{ Conversion} = \frac{H_{PSt}}{(H_{PSt} + H_{St})} \times 100$$

Equation 2.3: The equations used to calculate the percentage conversion of St and BzCl for P2.1.

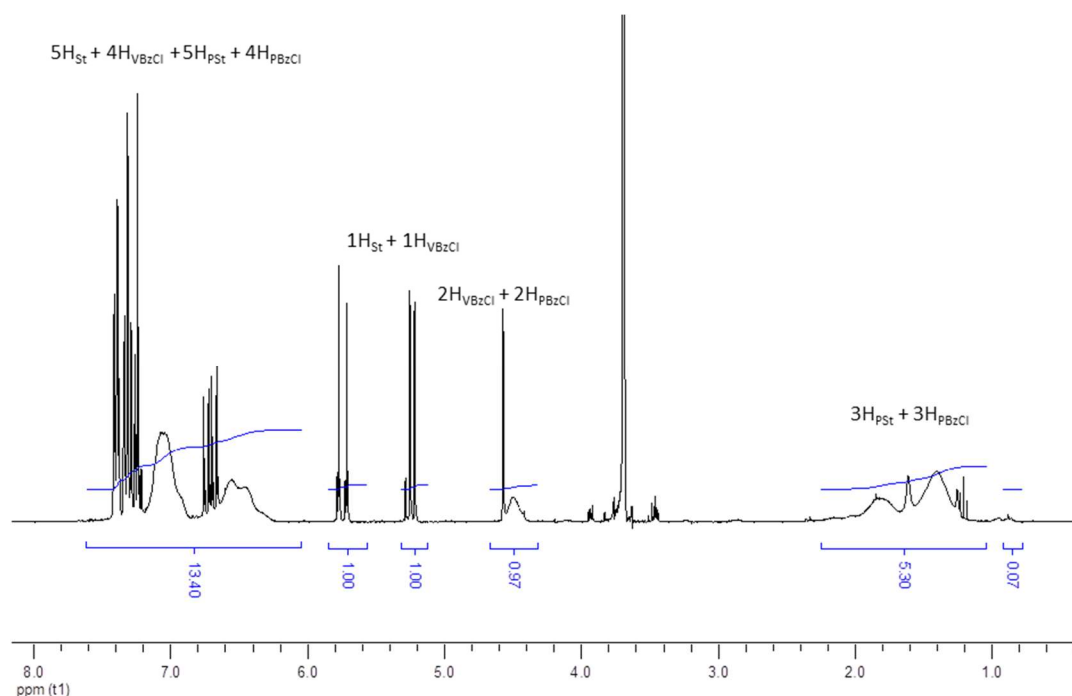


Figure 2.6: Conversion ^1H NMR spectrum for P2.1, in CDCl_3 at 400 MHz.

An overall conversion of 79% was achieved after 24 hours for the BzCl and 61% for St. The polymerisation was stopped *via* rapid cooling and subsequently precipitated three times into methanol, to yield a yellow solid. The degree of polymerisation (DP) for both monomers was calculated using a long acquisition ^1H NMR spectrum (Figure 2.7), where the signal at 0.8 ppm (**a**) accounts for three hydrogens (3H) on the polymer end group. Comparing this to the distinctive 2H of the methylene signal for PBzCl at 4.5 ppm (**d**), a DP of 10 was obtained. This is in agreement with the DP

calculated by conversion; the molecular weight of **P2.1** was determined as 5.8 kDa, with an overall DP of 47 with a 21% incorporation of PBzCl; the incorporation of BzCl is slightly higher than predicted, indicating that within this copolymerisation St and BzCl do not polymerise at the same rate.

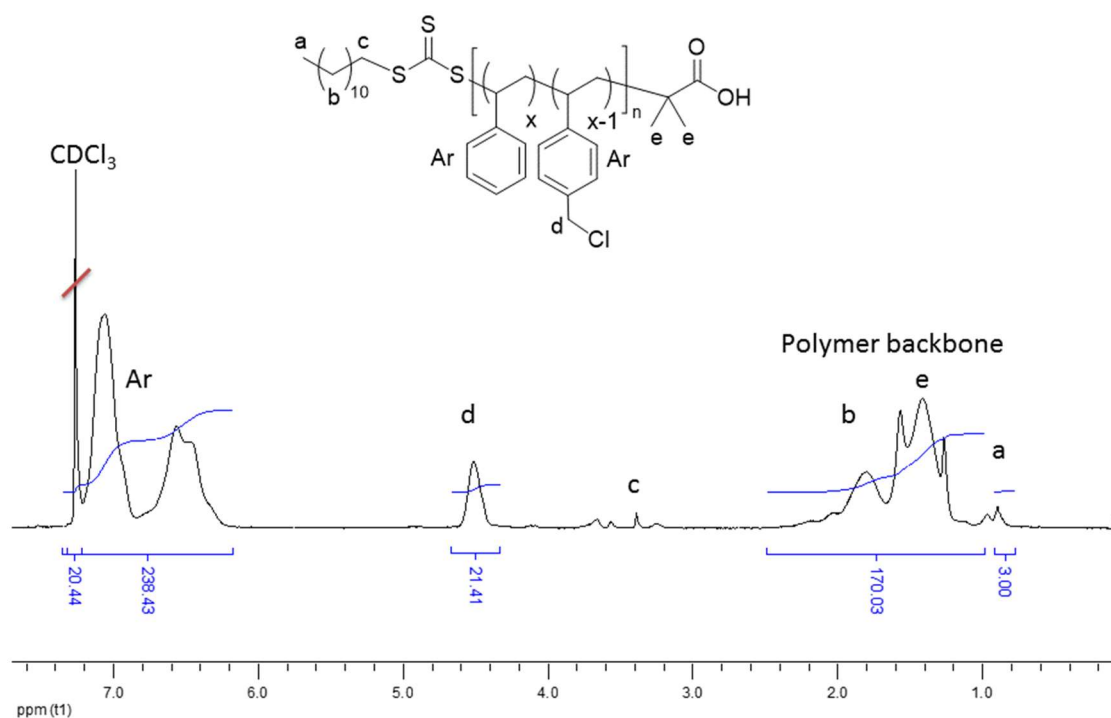


Figure 2.7: Long acquisition ^1H NMR spectrum for **P2.1**, in CDCl_3 at 400 MHz.

Size exclusion chromatography (SEC) (CHCl_3 , PSt standards) was in agreement with the ^1H NMR spectroscopy data, with a M_n of 7.1 kDa, and a narrow dispersity was achieved ($D_M = 1.19$). The thiocarbonylthio group absorbs strongly in the ultraviolet (UV) spectrum at 309 nm. By overlaying the differential refractive index (RI) and the 309 nm SEC traces the presence of end group on the polymer chain was confirmed. Here a good overlap of the RI and the UV trace is shown (Figure 2.8).

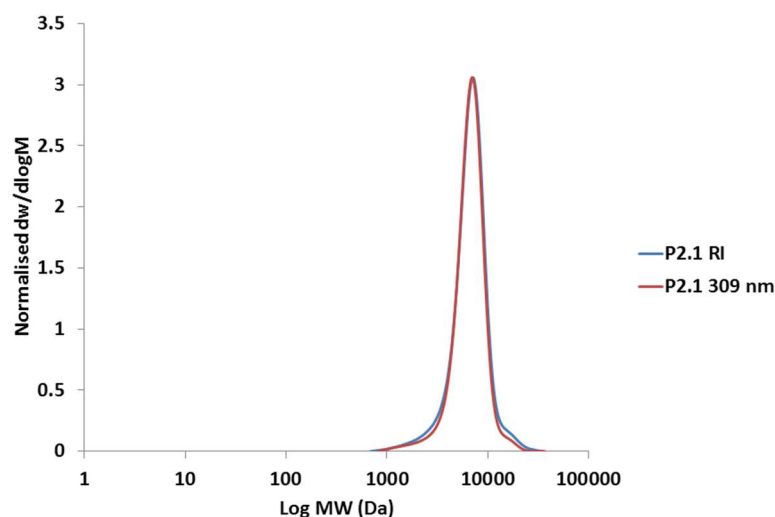
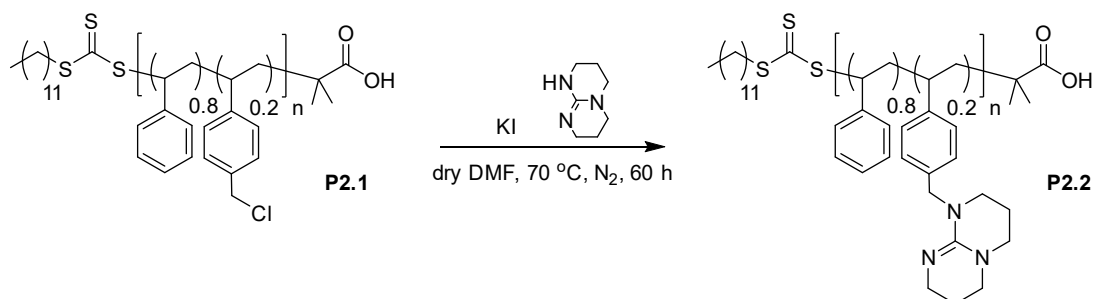


Figure 2.8: Overlay of the normalised SEC data in CHCl_3 (PSt standards) for the RI trace (blue) and the UV absorbance (red) for P2.1 as a function of differential weight fraction against molecular weight.

The TBD was then substituted onto the polystyrene scaffold (Scheme 2.6). The substitution of TBD onto chloromethylated styrene followed the same procedure described by Schuardt *et al.* where TBD was added in excess, with 2:1 TBD functionalities to PBzCl polymer units (40 eq.).⁸ Initially potassium iodide (KI) was stirred in dry DMF with TBD for 10 minutes, polymer **P2.1** was then added, and the reaction stirred at 70 °C under nitrogen for 60 hours.



Scheme 2.6: Schematic of the substitution of TBD onto the polymer scaffold P2.1 to form P2.2.

After 60 hours the substitution reaction was stopped and DMF was removed under vacuum. The polymer was then precipitated, filtered and re-dissolved three times in

methanol, to afford **P2.2**. Interestingly the polymer was a darker shade of yellow due to the presence of the yellow TBD catalyst. The resultant polymer was analysed *via* ^1H NMR spectroscopy which gave a M_n of 12.1 kDa.

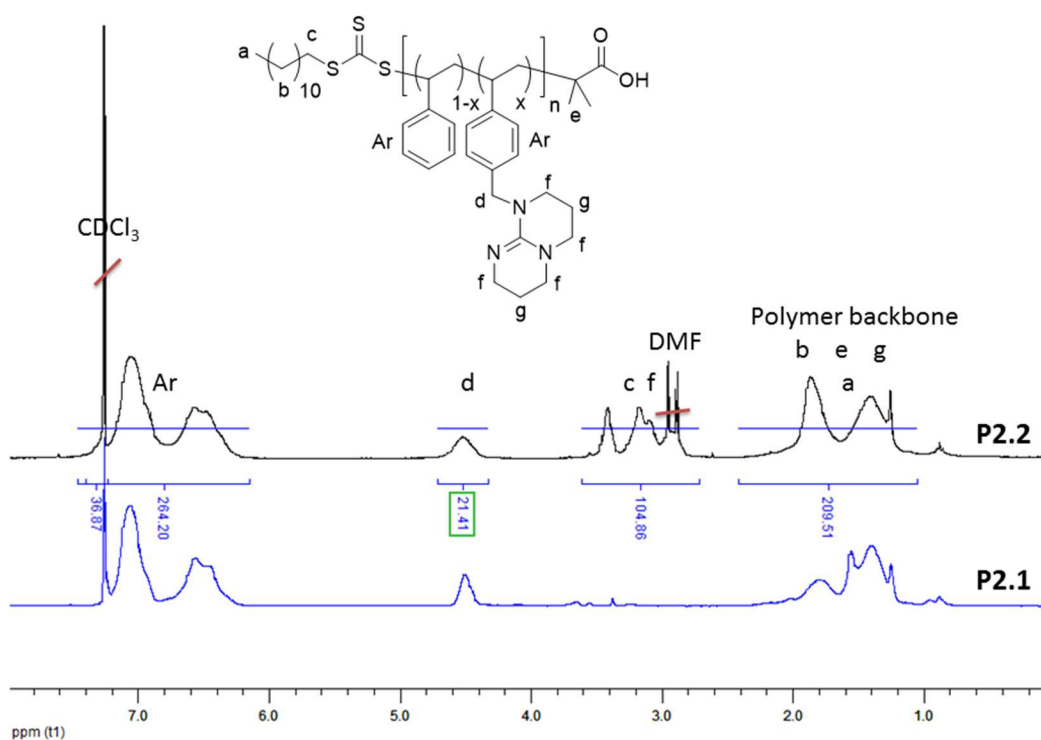


Figure 2.9: ^1H NMR spectrum for P2.2 (black) overlaid with P2.1 (blue), in CDCl_3 at 400 MHz.

The ^1H NMR spectrum (Figure 2.9) shows the inclusion of the TBD group onto the polymeric scaffold. Integration at δ 2.6-3.4 ppm represents the TBD functional group (f); hence the appearance of this broad peak as a result of integration of peaks f indicates $\sim 100\%$ incorporation of TBD onto the polymer scaffold when compared to the pendent methylene signal, d.

Diffusion-ordered spectroscopy (DOSY), Figure 2.10, was used to confirm the covalent attachment of TBD. This is through comparing the diffusion coefficient of the TBD signals (f, highlighted in green) to the polymer chain (highlighted in red). Here the overlapping diffusion coefficients (represented by the black line) are characteristic of covalently bound TBD to the polymeric scaffold. Unbound TBD will have a higher diffusion coefficient, thus will not overlap with the polymer backbone.²⁸

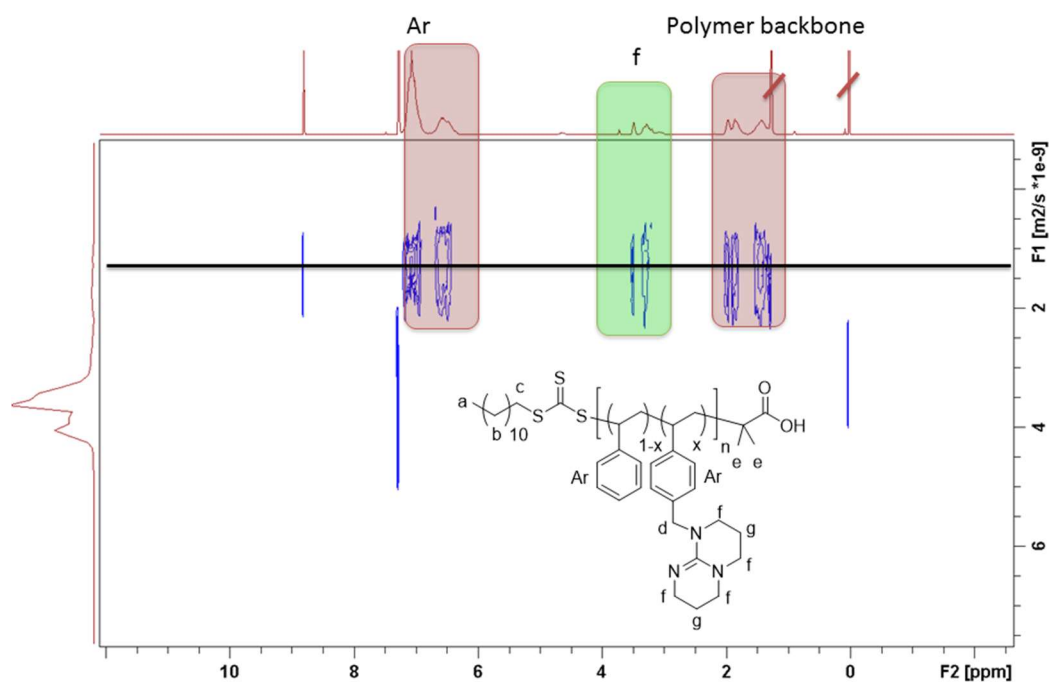


Figure 2.10: DOSY NMR spectrum for P2.2, in CDCl₃ at 500 MHz.

A significant reduction in the absorbance of the polymer at $\lambda = 309$ nm was observed by SEC analysis (Figure 2.11). Although a yellow solid had formed (due to the presence of the TBD), we hypothesise the decrease of the absorbance is due to the loss of the CTA end group. The end group is lost due to the harsh basic conditions

used in the substitution of the TBD. Using strong nucleophiles such as amines can lead to the loss of the trithiocarbonate end group from the polymer.²¹ Upon comparing the RI traces the molecular weight has increased dramatically (Figure 2.11, left) and the M_n was confirmed as 40 kDa, with an increased dispersity ($D_M = 2.03$). The molecular weight by SEC is much higher than predicted due to thiol coupling through the chain ends as a result of TBD degrading the RAFT end group. This conclusion is supported by comparing the response (mV) of the RI to the UV trace (Figure 2.11, right) as no absorbance (309 nm) was observed at the increased molecular weight.^{29, 30} This substitution took place at high polymer concentrations increasing the likelihood of disulfide bonds forming through the polymer end groups, increasing the molecular weight and dispersity.

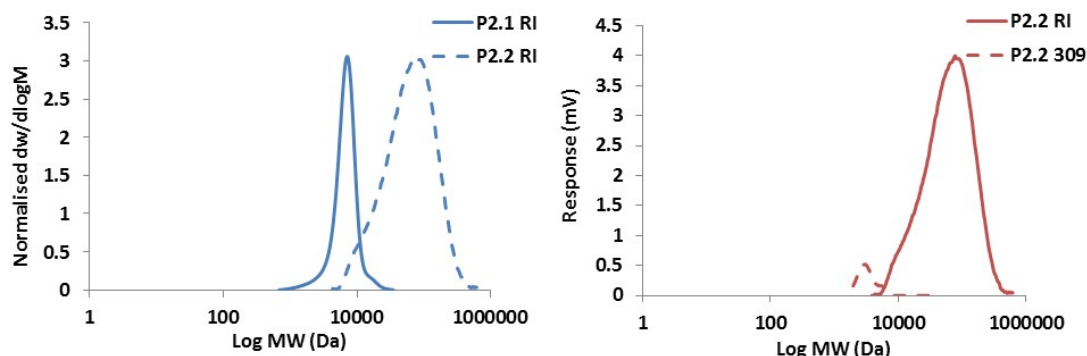
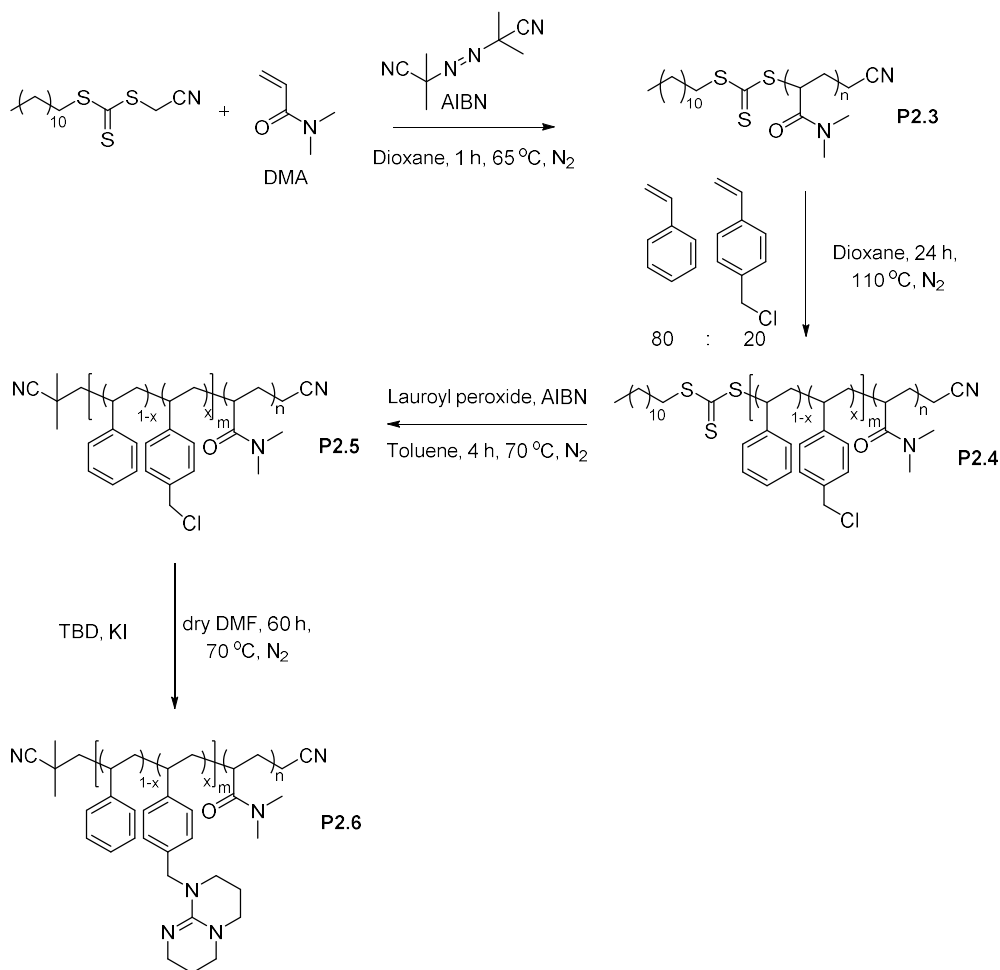


Figure 2.11: Overlay of the SEC traces in CHCl_3 (PSt standards), Left: RI trace of P2.1 (solid blue) and P2.2 (blue dashed) as a function of normalised differential weight fraction against molecular weight. Right: RI (solid red) and UV (red dashed) trace for P2.2 as a function of response to molecular weight.

As a result, chain extension of **P2.2** at this stage is not possible due to the loss of the RAFT end group. Hence, an alternative order of synthesis was selected (Scheme 2.7); here the end group of the polymer scaffold was removed prior to TBD substitution.



Scheme 2.7: Stepwise synthesis of the amphiphilic block copolymer with TBD functionality embedded into the hydrophobic domain.

The monomer DMA was polymerised first in dioxane with the commercially available RAFT agent cyanomethyl dodecyl trithiocarbonate. The hydrophilic block, DMA, was selected because of its hydrophilic nature as well as its lack of responsive features (such as pH or temperature). An ampoule was equipped with the DMA monomer, the thermal initiator azobisisobutyronitrile (AIBN) (0.01 eq.) and the CTA. The solution was freeze pump thawed for three cycles and was placed under nitrogen. The reaction was heated to 65 °C for 1 hour, and a conversion of 90% was achieved (calculated by ^1H NMR spectroscopy), and the polymerisation was subsequently stopped *via* rapid cooling. The resultant polymer **P2.3** was precipitated

three times in diethyl ether and dried under vacuum, to give **P2.3** as a yellow solid. This provided a DP of 129 for the hydrophilic block and a M_n of 12.8 kDa (^1H NMR spectroscopy, Figure 2.12) for the polymer **P2.3**.

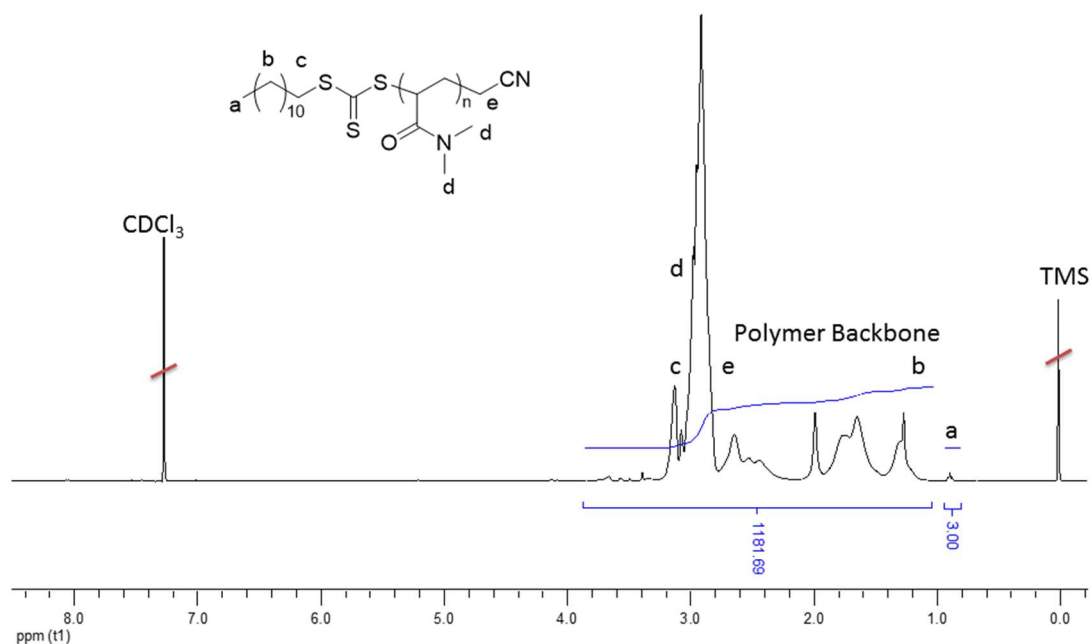


Figure 2.12: Long acquisition ^1H NMR spectrum of **P2.3**, in CDCl_3 at 400 MHz.

A plot overlaying the SEC data (CHCl_3 , PSt standards) for the RI trace and UV 309 nm trace (Figure 2.13) shows good overlap and incorporation of the RAFT end group for **P2.3**. The M_n was determined to be 9.7 kDa and a narrow dispersity was observed ($D_M = 1.20$).

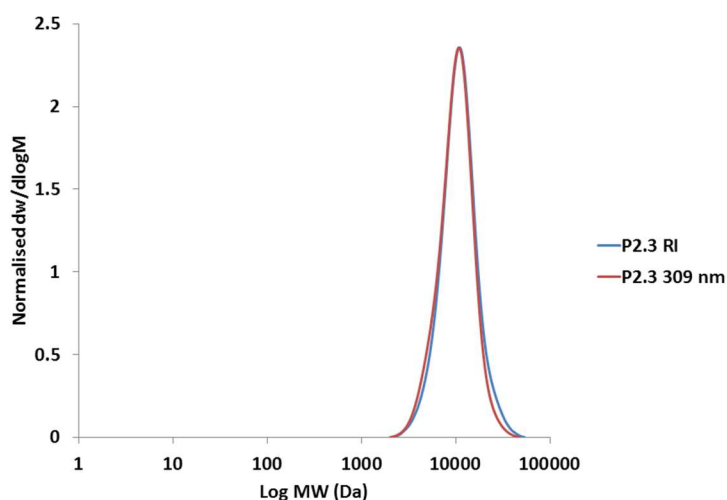


Figure 2.13: Overlay of the normalised SEC data in CHCl_3 (PSt standards) for the RI trace (blue) and the UV absorbance (red) for P2.3 as a function of differential weight fraction against molecular weight.

The polymer, **P2.3**, was used as a macro-RAFT agent for the preparation of a functional and amphiphilic block copolymer. The hydrophilic block was chain extended with the hydrophobic monomers, St and BzCl, and the polymerisation was stopped after 24 hours *via* rapid cooling. The reaction mixture was precipitated into ethyl acetate and dried under vacuum to afford **P2.4**. Analysis by ^1H NMR spectroscopy (Figure 2.14) provided a DP of 82 (for the hydrophobic block) with a loading of 24% for BzCl, the M_n was calculated as 22.6 kDa.

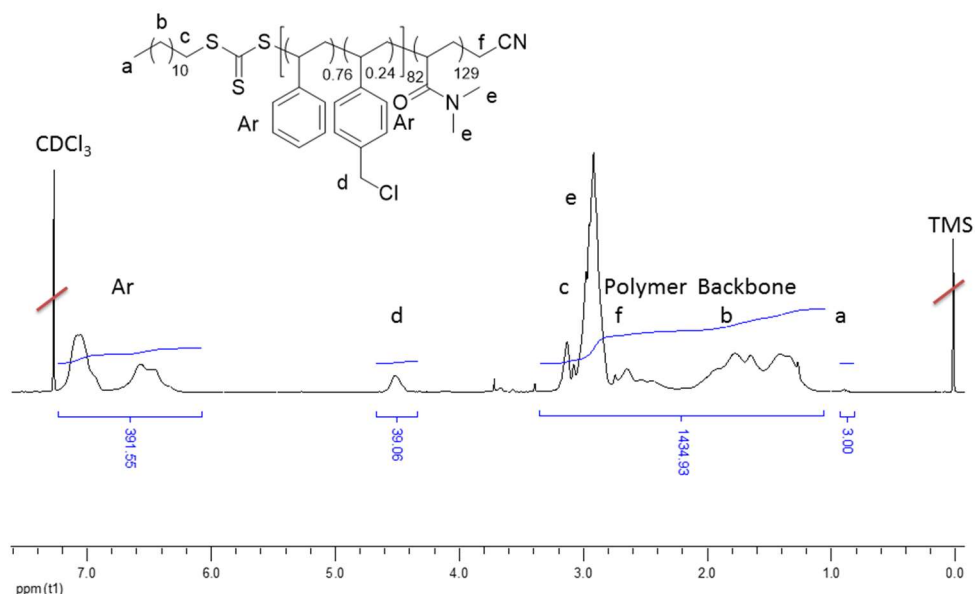


Figure 2.14: Long acquisition ^1H NMR spectrum of P2.4, in CDCl_3 at 400 MHz.

Analysis of the polymer *via* SEC (CHCl_3 , PSt standards, Figure 2.15) gave a M_n of 17.0 kDa with a broad dispersity ($D_M = 1.8$). The SEC trace is bimodal with the UV trace at 309 nm showing good overlap with the RI trace for both peaks. This indicates all end groups are still present, however not all of the homopolymer has been chain extended.

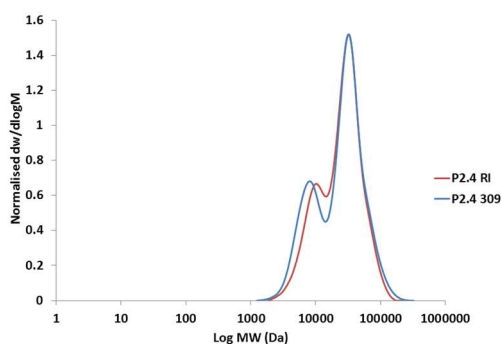
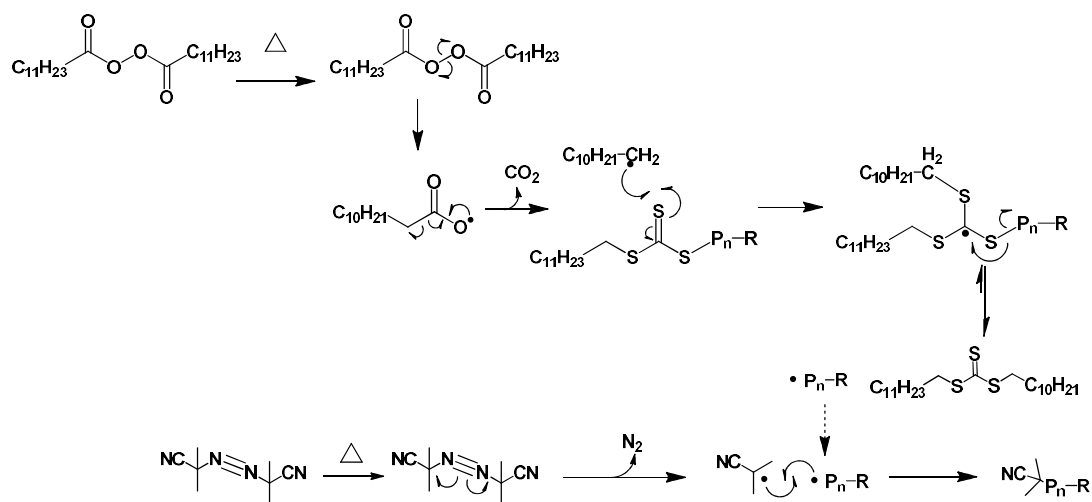


Figure 2.15: Overlay of the normalised SEC data in CHCl_3 (PSt standards) for the RI trace (blue) and the UV absorbance (red) for P2.4 as a function of normalised differential weight fraction against molecular weight.

Before substitution of the TBD onto **P2.4** the end group was removed to prevent any dithio-coupling. The end group removal was adapted from the method described by Rizzardo *et al.* using excess lauryl peroxide (LPO) and AIBN along with prolonged heating. The proposed mechanism for the end group removal is depicted in Scheme 2.8.³¹



Scheme 2.8: Schematic of the proposed mechanism for end group removal using AIBN and LPO, proposed by Rizzardo *et al.*³¹

Adding excess AIBN prevents polymer-polymer coupling which can lead to bimodal molecular weight distributions. This reaction was carried out at a low concentration of the macro-RAFT agent (0.4 mM); again reducing the formation of bimodal species due to the fast diffusion of the excess AIBN radicals. The lauryl group is a poor leaving group in comparison to the polymer chain formed, leading to the formation of a new thiocarbonylthio species. The end group removal of **P2.4** was carried out under a nitrogen atmosphere in toluene for 7 hours. The solvent was removed prior to precipitation in methanol giving **P2.5** as a white solid. Analysis by

^1H NMR spectroscopy (Figure 2.16), showed end group was still present at 0.88 ppm (highlighted by the blue box). This indicated an end group removal of 63%.

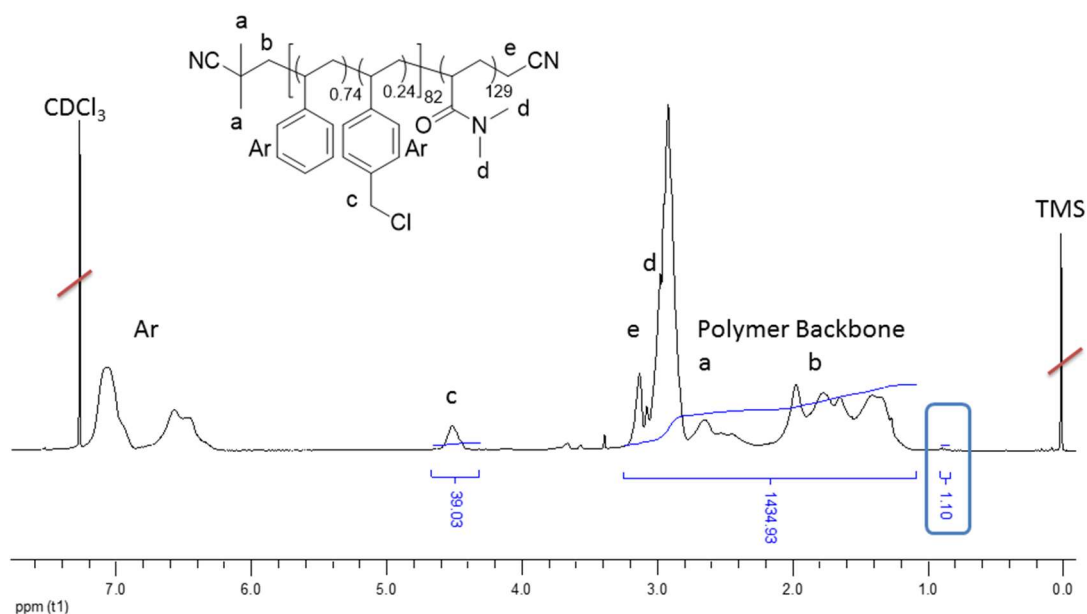


Figure 2.16: Long acquisition ^1H NMR spectrum of P2.5, in CDCl_3 at 400 MHz.

SEC analysis showed good overlap of the RI traces for **P2.4** and **P2.5** (Figure 2.17, A). The normalised UV trace at 309 nm (Figure 2.17, B) characteristic of the thiocarbonylthio end group, showed a significant decrease in the response. Through integration of the area under the SEC trace, a much higher end group removal of 90.5% was obtained.

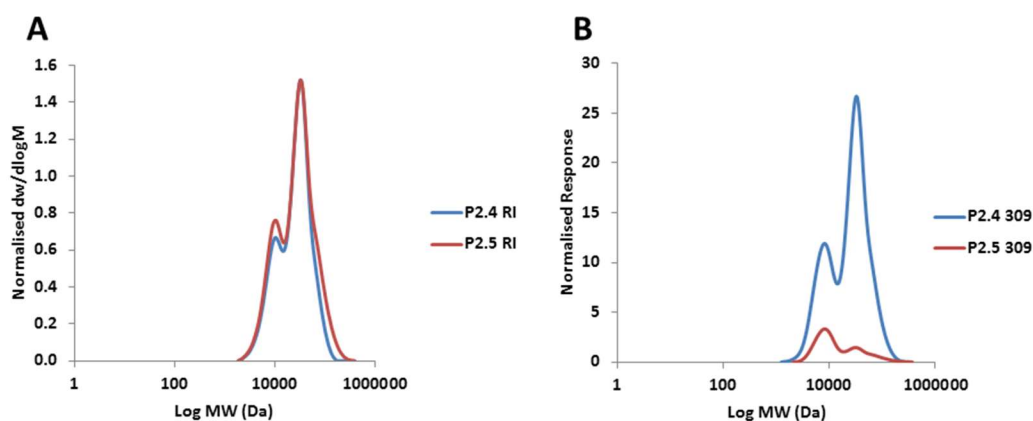


Figure 2.17: Overlay of the SEC traces in CHCl_3 (PSt standards), for P2.4 (blue), P2.5 (red). A: RI traces as a function of normalised differential weight fraction against molecular weight. B: 309 nm traces as a function of normalised response to molecular weight.

Substitution of TBD onto the hydrophobic domain of **P2.5** followed the same procedure as **P2.2**, where KI and TBD were stirred in dry DMF for 10 minutes. **P2.5** was subsequently added and the reaction was stirred for 60 hours at 75 °C. To remove the small molecule exhaustive dialysis (18 M Ω cm water, three changes a day for three days) was used to purify **P2.6**. ^1H NMR spectroscopy (Figure 2.18) showed a broadening of the methylene signal however the up-field shift was not seen, indicating a poor substitution of TBD. Notably the peaks observed at 0.88 ppm characteristic of the RAFT end group are no longer present.

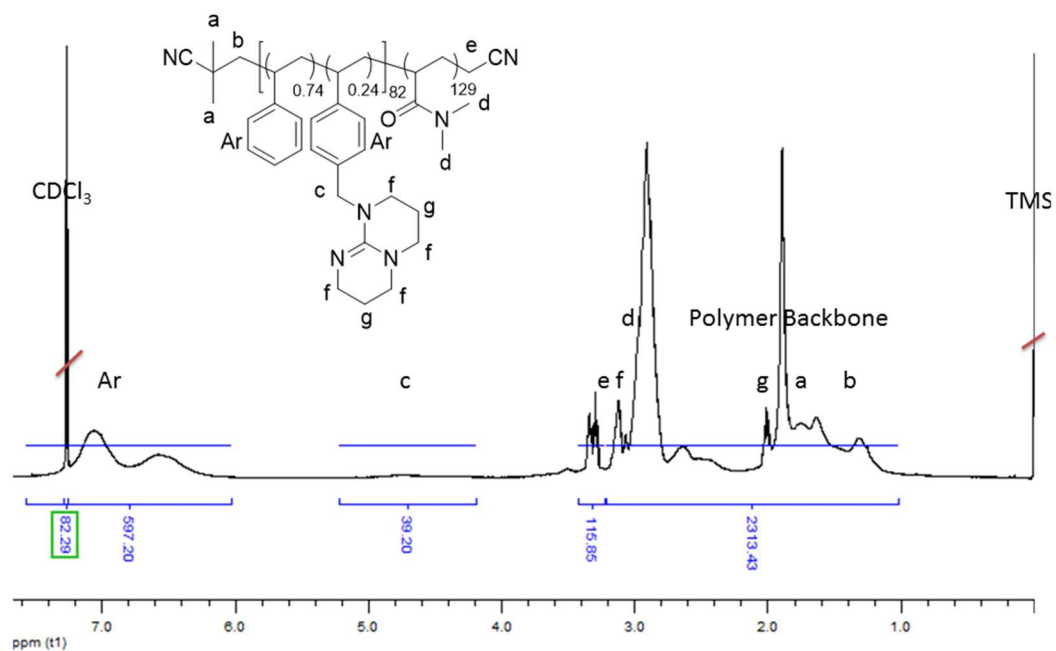


Figure 2.18: Long acquisition ^1H NMR spectrum of P2.6, in CDCl_3 at 400 MHz.

Upon analysis of the SEC data of **P2.6** a M_n of 62 kDa was observed (purple line, Figure 2.19, right); again the M_n was much higher than expected. This indicated that some thiocarbonylthio groups remain after end group removal. The presence of this functionality enables TBD to react with the end group generating thiol-terminated polymers, which form disulfide bonds. An overlay of the SEC data (Figure 2.19) shows the formation of the high molecular coupled species.

It is apparent that RAFT polymerisations are not compatible with the TBD catalyst, leading to broad dispersities. These poorly-defined polymers cannot form well-defined micellar structures; hence an alternative polymerisation technique was explored.

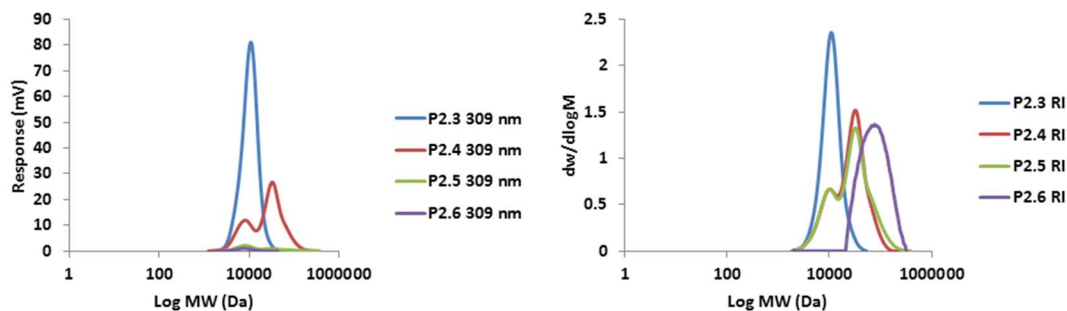
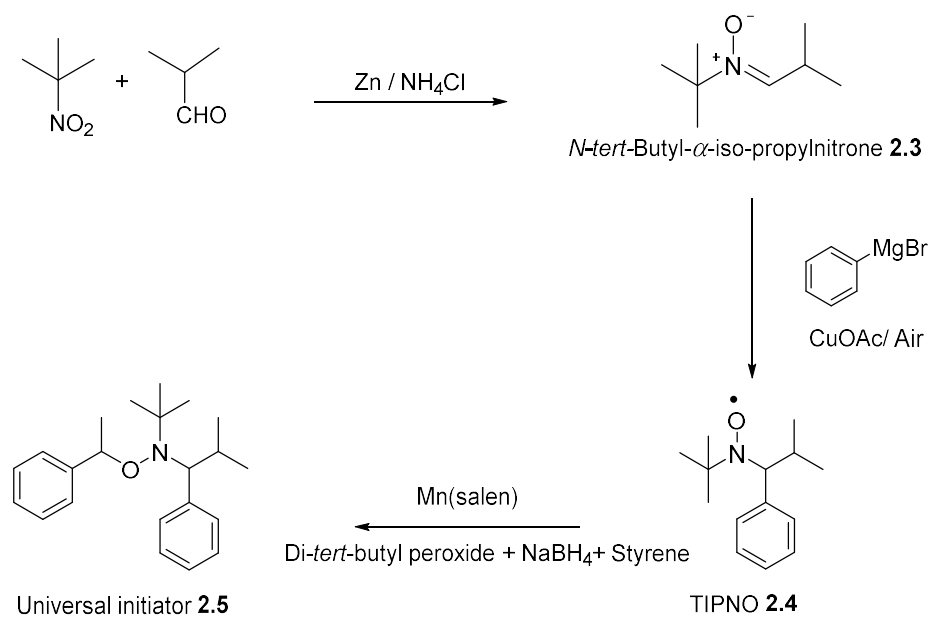


Figure 2.19: Overlay of the SEC traces in CHCl_3 , for P2.3 (blue), P2.4 (red), P2.5 (green), P2.6 (purple) Left: 309 nm traces as a function of response to molecular weight. Right: RI traces as a function of differential weight fraction against molecular weight.

2.3.3 Polymer synthesis using NMP

2.3.3.1 Synthesis of the universal initiator

Previously we have demonstrated that RAFT is an ineffective polymerisation technique for the TBD catalyst, due to aminolysis of the thiocarbonylthio end group.²¹ Thus, nitroxide mediated polymerisation (NMP), which has similar advantages such as good polymerisation control, was selected.^{24, 32, 33} The universal initiator, trimethyl-3-phenylethoxy-4-phenyl-3-azahexane first synthesised by Hawker *et al.*, enables polymerisation of a vast array of monomers.³⁴ The synthesis of this initiator is a three step process shown in Scheme 2.9.



Scheme 2.9: Synthesis of the universal initiator 2.5.

Firstly, *N*-tert-butyl- α -iso-propylnitron, **2.3**, was synthesised *via* a reductive condensation of 2-methyl-2-nitropropane with isobutyraldehyde, forming the nitron species. The reaction was monitored using thin layer chromatography (TLC, 10:1 ethyl acetate/ methanol $R_f = 0.49$); after 8 hours the reaction reached completion. The work-up consisted of a filtration of the reaction mixture followed by an extraction with dichloromethane and brine, dichloromethane was subsequently removed to afford a colourless liquid with a yield of 94%. Analysis of **2.3** by ¹H NMR and ¹³C NMR spectroscopy (Figure 2.20 and Figure 2.21), showed a good correspondence of the peaks to the literature values.³⁴

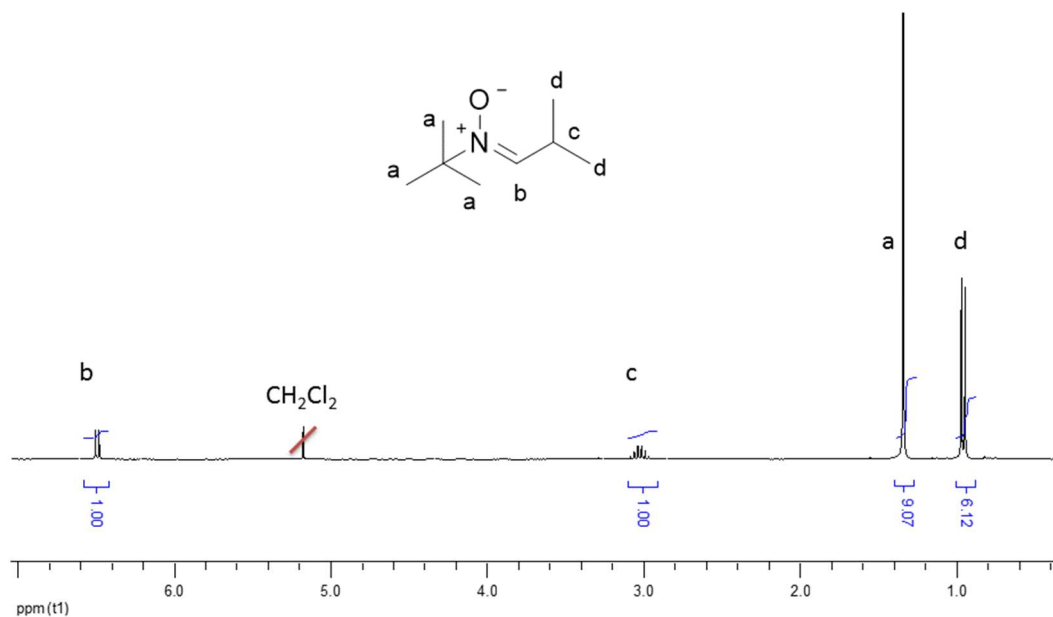


Figure 2.20: ¹H NMR spectrum of 2.3, in CDCl₃ at 300 MHz.

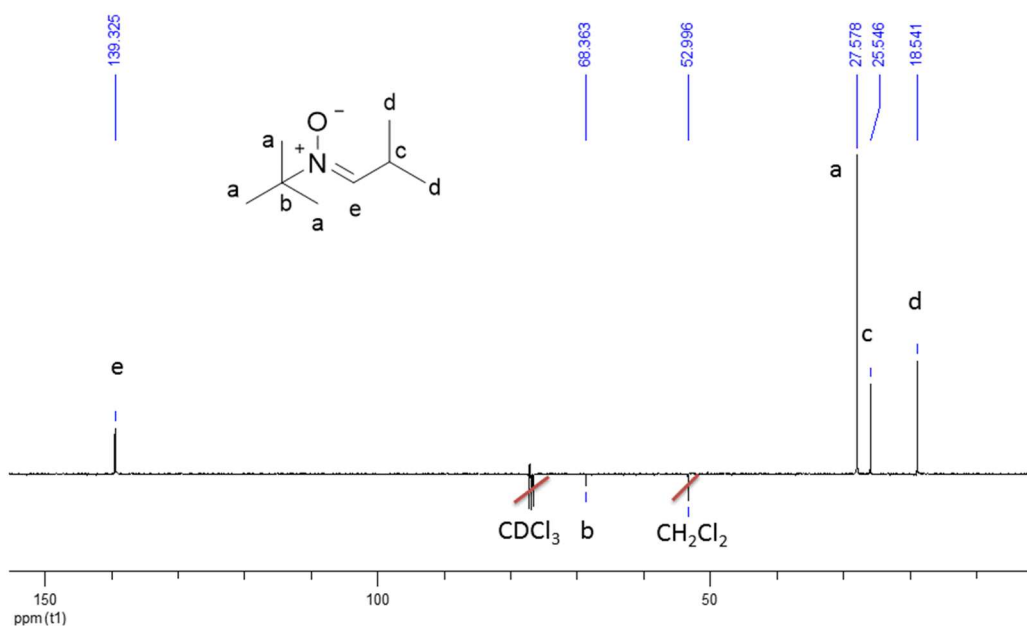
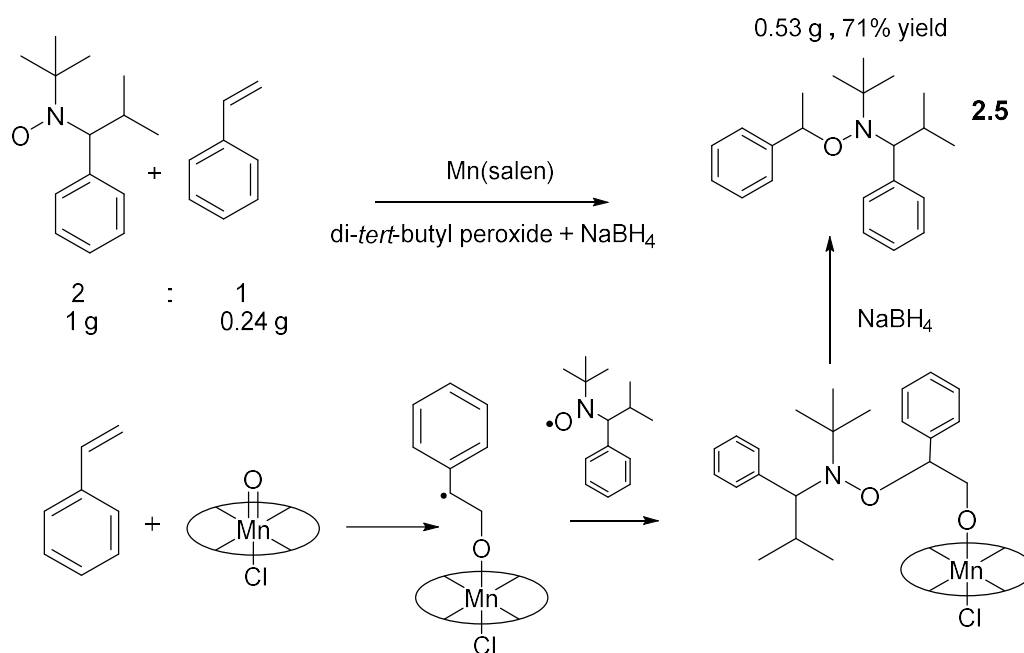


Figure 2.21: ¹³C NMR spectrum of 2.3, in CDCl₃ at 300 MHz.

The second step was the synthesis of the nitroxide species, trimethyl-4-phenyl-3-azahexane-3-nitroxide, (TIPNO) **2.4**. This was achieved *via* an arylation of the

nitron with an aryl Grignard reagent, followed by the oxidation of the nitron with copper (II) acetate.³⁴ The product **2.4** was formed with a low yield of 36%. Due to the radical species present in solution the formation of the product was confirmed qualitatively by electrospray ionisation mass spectroscopy (ESI-MS) giving a product peak of $[M + Na^+]$ 243.1. The final step afforded the production of the α -hydrogen using styrene and Jacobsen's reagent, with the mechanism depicted below.³⁵ The Jacobsen-Katsuki asymmetric catalyst Mn(salen) is activated using di-*tert*-butyl peroxide which forms a radical species with styrene that is then capped by the TIPNO radical. The addition of sodium borohydride yields the universal initiator **2.5** and regenerates the Mn(salen) catalyst.



Scheme 2.10: Schematic representation of the formation of **2.5**.

Initial attempts saw the formation of two additional peaks at 2.9 and 2.7 ppm via ¹H NMR spectroscopy in comparison to the reported values for the compound. The

Jacobsen's catalyst is known to form epoxides when styrene is present, with these peaks corresponding to the doublet of doublets found in styrene oxide.³⁵ This impurity was removed through the generation of the alkoxyamine salt, by stirring with 0.25 M hydrochloric acid and diethyl ether. Once a precipitate had formed this was then filtered and washed with basic water, to afford a yield of 49% of **2.5** as a white semicrystalline solid. To eliminate the formation of the side product the ratio of TIPNO to styrene was altered (2:1) to ensure the TIPNO radical was in excess to cap the new radical formed. The product was purified using flash column chromatography (100:1 hexane/ ethyl acetate) to give a mixture of stereoisomers with a yield of 71%. By comparison of peaks **f** and **f'** seen in the ¹H NMR spectrum at 0.53 ppm and 0.21 ppm (Figure 2.22), a diastereoisomer ratio of 1:1.1 was obtained. This is due to the two chiral centres present (**a** and **d**). Literature values report two hydrogens at 2.4 ppm for **e** however in this position integrals indicated only one stereoisomer.³⁴

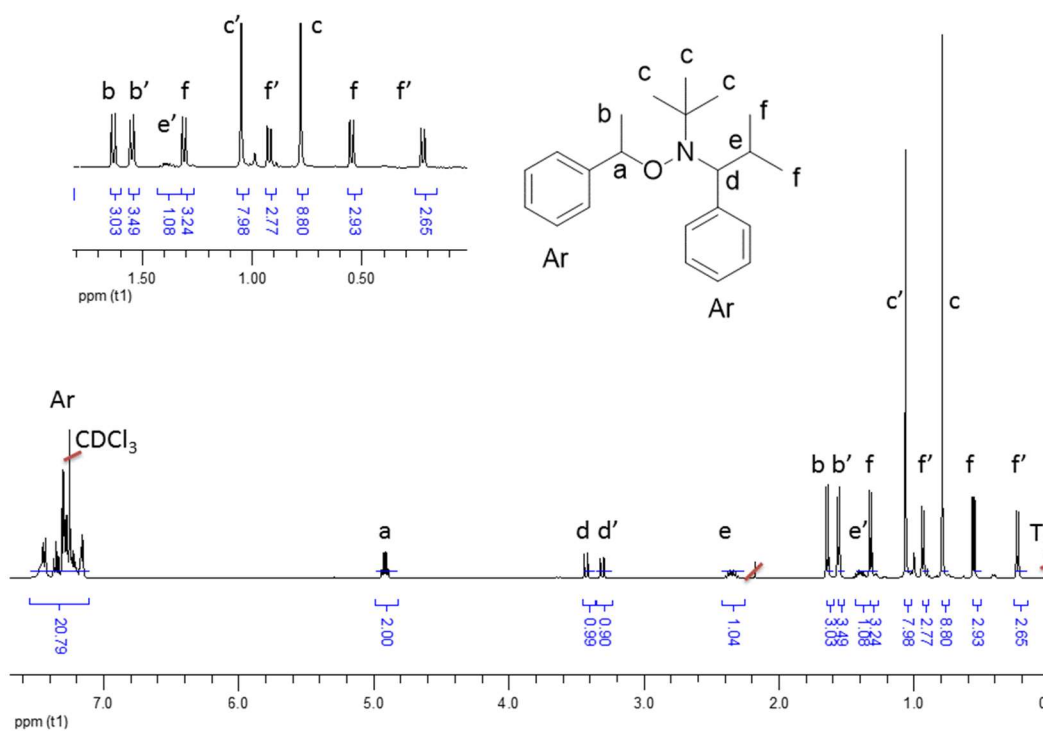


Figure 2.22: ^1H NMR spectrum of 2.5, in CDCl_3 at 400 MHz.

Correlation spectroscopy (COSY) analysis was run, with the spectrum (Figure 2.23) showing a larger separation for **e** and **e'**. The literature reports two hydrogens at 2.4 ppm however the COSY spectrum confirmed the presence of this large splitting with the peak at 1.3 ppm accounted for the minor stereoisomer **e'** as shown in Figure 2.23.

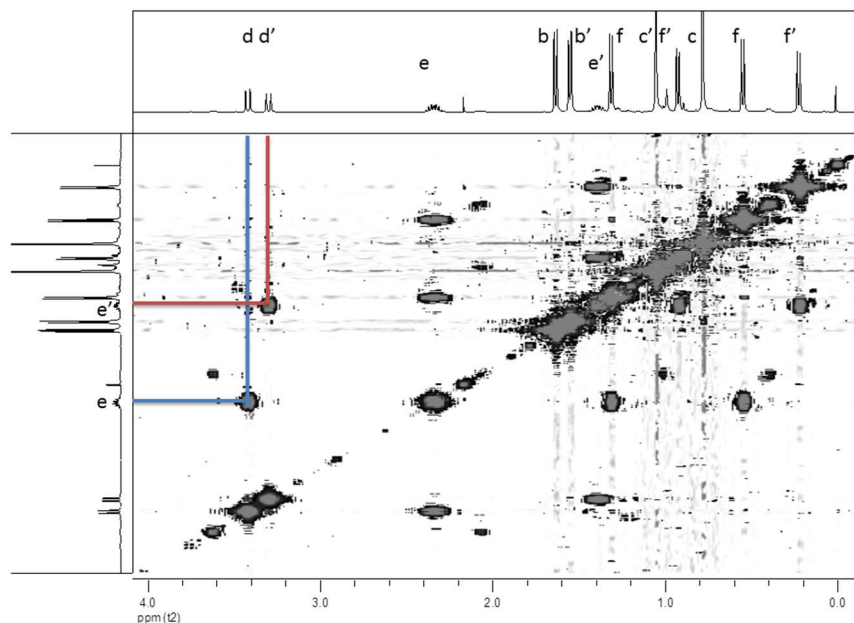


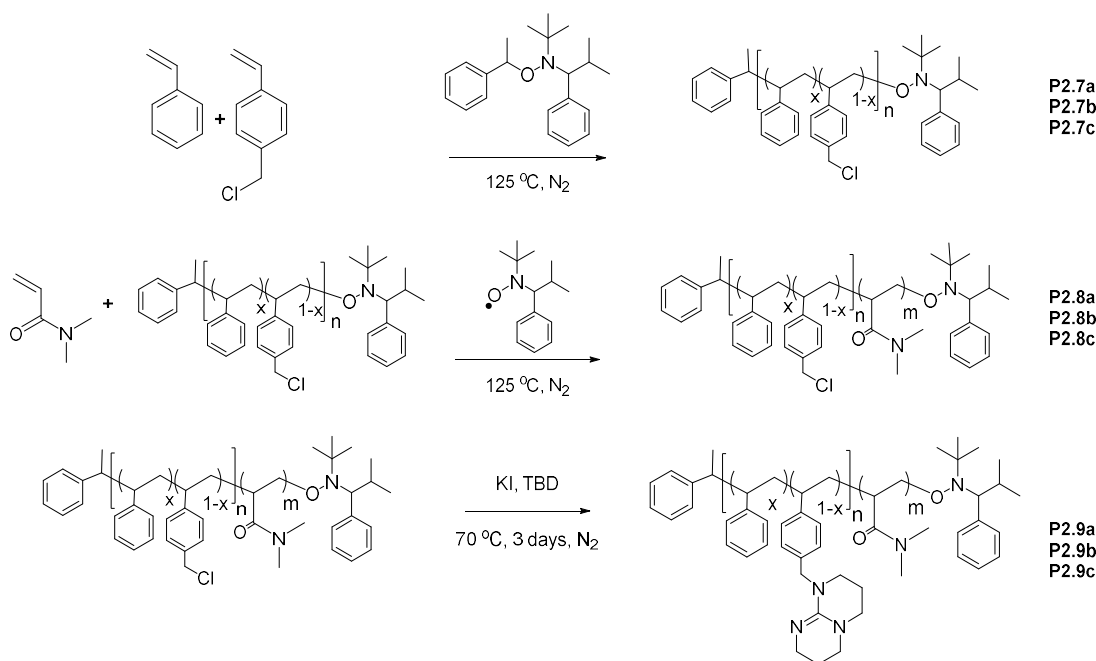
Figure 2.23: COSY NMR spectrum of **2.5**, in CDCl_3 at 400 MHz, the red line highlights the coupling of e' to d' and the blue line highlights the coupling of e to d .

The formation of the universal initiator **2.5** was further confirmed by ESI-MS $[M+1] = 326$ Da, again in good agreement with the reported values.³⁴ This initiator was used for the synthesis of various amphiphilic block copolymers *via* NMP.

2.3.3.2 Polymer Synthesis

The universal initiator **2.5** was utilised for the copolymerisation of St and BzCl .³⁴ Different loadings were targeted in order to explore the effects of core catalytic loading on catalysis. The subsequent polymers were then chain extended with DMA before substitution of TBD onto the polymer scaffold (Scheme 2.11). As the end group is not susceptible to degradation by the catalyst TBD, no end group removal step was required. The synthesis of the block copolymers is shown in Scheme 2.11

with loadings of 1%, 5 % and 10% targeted (labelled a-c respectively). This was achieved through altering the ratio of BzCl to styrene in the copolymerisation.



Scheme 2.11: Schematic representations of the formation of the amphiphilic block copolymers containing the catalyst TBD by NMP.

The following analysis relates to the formation of **P2.9b** (5% loading). The same procedures were followed for the synthesis of polymers **P2.9a** and **P2.9c**, with the data summarised in Table 2.1.

Initially St was copolymerised with BzCl; these two monomers were added to an ampoule and freeze pump thawed four times. The polymerisation proceeded under nitrogen at 125 °C. A high temperature was required (125 °C) to initiate the alkoxyamine breaking the C-O bond forming the nitroxide radical.²⁴ The polymerisation of **P2.7b** reached a conversion of 64% after 3 hours (Figure 2.24).

The reaction vessel was subjected to rapid cooling and the solution was precipitated into methanol three times and dried under vacuum, to provide **P2.7b** as a white solid.

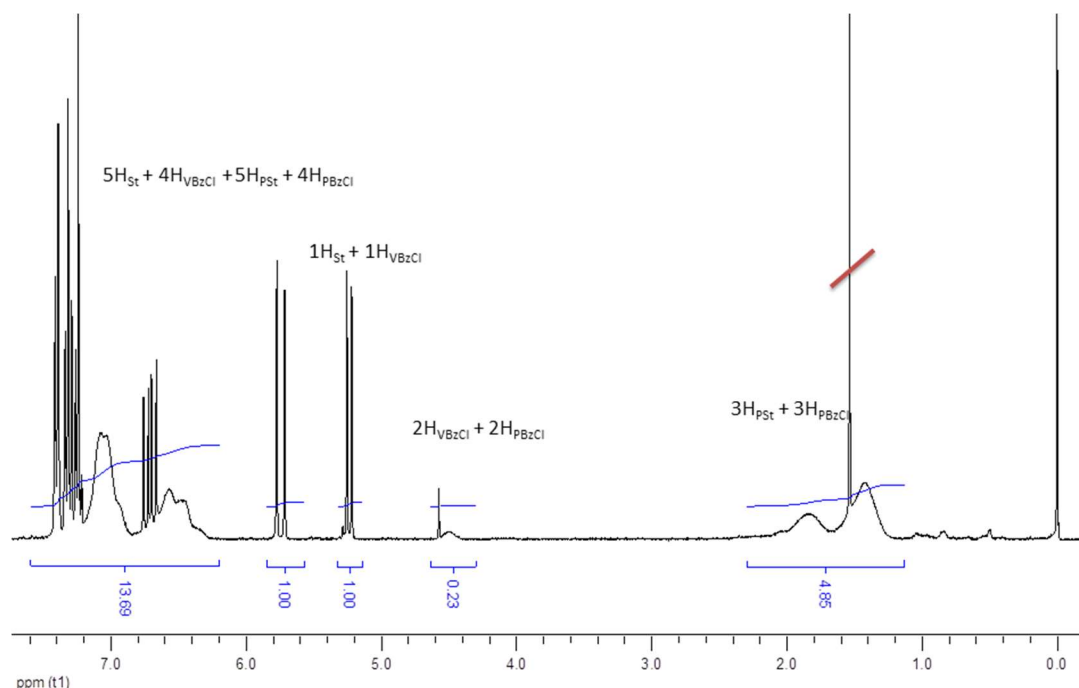


Figure 2.24: Conversion ^1H NMR spectrum of **P2.7b**, in CDCl_3 at 400 MHz.

The polymer was analysed utilising ^1H NMR spectroscopy to give a M_n of 6.5 kDa (Figure 2.25). The DP was calculated utilising the α -hydrogen of the nitroxide chain end at 3.2 ppm (e) which equates to one hydrogen species (DP = 65). The loading of BzCl was determined as 6%; this is slightly higher than the targeted loading of 5%. The reactivity ratios for the copolymerisation of St and BzCl for a free radical polymerisation have been shown by Kondo *et al.* as $r_{\text{St}} = 0.72$, and $r_{\text{BzCl}} = 1.31$.^{26, 27} As the monomer BzCl has a slightly higher reactivity, this will account for the higher incorporation observed. Finally, SEC (CHCl_3 , PSt standards) analysis was performed

and the M_n was determined as 5.2 kDa with a narrow dispersity obtained ($D_M = 1.10$).

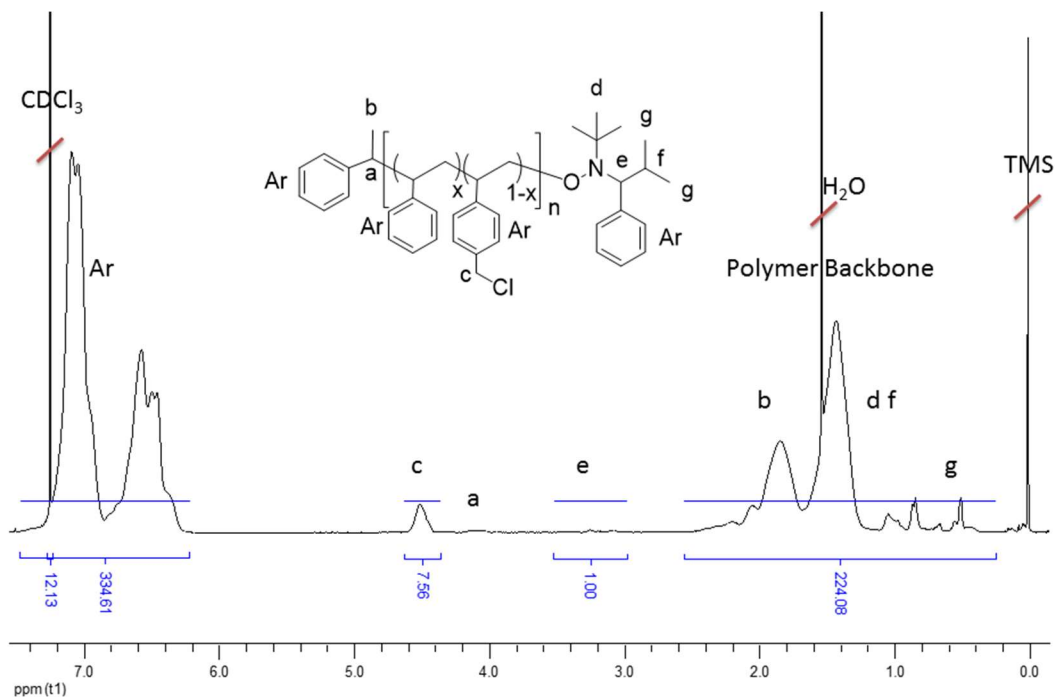


Figure 2.25: Long acquisition ^1H NMR spectrum of **P2.7b**, in CDCl_3 at 400 MHz.

The polymer **P2.7b** was chain extended with DMA. For this chain extension 0.05 equivalents of the TIPNO radical, **2.4**, was used. The excess nitroxide radical species was used to produce the persistent radical effect.^{32, 34, 36, 37} The macro-initiator was dissolved in an excess of DMA and freeze pump thawed four times. After heating at 125 °C for 24 hours the reaction had proceeded to a conversion of 70%. The reaction vessel was subjected to rapid cooling prior to three precipitations in diethyl ether. The resultant polymer was dried to give a white solid (**P2.8b**). The DP of PDMA was determined as 182, providing a M_n of 31.7 kDa

(^1H NMR spectroscopy, Figure 2.26). Analysis using SEC (CHCl_3 , PSt standards) gave a M_n of 33.0 kDa with a narrow dispersity of 1.20.

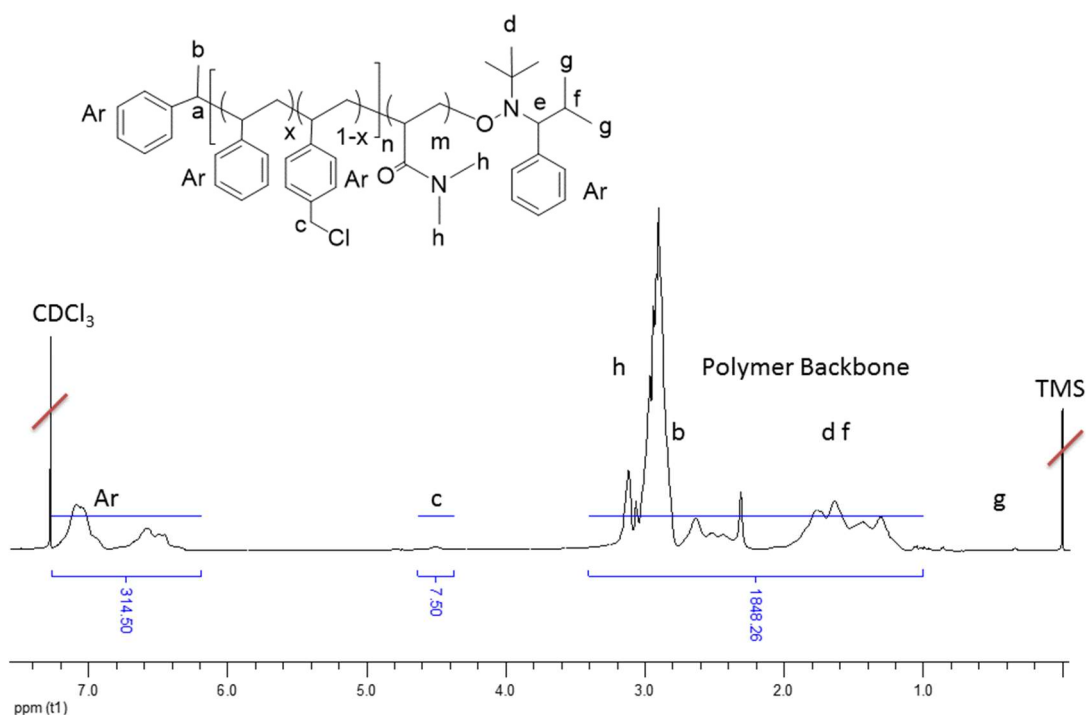


Figure 2.26: Long acquisition ^1H NMR spectrum of P2.8b, in CDCl_3 at 400 MHz.

The post polymerisation modification of the BzCl *via* an $\text{S}_{\text{N}}2$ substitution was demonstrated previously, and was carried out with no modifications being made to this method.⁸ A solution of TBD and KI was stirred under nitrogen (*ca.* 10 minutes), the amphiphilic block copolymer was dissolved in DMF under a nitrogen atmosphere and added to the flask, and the solution heated to 70 $^{\circ}\text{C}$. The substitution was monitored by ^1H NMR spectroscopy (Figure 2.27) through the downfield shift of the methylene group (c) from 4.4 ppm to 4.7 ppm. After 3 days the DMF was removed under vacuum and the polymer was dialysed to remove the small molecules. The resultant polymer was freeze-dried yielding a pale yellow solid. The

substitution of TBD resulting in **P2.9b** was characterised using long acquisition ^1H NMR spectroscopy (CDCl_3 , 400 MHz) as shown in Figure 2.27 and SEC analysis (CHCl_3 , PSt standards, Figure 2.28).

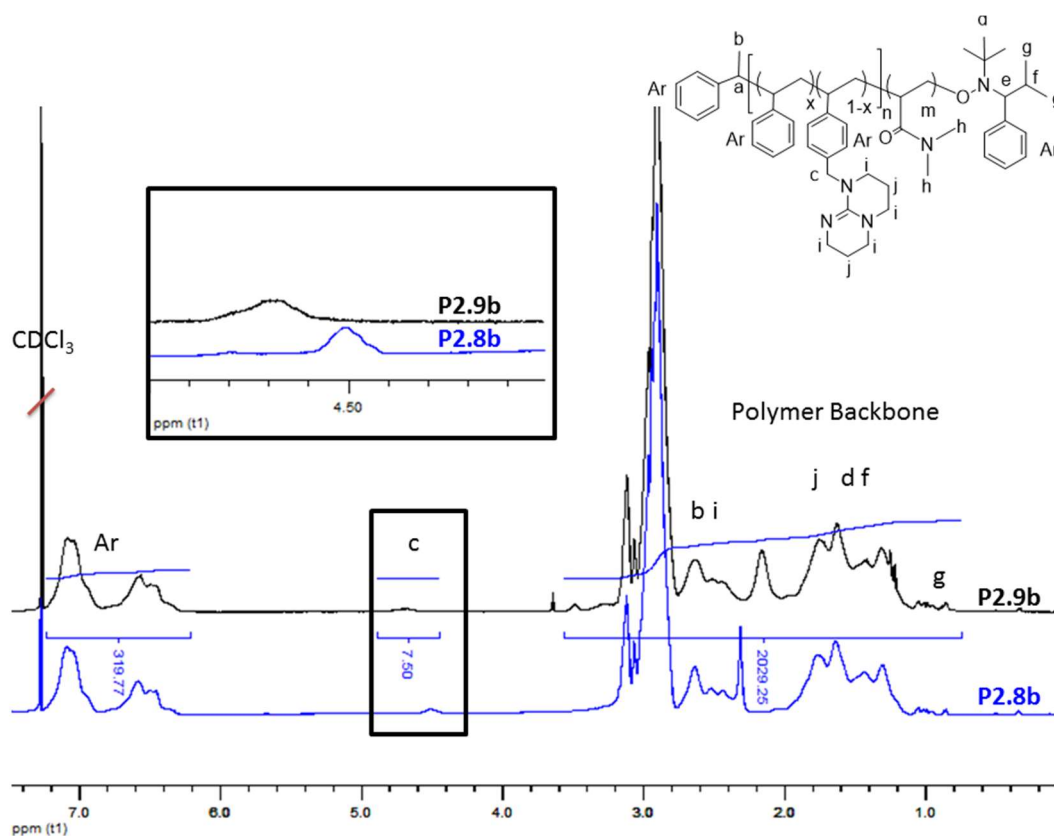


Figure 2.27: Long acquisition ^1H NMR spectrum of P2.8b (blue) and P2.9b (black), in CDCl_3 at 400 MHz.

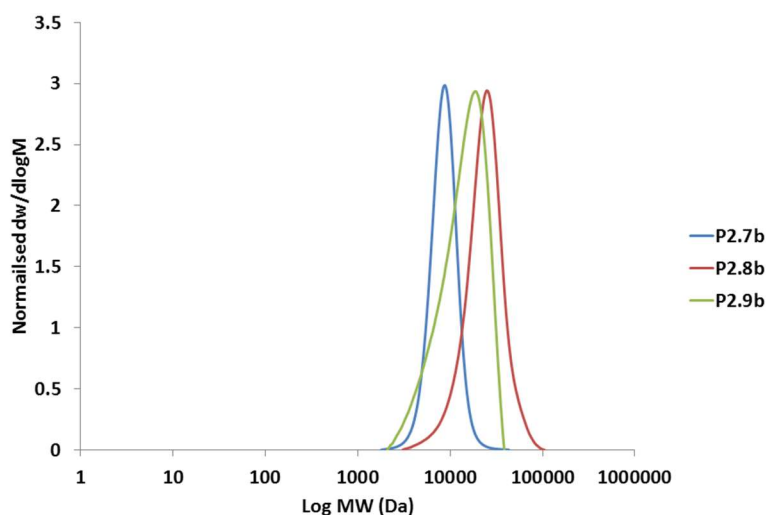


Figure 2.28: Overlay of the SEC data, for the RI traces of P2.7b (blue), P2.8b (red), P2.9b (green) as a function of normalised differential weight fraction against molecular weight in CHCl_3 (PSt standards).

By overlaying the SEC traces (above) a clear shift is observed as **P2.7b** is extended with DMA affording **P2.8b**. Upon the substitution of TBD a reduction in the molecular weight is observed with an increased dispersity. We hypothesise that the bound TBD is interacting with the SEC columns increasing the retention time, hence the observed increase in dispersity and decrease in molecular weight is not an accurate representation of the molecular weight. This procedure was repeated for **P2.9a** and **P2.9c**, with the results shown in Table 2.1. All of the polymers showed relatively narrow dispersities and indicated good substitution of TBD onto the polymeric backbone.

Table 2.1: Characterisation data of polymers P2.7a-P2.9c by ^1H NMR spectroscopy (CDCl_3 , 400 MHz) and SEC analysis (CHCl_3 , PSt standards), n represents the DP of St and BzCl, x is the fraction of St in the hydrophobic block and m is the DP of DMA.

Loading	Polymer	n	x	m	M_n (kDa)	M_n (kDa)	\bar{D}_M
					(SEC, CHCl_3)	(NMR)	
1%	P2.7a	59	0.99	-	5.2	6.5	1.10
	P2.8a	59	0.99	254	33.0	31.7	1.20
	P2.9a	59	0.99	254	28.6	31.7	1.34
5%	P2.7b	65	0.94	-	5.5	7.3	1.10
	P2.8b	65	0.94	182	20.4	25.3	1.25
	P2.9b	65	0.94	182	11.3	25.7	1.36
10%	P2.7c	75	0.89	-	7.0	8.7	1.08
	P2.8c	75	0.89	230	30.0	31.5	1.39
	P2.9c	75	0.89	230	20.5	32.4	1.27

2.3.4 Micelle assembly

The block copolymers synthesised in the previous section were assembled into micellar aggregates. Due to the glassy nature of the core the amphiphilic block copolymers were assembled using the solvent switch method.³⁸ The polymer was initially dissolved in DMF, which is a good solvent for both blocks, at a concentration of 10 mg mL^{-1} . Dynamic light scattering (DLS) analysis, confirmed the dissolution of the polymer, with the presence of unimers (at 10 mg mL^{-1}) with a size of 7 nm. The intensity of the correlation function graph was comparable to the measurement noise ($g_2(t) \text{ max} = 0.14$) which was attributed to the weak scattering of the analytes, thus suggesting the absence of particles. Water ($18.2 \text{ M}\Omega \text{ cm}$), a non-solvent for the hydrophobic block, was subsequently added using a peristaltic pump at 0.6 mL min^{-1} . The solution was then dialysed extensively with $18.2 \text{ M}\Omega \text{ cm}$ water to remove DMF. This yielded a solution of spherical micelles at a concentration of

2 mg mL⁻¹, encapsulating the TBD catalyst within the hydrophobic core with a PDMA corona (Figure 2.29).

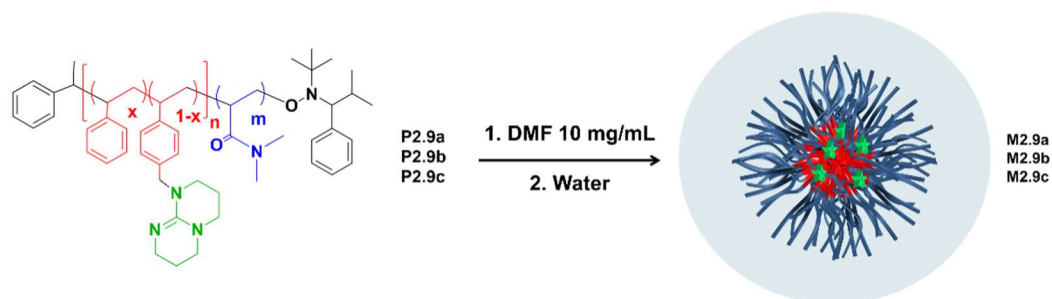


Figure 2.29: Schematic representation of the formation of M2.9a-c using the solvent switch method.

The spherical micelles were characterised using a combination of techniques utilising DLS to determine size data, static light scattering (SLS), and transmission electron microscopy (TEM) to determine morphology and shape. The particles were diluted to a concentration of 1 mg mL⁻¹ for DLS analysis; the data is shown in Figure 2.30, giving a D_h of 42 nm ($D = 0.05$), 30 nm ($D = 0.15$), and 44 nm ($D = 0.10$), for micelles **M2.9a-c** respectively, all with a relatively narrow dispersity.

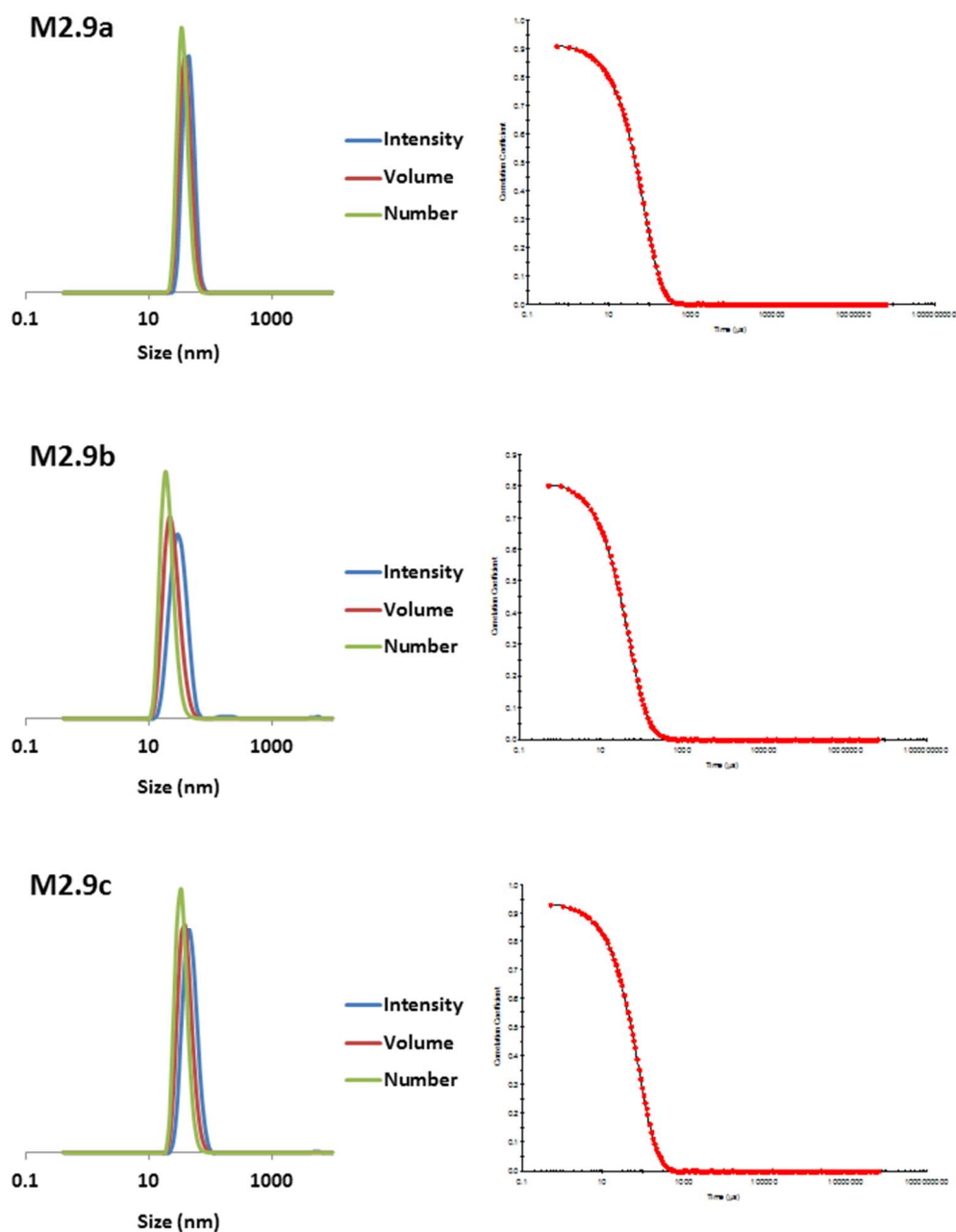


Figure 2.30: DLS data Left: Representation of the size distribution of M2.9a-c in water at 0.1 mg mL^{-1} obtained at 20°C , by intensity (blue), volume (red) and number (green). Right: the correlation function for M2.9a-c plotted against time (μs).

Analysis by SLS (performing tandem DLS at each measurement angle) was carried out at a concentration of 1 mg mL^{-1} (Table 2.2). The D_h obtained is in agreement with the data obtained from the single angle DLS measurements performed (Figure 2.30 and Table 2.2). Interestingly the aggregation number (N_{agg}) varied significantly

from **M2.9a** to **M2.9b**, this is a consequence of the shorter hydrophilic block (Table 2.2) which results in lower curvature of the corona increasing the aggregation number. A decrease in N_{agg} is also observed, as the TBD loading increased the core block becomes more hydrophilic. This was observed when a similar block copolymer was loaded with 20% TBD in the hydrophobic block (synthesis not shown) and no assembly was observed.

Table 2.2: SLS data of polymers **M2.9a-c**, determining hydrodynamic radius and aggregation number obtained by Lewis Blackman.

	R_h (nm)	N_{agg}	Degree of Polymerisation	
			Hydrophobic	Hydrophilic
M2.9a	24	60	59	254
M2.9b	18	115	65	182
M2.9c	22	25	75	230

The micelles **M2.9a-M2.9c** were further characterised by TEM, with the micellar solutions further diluted to a concentration of 0.1 mg mL^{-1} . The solutions were dropped onto a grid and freeze-dried to remove water. Graphene oxide (GO) treated lacy carbon grids were used requiring simpler sample preparation in comparison to staining techniques.^{39, 40} These images (Figure 2.31) confirm the presence of spherical nanoparticles within the solution.

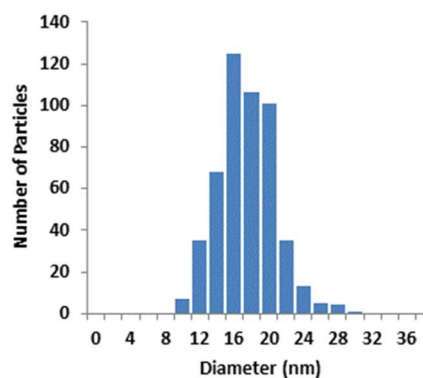
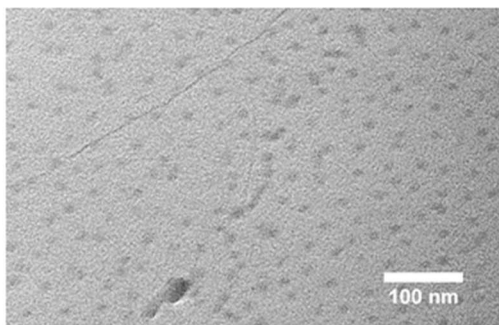
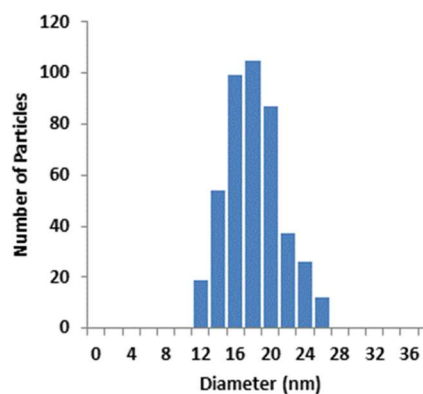
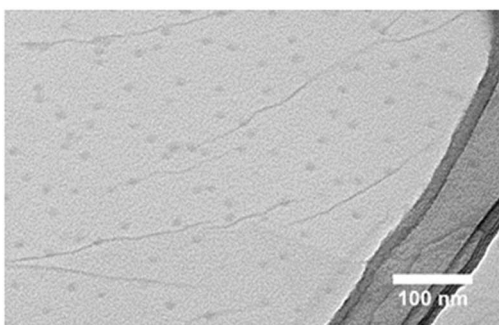
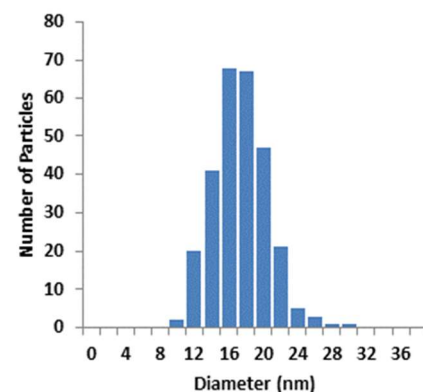
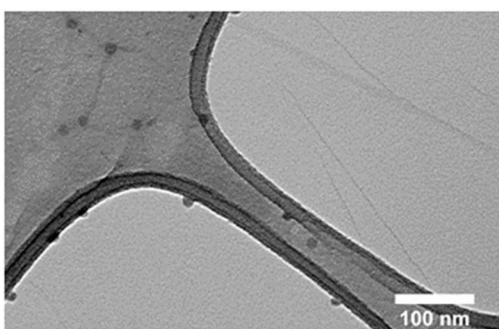
M2.9a**M2.9b****M2.9c**

Figure 2.31: Left: TEM images of M2.9a-c at 0.1 mg mL^{-1} scale bar = 100 nm Right: Histograms of the data obtained *via* TEM for M2.9a-c on GO. Images obtained by Dr Helen Wilcock.

The histograms were obtained through measuring the diameter of the nanoparticles from a minimum of 20 images from different areas of the grid. This data shows good correlation of size throughout the TEM grids. Upon comparison of the TEM data to the DLS data the micelles are observed to be much smaller, indicating that the PDMA corona cannot be visualised. Hence, micelles were stained with

phosphotungstic acid (PA) and analyzed *via* TEM, to ensure the images are showing both the core and corona blocks; this data is shown below.

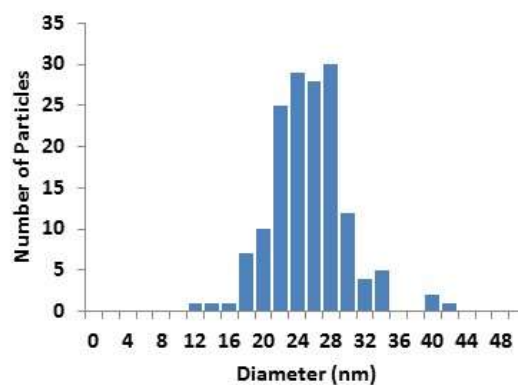
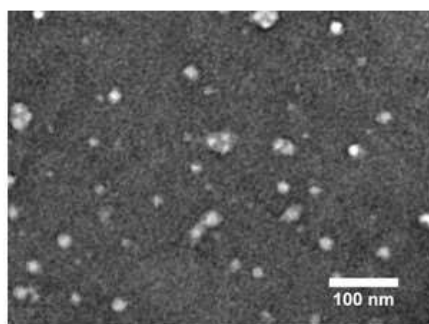
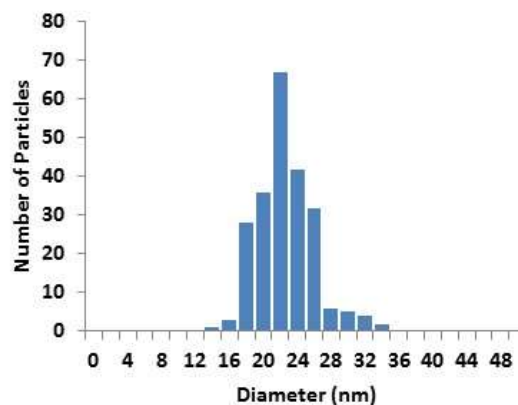
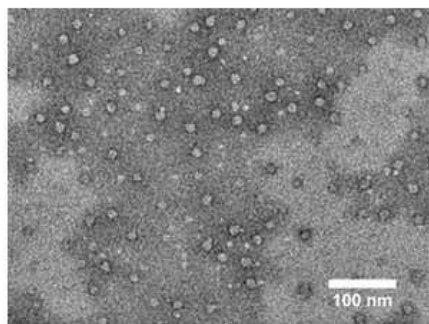
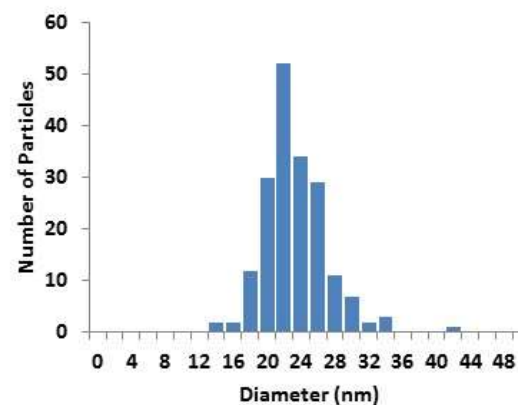
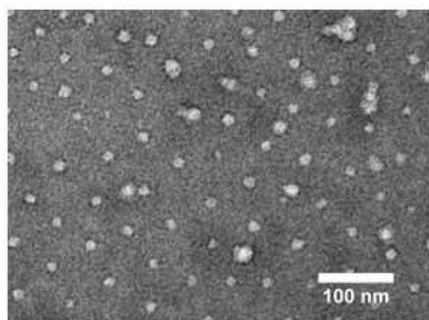
M2.9a**M2.9b****M2.9c**

Figure 2.32: Left: TEM images of M2.9a-c at 0.1 mg mL^{-1} scale bar (100 nm) Right: Histograms of the data obtained *via* TEM for M2.9a-c after staining with phosphotungstic acid. Images obtained by Dr Yan Kang.

Staining resulted in an increase in the average size, this accounts for the corona block which cannot be seen on the GO grids. A summary of the characterisation data is shown in Table 2.3, where an observable decrease in size of the micelles is observed *via* TEM. This is as a consequence of the micelles being in the hydrated state for both DLS and SLS, hence the corona is solvated. Upon dehydration for TEM these solvated chains dehydrate reducing the size of the nanoparticles.⁴⁰

Table 2.3: Characterisation data of the spherical micelles; ^a DLS (1 mg mL⁻¹), ^b SLS analysis (1 mg mL⁻¹), ^c TEM GO (0.1 mg mL⁻¹) and ^d TEM stained (0.1 mg mL⁻¹).

Micelles	D_h (nm), (PD) ^a	D_h (nm) ^b	N_{agg} ^b	D_{ave} (nm) ^c	D_{ave} (nm) ^d
M2.9a	42 (0.05)	48	60	16 ± 3	24 ± 5
M2.9b	30 (0.15)	36	115	17 ± 3	22 ± 4
M2.9c	44 (0.10)	44	25	16 ± 3	22 ± 4

Here we have shown these amphiphiles can be readily synthesised by NMP with tuneable loadings of the catalyst TBD onto the hydrophobic block. These amphiphiles were subsequently assembled to form the targeted micellar aggregates with TBD embedded within the hydrophobic domain.

2.4 Conclusions

Within this Chapter a new styrenic-TBD monomer has been synthesised, **2.1**. Polymerisation of this monomer *via* RAFT polymerisation was unsuccessful which was attributed to degradation of the RAFT CTA in the presence of the TBD catalyst. Latently functionalised polymer scaffolds synthesised by RAFT allowed for the immobilisation of TBD through the pendent chlorine functional groups. However, poorly defined polymers were obtained as a consequence of thiol coupling through the polymer chain ends which formed during TBD immobilisation. Based on these observations we have shown RAFT polymerisation to be incompatible with TBD immobilisation, both during polymerisation and in post-polymerisation approaches. Subsequently an alternative RDRP technique (NMP) was used, providing well-defined amphiphilic block copolymers with control over the targeted loadings of TBD onto the hydrophobic domain. These amphiphiles were assembled in water resulting in the formation of micellar structures containing the TBD catalytic functionality within the core, thus allowing for the development new catalytic nanoreactors. In the next Chapter we will explore the effects of this confined environment on the catalytic properties of immobilised TBD in aqueous media for Michael addition reactions.

2.5 Experimental

2.5.1 Materials

2,2-Azobis(2-methylpropionitrile), AIBN, was recrystallised twice from methanol and stored in the dark at 4 °C. Styrene was distilled over CaH₂ and stored at 4 °C. BzCl and DMA were all purified prior to use using basic alumina columns. Dialysis tubing was supplied by MediCell at molecular weight cut offs of 1 kDa and 3.5 kDa. All other chemicals were obtained from Sigma-Aldrich and used without further purification unless stated otherwise.

2.5.2 Instrumentation

Both ¹H and ¹³C NMR spectra were recorded on a Bruker DPX 400 FT-NMR spectrometer using deuterated solvents. The chemical shifts are reported as δ in parts per million. NMR data was analysed using MestRe-C software. Size exclusion chromatography (SEC) analysis was obtained using HPLC grade chloroform (CHCl₃) with 2% triethyl amine (TEA), with a flow rate of 1.0 mL per minute, on two PLgel 5 μ m Mixed-D columns, plus one guard column. The data was analysed using SEC Cirrus software with polystyrene (PSt) standards. Characterisation of the nanoparticles was carried out using a Zetasizer Nano series instrument (Malvern), at an angle of 173°. The DLS samples were filtered through a 0.45 μ m nylon membrane and left to stand for 30 minutes. The data was analysed using cumulant analysis of the correlation function using the Stokes-Einstein equation, as an average of four runs of 200 seconds. Multiple angle light scattering data was collected using an ALV/CGS-3 Compact Goniometer System. dn/dc values were determined using a Shodex RI-101 refractometer. The wavelength of the incident beam was 633 nm and

for each angle, two runs of 100 s were measured. Particles were filtered through 0.45 μ m nylon filters prior to measurement at multiple angles from 30-130° against a toluene standard. SLS data was obtained by Mr Lewis Blackman. Brightfield TEM images were captured with a transmission electron microscope (JEOL TEM-2011), operating at 200 kV. GO TEM images were taken by Dr Helen Willcock and stained images were obtained by Dr Yan Kang.

2.5.3 Synthesis of StTBD 2.1

Triazabicyclodec5-ene, TBD, (1 g, 7.18×10^{-3} mol) was added to a solution containing potassium hydroxide (0.4 g, 7.18×10^{-3} mol) in 10 mL of distilled water at ambient temperature. The water was removed by lyophilisation leading to a semi-solid residue. The solid was dissolved in 30 mL dry DMF under nitrogen. Meanwhile BzCl (1.096 g, 7.18×10^{-3} mol) and the inhibitor 2-6-ditertbutyl-4-methylphenol (4 mg, 1.82×10^{-4} mol) were dissolved in 20 mL dry DMF under nitrogen protection. The solution was added to the TBD solution at ambient temperature, and heated to 70 °C for 16 hours. The DMF was removed by lyophilisation. The resultant yellow oil was acidified with 1 M HCl and the aqueous layer washed three times with diethyl ether. The pH of the aqueous layer was adjusted to pH 12 and the organic layer was washed three times with CH₂Cl₂. The organic layer was dried over MgSO₄ filtered, and the solvent evaporated yielding a yellow oil (0.36 g, 20 %). ¹H NMR (400 MHz, CDCl₃) δ (ppm): 7.36 (2H, d, ³J_{H-H} = 8.2 Hz, **d**), 7.22 (2H, d, ³J_{H-H} = 8.2 Hz, **d**), 6.67 (1H, dd, ³J_{H-H} = 17.6, ³J_{H-H} = 10.9 Hz, HC=CHH, **c**), 5.72 (1H, d, ³J_{H-H} = 17.6 Hz, HC=CHH, **a**), 5.23 (1H, d, ³J_{H-H} = 10.9 Hz, HC=CHH, **b**), 4.76 (2H, s, CH₂, **e**), 3.4-3.5 (2H, m, CH₂, **h**), 3.0-3.3 (6H, m, 4 x CH₂, **f**), 1.89 (4H, m, 2 x CH₂, **g**). ¹³C NMR (100 MHz, CDCl₃) δ (ppm):

136.6, 128.4, 126.2, 113.3, 53.7, 46.1, 45.2, 44.9, 40.5, 22.2. ES-HRMS (MaXis) m/z calculated found $[M+1]$ 256.1807 Da.

2.5.4 Synthesis of 2-(dodecylthiocarbonothioylthio)-2-methylpropionic acid (DDMAT) 2.2.²⁵

Tripotassium phosphate (0.672 g, 4.9×10^{-3} mol) was suspended in 20 mL of acetone. 1-dodecanethiol (1 mL, 4.9×10^{-3} mol) was added to the suspension and stirred for 10 minutes. Carbon disulfide (0.75 mL, 1.3×10^{-2} mol) was added to the white solution and stirred. The suspension turned bright yellow. After 1 hour bromoisobutyric acid was added (0.75 mL, 4.9×10^{-3} mol), and the reaction stirred for 16 hours at room temperature. The solvent was removed, and the solution was acidified with HCl (1 M), and extracted with CH_2Cl_2 . The crude product was washed with water and brine. The CH_2Cl_2 was removed and the product collected by flash column chromatography (silica gel, EtOAc), affording a yellow crystalline solid (0.94 g, 53%). ^1H NMR (400 MHz, CDCl_3) δ (ppm): 3.25 (2H, t, $^3J_{\text{H-H}} = 7.5$ Hz, $\text{CH}_2\text{-S}$, **c**), 1.72 (6H, s, CH_3 , **d**), 1.62 (2H, m, CH_2 , **e**), 1.25-1.44 (18H, m, CH_2 , **b**), 0.85 (3H, t, $^3J_{\text{H-H}} = 6.9$ Hz, CH_3 , **a**).

2.5.5 RAFT polymerisation of St and BzCl, P2.1

Styrene (1 g, 9.6×10^{-3} mol), BzCl (0.37 g, 2.4×10^{-3} mol), DDMAT (CTA) (0.043 g, 1.2×10^{-4} mol), and dioxane (1 mL) were placed in a dried ampoule with a magnetic stirrer bar, under a constant nitrogen flow. The ampoule was degassed via freeze pump thaw cycles until the vacuum was stable. The ampoule was backfilled with nitrogen and placed in a pre-heated oil bath at 110 °C for 72 hours (64%

conversion). The polymerisation was rapidly cooled in liquid nitrogen. The polymer solution was precipitated into cold stirring methanol three times, filtered and dried in a vacuum oven overnight. ^1H NMR (400 MHz, CDCl_3) δ (ppm): 7.2-6.0 ($5\text{H}_{\text{st}} + 4\text{H}_{\text{BzCl}}$, *ArH*, **Ar**) 4.4-4.2 (2H_{BzCl} , CH_2 , **d**), 3.2 ($2\text{H}_{\text{end group}}$, t, **c**), 2.4-1.0 ($3\text{H}_{\text{backbone}} + 26\text{H}_{\text{end group}}$, $\text{CH}_2 + \text{CH}_3$, **b + c**), 0.88 ($3\text{H}_{\text{end group}}$, t, CH_3 , **a**). M_n (^1H NMR) = 5.8 kDa, $\text{DP}_{\text{St}} = 36$, $\text{DP}_{\text{BzCl}} = 11$, M_n (SEC, CHCl_3 , PSt calibration) = 7.1 kDa, $D_M = 1.19$.

2.5.6 TBD substitution on to the polymer, P2.2

TBD (0.19 g, 1.4×10^{-3} mol), KI (4 mg, 2.6×10^{-5} mol) and dry DMF (5 mL) were added to a dried round bottom flask (RBF) with a magnetic stirrer bar under nitrogen. The polymer P2.1 (0.25 g, 3.3×10^{-5} mol) was dissolved in dry DMF (5 mL) before being added to the RBF under nitrogen. The RBF was placed in a pre-heated oil bath at 70°C for 60 hours. The polymer was precipitated in cold stirring methanol, filtered and dried in a vacuum oven overnight. Yield: 66.5 %. ^1H NMR (400 MHz, CDCl_3) δ (ppm): = 7.4-6.0 ($5\text{H}_{\text{st}} + 4\text{H}_{\text{BzCl}}$, *ArH*, **Ar**), 4.8-4.2 (2H_{BzTBD} , CH_2 , **d**), 3.5-2.5 ($8\text{H}_{\text{TBD}} + 2\text{H}_{\text{end group}}$ CH_2 , **c + f**), 2.5-1.0 ($3\text{H}_{\text{backbone}} + 26\text{H}_{\text{end group}} + 4\text{H}_{\text{TBD}}$, CH_2 , **b + e + g**), 0.88 (3H, t, CH_3 , **a**). M_n (^1H NMR) = 12.1 kDa, M_n (SEC, CHCl_3 , PSt calibration) = 40.2 kDa, $D_M = 2.03$.

2.5.7 RAFT polymerisation of DMA, P2.3

Dimethylamine (0.5 g, 5.7×10^{-3} mol), cyanomethyl dodecyl trithiocarbonate (CTA) (0.0182 g, 5.7×10^{-5} mol), AIBN from stock solution (0.0009 g, 5.7×10^{-6} mol), and dioxane (1 mL) were placed in a dried ampoule with a magnetic stirrer bar, under a constant nitrogen flow. The ampoule was degassed *via* freeze pump thaw cycles until

the vacuum was stable. The ampoule was backfilled with nitrogen and placed in a pre-heated oil bath at 65 °C for 1 hour (90% conversion). The polymerisation was cooled in liquid nitrogen. The polymer solution was precipitated into cold stirring diethyl ether, filtered and dried in a vacuum oven overnight. ^1H NMR (400 MHz, CDCl_3) δ (ppm): = 3.6-1.0 ($12\text{H}_{\text{DMA}} + 24\text{H}_{\text{end group}}$, $\text{CH}_2 + \text{CH}_3$, **c** + **d** + **e** + **b**), 0.88 ($3\text{H}_{\text{end group}}$, t, $^3J_{\text{H-H}} = 7.1$ Hz, CH_3 , **a**). M_n (^1H NMR) = 12.2 kDa, DP = 119, M_n (SEC, CHCl_3 , PSt calibration) = 9.7 kDa, $D_M = 1.20$.

2.5.8 Chain extension to afford P2.4

The macro CTA **P2.3** (0.5 g, 3.19×10^{-5} mol), styrene (0.53 g, 5.11×10^{-3} mol), BzCl (0.20 g, 1.27×10^{-4} mol) and dioxane (1 mL) were all placed in a dried ampoule with a magnetic stirrer bar, under a constant nitrogen flow. The ampoule was degassed *via* freeze-pump-thaw cycles until the vacuum was stable. The ampoule was then backfilled with nitrogen and placed in a pre-heated oil bath at 110 °C for 72 hours (50% conversion). The polymerisation was quenched with THF and cooled in liquid nitrogen. The polymer solution was precipitated in cold stirring diethyl ether and filtered; the polymer was dried overnight in a vacuum oven. ^1H NMR (400 MHz, CDCl_3) δ (ppm): = 7.2-6.0 ($5\text{H}_{\text{st}} + 4\text{H}_{\text{BzCl}}$, ArH , **Ar**), 4.2-4.6 (2H_{BzCl} , CH_2 , **d**), 3.6-1.0 ($3\text{H}_{\text{st}} + 3\text{H}_{\text{BzCl}} + 12\text{H}_{\text{DMA}} + 24\text{H}_{\text{end group}}$, $\text{CH}_2 + \text{CH}_3$, **c** + **e** + **f** + **b**), 0.88 ($3\text{H}_{\text{end group}}$, t, $^3J_{\text{H-H}} = 7.1$ Hz, CH_3 , **a**). M_n (^1H NMR) = 23.6 kDa, DP = 117, M_n (SEC, CHCl_3 , PSt calibration) = 17.0 kDa, $D_M = 1.8$.

2.5.9 End group removal P2.5

The polymer **P2.4** (2.9 g, 1.24×10^{-4} mol), lauryl peroxide (0.10 g, 2.48×10^{-4} mol), AIBN (0.41 g, 2.48×10^{-3} mol) and toluene (310 mL, **P2.4** = 0.4 mM) were placed in a dried RBF with a magnetic stirrer bar, under a constant flow of nitrogen. The RBF was purged with nitrogen for 1 hour, put under a constant flow of nitrogen and placed in a pre-heated oil bath at 70 °C for 7 hours. The polymer was precipitated into cold stirring diethyl ether and filtered before drying in a vacuum oven overnight. ^1H NMR (400 MHz, CDCl_3) δ (ppm): = 7.2-6.0 ($5\text{H}_{\text{st}} + 4\text{H}_{\text{BzCl}}$, *ArH*, **Ar**), 4.2-4.6 (2H_{BzCl} , *CH*₂, **c**), 3.2-1.0 ($3\text{H}_{\text{St}} + 3\text{H}_{\text{BzCl}} + 12\text{H}_{\text{DMA}} + 10\text{H}_{\text{end group}}$, *CH*₂ + *CH*₃, **e** + **d** + **a** + **b**), 0.88 ($3\text{H}_{\text{end group}}$, t, $^3J_{\text{H-H}} = 7.1$ Hz, *CH*₃, **a**). M_n (^1H NMR) = 23.6 kDa, DP = 117, M_n (SEC, CHCl_3 , PSt calibration) = 17.4 kDa, $D_M = 2.05$.

2.5.10 TBD Substitution of P2.5

TBD (0.27 g, 2.0×10^{-3} mol), KI (0.013 g, 8.3×10^{-3} mol) and dry DMF (5 mL) were added to a dried round bottom flask (RBF) with a magnetic stirrer bar under nitrogen. The polymer **P2.5** (2.4 g, 1.0×10^{-4} mol) was dissolved in dry DMF (45 mL) before being added to the RBF under nitrogen. The RBF was placed in a pre-heated oil bath at 70 °C for 60 hours. The polymer was precipitated in cold stirring methanol, filtered and dried in a vacuum oven overnight. Yield: 66.5%. ^1H NMR (400 MHz, CDCl_3) δ (ppm): = 7.4-6.0 ($5\text{H}_{\text{st}} + 4\text{H}_{\text{BzCl}}$, *ArH*, **Ar**), 4.8-4.2 (2H_{BzTBD} , *CH*₂, **d**), 3.5-2.5 ($8\text{H}_{\text{TBD}} + 2\text{H}_{\text{end group}}$ *CH*₂, **c** + **f**), 2.5-1.0 ($3\text{H}_{\text{backbone}} + 10\text{H}_{\text{end group}} + 4\text{H}_{\text{TBD}}$, *CH*₂, **b** + **e** + **g**), 0.88 3H, t, *CH*₃, **a**). M_n (^1H NMR) = 12.1 kDa, M_n (SEC, CHCl_3 , PSt calibration) = 40.2 kDa, $D_M = 2.03$.

2.5.11 Synthesis of the Universal alkoxyamine initiator.³⁴

2.5.11.1 *N-tert- α -iso-propylnitrone*, **2.3**

2-methyl-2-nitropropane (5.15 g, 0.05 mol), isobutyraldehyde (3.6 g, 0.05 mol) and ammonium chloride (2.94 g, 0.055 mol) were added to a RBF and stirred at 0 °C in 200 mL of water and 100 mL of diethyl ether. Zinc powder (13 g, 0.2 M) was added portion wise over an hour, the solution allowed to warm to room temperature and stirred overnight. The reaction mixture was filtered and the slurry washed three times with methanol. The organic layer was extracted four times with CH₂Cl₂ (50 mL). The organic layers were washed with brine (80 mL), dried over magnesium sulphate and the solvent carefully removed (to avoid loss of the volatile product), yielding a colourless product (6.5 g, 94%) which was stored in the freezer. ¹H NMR (400 MHz, CDCl₃) δ (ppm): 6.60 (1H, d, ³J_{H-H} = 7.0 Hz, N=CH-CH₂, **b**), 3.15 (1H, m, CH, **c**), 1.42 (9H, s, CH₃, **a**), 1.03 (6H, d, ³J_{H-H} = 6.9 Hz, CH₃, **d**). ¹³C NMR (400 MHz, CDCl₃) δ (ppm): 139.3, 68.4, 27.6, 25.5, 18.5.

2.5.11.2 *Trimethyl-4-phenyl-3-azahexane-3-nitroxide*, **2.4**

N-tert- α -iso-propylnitrone (**2.3**) (10 g, 70 mmol) was dissolved in THF (75 mL) and cooled to 0 °C. A 2.8 M solution of phenylmagnesium bromide (10 mL, 140 mmol) in diethyl ether was added to the solution by cannula over 10 minutes. The solution was then stirred at room temperature overnight (*ca.* 12 hours.). A concentrated solution of ammonium chloride was added (1 M, 20 mL) along with 50 mL of water to dissolve the solids that had formed. The organic layer was extracted four times with diethyl ether (80 mL) and combined. This layer was dried over magnesium sulfate and concentrated. To the concentrated residue, 300 mL of methanol, NH₄OH (1 M, 30 mL) and Cu(OAc)₂ (636 mg, 3.5 mmol) were added. The reaction mixture

was stirred and bubbled with air for 2 hours. The resultant blue solution was concentrated, dissolved in chloroform (300 mL), and a concentrated solution of NaHSO₄ (1 M, 80 mL) was added. The layers were separated with chloroform and the organic layer was combined and washed with a solution of saturated sodium bicarbonate (90 mL). The organic layer was then dried over magnesium sulfate and concentrated. The crude product reaction was further purified by flash column chromatography (silica gel, 20:1 hexane/ethyl acetate) to obtain an orange oil. Fractions with R_f 0.2 (20:1 hexane: EtOAc) were collected giving a yield of 36%, 5 g. ¹H NMR (400 MHz, CDCl₃, in the presence of pentafluorophenyl hydrazine, due to the radical present) δ (ppm): 7.26-1.13 (5H, m, ArH), 3.40 (1H, d, ³J_{H-H} = 8.5 Hz, CH), 2.28 (1H, m, CH), 1.31 and 0.92 (9H, s, CH₃), 1.26 and 0.58 (6H, d, ³J_{H-H} = 3.8 Hz, CH₃). ESI-MS m/z 221 [M + 1], as reported in the literature.

2.5.11.3 Trimethyl-3-phenylethoxy-4-phenyl-3-azahexane, 2.5

Both trimethyl-4-phenyl-3-azahexane-3-nitroxide (**2.4**) (1 g, 4.5 mmol) and styrene (0.24 g, 2.3 mmol) were added to a 1:1 solution of toluene and ethanol (25 mL). *N,N'*-bis(3,5-di-*tert*-butylsalicylidene)-1,2-cyclohexanediaminomanganese(III) chloride (0.29 g, 0.45 mmol), di-*tert*-butyl-peroxide (0.5 g, 2.25 mmol) and NaBH₄ (0.26 g, 13.5 mmol) were added and the reaction left to stir overnight. The crude reaction slurry was then filtered through a silica plug several times until the reaction mixture was light brown. The solution was then reduced before being extracted with CH₂Cl₂ (25 mL) and water (35 mL). The aqueous layer was washed further with CH₂Cl₂ (3 x 15 mL). The organic layers were dried with magnesium sulfate and evaporated to dryness. The crude product was then purified by flash column chromatography with an eluent of 1:9 CH₂Cl₂/hexane to a final eluent composition of 1:3 CH₂Cl₂/hexane. The universal initiator was obtained as a colourless oil at

room temperature (0.81 g, 71%). ^1H NMR (400 MHz, both diastereoisomers, CDCl_3) δ (ppm): 7.0-7.5 (20H, both diastereoisomers ArH , **Ar**), 4.91 (2H, 2 X q, both diastereoisomers, **a**), 3.42 (1H, d, $^3J_{\text{H-H}} = 10.6$ Hz, major diastereoisomer, CH , **d**), 3.30 (1H, d, $^3J_{\text{H-H}} = 10.8$ Hz, minor diastereoisomer, **d'**), 2.33 (1H, m, major diastereoisomer, CH , **e**), 1.63 (3H, d, $^3J_{\text{H-H}} = 6.6$ Hz, major diastereoisomer, CH_3 , **b**), 1.54 (3H, d, $^3J_{\text{H-H}} = 6.6$ Hz, minor diastereoisomer, CH_3 , **b'**), 1.40 (1H, m, minor diastereoisomer, CH , **e'**), 1.31 (3H, d, $^3J_{\text{H-H}} = 6.4$ Hz, major diastereoisomer, CH_3 , **f**), 1.05 (9H, s, minor diastereoisomer, CH_3 , **c'**), 0.92 (3H, d, $^3J_{\text{H-H}} = 6.3$ Hz, minor diastereoisomer, CH_3 , **f'**), 0.77 (9H, s, major diastereoisomer, CH_3 , **c**), 0.54 (3H, d, $^3J_{\text{H-H}} = 6.6$ Hz, major diastereoisomer, CH_3 , **f**), 0.22 (3H, d, $^3J_{\text{H-H}} = 6.31$ Hz, minor diastereoisomer, CH_3 , **f'**). ^{13}C NMR (100 MHz, CDCl_3 , both diastereoisomers) δ (ppm): 145.9, 145.2, 142.5, 142.3, 131.0, 131.0, 128.1, 127.4, 127.2, 127.0, 126.6, 126.2, 126.2, 83.5, 82.8, 72.2, 72.2, 60.41, 32.0, 31.6, 28.4, 25.8, 24.7, 22.1, 22.0, 21.2, 21.1. MS (ES) m/z 326 [$\text{M} + 1$] as reported in the literature.³⁴

2.5.12 A general polymerisation *via* NMP of DMA

The following procedure is a typical polymerisation *via* NMP. To a dried ampoule, St (5 g, 0.048 mol), BzCl (0.4g, 0.0025 mol) and trimethyl-3-phenylethoxy-4-phenyl-3-azahexane (0.39 g, 0.001.2 mol) were added. The ampoule was degassed *via* four freeze pump thaw cycles until a stable vacuum was obtained. The ampoule was then back filled with nitrogen and heated to 125 °C for 3 hours (65% conversion). The polymerisation was quenched by rapid cooling in liquid nitrogen.

P2.7a: ^1H NMR (400 MHz, CDCl_3) δ (ppm): 6.2-7.2 ($5\text{H}_{\text{st}} + 4\text{H}_{\text{BzCl}}$, ArH), 4.6-4.2 (2H_{BzCl} , CH_2), 3.2 ($1\text{H}_{\text{end group}}$, d), 2.4-1.0 ($3\text{H}_{\text{backbone}} + 13\text{H}_{\text{end group}}$, $\text{CH}_2 + \text{CH}_3$), 0.6-0.2 ($3\text{H}_{\text{end group}}$, d, CH_3). ^1H NMR spectroscopy assignment gave a conversion of

65%. M_n (^1H NMR) = 6.5 kDa, $\text{DP}_{\text{St}} = 58.5$, $\text{DP}_{\text{BzCl}} = 0.5$. M_n (SEC, CHCl_3 , PSt calibration) = 5.2 kDa, $D_M = 1.10$. **P2.7b**: ^1H NMR (400 MHz, CDCl_3) δ (ppm): 6.2-7.2 ($5\text{H}_{\text{st}} + 4\text{H}_{\text{BzCl}}$, ArH, **Ar**), 4.6-4.2 (2H_{BzCl} , CH_2 , **c**), 3.2 ($1\text{H}_{\text{end group}}$, **d**, **e**), 2.4-1.0 ($3\text{H}_{\text{backbone}} + 13\text{H}_{\text{end group}}$, $\text{CH}_2 + \text{CH}_3$, **b + d + f**), 0.6-0.2 ($3\text{H}_{\text{end group}}$, **d**, CH_3 , **g**). ^1H NMR spectroscopy assignment gave a conversion of 65%. M_n (^1H NMR) = 7.3 kDa, $\text{DP}_{\text{St}} = 61$, $\text{DP}_{\text{BzCl}} = 4$. M_n (SEC, CHCl_3 , PSt calibration) = 5.5 kDa, $D_M = 1.10$. **P2.7c**: ^1H NMR (400 MHz, CDCl_3) δ (ppm): 6.2-7.2 ($5\text{H}_{\text{st}} + 4\text{H}_{\text{BzCl}}$, ArH), 4.6-4.2 (2H_{BzCl} , CH_2), 3.2 ($1\text{H}_{\text{end group}}$, **d**), 2.4-1.0 ($3\text{H}_{\text{backbone}} + 13\text{H}_{\text{end group}}$, $\text{CH}_2 + \text{CH}_3$), 0.6-0.2 ($3\text{H}_{\text{end group}}$, **d**, CH_3). ^1H NMR spectroscopy assignment gave a conversion of 65%. M_n (^1H NMR) = 7.0 kDa, $\text{DP}_{\text{St}} = 69$, $\text{DP}_{\text{BzCl}} = 6$. M_n (SEC, CHCl_3 , PSt calibration) = 7.0 kDa, $D_M = 1.08$.

2.5.13 Chain extension of P2.7b to afford P2.8b

The macro-initiator **P2.7b** (1.35 g, 0.1 mmol) was dissolved in DMA (4.71 g, 0.05 mol) and added to a dried ampoule with a magnetic stirrer bar. The ampoule was degassed *via* four freeze pump thaw cycles until a stable vacuum was obtained. The ampoule was then back filled with nitrogen and heated to 125 °C for 24 hours (70% conversion). The polymerisation was stopped by rapid cooling in liquid nitrogen. **P2.8a**: ^1H NMR (400 MHz, CDCl_3) δ (ppm): 6.2-7.2 ($5\text{H}_{\text{st}} + 4\text{H}_{\text{BzCl}}$, ArH), 4.6-4.2 (2H_{BzCl} , CH_2), 3.2 - 1.0 ($3\text{H}_{\text{backbone}} + 6\text{H}_{\text{DMA}} + 14\text{H}_{\text{end group}}$, $\text{CH} + \text{CH}_2 + \text{CH}_3$), 0.6-0.2 ($3\text{H}_{\text{end group}}$, **d**, CH_3). ^1H NMR spectroscopy gave a conversion of 70%. M_n (^1H NMR) = 31.7 kDa, $\text{DP}_{\text{St}} = 58.5$, $\text{DP}_{\text{BzCl}} = 0.5$, $\text{DP}_{\text{DMA}} = 254$. M_n (SEC, CHCl_3 , PSt calibration) = 33.0 kDa, $D_M = 1.20$. **P2.8b**: ^1H NMR (400 MHz, CDCl_3) δ (ppm): 6.2-7.2 ($5\text{H}_{\text{st}} + 4\text{H}_{\text{BzCl}}$, ArH, **Ar**), 4.6-4.2 (2H_{BzCl} , CH_2 , **c**), 3.2 - 1.0 ($3\text{H}_{\text{backbone}} + 6\text{H}_{\text{DMA}} + 14\text{H}_{\text{end group}}$, $\text{CH} + \text{CH}_2 + \text{CH}_3$, **h + b + d + f**), 0.6-0.2 ($3\text{H}_{\text{end group}}$, **d**, CH_3 ,

g). ^1H NMR spectroscopy assignment gave a conversion of 70%. M_n (^1H NMR) = 25.3 kDa, $\text{DP}_{\text{St}} = 61$, $\text{DP}_{\text{BzCl}} = 4$, $\text{DP}_{\text{DMA}} = 182$. M_n (SEC, CHCl_3 , PSt calibration) = 20.4 kDa, $\bar{D}_M = 1.25$. **P2.8c**: ^1H NMR (400 MHz, CDCl_3) δ (ppm): 6.2-7.2 ($5\text{H}_{\text{st}} + 4\text{H}_{\text{BzCl}}$, ArH), 4.6-4.2 (2H_{BzCl} , CH_2), 3.2 - 1.0 ($3\text{H}_{\text{backbone}} + 6\text{H}_{\text{DMA}} + 14\text{H}_{\text{end group}}$, $\text{CH} + \text{CH}_2 + \text{CH}_3$), 0.6-0.2 ($3\text{H}_{\text{end group}}$, d , CH_3). ^1H NMR spectroscopy gave a conversion of 70%. M_n (^1H NMR) = 32.4 kDa, $\text{DP}_{\text{St}} = 69$, $\text{DP}_{\text{BzCl}} = 6$, $\text{DP}_{\text{DMA}} = 230$. M_n (SEC, CHCl_3 , PSt calibration) = 30.0 kDa, $\bar{D}_M = 1.39$.

2.5.14 TBD substitution onto P2.8b to produce P2.9b

TBD (0.33 g, 2.4×10^{-3} mol), KI (0.008 g, 4.6×10^{-4} mol) and dry DMF (5 mL) were added to a dried RBF with a magnetic stirrer bar under nitrogen. The polymer **P2.28b** (3 g, 1.2×10^{-4} mol) was dissolved in dry DMF (20 mL) before being added to the RBF under nitrogen. The RBF was placed in a pre-heated oil bath at 70 °C for 60 hours. The polymer was dialysed extensively and freeze dried. Yield: 66.5%. **P2.8a**: ^1H NMR (400 MHz, CDCl_3) δ (ppm): 6.2-7.2 ($5\text{H}_{\text{st}} + 4\text{H}_{\text{BzCl}}$, ArH), 4.8-4.4 (2H_{BzTBD} , CH_2), 3.2 - 1.0 ($3\text{H}_{\text{backbone}} + 6\text{H}_{\text{DMA}} + 12\text{H}_{\text{TBD}} + 14\text{H}_{\text{end group}}$, $\text{CH} + \text{CH}_2 + \text{CH}_3$), 0.6-0.2 ($3\text{H}_{\text{end group}}$, d , CH_3). ^1H NMR spectroscopy M_n (^1H NMR) = 31.7 kDa, $\text{DP}_{\text{St}} = 58.5$, $\text{DP}_{\text{BzTBD}} = 0.5$, $\text{DP}_{\text{DMA}} = 254$. M_n (SEC, CHCl_3 , PSt calibration) = 28.6 kDa, $\bar{D}_M = 1.34$. **P2.8b**: ^1H NMR (400 MHz, CDCl_3) δ (ppm): 6.2-7.2 ($5\text{H}_{\text{st}} + 4\text{H}_{\text{BzCl}}$, ArH , Ar), 4.6-4.2 (2H_{BzCl} , CH_2 , c), 3.2 - 1.0 ($3\text{H}_{\text{backbone}} + 6\text{H}_{\text{DMA}} + 12\text{H}_{\text{TBD}} + 14\text{H}_{\text{end group}}$, $\text{CH} + \text{CH}_2 + \text{CH}_3$, $\text{h} + \text{b} + \text{i} + \text{j} + \text{d} + \text{f}$), 0.6-0.2 ($3\text{H}_{\text{end group}}$, d , CH_3 , g). ^1H NMR spectroscopy assignment gave a conversion of 70%. M_n (^1H NMR) = 25.7 kDa, $\text{DP}_{\text{St}} = 61$, $\text{DP}_{\text{BzCl}} = 4$, $\text{DP}_{\text{DMA}} = 182$. M_n (SEC, CHCl_3 , PSt calibration) = 11.3 kDa, $\bar{D}_M = 1.36$. **P2.8c**: ^1H NMR (400 MHz, CDCl_3) δ (ppm): 6.2-7.2 ($5\text{H}_{\text{st}} + 4\text{H}_{\text{BzCl}}$, ArH), 4.6-4.2 (2H_{BzCl} , CH_2), 3.2 - 1.0 ($3\text{H}_{\text{backbone}} + 6\text{H}_{\text{DMA}} +$

$^{14}\text{H}_{\text{end group}}$, $\text{CH} + \text{CH}_2 + \text{CH}_3$), 0.6-0.2 ($^3\text{H}_{\text{end group}}$, d, CH_3). ^1H NMR spectroscopy assignment gave a conversion of 70%. M_n (^1H NMR) = 32.4 kDa, $\text{DP}_{\text{St}} = 69$, $\text{DP}_{\text{BzCl}} = 6$, $\text{DP}_{\text{DMA}} = 230$. M_n (SEC, CHCl_3 , PSt calibration) = 32.4 kDa, $D_M = 1.27$.

2.5.15 Micellar assembly

The amphiphilic block copolymer (50 mg) was dissolved in DMF (5 mL) at a concentration of 10 mg mL^{-1} . The solution was stirred rapidly and water (18 M Ω cm, 20 mL) was slowly added at a rate of 0.6 mL h^{-1} using a peristaltic pump. After the addition of water, the solution was dialysed extensively (three water changes per day 9 am, 12 pm and 6 pm over three days) against 18 M Ω cm water producing a solution of micelles at a concentration of 2 mg mL^{-1} .

2.5.16 TEM Sample preparation

2.5.16.1 Graphene oxide

Solutions of graphene oxide were synthesised as reported previously.⁴¹ Aqueous solutions of graphene oxide (0.02 mg mL^{-1}) were stirred for at least 48 hours prior to use. Lacey carbon grids (400 Mesh, Cu) (Agar Scientific) were cleaned using air plasma from a glow-discharge system (2 min, 20 mA). The TEM grids were placed on a filter paper and one drop (*ca.* 0.08 mL) of the sonicated GO solution was deposited onto each grid from a height of *ca.* 1 cm, allowing the filter paper to absorb the excess solution, and the grids were left to air-dry in a desiccator cabinet for *ca.* 60 min. 5 μL of the nanoparticle dispersion (0.1 mg mL^{-1}) was pipetted onto a GO grid. The grid was frozen in liquid nitrogen in a small vial and freeze dried

overnight. Average sizes of the nanoparticles were determined from counting the size of a minimum of two hundred particles for each sample.

2.5.16.2 *Phosphotungstic acid stain*

From the sample at 0.1 mg ml^{-1} , $5 \text{ }\mu\text{L}$ of the nanoparticle dispersion was deposited on a TEM grid (Formvar carbon grid), blotted immediately and left to air dry. A 2% solution of phosphotungstic acid (pH adjusted to 7) was deposited on the grid ($5 \text{ }\mu\text{L}$). After 20-30 seconds the grid was blotted and left to air dry.

2.6 References

1. W. Ye, J. Xu, C.-T. Tan and C.-H. Tan, *Tetrahedron Lett.*, 2005, **46**, 6875-6878.
2. C. Ghobril, C. Sabot, C. Mioskowski and R. Baati, *Eur. J. Org. Chem.*, 2008, **2008**, 4104-4108.
3. M. K. Kiesewetter, M. D. Scholten, N. Kirn, R. L. Weber, J. L. Hedrick and R. M. Waymouth, *J. Org. Chem.*, 2009, **74**, 9490-9496.
4. L. Simón and J. M. Goodman, *J. Org. Chem.*, 2007, **72**, 9656-9662.
5. P. Cotanda, A. Lu, J. P. Patterson, N. Petzetakis and R. K. O'Reilly, *Macromolecules*, 2012, **45**, 2377-2384.
6. S. Bonollo, D. Lanari, T. Angelini, F. Pizzo, A. Marrocchi and L. Vaccaro, *J. Catal.*, 2012, **285**, 216-222.
7. Y. V. S. Rao, D. E. De Vos and P. A. Jacobs, *Angew. Chem. Int. Ed.*, 1997, **36**, 2661-2663.
8. U. Schuchardt, R. M. Vargas and G. Gelbard, *J. Mol. Catal. A: Chem.*, 1996, **109**, 37-44.
9. M. K. Muthyala, B. S. Chhikara, K. Parang and A. Kumar, *Can. J. Chem.*, 2012, **90**, 290-297.
10. P. Kalita and R. Kumar, *Appl. Catal., A*, 2011, **397**, 250-258.
11. I. Kaljurand, A. Kütt, L. Sooväli, T. Rodima, V. Mäemets, I. Leito and I. A. Koppel, *J. Org. Chem.*, 2005, **70**, 1019-1028.

12. U. Schuchardt, R. M. Vargas and G. Gelbard, *J. Mol. Catal. A: Chem.*, 1995, **99**, 65-70.
13. G. Gelbard and F. Vielfaure-Joly, *React. Funct. Polym.*, 2001, **48**, 65-74.
14. Z. Dong, W. Yongguo, Y. Yin and J. Liu, *Curr. Opin. Colloid Interface Sci.*, 2011, **16**, 451-458.
15. Z. Dong, Q. Luo and J. Liu, *Chem. Soc. Rev.*, 2012, **41**, 7890-7908.
16. A. Lu and R. K. O'Reilly, *Curr. Opin. Biotechnol.*, 2013, **24**, 639-645.
17. B. Helms, C. O. Liang, C. J. Hawker and J. M. J. Fréchet, *Macromolecules*, 2005, **38**, 5411-5415.
18. R. Nagarajan, in *Nanoparticles: Synthesis, Stabilization, Passivation, and Functionalization*, American Chemical Society, First edn., 2008, vol. 996, ch. 24.
19. G. M. T. Genski, X. Wei, N. Lewis, and R. J. K. Taylor, *Arkivoc*, 2000, **2000**, 266-273.
20. X. P. Yang, P. S. Xu, S. J. Ding, M. Radosz and Y. Q. Shen, *Abstr. Pap. Am. Chem. Soc.*, 2004, **227**, U380-U380.
21. H. Willcock and R. K. O'Reilly, *Polym. Chem.*, 2010, **1**, 149-157.
22. G. Moad, *Aust. J. Chem.*, 2006, **59**, 661-662.
23. D. J. Keddie, G. Moad, E. Rizzardo and S. H. Thang, *Macromolecules*, 2012, **45**, 5321-5342.
24. G. Moad and E. Rizzardo, *Macromolecules*, 1995, **28**, 8722-8728.
25. J. Skey and R. K. O'Reilly, *Chem. Commun.*, 2008, 4183-4185.

26. M. Negre, M. Bartholin and A. Guyot, *Angew Makromol Chem*, 1979, **80**, 19-30.
27. S. Kondo, T. Ohtsuka, K. Ogura and K. Tsuda, *J. Macromol. Sci., Part A: Pure Appl. Chem.*, 1979, **13**, 767-775.
28. P. Boehm, M. Mondeshki and H. Frey, *Macromol. Rapid Commun.*, 2012, **33**, 1861-1867.
29. M. Deletre and G. Levesque, *Macromolecules*, 1990, **23**, 4733-4741.
30. A. B. Lowe and C. L. McCormick, *RAFT Polymerization in Homogeneous Aqueous Media: Initiation Systems, RAFT Agent Stability, Monomers and Polymer Structures*, Wiley-VCH Verlag GmbH & Co. KGaA, 2008.
31. M. Chen, G. Moad and E. Rizzardo, *J. Polym. Sci., Part A: Polym. Chem.*, 2009, **47**, 6704-6714.
32. J. Nicolas, Y. Guillaneuf, C. Lefay, D. Bertin, D. Gigmes and B. Charleux, *Prog. Polym. Sci.*, 2013, **38**, 63-235.
33. G. Moad, E. Rizzardo and S. H. Thang, *Aust. J. Chem.*, 2006, **59**, 669-692.
34. D. Benoit, V. Chaplinski, R. Braslau and C. J. Hawker, *J. Am. Chem. Soc.*, 1999, **121**, 3904-3920.
35. J. Dao, D. Benoit and C. J. Hawker, *J. Polym. Sci., Part A: Polym. Chem.*, 1998, **36**, 2161-2167.
36. H. Fischer, *Macromolecules*, 1997, **30**, 5666-5672.
37. D. Bertin, D. Gigmes, S. R. A. Marque and P. Tordo, *Chem. Soc. Rev.*, 2011, **40**, 2189-2198.

38. N. S. Cameron, M. K. Corbierre and A. Eisenberg, *Can. J. Chem.*, 1999, **77**, 1311-1326.
39. J. P. Patterson, A. M. Sanchez, N. Petzetakis, T. P. Smart, T. H. Epps III, I. Portman, N. R. Wilson and R. K. O'Reilly, *Soft Matter*, 2012, **8**, 3322-3328.
40. J. P. Patterson, M. P. Robin, C. Chassenieux, O. Colombani and R. K. O'Reilly, *Chem. Soc. Rev.*, 2014, **43**, 2412-2425.
41. N. R. Wilson, P. A. Pandey, R. Beanland, R. J. Young, I. A. Kinloch, L. Gong, Z. Liu, K. Suenaga, J. P. Rourke, S. J. York and J. Sloan, *ACS Nano*, 2009, **3**, 2547-2556.

3 Catalysis in aqueous environments using TBD-loaded nanoreactors

3.1 Abstract

The Michael addition utilising small molecules TBD and MTBD have shown no conversions in aqueous conditions. Subsequently previously synthesised micellar nanoreactors containing TBD-core functionality was used for Michael additions. Catalysis with these nanoreactors successfully yielded Michael addition products with hydrophobic substrates in water, demonstrating the efficiency of these micellar nanoreactors for environmentally friendly catalysis. Increased catalytic loading within the micellar cores resulted in higher conversions. Henceforth, the assembly of two blended polymers of differing catalyst loadings was carried out, increasing the rate of catalysis as a consequence of efficient diffusion of the substrates into the micellar core.

3.2 Introduction

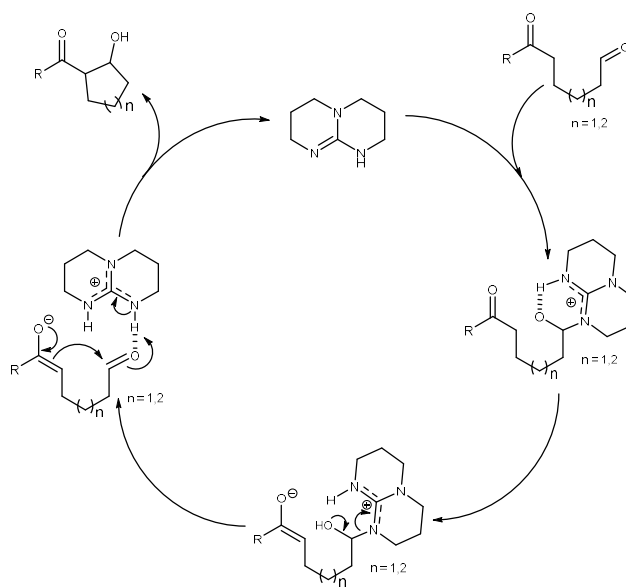
3.2.1 TBD Catalysis

Previously in Chapter 1 we have discussed the mechanism of TBD in ring-opening polymerisations and acylation reactions; however, this strong base ($pK_a = 26.1$) can catalyse numerous reactions such as aldol reactions,^{1, 2} ester hydrolysis,^{3, 4} Wittig reactions,⁵ Horner-Wadsworth-Emmons reactions,⁵ amidations,^{6, 7} Henry reactions (nitroaldol),⁸ and Michael additions.⁹⁻¹¹

3.2.1.1 Aldol Reaction

The TBD-catalysed intramolecular aldol reaction of a keto-aldehyde has been demonstrated by Baati *et al.* (Scheme 3.1).¹ TBD was found to catalyse the formation of the cyclic aldol product in 30 minutes with 8% catalytic loading giving a 94% yield. TBD was subsequently compared to other guanidine catalysts a bicyclic

methylated-TBD and the acyclic tetramethylguanidine (TMG) which have similar pK_a values namely 25.5 and 23.7 respectively (in acetonitrile).¹¹ Despite these similarities the yield of the cyclic ketol was significantly lower than TBD (MTBD = 39% and TMG = 17%) after 72 hours.¹ It was proposed that the TBD catalyst acts as a bifunctional catalyst: initially TBD acts as a nucleophile generating a tetrahedral intermediate which is stabilised by the catalyst. This then allows enolisation of the intermediate formed, releasing the guanidinium cation. The aldehyde is activated by the cation enabling intramolecular addition of the ketone enolate, regenerating the catalyst and forming the cyclic aldol addition product.^{2, 12} In contrast both MTBD and TMG cannot facilitate this proton shuttling mechanism hence a higher reaction barrier for the enolisation was observed. The energy barrier was calculated utilising density function theory where the enolisation reaction barriers were determined for guanidine catalysts MTBD (21.6 kcal mol⁻¹), TMG (25.5 kcal mol⁻¹) and TBD (15.4 kcal mol⁻¹).¹



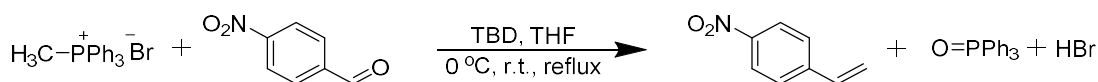
Scheme 3.1: The TBD-catalysed aldol reaction of a keto-aldehyde resulting in the formation of a cyclic aldol product. Reproduced from Baati *et al.*²

3.2.2 Transesterification

Improvements to transesterification reactions are of particular significance, due to the raised interest in renewable resources such as the formation of biodiesel. Biodiesel is obtained by the transesterification of vegetable oils to form a mixture of fatty acid methyl esters (biodiesel). Traditionally, expensive enzymes such as lipases or strong acids and bases are used.¹³ Bases such as sodium hydroxide (NaOH) require the absence of water, and saponification side reactions are found to occur. This is undesirable for industrial processes as the emulsion formed leads to difficult separation of the glycerol and the fatty acids formed.³ The Gelbard group have explored the use of guanidinium catalysts for the transesterification of vegetable oils in comparison to NaOH. The catalytic activity of TBD was compared to NaOH where a 93.8% yield of fatty acid was obtained with TBD after 3 hours with a loading of 1 mol%.^{4, 14} Although lower yields were obtained with TBD when compared to NaOH (98.7% yield, 1 mol% loading, 3 hours), one of the main advantages of using these non-ionic bases is the absence of saponification products, thus rendering TBD more economical for industrial processes.¹⁵

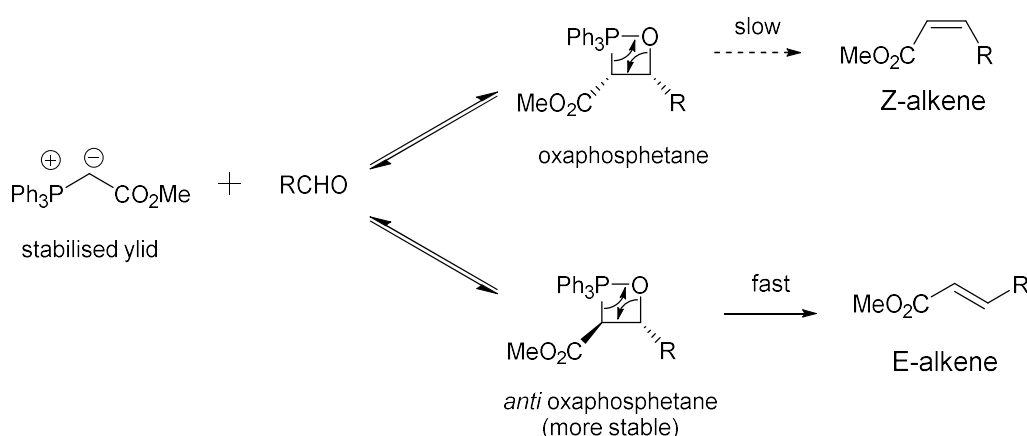
3.2.2.1 Wittig and Horner-Wadsworth-Emmons reactions

The Wittig reaction is the formation of an alkene bond from a carbonyl bond, *via* a reaction between the carbonyl and a phosphonium ylide. Commonly, organolithium reagents are used for ylide formation therefore the reaction requires inert conditions.



Scheme 3.2: Example of the Wittig reaction between methyltriphenylphosphonium bromide and 4-nitrobenzaldehyde in the presence of TBD, to form 4-nitrostyrene.

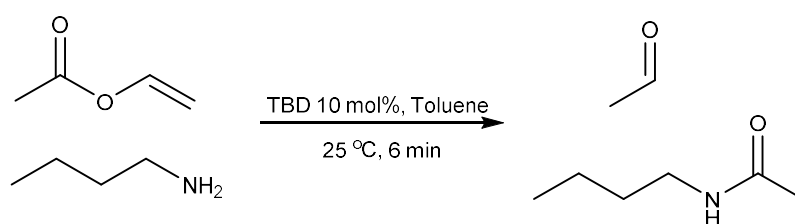
Simoni *et al.* have found that using TBD as a strong base promoted ylide formation enabling the Wittig reaction to proceed *via* the oxaphosphetane intermediate in both inert and non-inert conditions (Scheme 3.2) providing a more industrially viable route for the Wittig reaction.⁵ The Horner-Wadsworth-Emmons Wittig modification is the formation of a C=C bond from a carbonyl compound with an α -methylated phosphonate, to produce E-alkenes.⁵ The formation E-alkenes are favoured due to thermodynamic control of the reaction as a consequence of the reversibility of the oxaphosphetane intermediate (Scheme 3.3) forming the more stable *anti* oxaphosphetane intermediate.¹⁶ In the presence of the guanidine-based catalyst this reaction required non-inert conditions with relatively simple purification steps.



Scheme 3.3: A schematic representation of the Horner-Wadsworth-Emmons Wittig reaction. Reproduced from Clayden *et al.*¹⁶

3.2.3 Amidations

Waymouth and co-workers have demonstrated the use of TBD as a catalyst in the amidation of vinyl acetate with *n*-butylamine (Scheme 3.4).⁷ Although these reactions can proceed in the absence of the catalyst the introduction of TBD rapidly accelerates the rate of the reaction from 24 hours to 6 minutes giving high conversions of 99%.⁷

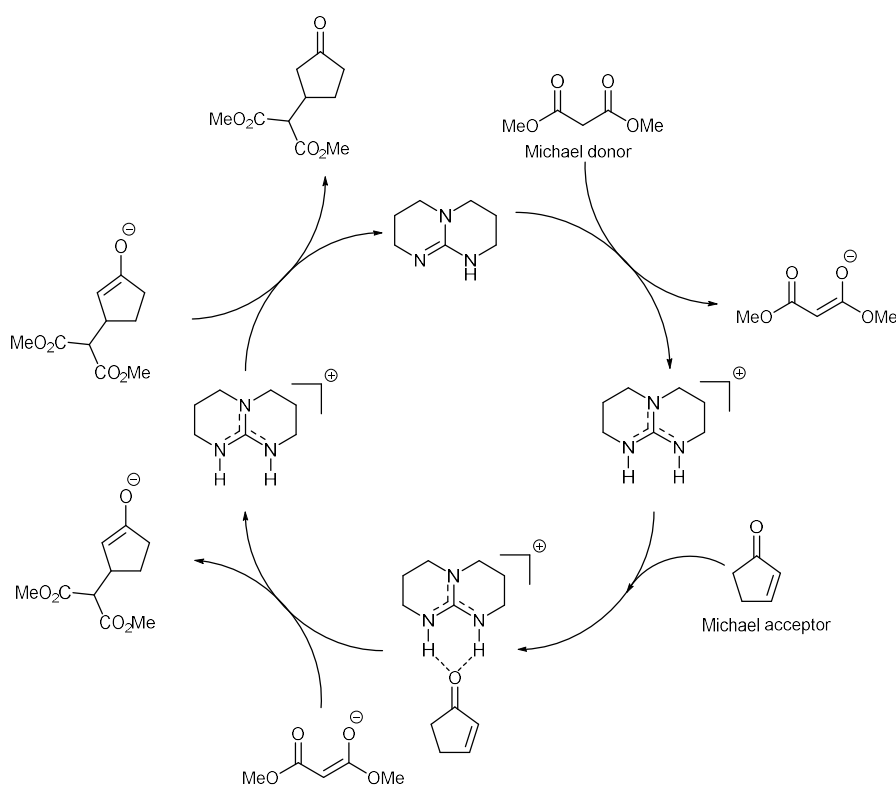


Scheme 3.4: Amidation of vinyl acetate with *n*-butylamine.

Here the catalyst forms an acyl-TBD intermediate, a “twisted” species (as described in Chapter 1), which is highly susceptible to nucleophilic attack from the amine thus promoting amide formation.⁷ Mioskowski also demonstrated the aminolysis of esters with TBD under solvent free conditions.⁶ In comparison to other bases (such as MTBD and TMG) only the TBD catalyst obtained a good yield (75%), for the aminolysis of benzylamine with methyl phenylacetate, whereas the other guanidine based catalysts showed no conversion. Again this is attributed to the ability of TBD to act as a bifunctional catalyst.²

3.2.4 Michael addition

Michael additions using TBD have been explored by many groups,^{10, 17-20} and involve the conjugate addition of a α,β -unsaturated carbonyl compound to a nucleophile. The reaction between a Michael acceptor (carbonyl species) and the Michael donor (nucleophile) requires the addition of a strong base to form a carbanion species.¹² Ye *et al.* have utilised the catalyst TBD for the Michael addition for numerous substrates, for example 2-cyclopenten-1-one and dimethyl malonate (Scheme 3.5).¹⁰



Scheme 3.5: Schematic representation of the Michael addition of dimethyl malonate and 2-cyclopenten-1-one, catalysed by TBD in toluene.

TBD deprotonates dimethyl malonate to form an enolate species, in a 95% yield of product after 5 minutes with 10 mol% TBD, yet under the same reaction conditions

MTBD required longer reaction times (6 hours) to achieve a 91% yield.¹⁰ This highlights the importance of the formation of the double hydrogen bonding species to activate the Michael acceptor (Scheme 3.5), MTBD is hindered by a methyl group hence lower yields were observed.

Immobilisation of TBD has attracted much interest as it allows for simpler work-up conditions and improved recyclability of the catalyst.^{17, 20-22} Srivastava *et al.* have explored mesoporous silica SBA-15 as a support for the catalyst, TBD, demonstrating high recyclability in aldol reactions, maintaining yields of 68% in solvent free conditions over three cycles.²² More recently the Vaccaro group has studied the immobilisation of TBD onto Rasta resin (a commercially available polystyrene, PSt, support) for use in a continuous flow reactor for Michael additions.²⁰ It was found that the supported catalyst could be used for five consecutive runs, however when compared to the unsupported MTBD much longer reaction times were required (1 hour vs 15 hours) to obtain similar yields greater than 90%. The same group has investigated the use of these PSt-TBD supports for the synthesis of WarfarinTM in solvent free conditions (solFC) as a greener alternative to the organic solvents currently used in the synthesis.⁹ Good conversions were obtained (63-82%) at 70 °C after 72 hours with the immobilised catalyst for the Michael addition reactions. The recyclability of the catalyst was also tested, with the catalyst recycled three times giving 86-96% conversion.⁹

Although these catalyst-supported systems yield good conversions, relatively long reaction times are needed for high conversions. We aim to use the previously synthesised nanoreactors (Chapter 2) for the catalysis of Michael additions, we

suggest that tethering the catalyst to the hydrophobic domain of a micelle will increase the activity of the catalyst through the utilisation of the concentrator effect (Figure 3.1).²³

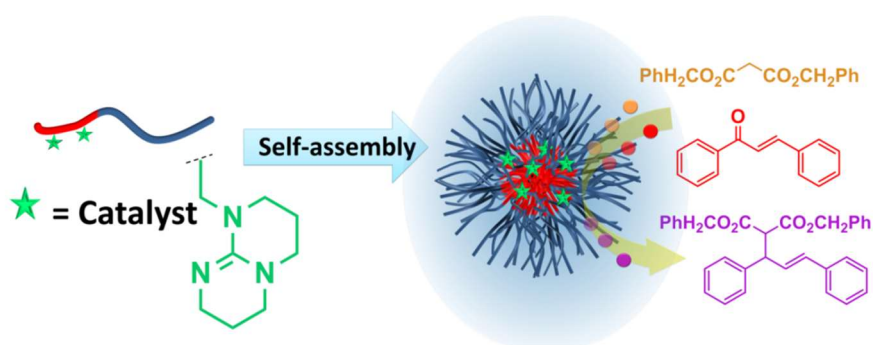


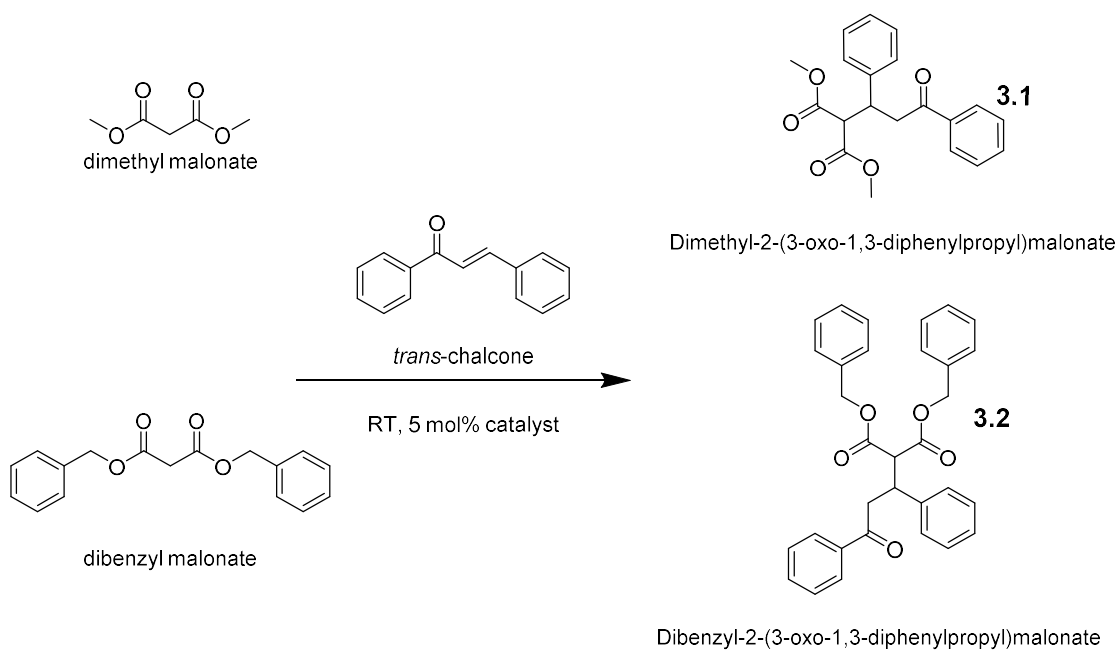
Figure 3.1: An illustrative representation of catalytic TBD tethered to the core of a micelle for the Michael addition within the core.

One of the main disadvantages of the current immobilisation techniques (through which immobilisation proceeds *via* the nitrogen) is that the catalytic site is hindered, resulting in a similar structure to MTBD. Therefore, the activity of the micellar nanoreactors will be compared to both TBD and MTBD.

3.3 Results and discussion

3.3.1 Michael addition on solution

Initially the Michael addition was explored with the small molecule catalysts TBD and MTBD. A well-established Michael addition utilising *trans*-chalcone (Michael donor) and both dimethyl malonate and dibenzyl malonate (Michael acceptors) were used as the model reaction. Catalysis was carried out at 5 mol% catalyst loading in comparison to the malonate substrate, with four equivalents of the Michael donor (to solubilise the *trans*-chalcone in the bulk reaction) and one equivalent *trans*-chalcone. The reaction was monitored *via* high pressure liquid chromatography (HPLC), with an ultraviolet (UV) detector at 254 nm and 280 nm. The reaction was monitored for 24 hours prior to washing with diethyl ether and extraction with water to yield the product. The Scheme below depicts the model reactions.



Scheme 3.6: Michael addition reactions for the formation of 3.1 and 3.2 in bulk.

The products **3.1** and **3.2** were characterised by ^1H NMR spectroscopy (Figure 3.3 and Figure 3.4 respectively). A mixture of diastereotopic methyl groups were observed (using 5 mol% TBD), these methyl groups are none equivalent hence can be seen through a comparison of peaks **a**. This is due to the availability of the p-orbitals for front and back-side attack by the nucleophile generating the *R* and *S* enantiomers (Figure 3.2).

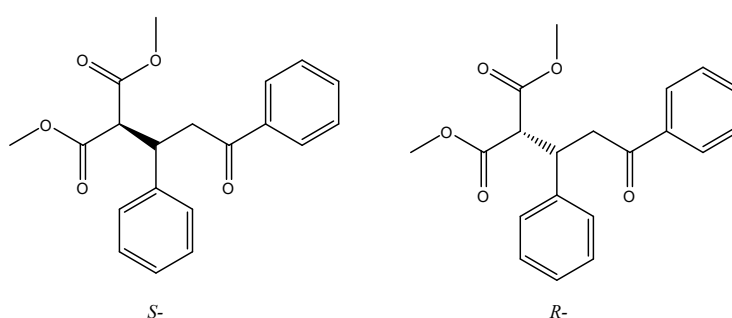


Figure 3.2: Isomers formed by the Michael addition with MTBD and TBD.

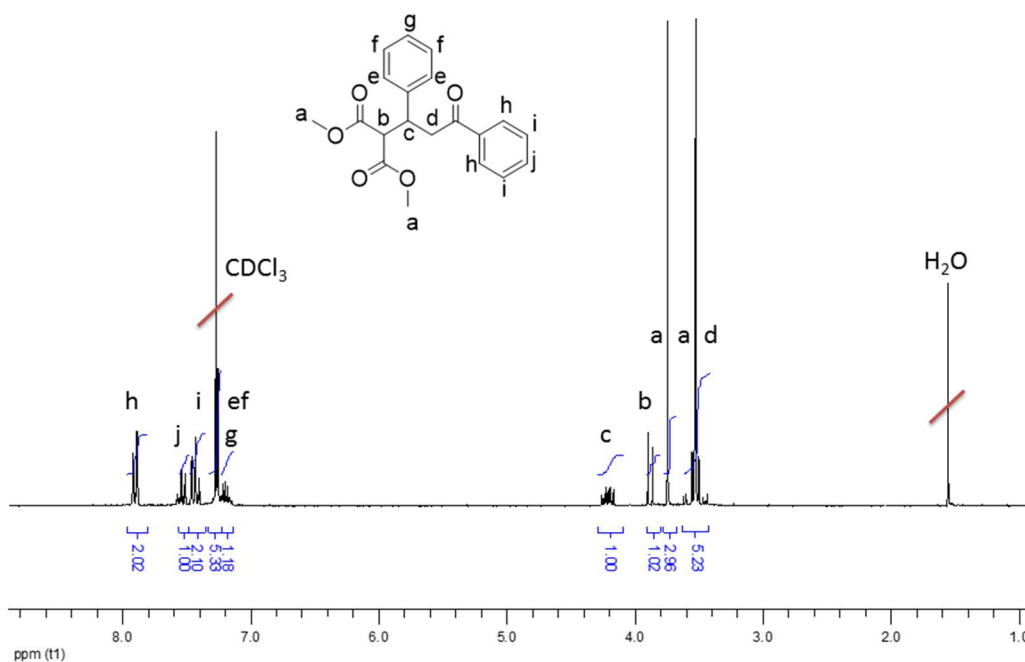


Figure 3.3: ^1H NMR spectrum of purified **3.1**, in CDCl_3 at 400 MHz.

For **3.1** the protons **d** are split (3.5 ppm), this is because **d** is diastereotopic, where **d** is split by both **c** and itself, which is in agreement with the literature values.²⁴ Analysis of the ¹H NMR spectrum of **3.2** (Figure 3.4), showed different environments for protons **j**; here the axial protons were aligning with the aromatic rings leading to a downfield shift (Figure 3.5). This gave rise to a multiplet, due to the splitting for the axial **j** proton, by interactions of equatorial **j** with the aromatic protons in the *ortho* positions (**k**).

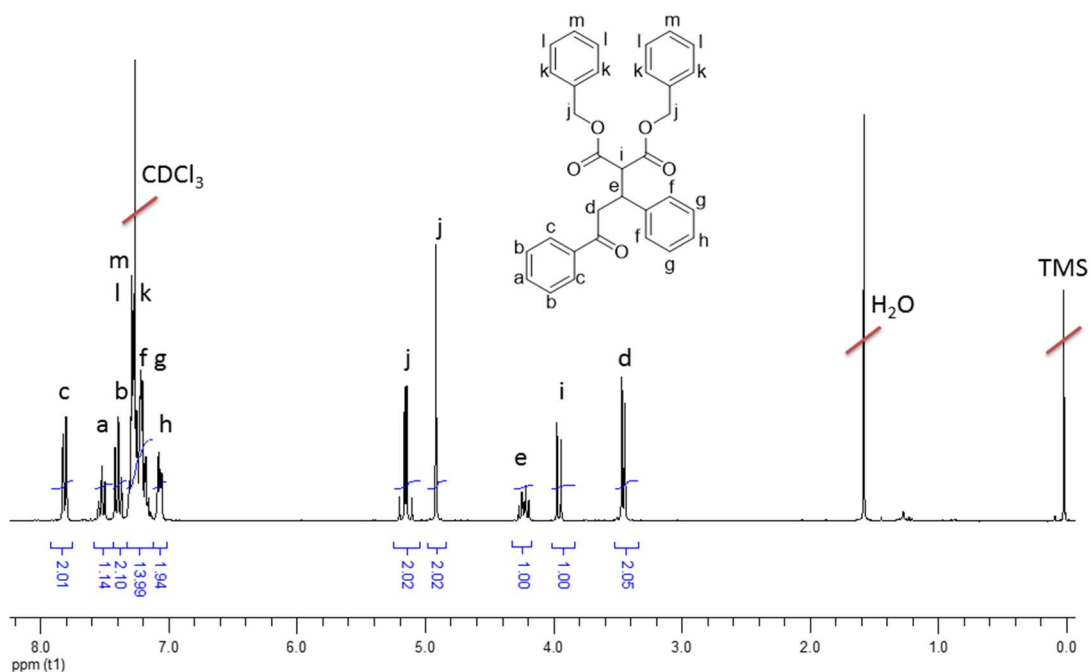


Figure 3.4: ¹H NMR spectrum of **3.2**, in CDCl₃ at 400 MHz.

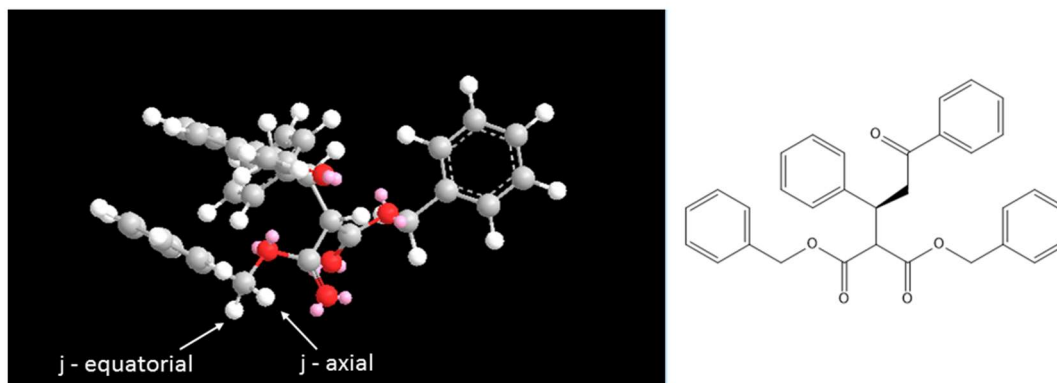


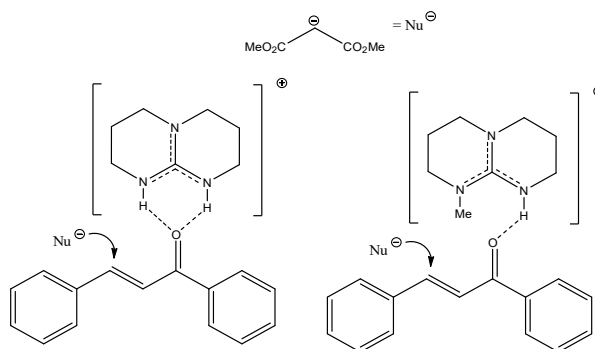
Figure 3.5: A computational model demonstrating the positions of protons *j* in **3.2**, using ChemBio3D version 14.

Both the TBD and MTBD-catalysed Michael addition reactions were carried out in numerous solvents at 5 mol%, catalytic loadings (Table 3.1). Similar conversions were observed for both **3.1** and **3.2** in bulk conditions with MTBD and TBD. In acetonitrile similar conversions of **3.1** and **3.2** were also obtained for both MTBD and TBD; this is because MTBD and TBD have comparable pK_a values in acetonitrile (25.5 and 26.0 respectively). During the first step of the Michael addition the catalyst acts as a general base, deprotonating the malonate species, hence similarities in pK_a values account for the observed conversions.¹¹

Table 3.1: The percentage product formation (3.1 and 3.2) with catalysts TBD and MTBD at 5 mol% catalyst loading in different solvents, monitored via HPLC (95:5 water: methanol gradient to 5:95 water: methanol for 16 min, flow rate: 2 ml min⁻¹) using a UV detector at 280 nm at 7 hours and 24 hours.

Solvent	pK _a of Catalyst ^{11, 25}	Product	Catalyst	Percentage conversion	
				7 hours	24 hours
Bulk	-	3.1	TBD	100	100
Acetonitrile	26.0	3.1	TBD	100	100
Water	15.2	3.1	TBD	0	0
Toluene	-	3.1	TBD	99	100
Bulk	-	3.1	MTBD	99	99
Acetonitrile	25.5	3.1	MTBD	93	95
Water	15.0	3.1	MTBD	0	0
Toluene	-	3.1	MTBD	0	0
Bulk	-	3.2	TBD	100	100
Acetonitrile	26.0	3.2	TBD	100	100
Water	15.2	3.2	TBD	0	0
THF	21.0	3.2	TBD	96	98
Bulk	-	3.2	MTBD	100	100
Acetonitrile	25.5	3.2	MTBD	100	100
Water	15.0	3.2	MTBD	0	0
THF	17.9	3.2	MTBD	46	69

For both catalysts the Michael addition did not take place in water. This is a consequence of the insolubility of the *trans*-chalcone species leading to an observable phase separation during the reaction. In contrast to MTBD in toluene TBD was found to effectively catalyse the reaction to high conversion. We hypothesise that the reaction is facilitated by the presence of the free N-H on the TBD, which can hydrogen bond, activating the Michael acceptor (Scheme 3.7) enabling the Michael addition to take place. Whilst TBD can form a double hydrogen bond complex MTBD is unable to do so resulting in no conversion when a non-polar solvent is used.



Scheme 3.7: The activated species formed for the Michael addition with TBD (left) and MTBD (right).

A higher conversion was observed for TBD in THF, attributed to the significantly lower pK_a of MTBD in THF (TBD = 21, MTBD = 17.9); hence the initial activation of the nucleophilic species is slower due to the lower basicity of the catalyst.¹¹

3.3.2 Micellar Michael additions

Previously we have discussed the influence of solvent on Michael additions with guanidine catalysts, where no conversion was observed in water for either catalyst. In the previous Chapter, amphiphilic block copolymers were synthesised immobilising TBD within the hydrophobic domain. These amphiphilic block copolymers were subsequently assembled in forming micelles **M2.9a** (Figure 3.6).

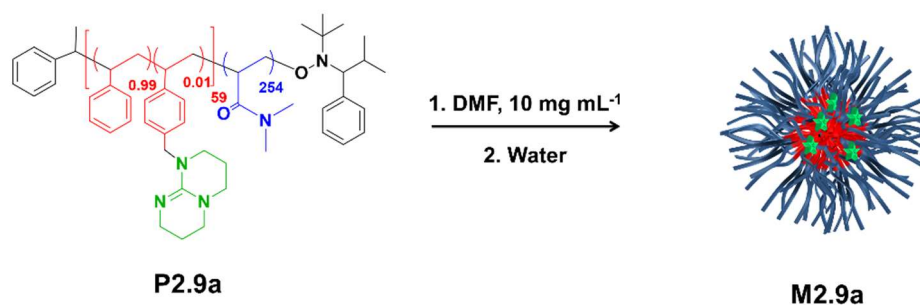


Figure 3.6: The formation of micelles from P2.9a to M2.9a.

3.3.2.1 Michael addition with dimethyl malonate and **M2.9a**

Trans-chalcone (four equivalents) was mixed with dimethyl malonate (one equivalent) as well as with an internal standard 1,2,4 trimethoxybenzene (TMB) (one equivalent). This solution was added to the assembled micelles **M2.9a** to reach a 5 mol% catalyst loading (compared to the *trans*-chalcone concentration). The reaction was monitored *via* HPLC analysis; the samples were prepared through disassembling the micelles in DMF, forming unimers (Figure 3.7), and the substrates and product were subsequently removed by extraction with diethyl ether and water, prior to HPLC analysis.

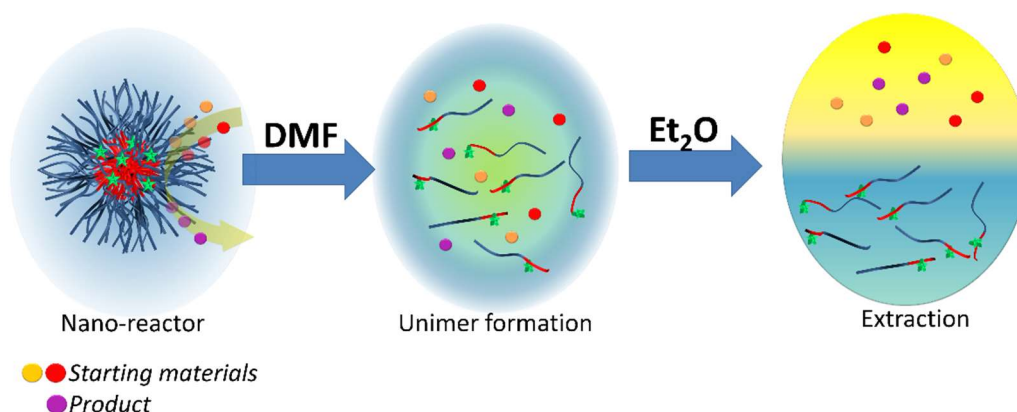


Figure 3.7: Schematic of the micellar catalysis work-up.

After 4 days no change was observed in the HPLC chromatograms while ¹H NMR spectroscopy revealed the presence of peaks solely corresponding to *trans*-chalcone (Figure 3.8). The absence of the product peak (expected at 4.2 ppm, Figure 3.8, green box) further confirmed the reaction had not taken place.

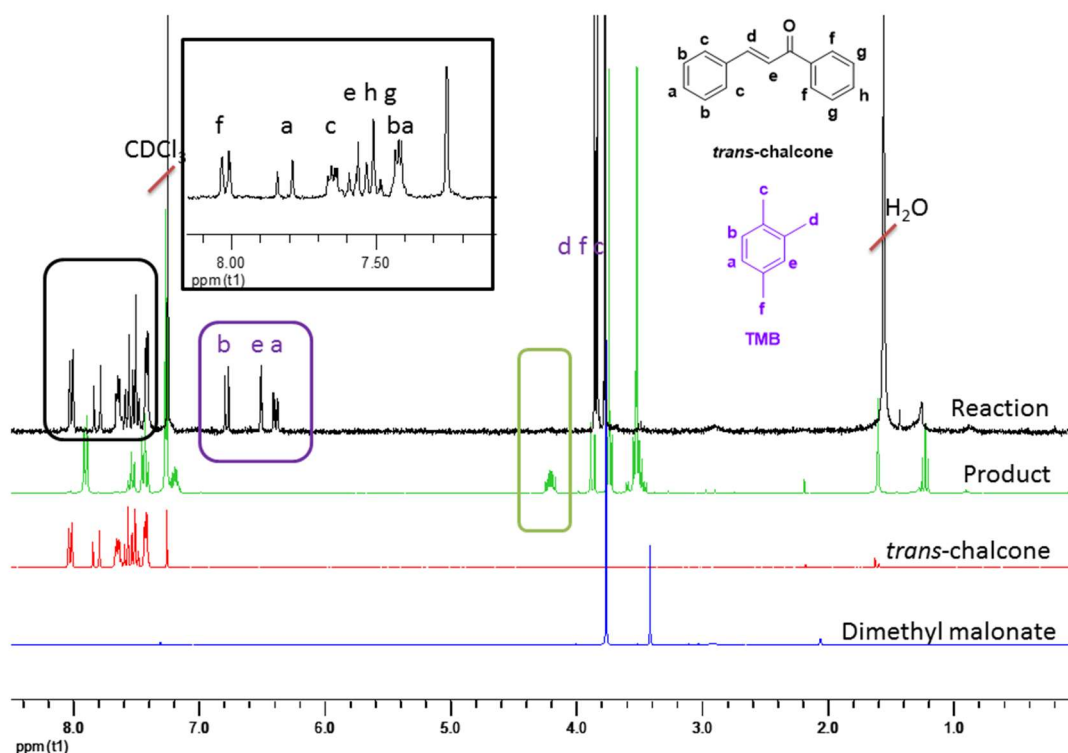


Figure 3.8: ^1H NMR spectrum of the worked up reaction (black) overlaid with expected product 3.1 synthesised *via* conventional synthesis shown in Paragraph 3.3.1 (green), *trans*-chalcone (red) and dimethyl malonate (blue), in CDCl_3 at 400 MHz.

The importance of hydrophobic substrates for micellar catalysis in aqueous conditions has been highlighted in previous work.²⁶ Here the substrate dimethyl malonate is soluble in water hence there is no preferential diffusion into the hydrophobic core, and subsequently the Michael addition does not take place, within the micellar nanoreactor.

3.3.2.2 Michael addition with dibenzyl malonate and **M2.9a**

The Michael addition of *trans*-chalcone was repeated with dibenzyl malonate, a more hydrophobic substrate containing two aromatic groups, using micelles **M2.9a**. Dibenzyl malonate and the internal standard TMB were dissolved in *trans*-chalcone in excess (four equivalents) and added to a stirring solution of **M2.9a**, with a 5 mol%

catalyst loading. During the reaction 0.2 mL aliquots were removed and the samples subsequently quenched following the method previously described (Figure 3.7), and analysed by HPLC.

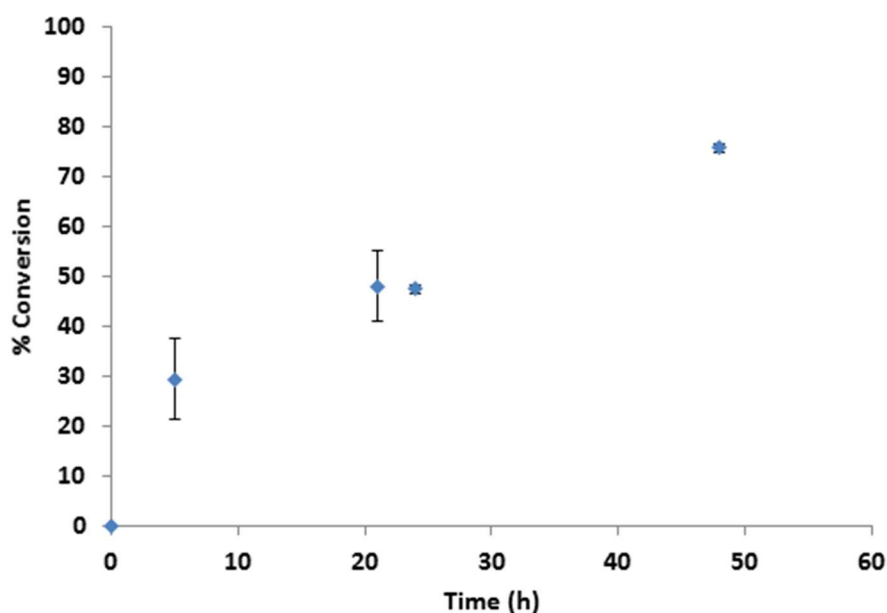


Figure 3.9: Percentage conversion for the Michael addition reaction vs time (h) with 5 mol% TBD catalyst in M2.9a in triplicate, monitored *via* HPLC (95:5 water: methanol gradient to 5:95 water: methanol for 16 min, flow rate: 2 mL min⁻¹) using a UV detector at 280 nm and 254 nm; error bars represent standard deviation from averaged multiple measurements.

After 24 hours a 47% conversion was observed indicating that these nanoreactors facilitate catalysis within the micellar core and therefore enable the reaction to proceed in water. In comparison, both free small molecule MTBD and TBD showed no catalysis in water. Thus we can conclude that immobilising the catalyst within the core has enabled the Michael addition reaction to take place. Unlike previous supports, discussed earlier, this reaction takes place at room temperature, whereas temperatures of 60 °C have previously been demonstrated.^{17, 20} On top of this lower catalytic loadings have been used (5 mol% vs 20 mol%).²⁰

To highlight the importance of tethering the catalyst to the core of the micelle, the precursor polymer **P2.8a** (a polymer containing no catalytic functionality) was assembled to afford **M2.8a** (Figure 3.10).

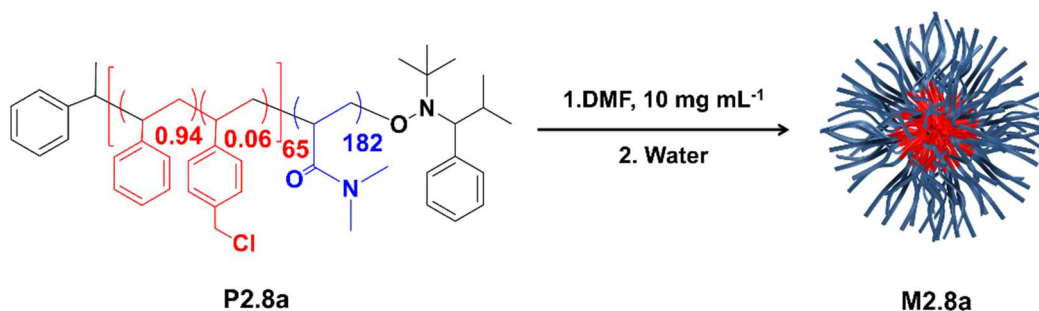


Figure 3.10: The formation of **M2.8a** from **P2.8a**.

The polymer (**P2.8a**) was dissolved in DMF at a concentration of 10 mg mL⁻¹ and water (18.2 MΩ cm, 4 mL) was slowly added using a peristaltic pump at a rate of 0.6 mL min⁻¹. The DMF was removed by exhaustive dialysis to give **M2.8a** (2 mg mL⁻¹). Dynamic light scattering (DLS, 0.1 mg mL⁻¹) was used to characterise the nanoparticles **M2.8a** in addition to transmission electron microscopy (TEM) using phosphotungstic acid (PA) to stain the assembled structures (Figure 3.11). Histograms of the TEM images were obtained through measuring the diameter of the nanoparticles on a minimum of 20 images and afforded an average particle diameter of 18 ± 3 nm. This is in agreement to the observations discussed in the previous Chapter, where the particle diameter is reduced when the particles are in the non-hydrated state. In comparison, the DLS data in which the micelles are fully solvated yields a particle size of 29 nm and a dispersity of 0.16, all of which indicate assembly formation.

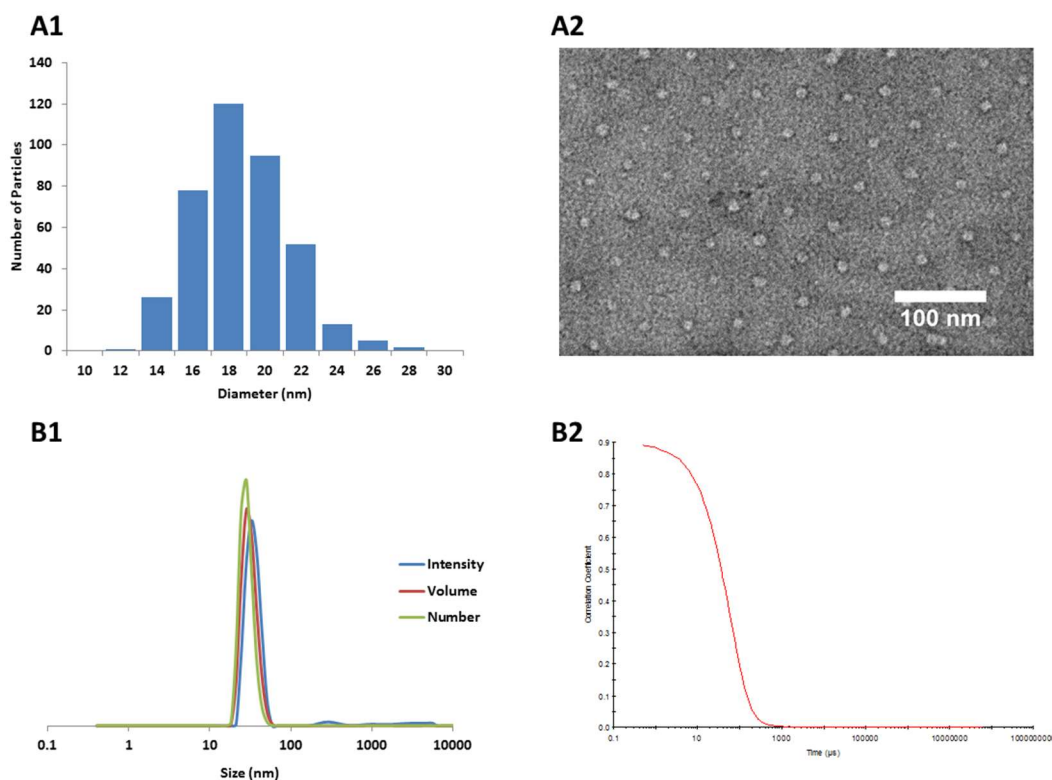


Figure 3.11: Particle size analysis of M2.8a. (A1) Histogram of particle size as determined by PA-stained TEM images at 0.1 mg mL^{-1} . (A2) PA-stained TEM image at 0.1 mg mL^{-1} (scale bar – 100 nm). (B1) Size distribution, in water at 0.1 mg mL^{-1} obtained by DLS: by intensity (blue), volume (red) and number (green) at $20 \text{ }^{\circ}\text{C}$. (B2) DLS correlation function. TEM Images obtained by Dr Yan Kang.

To this micellar solution (**M2.8a**) stock solution of catalytic MTBD was added at 5 mol% loading. Following 24 hours of catalysis, a conversion 3% was observed. This low conversion is attributed to the presence of MTBD in the aqueous environment, whereas the substrates will preferentially diffuse into the micellar core, thus preventing the reaction occurring.

The polymer **P2.9a** (a polymer with tethered TBD, which was previously self-assembled forming micelles **M2.9a**) was dissolved in THF and also used as a control at a loading of 5 mol% catalyst, to determine the effect of tethering the catalyst within the core vs the linear unimer. As the polymer formed unimeric chains in THF,

the effects of the assembled micelles on the conversion were observed. These reactions have been compared in the table below.

Table 3.2: Comparison of the Michael addition reaction for MTBD in THF, and micellar solution M2.8a, to M2.9a and P2.9a in THF after 1 hour and 24 hours with 5 mol% catalyst loading.

Catalyst	Solution	Conversion % 1 hour	Conversion % 24 hours
MTBD	THF	14	69
P2.9a	THF	0	29
MTBD	M2.8a in water	0	3
M2.9a	M2.9a in water	6	47

When comparing MTBD and P2.9a in THF, low conversion is seen with the immobilised catalyst in comparison to the small molecule, with MTBD having a conversion of 69% vs 29% after 24 hours. Here the immobilised catalyst (P2.9a) will be both sterically hindered and have slower diffusion than the small molecule, accounting for the lower conversion. The presence of the unfunctionalised micelles mixed with MTBD in solution exhibited a low conversion after 24 hours (3%) as a consequence of MTBD being required to diffuse into the micelles to enable reaction to occur. In contrast M2.9a in aqueous solution had a 47% conversion after 24 hours, indicating that fixing the catalyst within the hydrophobic core enables efficient catalysis in water. Moreover the catalysis rate is higher than for non-assembled P2.9a (29%). In aqueous solutions the micelles form a concentrated hydrophobic pocket bringing the substrates into close proximity; this is known as the “concentrator effect” which was first described by Fréchet and Hawker in 2005.²³

3.3.2.3 Altering substrate loading with M2.9a

To monitor the effect of substrate concentration on the nanoreactors, the molar percentage of catalyst with respect to the combined reaction mixture concentration was altered to produce three catalyst concentrations (1, 5 and 10 mol%). To achieve this, solutions of differing substrate concentrations were added to the micelles made up from polymers with a 1% core-catalyst loading (**P2.9a**), thus ensuring the same number of micelles and the same reaction volume, yet changing the ratio of catalyst to substrate (*i.e.* 1 mol% catalyst loading with respect to the reaction concentration will have more substrate added than 10%, Figure 3.12).

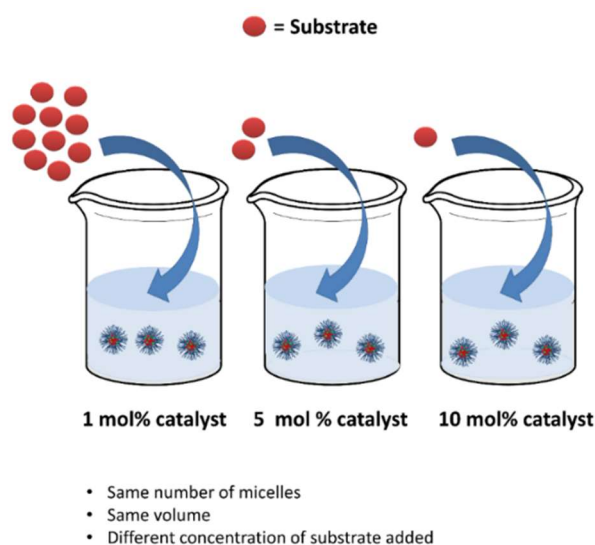


Figure 3.12: Altering the mol% catalyst vs substrate through changing the concentration of the substrate solution added. This schematic is not to scale.

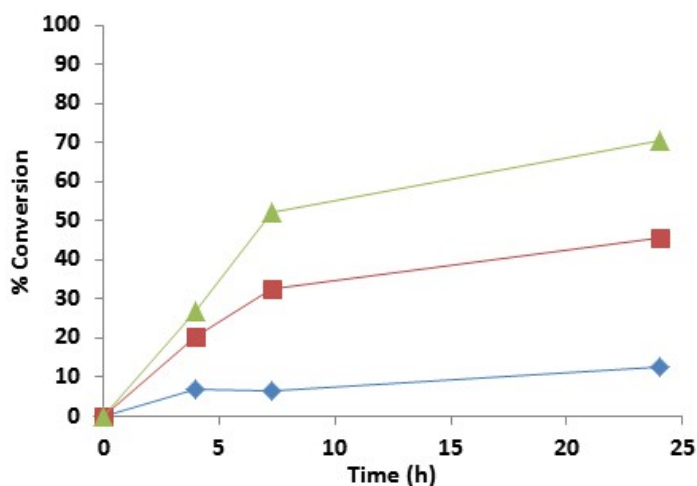


Figure 3.13: Percentage conversion for the Michael addition reaction vs time (h) with 1 mol% (diamonds), 5 mol% (squares) and 10 mol% catalyst (triangles) vs substrate. Monitored *via* HPLC (95:5 water: methanol gradient to 5:95 water: methanol for 16 min, flow rate: 2 mL min⁻¹) using a UV detector at 280 nm and 254 nm.

This reaction was again monitored by HPLC, as expected the activity increased as the catalyst loading increased (Figure 3.13). At lower catalyst loadings a higher substrate concentrations were present; hence longer induction times are required for the diffusion of the substrates into the core of the micelle, resulting in lower conversions after 24 hours.

3.3.3 Altering core loading

For micellar catalysis numerous parameters can be changed, including the number of micelles, amount of catalyst used and the catalyst loading on the support. To further explore the Michael addition in polymeric nanoreactors, polymers with different catalyst loadings were synthesised (as discussed in Chapter 2, Figure 3.14). The catalyst was incorporated into an amphiphilic block copolymer using post-polymerisation modification where the catalyst was tethered to the hydrophobic

block. Once assembled into micelles, the hydrophobic domain (PSt) is protected by the surrounding hydrophilic corona (PDMA).

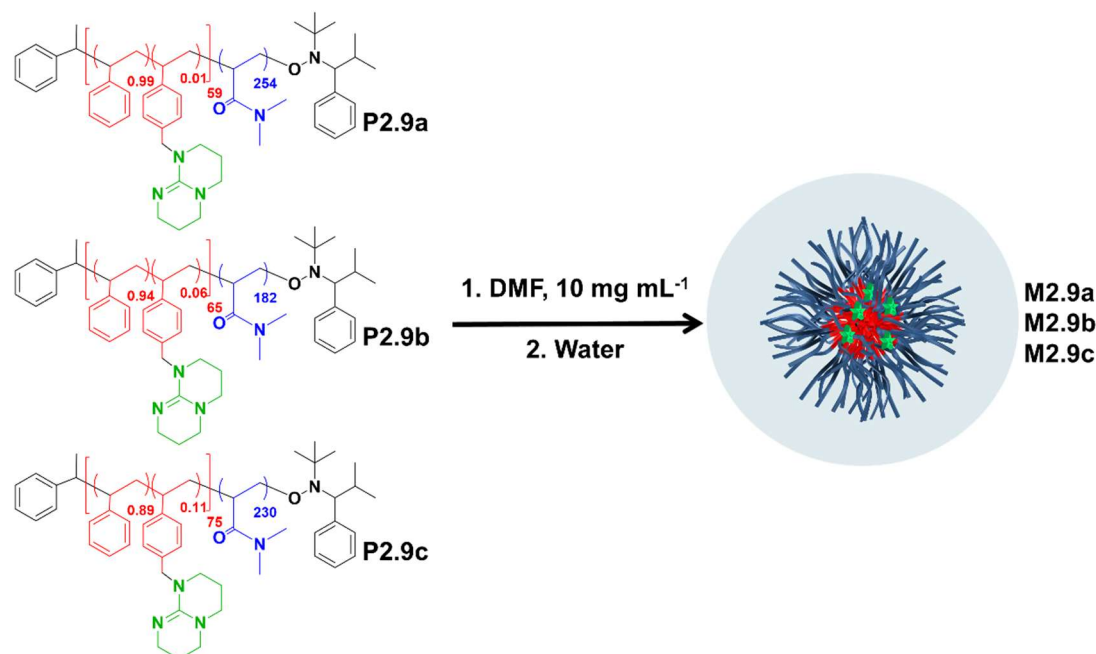


Figure 3.14: Altering the catalyst loading; red represents the hydrophobic block, blue the hydrophilic block, and the green represents the catalyst, and subsequently assembled to M2.9a-c.

It is possible to calculate the number of micelles in solution and the aggregation number (N_{agg}) using the particle molecular weight ($M_{W\ particle}$). $M_{W\ particle}$ was calculated using static light scattering (SLS) at multiple angles (θ) using the Zimm equation (Equation 3.1 (a)).²⁷ The molecular weight of a particle is determined by plotting Kc/R_θ vs q^2 ; where q^2 is the wave vector defined in Equation 3.1 (b), n is the refractive index of the solvent, and λ is the wavelength of the laser (633 nm). R_θ is the Rayleigh ratio; this is based on the average scattering intensity (I_{sample}) of the solution when compared to the intensity of the solvent ($I_{solvent}$) and the intensity of a standard ($I_{standard}$, toluene) as shown in Equation 3.1 (c). K represents the contrast

factor calculated using Equation 3.1 (d) while $\frac{dn}{dc}$ is equivalent to the polymer refractive index increment, and N_A is Avogadro's constant.

Equation 3.1: The Zimm equation and its derivatives for calculation of N_{agg} from the M_w of the particle and the polymer (determined by SLS).^{27, 28}

$$\frac{Kc}{R_\theta} = \frac{q^2 R_g^2}{3M_{W \text{ particle}}} + \frac{1}{M_{W \text{ particle}}} + 2A_2c \quad (\mathbf{a})$$

$$q^2 = \sin^2(\theta/2) \times \left(\frac{4\pi n_{\text{solvent}}}{\lambda}\right)^2 \quad (\mathbf{b})$$

$$R_\theta = \frac{I_{\text{sample}} - I_{\text{solvent}}}{I_{\text{standard}}} R_{\theta, \text{standard}} \quad (\mathbf{c})$$

$$K = \frac{4\pi n_{\text{solvent}} \left(\frac{dn}{dc}\right)^2}{N_A \lambda^4} \quad (\mathbf{d})$$

$$\frac{Kc}{R_\theta} = \frac{1}{M_{W \text{ particle}}} \quad (\mathbf{e})$$

$$N_{agg} = \frac{M_{W \text{ particle}}}{M_{W \text{ polymer}}} \quad (\mathbf{f})$$

For each sample, SLS measurements were carried out at a single concentration to produce a partial Zimm plot (Figure 3.15). Extrapolation of the linear fit of the partial Zimm plot to $q^2 = 0$ gives the molecular weight of the particle ($M_{W \text{ particle}}$) at a given concentration (c), as shown in Equation 3.1 (e), hence the first term of the Zimm equation is equal to zero. By assuming that the second virial coefficient (A_2) is negligible, the third term in Equation 3.1 (a) equals zero, thus allowing for $M_{W \text{ particle}}$, to be calculated from Equation 3.1 (e).²⁸

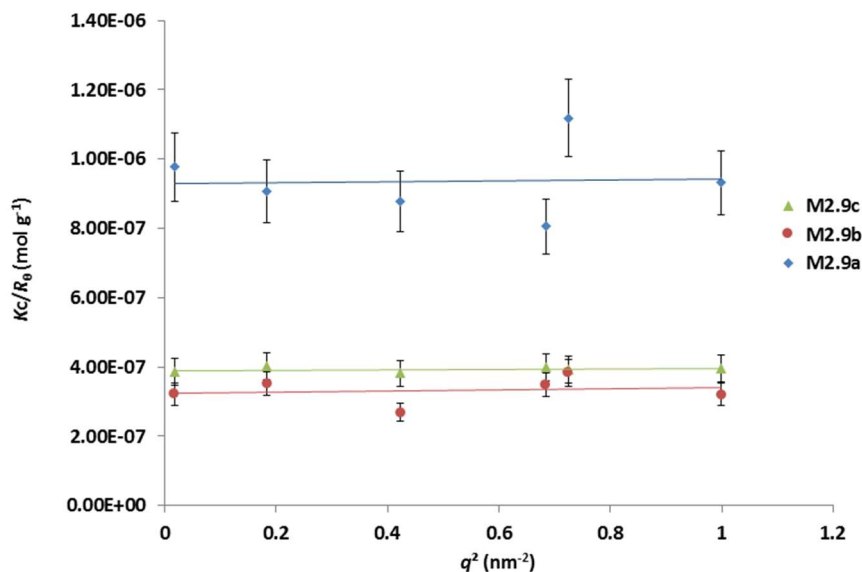


Figure 3.15: Zimm plot for M2.9a (blue), M2.9b (red) and M2.9c (green) at a concentration of 1 mg mL⁻¹.

N_{agg} represents the number of polymeric chains per micelle; therefore, a decrease in the N_{agg} will result in more nanoparticles forming (per mass of polymer) within the solutions. N_{agg} was subsequently calculated using the $MW_{particle}$ and $MW_{polymer}$, Equation 3.1 (e). A larger N_{agg} was observed for **M2.9b** (Table 3.3), which is attributed to the shorter PDMA block (DP = 182) in comparison to **M2.9a** and **M2.9c** (DP = 254 and 230 respectively). As a consequence of the shorter hydrophilic block the corona of these micelles (**M2.9b**) will have lower curvature allowing for a higher aggregation number.²⁹ The number of micelles used for the Michael addition within each solution was calculated using Equation 3.2 (a-b) (Table 3.3).

Equation 3.2: Calculation of the number of micelles using $MW_{particle}$ as determined by SLS.

$$\text{moles of micelles} = \text{Pol} \quad \text{Mass} \div MW_{particle} \quad (a)$$

$$\text{number of micelles} = \text{mol of micelles} \times N_A \quad (b)$$

Table 3.3: A summary of the number of nanoparticles in the reaction solution for M2.9a, M2.9b and M2.9c.

	Core Loading %	N_{agg}	Number of micelles
M2.9a	1	26	1.9×10^{18}
M2.9b	6	115	4.15×10^{17}
M2.9c	11	60	7.61×10^{17}

As well as a difference in core-catalyst loading these nanoreactors had different N_{agg} values, this can potentially affect the catalytic efficiencies of the micelles, as a result of an increased number of nanoreactors.³⁰

To account for the effects of core loading and the number of nanoreactors present, two methods were adopted for the Michael addition reactions as shown in Figure 3.17. Method A, maintained the number of micelles however the substrate loading was altered to preserve a constant catalyst loading. Method B, decreased the number of micelles present as the core-loading increased, however the same amount of substrate was added and the catalyst loading was maintained at 5 mol%. Both approaches were carried out with the micellar nanoreactors, **M2.9b** and **M2.9c**, this was used to monitor the effect of both core loading and substrate loading on the micellar nanoreactors.

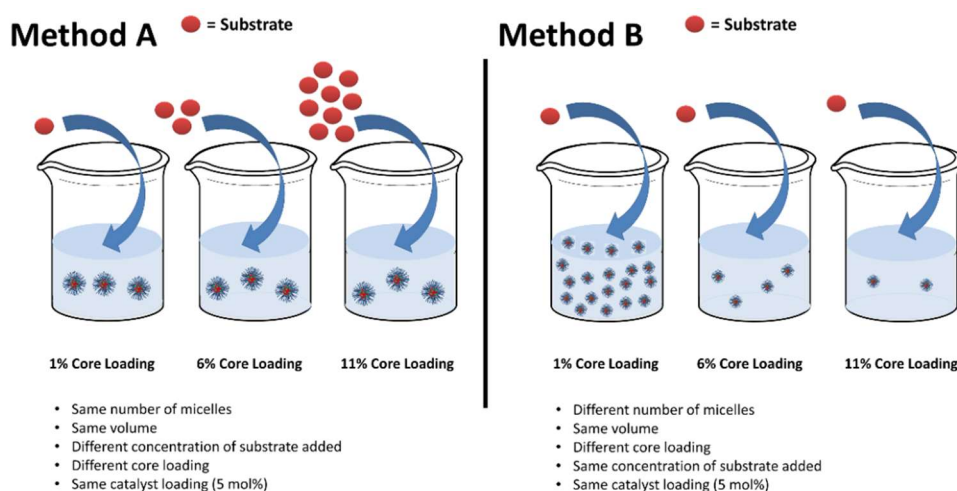


Figure 3.16: Preparation of catalytic solutions with 5 mol% catalyst concentration with respect to the reaction mixture using micelles of different core loadings. (A) Addition of different concentrations of substrates ensuring the same reaction volume and number of micelles. (B) Changing the number of micelles added yet maintaining a constant volume and concentration of substrate. These schematics are not to scale.

Comparison of **M2.9b** and **M2.9c** prepared *via* method A, therefore resulting in a similar number of micelles in the reaction, indicated that core loading increased the efficiency of the catalysis. Initial catalysis showed higher conversions with the **M2.9c**, as a consequence of the increased number of active sites within the core of the micelle. Similar conversions were found after 24 hours with 5% core loading reaching 85% conversion over 24 hours compared to 83% conversion for the 10% core loading (Table 3.4). These initial micellar solutions were then diluted, decreasing the number of micelles in solution but ensuring the same substrate concentration (method B), and the catalysis activity was then investigated.

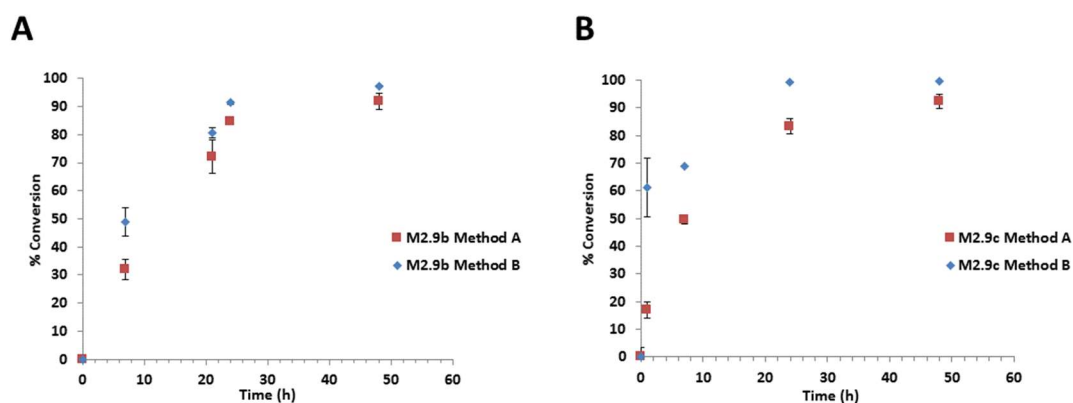


Figure 3.17: The percentage conversion for the Michael addition against time, with (A) M2.9b and (B) M2.9c in triplicate, before dilution (method A, red) and after dilution (method B, blue), in triplicate: error bars represent standard deviation from averaged multiple measurements.

Notably, diluting the system (method B) leads to higher initial conversions (Figure 3.17, blue diamonds). This was attributed to the lower concentration of the substrates, *trans*-chalcone and dibenzyl malonate, used in method B (as shown in Table 3.5). At this lower concentration the substrates can readily disperse into the core of the micelles allowing for catalysis to take place. In contrast higher substrate concentrations (method A) decrease the availability of the TBD catalyst within the core, leading to longer reaction times.

Table 3.4: A summary of the number of nanoparticles in the reaction solution for the diluted and non-diluted micelles (M2.9b and M2.9c) in triplicate.

Micelles	Method	Concentration of dibenzyl malonate (mM)	Number of micelles	%Conversion 24 hours
M2.9b	A	2.2×10^{-2}	4.2×10^{17}	85 ± 1.0
M2.9b	B	5.7×10^{-3}	1.0×10^{17}	91 ± 0.6
M2.9c	A	4.9×10^{-2}	7.6×10^{17}	83 ± 1.6
M2.9c	B	5.7×10^{-3}	7.2×10^{16}	99 ± 0.6
M2.9a	-	5.7×10^{-3}	3.0×10^{18}	46 ± 0.8

The core loading of the micelles was subsequently compared. After dilution of the micelle solutions (method B) containing **M2.9b** and **M2.9c**, the molar concentration of TBD within the Michael addition reaction was the same as for **M2.9a** (0.0375 mM). Through altering the core loading of TBD within the micellar nanoreactors, increased conversions were observed, Figure 3.18.

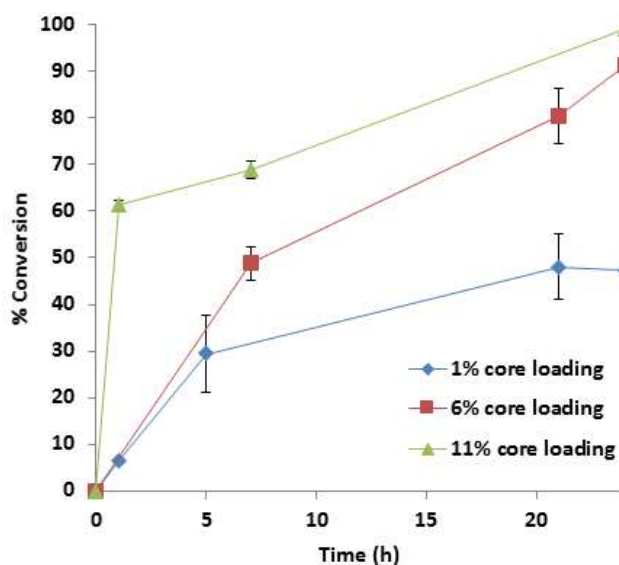


Figure 3.18: The percentage conversion for the Michael addition reaction with different catalyst core loadings, with **M2.9a** (blue diamonds, 1% core loading) **M2.9b** (red squares, 6% core loading) and **M2.9c** (green triangles, 11% core loading) against time with 5 mol% catalyst loading, in triplicate: error bars represent standard deviation from averaged triplicate measurements.

It has been hypothesised in the literature that the number of nanoreactors present within a solution is directly proportional to the rate of catalysis.³⁰ Indeed, we have shown that dilution of a micellar sample resulted in an increase in the conversion after 24 hours. Through dilution of the nanoparticles **M2.9c**, the number of micelles has decreased by an order of magnitude, yet the conversion increased from 83% after 24 hours to 99%. Hence decreasing the number of micelles has given rise to higher conversions, which is contradictory to previous reports.³⁰ We attribute this to the

greater accessibility of the catalyst to the substrate. Moreover, increasing the core loading has led to a prominent increase in activity of the micellar nanoreactors; when changing the core loading from 1% to 11% the conversion after 24 hours has increased from 46% conversion to 99%.

We can summarise that, for this system, increasing catalyst loading within the core improved accessibility of TBD for catalysis. Based on the information garnered about these micellar nanoreactors up to this point, we propose this covalently bound catalysis is now limited by two factors: diffusion of substrates into the core and the accessibility of the catalyst.

3.3.4 Blended Micelles

3.3.4.1 *Assembly of blended micelles*

The previous micellar systems utilised well-defined micelles, the synthesis of which requires the use of controlled radical polymerisation techniques to target specific catalytic loadings. Through mixing varying ratios of two polymers with different catalyst loadings, a range of catalytic loadings in the core of the micelles can be targeted (Figure 3.19). As a consequence of the high T_g of the styrenic core of these amphiphilic block copolymers, the solvent switch method was used to obtain micelles, leading to kinetically frozen blended micelles. Polymers **P2.9a** and **P2.9c** were blended and assembled giving an overall TBD concentration equivalent to 6% core loading, analogous to **M2.9b**. Formation of the blended micelles was achieved by the solvent switch method, through dissolution of the polymer mixture in DMF at a concentration of 10 mg mL⁻¹ and subsequent water addition using a peristaltic

pump. The DMF was then removed *via* extensive dialysis with 18 M Ω ·cm water to afford **M2.9m**.

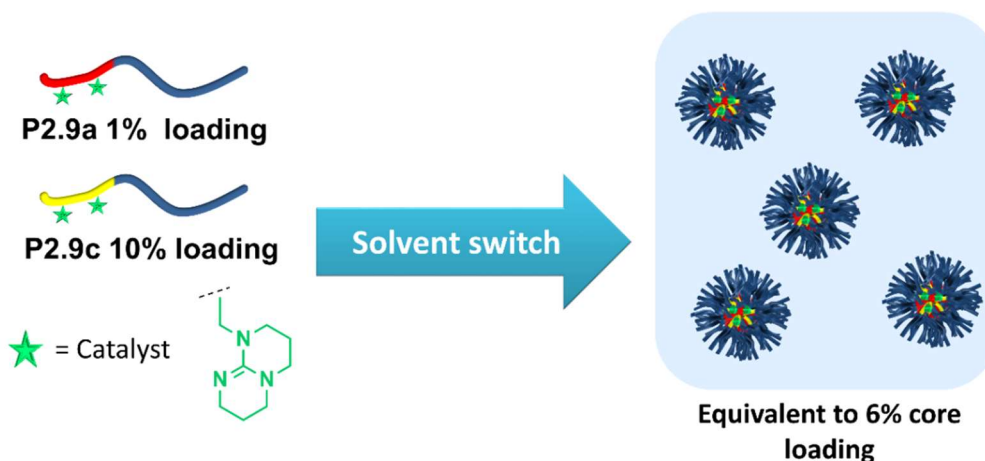


Figure 3.19: Assembly of blended micelles with 6% loading.

The nanoparticles (**M2.9m**) were analysed *via* DLS and TEM (Figure 3.20). Histograms were obtained through measuring the diameter of the nanoparticles from a minimum of 20 TEM images from different areas of the grid and over 100 particles. The particle size was determined to be $D_{ave} = 24 \pm 3.7$ nm. Which is similar to **M2.9a**, **M2.9b** and **M2.9c** where $D_{ave} = 24$, 22 and 22 nm respectively. When compared to the DLS analysis (34 nm, PD = 0.2) a decrease in size was observed, attributed to the dry state in which the particles were analysed by TEM.

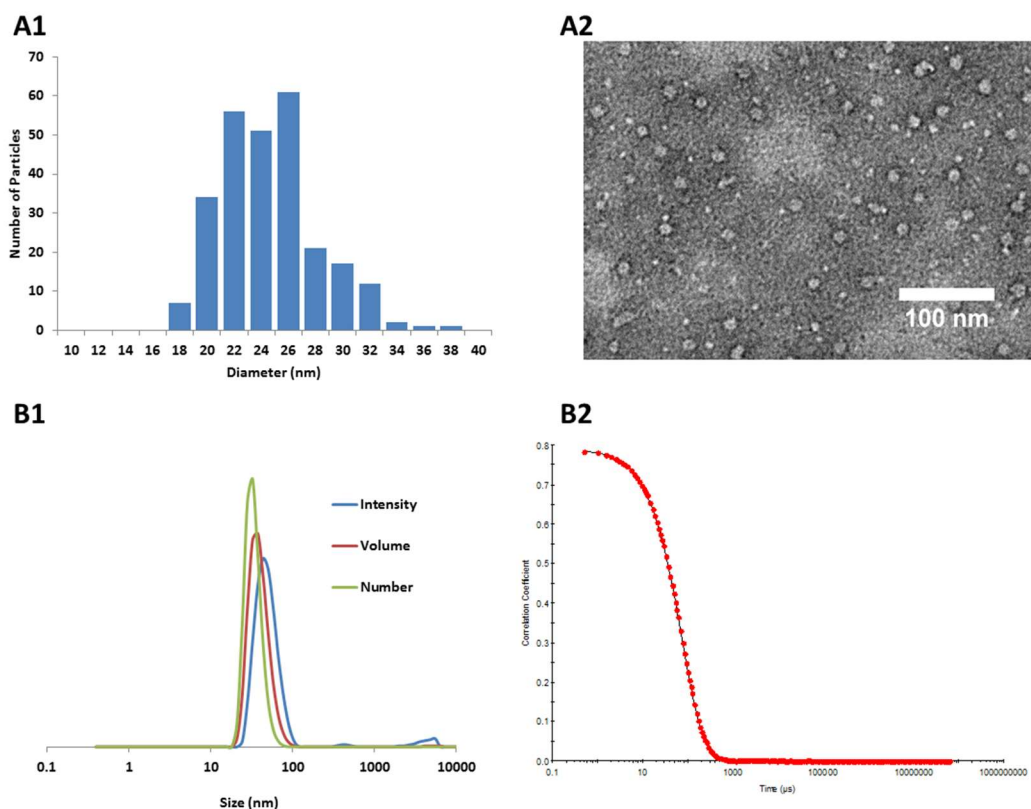


Figure 3.20: Particle size analysis of M2.9m. (A1) Histogram of particle size as determined by PA stained TEM analysis at 0.1 mg mL^{-1} . (A2) PA stained TEM image at 0.1 mg mL^{-1} (scale bar 100 nm). (B1) Size distribution by intensity (blue), number (red) and green (volume), in water at 0.1 mg mL^{-1} obtained by DLS at $20 \text{ }^\circ\text{C}$. (B2) DLS correlation function.

Interestingly when comparing the aggregation numbers, as determined by SLS analysis, N_{agg} for the mixed micelle **M2.9m** was found to be 45, a hybrid between the two component micelles **M2.9a** ($N_{\text{agg}} = 26$) and **M2.9c** ($N_{\text{agg}} = 60$) (Figure 3.21). All aggregation numbers are strongly dependent on the length of the corona-forming block; mixing these different coronas results in hybrid nanoreactors. **M2.9m** (Figure 3.21, red square).had lower N_{agg} when compared to **M2.9b**; this is associated with the shorter corona-forming block in **M2.9b**, resulting in lower curvature and increased N_{agg}

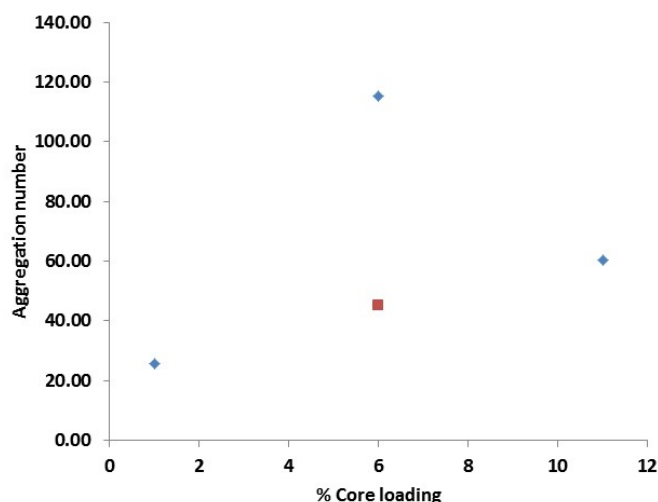


Figure 3.21: The aggregation numbers, determined by SLS, against percentage core loading for the pure systems (blue diamonds) and the mixed system M2.9m (red square). SLS data obtained by Mr Lewis Blackman.

The Michael addition with the mixed micelles (with a core catalyst loading equivalent to 6% core loading) was carried out with a 5 mol% catalyst concentration, using the previously described reaction conditions, Table 3.5.

Table 3.5: The number of micelles in the reaction solution, calculated using N_{agg} as determined by SLS. Percentage conversion for the Michael addition of *trans*-chalcone and dibenzyl malonate to afford 3.2 with catalysts M2.9a-c and M2.9m, after 24 hours, calculated by HPLC (analysis in triplicate).

	Catalyst core loading %	Number of micelles	% Conversion 24 hours
M2.9a	1	3.0×10^{18}	89 ± 4
M2.9b	6	1.0×10^{17}	91 ± 1
M2.9c	11	7.2×10^{16}	86 ± 3
M2.9m	6	2.3×10^{17}	99 ± 1

Interestingly the mixed system produced much higher conversions after 24 hours than its pure counterpart (**M2.9b**). Comparing the number of micelles present for the catalysis, there are twice as many micelles present for **M2.9m** which could account

for the higher conversion seen. The increase number of micelles is attributed to the lower aggregation number for **M2.9m** ($N_{\text{agg}} = 45$) when compared to **M2.9b** ($N_{\text{agg}} = 115$). Over twice the numbers of polymer chains are present within each micelle for **M2.9b**, decreasing the total number of micelles. This led to a higher catalytic efficiency for **M2.9m** despite having the same catalytic core loadings. From this banded system increased conversions were observed attributed to lower aggregation numbers. Hence, we have shown that assembling blended polymeric systems allows for the assembly of well-defined micelles, where the core catalytic loadings can be tuned without compromise on catalytic efficiency.³¹

3.3.4.2 *Michael addition using pre-assembled micelles*

Due to the high T_g of the styrenic core the micelles are kinetically frozen, and therefore no unimer exchange will take place by mixing the pre-assembled micelles.^{32, 33} This was used as a control to confirm the formation of a blended system. Two pre-assembled micelles were mixed together (**M2.9a** and **M2.9c**) to produce micelles with the same overall loading as the 6% system (Figure 3.22), and the Michael addition reaction was subsequently monitored. Owing to the frozen nature of the micelles, we propose that the mixture formed from pre-assembled micelles will have lower conversions after 24 hours than **M2.9m** (the blended system formed by assembling two blended polymers).

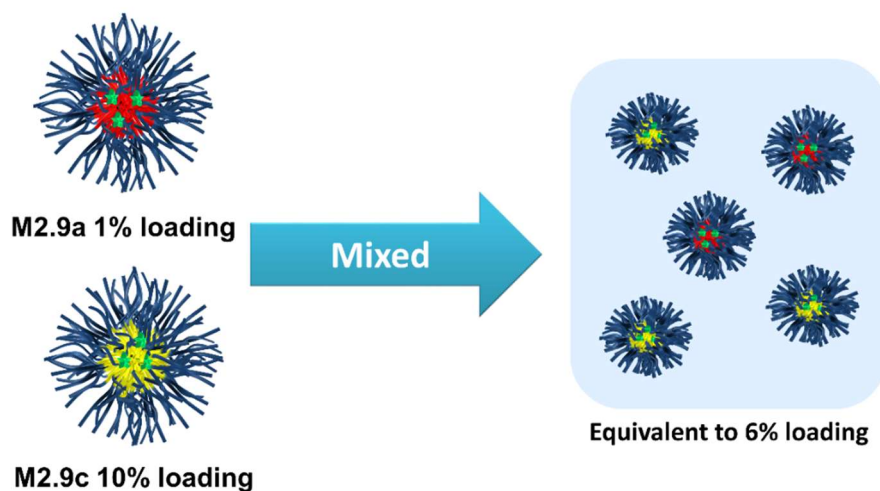


Figure 3.22: Mixing of the pre-assembled micelles M2.9a and M2.9c to yield a 6% loading.

The Michael addition with the mixed post-assembly system underwent the same reaction conditions as previously described where the concentration of dibenzyl malonate was 5.7×10^{-3} mM and the reaction was monitored *via* HPLC analysis. This system was subsequently compared to **M2.9b** and **M2.9m** (Figure 3.23). Both of the mixed systems (blended and pre-assembled micelles) have an increased number of nanoparticles available for catalysis when compared to **M2.9b** (**M2.9b** = 2.35×10^{17} , mixed post-assembly = 2.45×10^{17} and **M2.9b** = 1.01×10^{17}) this accelerated the substrate uptake and increasing the initial reaction rates.

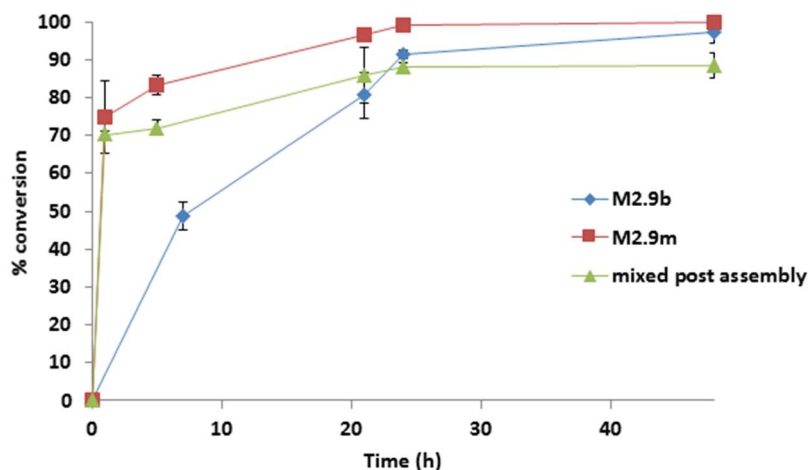


Figure 3.23: The percentage conversion for the Michael addition of dibenzyl malonate and *trans*-chalcone against time (hours) for M2.9b (blue diamonds), M2.9m (red squares) and the pre-assembled micelles mixed system (green triangles). In triplicate, and monitored *via* HPLC.

As a result of more substrate diffusing into the core of the micelle **M2.9b**, the conversion after 48 hours surpasses the mixed post-assembly (97% vs 88%). Similar conversions were obtained after 48 hours for both **M2.9b** and **M2.9m**, accounted for by the availability of TBD within the core. This has again highlighted the importance of the amount of catalyst within the core for catalysis.

3.4 Conclusions

Comparing MTBD with TBD as catalysts for Michael addition reactions was carried out in different solvents; the observed superior properties of TBD were attributed to the less hindered catalytic centre.

Based on the micellar nanoreactors we synthesised in Chapter 2 we assessed their catalytic efficiencies in Michael addition reactions in water. Interestingly we have shown that tethering TBD into the core of nanoreactors enable catalysis to proceed in water in contrast to MTBD, which serves as an analogue to the tethered TBD catalysts, in which no reaction was observed. This is a consequence of the catalytic core generated upon the assembly of these amphiphilic block copolymers resulting in the “concentrator effect”.

These nanoreactors rely on the partition coefficient of the substrates used. As a result, hydrophobic substrates led to the formation of the Michael addition products yet more hydrophilic substrates were unsuccessful. Through increasing the loading of the catalyst within the micelle core, higher conversions were achieved, however upon the addition of higher concentrations of substrate, lower conversions were observed. This is proposed to be a result of diffusion of these reagents into the hydrophobic domain of the micelle and retention of the product in the core hindering catalyst accessibility.

Creating a blended micellar system has proven the simplicity of targeting alternative catalyst loadings. As such it was demonstrated targeting homogeneous catalyst loading throughout the polymers that constitute a micelle is not necessary. In this case the mixed system displays hybrid characteristics of the previously assembled micelles **M2.9a** and **M2.9c**. Moreover, with the blended system, the number of

micelles also increased resulting in lower diffusion times for the substrate within the hydrophobic domain, increasing the overall catalytic efficiency. As TBD is a diverse catalyst this opens up routes for the application of other reactions such as transesterification reactions for use in home and personal care products.

3.5 Experimental

3.5.1 Materials and Methods

^1H NMR spectra were recorded at 300 MHz or 400 MHz (unless stated otherwise) on a Bruker DRX 300 and DRX 400 FT-NMR spectrometer respectively. Spectra were recorded using deuterated solvents and the chemical shifts are reported as δ in parts per million. NMR data was analysed using MestRe-C software. Size exclusion chromatography (SEC) analysis was carried out using HPLC grade chloroform (CHCl_3) with 2% triethylamine (TEA), with a flow rate of 1.0 mL per minute on two PLgel $5\mu\text{m}$ Mixed-D columns, and one guard column. The data was analysed using SEC Cirrus software (v.3.3) with polystyrene (PSt) calibration standards (Varian Polymer Laboratories). Characterisation of the nanoparticles was carried out using a Zetasizer Nano series instrument (Malvern) equipped with a 4 mW He-Ne 633nm laser module, at an angle of 173° (backscattering). The DLS data was interpreted using cumulant analysis of the correlation function using the Stokes-Einstein equation. The data reported was an average of four runs. Light scattering data was collected using an ALV/CGS-3 Compact Goniometer System. Particles were filtered through $0.45\mu\text{m}$ nylon filters prior to analysis at multiple angles from 30 - 130° against a toluene standard. The wavelength of the incident beam was 633 nm and for each angle, two runs of 100 s were measured. dn/dc values were determined using a Shodex RI-101 refractometer. All SLS data was obtained by Mr Lewis Blackman. Brightfield TEM images were captured with a transmission electron microscope (JEOL TEM-2011), operating at 200 keV. TEM images were taken by Dr Helen Willcock and Dr Yan Kang.

3.5.2 Micellar assembly

The amphiphilic block copolymer (50 mg) was dissolved in DMF (5 mL) at a concentration of 10 mg mL⁻¹. The solution was stirred rapidly and water (18 MΩ·cm, 20 mL) was slowly added at a rate of 0.6 mL h⁻¹ using a peristaltic pump. After the addition of water, the solution was dialysed extensively (three water changes over three days) against 18 MΩ cm water to give a solution of nanoparticles at a concentration of 2 mg mL⁻¹.

3.5.3 TEM sample preparation

From the sample at 0.1 mg ml⁻¹, 5 μL of the nanoparticle dispersion was deposited on a TEM grid (Formvar carbon grid), blotted immediately and left to air dry. A 2% solution of phosphotungstic acid (pH adjusted to 7) was deposited on the grid (5 μL). After 20-30 seconds the grid was blotted and left to air dry.

3.5.4 Michael addition reaction to afford 3.1 and 3.2

To a vial equipped with a magnetic stirrer bar, *trans*-chalcone (0.21 g, 1 mM) was dissolved in four equivalents of dimethyl malonate (5.3 g, 4 mM) or dibenzyl malonate (1.14 g, 4 mM), and 8 mL of the selected solvent (THF, MeCN, water) was added to the solution. Either TBD (7 mg, 5 × 10⁻³ mM) or MTBD (7 mg, 5 × 10⁻³ mM) was added to start the reaction. Aliquots were taken from the solution (0.2 mL) and subsequently quenched using Amberlyst® -15 resin to remove the catalyst. The beads were washed in water and the substrates extracted using diethyl ether and water (three times, 2 mL). The organic phase was dried and analysed *via* HPLC analysis. HPLC Conditions: A Supelco Discovery C18 column was used (5 μm,

4.6 mm × 10 cm) with gradient applied from 95:5 (water: methanol) to 5:95 (water: methanol) over 16 min with a flow rate of 2 ml min⁻¹. The samples were monitored using a photodiode array (PDA) detector with wavelengths set at both 280 and 254 nm. **3.1** $t_R = 8.66$, **3.2** $t_R = 9.37$.

Purification of **3.1** was carried out by column chromatography (95:5, DCM: MeOH, $R_f = 0.26$) yielding 82%, as a white solid. ¹H NMR (400 MHz, CDCl₃): δ (ppm) 7.90 (2H, d, ³ $J_{H-H} = 7.2$ Hz, **h**), 7.51 (1H, m, **j**), 7.41 (2H, m, **i**), 7.26-7.22 (4H, m, **e** and **f**), 7.19 (1H, m, **g**), 4.19 (1H, m, **c**), 3.86 (1H, d, ³ $J_{H-H} = 9.42$ Hz, **b**), 3.72 (3H, s, **a**), 3.51 (3H, s, **a**), 3.59 (2H, m, ³ $J_{H-H} = 11.2, 5.3$ Hz, **d**).

Purification of **3.2** was carried out using column chromatography (4:1, Hexane: EtOAc, $R_f = 0.2$) yielding 72%, as a white solid. ¹H NMR (400 MHz, CDCl₃): δ (ppm) 7.80 (2H, d, ³ $J_{H-H} = 7.2$ Hz, **c**), 7.50 (1H, t, ³ $J_{H-H} = 7.4$ Hz, **a**), 7.38 (2H, t, ³ $J_{H-H} = 7.5$ Hz, **b**), 7.15 – 7.30 (14H, **m, l, m, k, f** and **g**), 7.06 (1H, d, ³ $J_{H-H} = 5.6$ Hz, **h**), 5.14 (2H, td, 12.2 Hz, **j_{axial}**), 5.11 (1H, s, **j_{equatorial}**), 4.21 (1H, td, ³ $J_{H-H} = 13.7$ Hz and 4.3 Hz, **e**), 3.94 (1H, d, ³ $J_{H-H} = 9.5$ Hz, **i**), 3.44 (2H, d, ³ $J_{H-H} = 6.8$ Hz, **d**).

3.5.5 Michael addition reactions in micelles

A typical Michael addition is carried out as follows. To a flask with 10 mL of the micelle solution containing 5 mol% catalyst (typically 3.6×10^{-4} mM) the internal standard trimethoxybenzene (1 eq. to *trans*-chalcone, 1.2 mg, and 7.1×10^{-3} mM) was added. An excess of dibenzyl malonate was added (4 eq., 8.1 mg, 2.0×10^{-2} mM) to dissolve the *trans*-chalcone (1.5 mg, 7.1×10^{-4} mM) for addition to the incompatible solvent such as water. Aliquots of 1 mL were sampled at selected time intervals. The reaction was stopped by adding these aliquots to DMF (to

disassemble) The sample was washed three times with diethyl ether and water (*ca.* 2 mL) and the organic phase dried. The reaction was monitored *via* HPLC analysis. The areas of the peaks were calibrated to $t_R = 6.30$ (trimethoxybenzene), with $t_R = 9.32$ (*trans*-chalcone) and $t_R = 11.35$ (dibenzyl malonate).

3.6 References

1. C. Ghobril, P. Hammar, S. Kodepelly, B. Spiess, A. Wagner, F. Himo and R. Baati, *ChemCatChem*, 2010, **2**, 1573-1581.
2. C. Ghobril, C. Sabot, C. Mioskowski and R. Baati, *Eur. J. Org. Chem.*, 2008, **2008**, 4104-4108.
3. U. Schuchardt, R. Sercheli and R. M. Vargas, *J. Braz. Chem. Soc.*, 1998, **9**, 199-210.
4. U. Schuchardt, R. M. Vargas and G. Gelbard, *J. Mol. Catal. A: Chem.*, 1995, **99**, 65-70.
5. D. Simoni, M. Rossi, R. Rondanin, A. Mazzali, R. Baruchello, C. Malagutti, M. Roberti and F. P. Invidiata, *Org. Lett.*, 2000, **2**, 3765-3768.
6. C. Sabot, K. A. Kumar, S. Meunier and C. Mioskowski, *Tetrahedron Lett.*, 2007, **48**, 3863-3866.
7. M. K. Kiesewetter, M. D. Scholten, N. Kirn, R. L. Weber, J. L. Hedrick and R. M. Waymouth, *J. Org. Chem.*, 2009, **74**, 9490-9496.
8. D. Simoni, R. Rondanin, M. Morini, R. Baruchello and F. P. Invidiata, *Tetrahedron Lett.*, 2000, **41**, 1607-1610.
9. M. Alonzi, M. P. Bracciale, A. Broggi, D. Lanari, A. Marrocchi, M. L. Santarelli and L. Vaccaro, *J. Catal.*, 2014, **309**, 260-267.
10. W. Ye, J. Xu, C.-T. Tan and C.-H. Tan, *Tetrahedron Lett.*, 2005, **46**, 6875-6878.

11. I. Kaljurand, A. Kütt, L. Sooväli, T. Rodima, V. Mäemets, I. Leito and I. A. Koppel, *J. Org. Chem.*, 2005, **70**, 1019-1028.
12. J. E. Taylor, S. D. Bull and J. M. J. Williams, *Chem. Soc. Rev.*, 2012, **41**, 2109-2121.
13. A. Salis, M. Monduzzi and V. Solinas, in *Industrial Enzymes*, Springer Netherlands, 2007.
14. R. Sercheli, R. Matheus Vargas and U. Schuchardt, *J. Am. Oil Chem. Soc.*, 1999, **76**, 1207-1210.
15. U. Schuchardt, R. M. Vargas and G. Gelbard, *J. Mol. Catal. A: Chem.*, 1996, **109**, 37-44.
16. G. Clayden, W. Warren, N. Greeves and P. Wothers, *Organic Chemistry* Oxford University Press, 2001.
17. F. Fringuelli, F. Pizzo, C. Vittoriani and L. Vaccaro, *Chem. Commun.*, 2004, 2756-2757.
18. P. Kalita and R. Kumar, *Appl. Catal., A*, 2011, **397**, 250-258.
19. M. K. Muthyala, B. S. Chhikara, K. Parang and A. Kumar, *Can. J. Chem.*, 2012, **90**, 290-297.
20. S. Bonollo, D. Lanari, T. Angelini, F. Pizzo, A. Marrocchi and L. Vaccaro, *J. Catal.*, 2012, **285**, 216-222.
21. S. Carloni, D. E. De Vos, P. A. Jacobs, R. Maggi, G. Sartori and R. Sartorio, *J. Catal.*, 2002, **205**, 199-204.
22. R. Srivastava, *J. Mol. Catal. A: Chem.*, 2007, **264**, 146-152.

23. B. Helms, C. O. Liang, C. J. Hawker and J. M. J. Fréchet, *Macromolecules*, 2005, **38**, 5411-5415.
24. J. Wang, H. Li, L. Zu, W. Jiang, H. Xie, W. Duan and W. Wang, *J. Am. Chem. Soc.*, 2006, **128**, 12652-12653.
25. K. Kaupmees, A. Trummal and I. Leito, *Croat. Chem. Acta*, 2014, **87**, 385-395.
26. P. Cotanda and R. K. O'Reilly, *Chem. Commun.*, 2012, **48**, 10280-10282.
27. J. P. Patterson, M. P. Robin, C. Chassenieux, O. Colombani and R. K. O'Reilly, *Chem. Soc. Rev.*, 2014, **43**, 2412-2425.
28. D. B. Wright, J. P. Patterson, A. Pitto-Barry, P. Cotanda, C. Chassenieux, O. Colombani and R. K. O'Reilly, *Polym. Chem.*, 2015, **6**, 2761-2768.
29. A. Blanz, S. P. Armes and A. J. Ryan, *Macromol. Rapid Commun.*, 2009, **30**, 267-277.
30. A. Lu, D. Moatsou, D. A. Longbottom and R. K. O'Reilly, *Chem. Sci.*, 2013, **4**, 965-969.
31. D. B. Wright, J. P. Patterson, A. Pitto-Barry, A. Lu, N. Kirby, N. C. Gianneschi, C. Chassenieux, O. Colombani and R. K. O'Reilly, *Macromolecules*, 2015, **48**, 6516-6522.
32. R. Nagarajan, in *Nanoparticles: Synthesis, Stabilization, Passivation, and Functionalization*, American Chemical Society, First edn., 2008, vol. 996, ch. 24.
33. T. Nicolai, O. Colombani and C. Chassenieux, *Soft Matter*, 2010, **6**, 3111-3118.

4 Stabilisation of Lipases from *Thermomyces lanuginosus*, in Polymer Solutions

4.1 Abstract

Within this Chapter the structures and activities of lipases from *Thermomyces lanuginosus*, Lipolase and Lipex were examined in order to determine the structural parameters that affect their activity and stability in solutions. These enzymes were then mixed with polymers synthesized from different monomers in order to evaluate the synergistic effects of the two macromolecules. Furthermore, the immobilisation of the organocatalyst (TBD) onto the polymer chains, which would introduce the ability to hydrolyse esters and thus enhance the cleaning properties of a detergent formulation was also carried out.

4.2 Introduction

Laundry detergents mainly consist of builders and surface active agents (surfactants). Builders reduce water hardness as well as preventing redistribution of soils.¹ The first builders were used by the ancient Egyptians who used sodium carbonate which can be derived from burnt plants. Henkel's "Bleich-Soda" created in 1878 was the first ever detergent, combining sodium carbonate and sodium silicate.² The problem with these builders is they precipitate calcium and magnesium ions as well as iron salts, which turn clothing yellow.² These builders were rapidly changed to complexing agents, such as sodium triphosphate, however due to phosphate regulations (because of eutrophication issues) these have since been replaced with zeolites.² The second component in laundry formulations, the surfactant, also has a long history. The first surfactant, soap, was used by the Sumerians in 2500 BC. Soap is a fatty acid salt containing a long alkyl hydrophobic chain and a hydrophilic head. Soap is sensitive to water hardness so to maintain effectiveness across differing water supplies,

synthetic detergents have now taken its place.² However, following a drought in Germany in 1959, stable foams caused by synthetic surfactants were found in the water-ways. Furthermore, these surfactants were seemingly unaffected by the water sewage treatment. This led to the first detergent law in 1961, stating that all detergents must be 80% biodegradable as measured by a test devised by the detergent commission.² This legislation was then voluntarily brought into many countries all over the globe.² The drive for sustainability has meant that the use of sugar-based surfactants has increased along with more concentrated detergents, led by Unilever in 2006 with ‘All Small and Mighty’.^{3,4} As well as changes in laws and technology, formulations have changed as a result of user technology advances, such as changes from hand washing to machine washing. Hence, detergents have been developed to accommodate these changes leading to the formulations that are used nowadays. The common components found in modern laundry products are:¹

- Anti-redeposition agents
- Bleaches
- Colourants
- Fabric softeners
- Fluorescent whitening agents
- Fragrances
- Opacifiers
- Processing aids
- Foam regulators

- Enzymes

Enzymes were first introduced into detergents in 1959, this was protease which was then followed by amylase (1973), cellulase (1987), and lipase (1988).² Enzymes provide a cleaner wash and also enable the consumer to wash their clothes at lower operating temperatures given their higher activity at low temperatures.⁵ Although enzyme-containing detergents occupy over 80% of the laundry market in the United States, there is still much room for improvement in the performance of these combinations of enzymes added to our laundry products used nowadays.⁶ The main issue with enzymes is that they are sensitive to a number of factors, including:

- Detergents- this is due to the pH, ionic strength, surfactants, bleach and stain in the formulations;⁷
- Temperature- enzymes are prone to denaturing and hence exhibit loss of activity outside their optimal performance window;
- Each other- for instance protease can catalyse the lytic degradation of other enzymes.

Further advances in this field are needed to improve the stability of the enzymes in the presence of the detergents, and to enhance efficacy and cleaning performance.⁷

The enzyme lipase is thought to be of significant importance as it has been linked to applications in the food, paper, drug manufacturing, biofuels and detergent industries.⁸⁻¹²

4.2.1 Lipase

This work will concentrate on lipase which catalyses the hydrolysis of ester bonds such as the triglycerides found in oils and fats.⁸ The structure of a basic triglyceride is depicted below, lipases hydrolyse the ester bonds resulting in glycerol and three fatty acids. Due to their ability to hydrolyse ester bonds lipases are a subcategory of esterase, where lipases have a higher specificity to hydrolysing triglycerides at the water-oil boundary.^{13, 14} Subsequently, these enzymes are industrially relevant for the production of energy (biodiesel), and food manufacturing.¹³⁻¹⁶

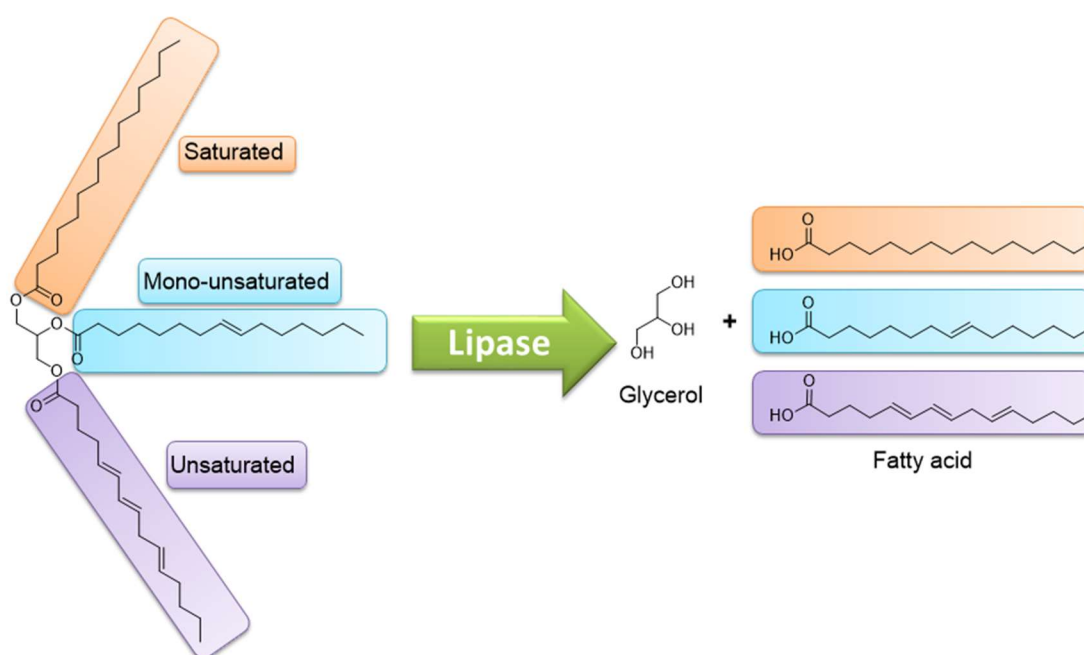


Figure 4.1: The general structure of a triglyceride and the formation of glycerol and fatty acid chains.

Lipase has a vast diversity in its origin, and as a result there is significant difference in its optimal operating conditions. Large discrepancies in optimal pH and operating temperatures are observed when selecting lipases from different organisms. These discrepancies are advantageous as different lipases can be selected depending on the

desired operating conditions. For this reason, lipase from *Thermomyces lanuginosus* (TLL) is commonly used. This organism is known to be thermophilic, producing lipases that are stable at higher operating temperatures (50-60 °C).⁹ Due to this thermostability TLL has attracted much interest as an industrial enzyme, catalysing reactions with high specificity, at higher temperatures with high activity.¹⁶ TLL is part of the α/β hydrolase family containing eight-strands of β -sheets and five α -helices.^{17, 18} It is thought that this structure provides a stable scaffold for the positioning of the active site.¹⁸ TLL is similar to the protease chymotrypsin, utilising the same catalytic amino acid residues, Serine (Ser), Aspartic acid (Asp) and Histidine (His) - the catalytic triad containing Ser146, Asp201, and His258. Hydrolysis takes place within this triad with the aid of an oxyanion hole.¹⁹ The nucleophilic serine is activated by proton transfer with histidine and aspartate as shown below.²⁰

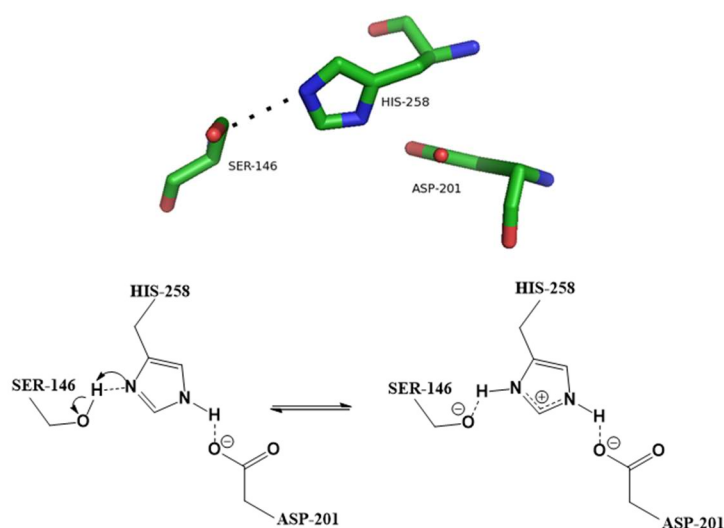


Figure 4.2: Active site of TLL from 1DU4 (The PyMOL Molecular Graphics System, Version 1.5.0.4 Schrödinger, LLC.).²¹

Unlike protease, the lipase active centre is shielded by a helical loop on the surface referred to as the “lid”.²⁰ In the absence of a water-in-oil interface (a purely aqueous environment) the lid remains in the “closed” position. Upon the introduction of hydrophobic material the lid moves into the “open” active conformation, as demonstrated in Figure 4.3.²² This interfacial activation exposes the active site to the substrates thus enabling hydrolysis.²³

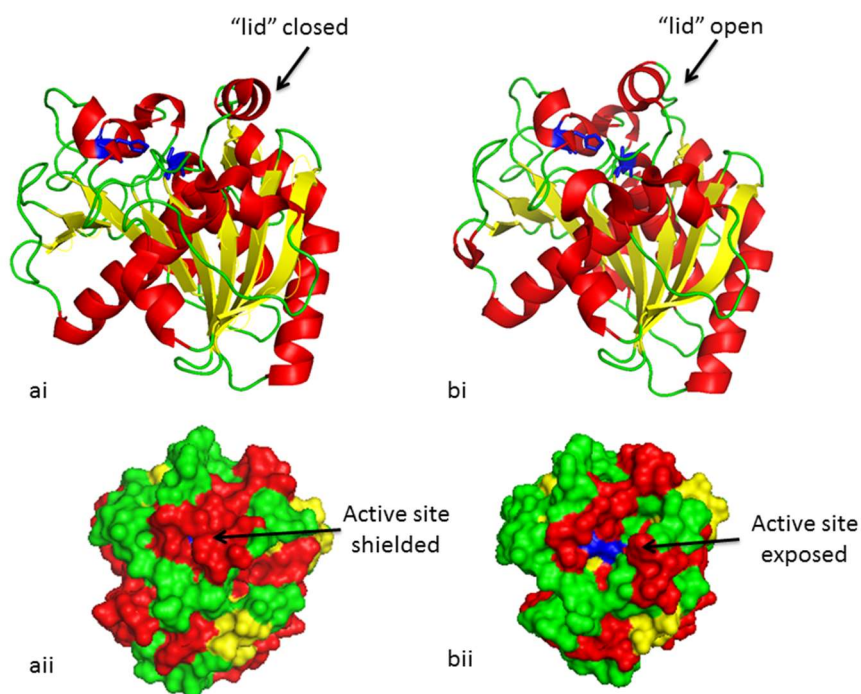


Figure 4.3: Crystal structure of TLL in the closed 1DU4 (a) and open 1EIN (b) positions, with the active site shown in blue. (i) The secondary structure. (ii) The surface structure (The PyMOL Molecular Graphics System, Version 1.5.0.4 Schrödinger, LLC.).²¹

Through the analysis of the crystal structure of TLL in the presence of different surfactant concentrations, the Patkar group divided TLL into three different categories: the low activity form, the active form, and the fully active form.²³ Patkar *et al.* proposed the cysteine (Cys) residues Cys22-Cys268 and arginine (Arg)

residues Arg84 play a role in the opening of the lid forming the activated lipase. The residue Cys22-Cys268 forms a disulphide bridge which isomerises from the left to the right handed form. Arg84 (found within the hinge) can flip to enable hydrogen bonding with Cys268 in the presence of anionic surfactants, thus opening the lid. This work suggested that TLL contains an Arg switch which is sensitive to electrostatic interactions, enabling the Arg residues on the hinge to lock open the structure.^{20, 22} Recent work from the Bjerrum group has explored this lidded region in great detail, and attempts to alter the activation mechanism were made, through genetic modification of the protein sequence.²⁴ Residues 82-98 spanning the hinge domains 1 and 2 and the α -helix lid were modified to resemble different components of the ferulic acid esterase (FAEA). FAEA was chosen as its activity is independent of the presence of an interfacial activation step. Activity was lost when the lid was replaced with FAEA sequences due to the loss of the hydrophobic residues at the interface, thus highlighting the importance of the lid for lipase activity.²⁴

Here we aim to compare the industrial enzyme Lipex to its precursor Lipolase utilising stain tests (to be described later) and circular dichroism (CD) spectroscopy. We also aim to determine if the presence of the styrenic polymer PSt-*co*-PBzCl, poly(*N,N*-dimethyl acrylamide) (PDMA), as well as the copolymers PDMA-*co*-PBzCl and PDMA-*co*-PStTBD (triazabicyclodec-5-ene) affect the activity of Lipolase and Lipex, or the secondary structures, when in solution. We aim to use both small angle X-ray scattering (SAXS) and CD spectroscopy to establish if we can predict how the lipase will behave in solution with these polymers. We aim to show how these non-invasive techniques can be used as a tool to relate activity to the enzyme stability in solution.

4.3 Results and Discussion

4.3.1 Comparison of TLL and Lipex

4.3.1.1 *Structural differences*

Derived from TLL, and containing eight mutations, Lipolase is the first industrial lipase.²⁵ The enzyme Lipex is the next generation lipase; this is Lipolase with the attained mutations, T231R and N233R. Lipex and commercially available Lipolase were initially compared by Kyte-Doolittle plots, CD spectroscopy and activity studies (hydrolysis assays and stain tests) to determine the structural similarities. Lipex is relatively unknown hence discrepancies from the Lipolase will highlight how these modifications (discussed later) affect the enzyme. Kyte-Doolittle plots compare the hydrophobicity of the proteins (TLL, Lipolase and Lipex), generating a map of the proteins' hydrophobicity along the sequence. Each amino acid has a hydrophobicity score which is averaged over three amino acids.²⁶ A more positive score suggests the presence of more hydrophobic residues. This data is represented in the following Kyte-Doolittle plot (Figure 1.5). The plots in Figure 4.4 show a change in the amino acid sequence at positions *ca.* 51 (highlighted in red) and 231 (highlighted in green). Notably, a decrease in hydrophobicity score was observed at 51-58 for Lipolase (red region) indicating the mutation of hydrophobic amino acids in exchange for hydrophilic residues. Specifically, the sequence of TLL for residues 51-58 is FLYSFEDS (hydrophobic residues in red, hydrophilic in blue and neutral are black). We hypothesise that these hydrophobic residues has been mutated during the formation of Lipolase. Upon looking at this sequence the large decrease in hydrophobicity score at 231 for Lipex will account for the known mutations T231R and N233R, where threonine and asparagine have been substituted by the more

hydrophilic arginine residues. This changes the hydrophathy scores from -0.7 (threonine) and -3.5 (asparagine) to -4.5 (arginine).²⁶

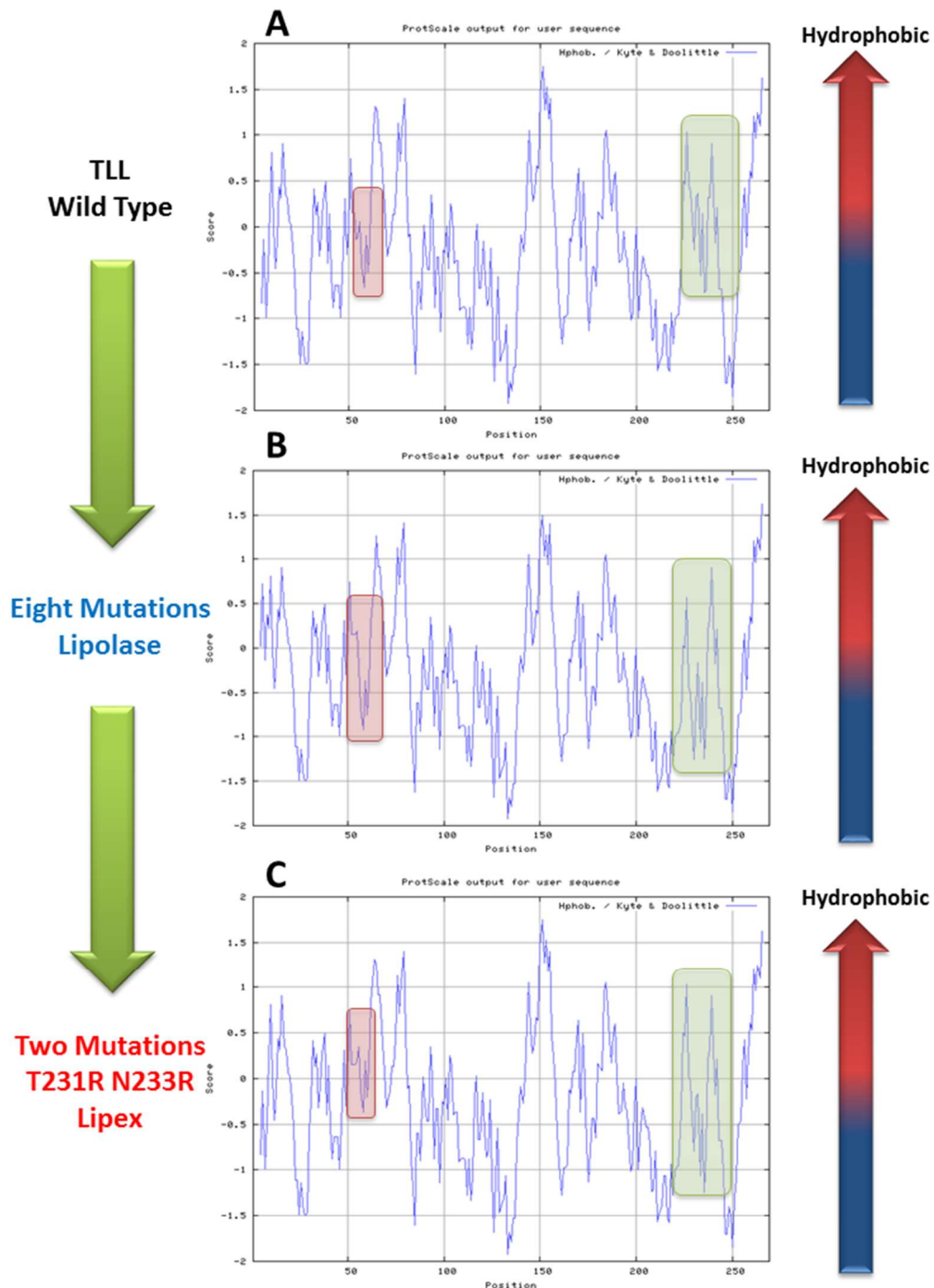


Figure 4.4: Kyte-Doolittle plot of TLL (A), Lipolase (B) and Lipex (C) were the highlighted boxes represent were a change in the hydrophobicity is observed, with thanks to Dietmar Lang, Unilever.

The observed mutations within the Kyte-Doolittle plot were mapped using PyMol, shown in Figure 4.5, with the green residues representing Arg231 and Arg233, and the residues 51-58. The known mutations T231R and N233R (Arg mutation, Figure 4.5) are found on a small α -helix, hence a change in the secondary structure may be observed.

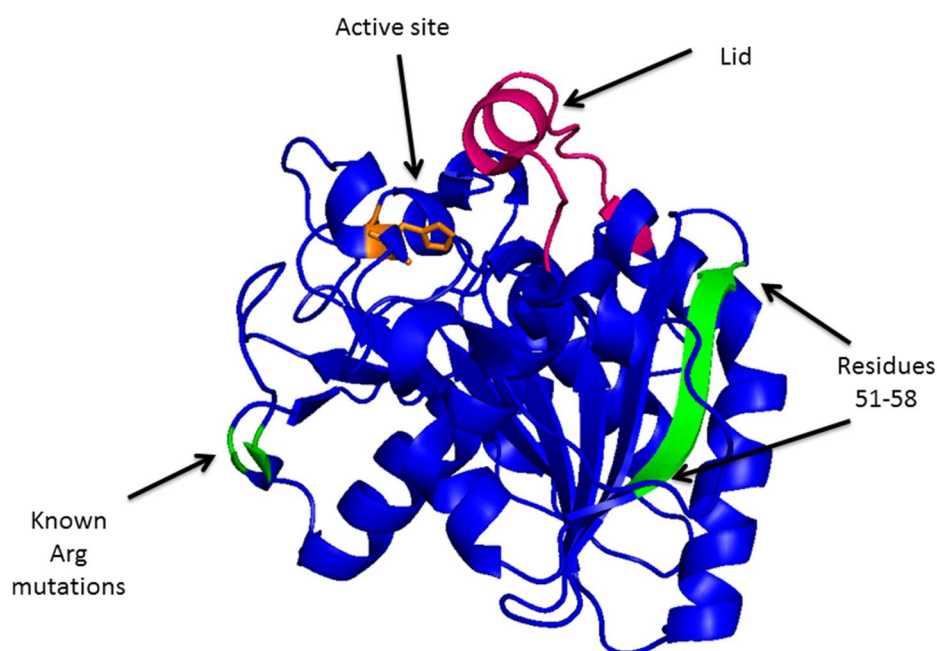


Figure 4.5 Crystal structure of TLL, the known arginine mutations in Lipex and the observed mutations for residues 51-58 are highlighted in green, the lid is pink with the orange residues representing the active site. (The PyMOL Molecular Graphics System, Version 1.5.0.4 Schrödinger, LLC.).²¹

CD spectroscopy is a common technique used to analyse the secondary structure of a protein. Through our insight into the structure from the Kyte-Doolittle plots, we hypothesise that a small change will be observed from Lipolase to Lipex, due to the known and hypothesised mutations. The secondary structures of Lipolase and Lipex were compared by CD spectroscopy on a J720 CD spectrometer (JASCO) using a 0.1 cm cuvette, the data was given as ellipticity, θ , which was converted to change in

molar ellipticity, $\Delta\epsilon$, using Equation 4.1, with a concentration of 0.1 mg mL^{-1} of Lipex and 0.05 mg mL^{-1} of Lipolase in 1 mM Tris-HCl buffer at pH 8.5. Different concentrations were used to maintain a High Tension voltage (voltage applied to the photomultiplier) lower than 600 V to reduce the signal to noise ratio, this value was then normalised utilising Equation 4.1.

Equation 4.1: $\Delta\epsilon$, the change in ellipticity per residue absorption ($\text{M}^{-1} \text{ cm}^{-1}$) where θ is ellipticity (mdeg), MRW is the mean residue weight (g mol^{-1}), l is the path length (cm) and c is the concentration (mg mL^{-1}).

$$\Delta\epsilon = \frac{\theta(0.1 \times MRW)}{(3298lc)}$$

Overlaying the spectra obtained *via* far-UV CD spectroscopy analysis of Lipolase and Lipex indicated that similar protein folding was present in both enzymes (Figure 4.6).²⁷

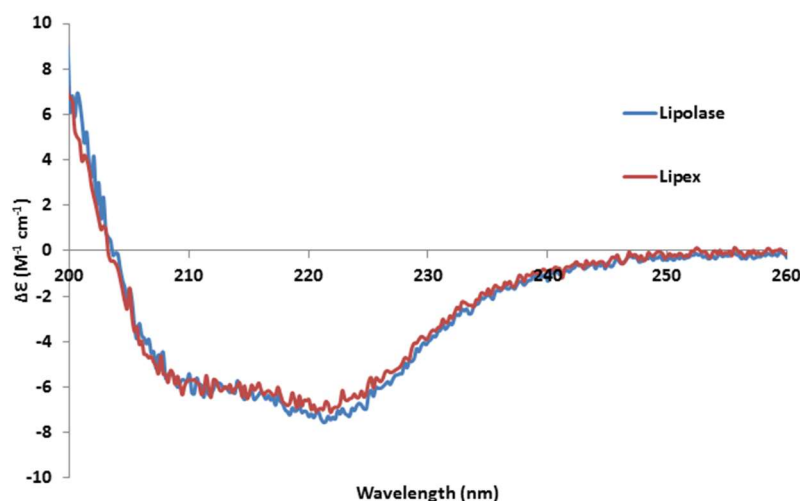


Figure 4.6: Far-UV CD spectra of Lipolase and Lipex as molar circular dichroism ($\Delta\epsilon$) as a function of wavelength. Run at $20 \text{ }^\circ\text{C}$. The spectra were averaged over three runs and three accumulations, buffer was subtracted.

The online analysis programme DICHROWEB was also utilised to further explore the secondary structure. This software uses a protein reference set to estimate the percentage of α -helices, β -sheets, turns and unordered structures within a protein and can be used as a guide to estimate changes to the secondary structure.^{28, 29} The breakdown of the secondary structure is shown in Table 4.1.

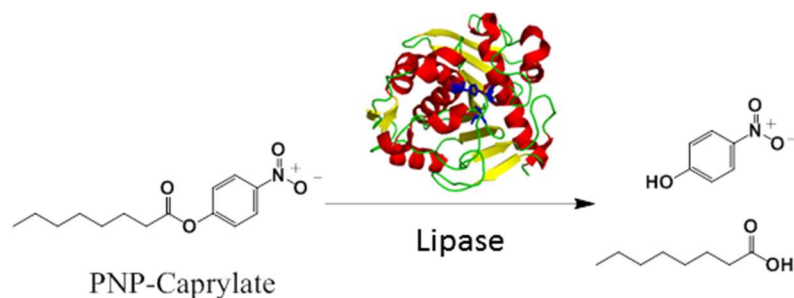
Table 4.1: The secondary structure content of Lipolase and Lipex determined by CD spectroscopy and interpreted using DICHROWEB using CONTIN/LL analysis programme and reference set 4. Normalised root-mean-square deviation (NRMSD) gives the deviation of the data set to the model used.^{28, 30}

Protein	% α-helix	% β-sheet	% β-turns	% unordered	NRMSD
Lipolase	60.5	7.0	11.6	20.9	0.029
Lipex	66.4	4.4	13.4	15.8	0.043

The analysis programme gives low NRMSD values indicate good correlation with the model data set. A decrease in the percentage of β -sheets is seen between Lipolase and Lipex, in agreement to previous observations, where a change in the β -strand was predicted by the Kyte-Doolittle plot. This can increase the percentage of α -helices and turns within the secondary structure. Interestingly a 5% difference in the unordered coils is seen between Lipex and Lipolase. This decrease in unordered structure could be directly related to the unknown mutations seen at 51-58 in the Kyte-Doolittle plot.

4.3.1.2 *Activity comparison of Lipex and Lipolase*

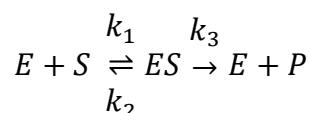
The common assay for lipase uses the substrate *p*-nitrophenyl caprylate (PNP-caprylate) where the release of *p*-nitrophenolate (PNP) can be detected spectroscopically at 405 nm (Scheme 4.1).³¹



Scheme 4.1: Schematic of the PNP-assay for lipases.

Steady-state kinetics used to monitor enzymatic activity. As the concentration of substrate changes gradually with time, in the presence of the active enzyme.³² Hypothetically the general equation for the catalysis is equivalent of Substrate \rightarrow Product, however in reality an enzyme substrate complex (ES) forms prior to product formation (Equation 4.2).³²

Equation 4.2: An equation showing the overall reaction used in enzyme kinetics.



For Michaelis-Menten kinetics the initial rate is directly proportional to the concentration of substrate, S. At a high concentration of S the enzyme reaches its maximum rate of catalysis, otherwise known as reaching saturation, this is represented as the maximum velocity (V_{\max}). The reaction rate (v) of product formation, P, is directly proportional to the concentration of enzyme-substrate complex, ES.³³ Steady-state kinetics assumes a low concentration of enzyme (E) in comparison to substrate, with product formation being (k_3) faster than ES

formation.³² This means the rate limiting step is the equilibrium step, in which ES is formed. These assumptions are the foundations in which the Michaelis-Menten equation (Equation 4.3) can be derived.

Equation 4.3: The Michaelis-Menten Equation.

$$v = \frac{V_{max}[S]}{K_m + [S]}$$

When [S] is equal to K_m (the Michaelis constant) the rate of the reaction is equal to half V_{max} , this is the definition of the Michaelis constant. It is also possible to determine the turnover number, k_{cat} , if the enzyme concentration is known, by dividing V_{max} by enzyme concentration. Hence both the activity of Lipolase and Lipex in the PNP-assay were compared, using an enzyme concentration of 1.0×10^{-2} mg mL⁻¹ and a range of substrate concentrations (from 0-100 μ M) in Tris-HCl (50 mM pH 8.5).

Table 4.2: Activity of lipase, measured using PNP-caprylate as a substrate, observed at 405 nm with six repeats.

	V_{max} (μ M s ⁻¹)	K_m (μ M)	k_{cat} (s ⁻¹)	k_{cat}/K_m (s ⁻¹ μ M ⁻¹)
Lipolase	2.3×10^{-5}	18.3	6.64	0.37
Lipex	1.4×10^{-4}	31.3	41.3	0.88

Comparing the rates of reaction, a significant increase in the enzymatic efficiency is observed for Lipex, this could be accounted for by the mutations in Lipex previously

discussed; increasing the hydrophobicity of the lipase (Lipex) may have led to more favourable interactions with the substrate, thus enhancing activity.

Another technique for monitoring the enzyme activity are stain tests, these are widely used industrially to determine the level of cleaning of stains from fabric using enzymes. These tests utilise microtiter plates containing cotton fabrics which are stained; for lipase studies different fats are used such as beef fat, lard and cooking oil. Due to the difference in structure of these triglycerides a difference in stain removal can be observed. These stains are washed in the presence of the Unilever formulation, Blackbull^{TM1} formulation, and either Lipex or Lipolase to determine the degree of stain removal when compared to the non-stained white cotton fabric, thus producing a stain removal index (SRI). The basic set up is shown in Figure 4.7; the formulation, Prenton water (a locally sourced water supply with 12 French Hard, FH, 2:1 Ca:Mg), buffer and enzyme is added to a well containing stained cotton fabric (diameter = 5 mm, height = 1 mm). This is then heated to 30 °C and shaken at 250 rpm for 30 minutes. The solution is removed and each well is washed three times and shaken at 250 rpm for 1 minute using 12 FH water, then the plates are dried overnight.

¹ Blackbull formulation is trademarked formulation from Unilever containing 33-35 wt.% surfactant which is a combination anionic and non-ionic surfactants with calcium binders.

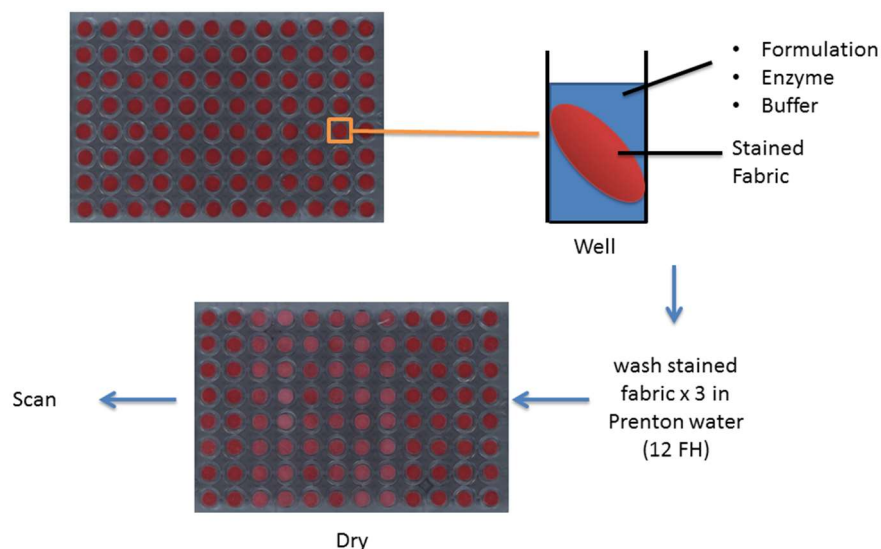


Figure 4.7: Experimental set up for stain testing.

These stains are then scanned using a flatbed scanner to determine the change in colour (ΔE) using colourimetry. The most common technique for analysing colour changes in the food industry is the Hunters LAB analysis.³⁴ This analysis is depicted in Equation 4.4 (a) where L , a and b represent the brightness, redness to greenness, and yellowness to blueness respectively.³⁵ The final scans are then compared to non-stained cotton fabric calibrants.

Equation 4.4(a-c): colour difference, SRI and ΔSRI equations.

$$\Delta E = \sqrt{(L_o - L)^2 + (a_o - a)^2 + (b_o - b)^2} \quad \text{(a)}$$

$$SRI = 100 - \Delta E \quad \text{(b)}$$

$$\Delta SRI = \text{Experimental SRI} - \text{control SRI} \quad \text{(c)}$$

To determine the stain removal of Lipolase and Lipex, a stain test study was carried out with the beef fat stain at pH 8.5, with 0.8 mg mL⁻¹ of Blackbull formulation. The standard concentration used for Lipex was 10 mg L⁻¹, and concentration of Lipolase

was varied from 1 mg L⁻¹ to 100 mg L⁻¹ (Figure 4.8). A large difference in activity was observed between Lipex and Lipolase and even at higher Lipolase concentrations a superior cleaning performance was observed for Lipex.

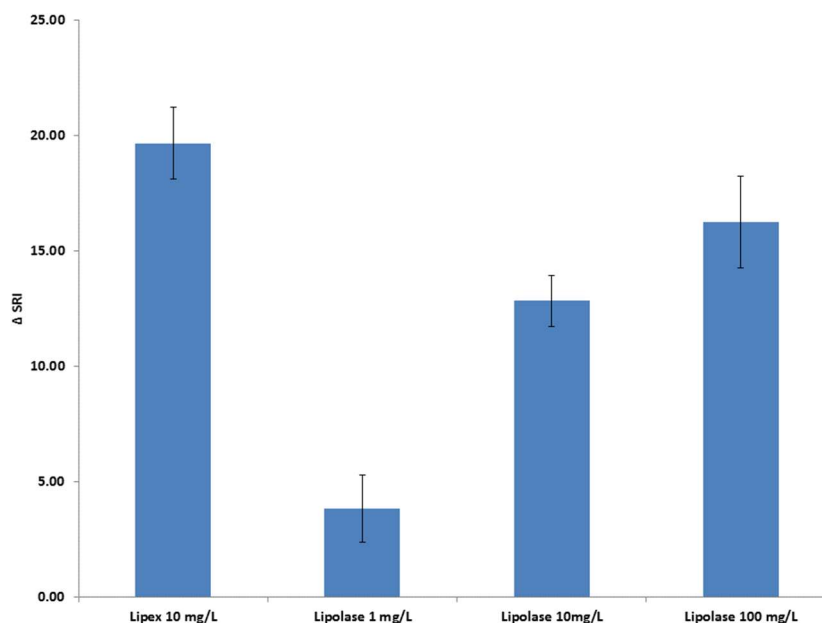


Figure 4.8 A bar chart representing the Δ SRI for the beef fat stain when subtracted from the blank surfactant for Lipex and Lipolase in Blackbull formulation. Each stain test was repeated four times over four plates and averaged.

We hypothesise that the arginine mutations on the Lipex surface will affect how the enzyme interacts with the formulation; potentially leading to enhanced stability of the Lipex compared to Lipolase. For this reason a study comparing the Unilever formulations; Blackbull and Ecoboost^{TM2} was carried out, where Blackbull formulation has a much higher concentration of surfactants present in comparison to Ecoboost (33% and 15% respectively). For the control reaction, using beef fat stain, a higher SRI was observed with the Blackbull formulation (49.1 ± 1.1) in

² Ecoboost formulation is trademarked formulation from Unilever containing 15 wt.% surfactant which is a combination anionic and non-ionic surfactants with calcium binders.

comparison to Ecoboost (45.5 ± 0.4). A stain removal comparison for Lipolase and Lipex at 10 mg L^{-1} with 0.8 mg mL^{-1} of formulation is shown in Figure 4.9. Here, no obvious change was found upon changing formulation for Lipolase. In contrast Lipex had a higher ΔSRI in Blackbull formulation when compared to Ecoboost, thus implying preferential conditions at higher surfactant concentrations for Lipex.

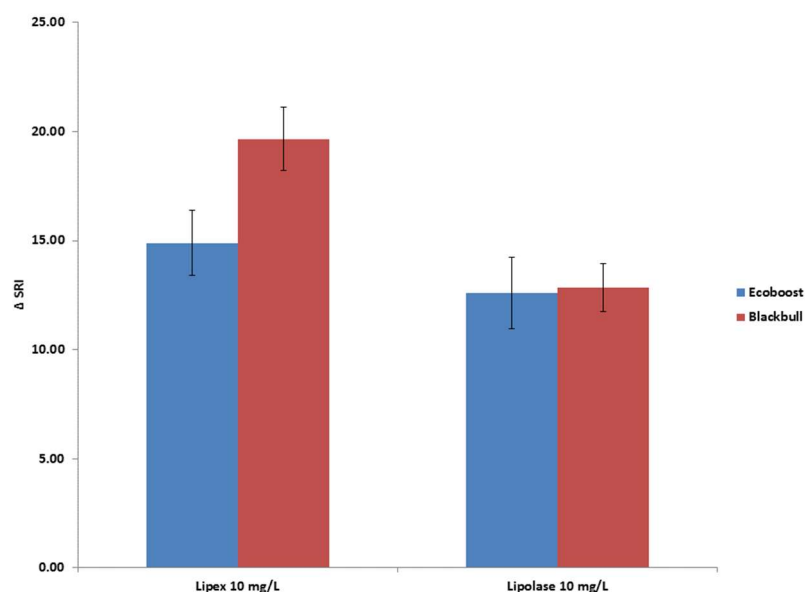


Figure 4.9: A bar chart representing the ΔSRI of beef fat stain when subtracted from the blank surfactant for Lipex and Lipolase in Ecoboost and Blackbull formulations. Each stain test was repeated four times over four plates and averaged.

The arginine mutations T231R and N233R are found on the surface of the Lipex, which increases the proteins ability to interact with ionic surfactants. When the enzyme is active, in an “open” conformation these mutations reside on the opposing side to the hydrophobic active site. This separation of areas of varying hydrophobicity is comparable to Janus particles which have two surfaces with different hydrophobicities, this is shown below. Here the hydrophobic active site is

in the “open” conformation interacting with the core of the micellar structure (Figure 4.10 B), and the hydrophilic surface will sit in the corona of the micelle.²¹

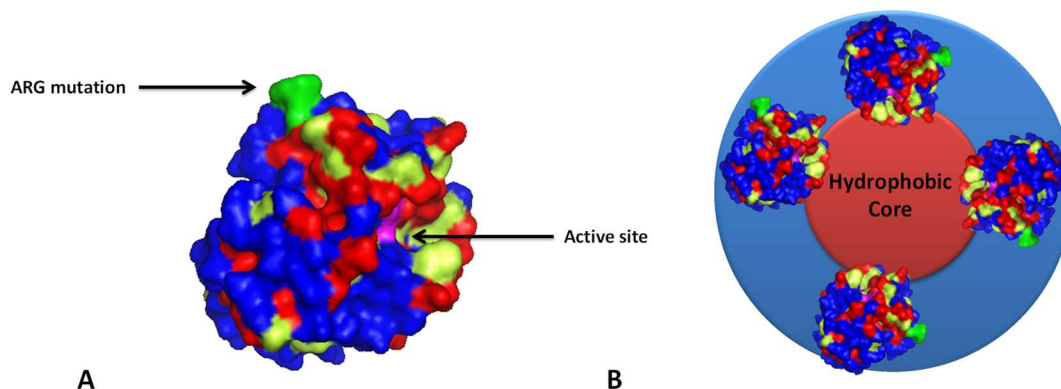


Figure 4.10: Green represents the mutated residues on TLL, (PDB: 1EIN) at T231R and N233R, Active site (pink), hydrophobic residues (red), and hydrophilic residues (blue).²² (A) The mutated TLL with ARG mutations found in Lipex (B) stabilisation of Lipex at the core corona interface of surfactant micelles. (The PyMOL Molecular Graphics System, Version 1.5.0.4 Schrödinger, LLC.).²¹

Otzen and co-workers have explored various TLL mutations where changes were made to the anionic side chains to form both neutral and cationic chains.³⁶ This increases the interactions with charged anionic surfactants protecting the enzyme from changes in the surrounding environment. Fernandez-Lorente *et al.* demonstrated how low concentrations of detergents improved the catalytic properties of enzymes.^{16, 37} Detergents can shield the hydrophobic pocket from water stabilising the enzyme in its “open” conformation, increasing activity.³⁷ It is proposed that the position of these mutations on the surface of Lipex allows for additional surfactant stabilisation in the presence of ionic surfactants. This stabilisation is supported by the Δ SRI values obtained for Lipolase, here no change was observed upon changing formulation which is accounted for by the absence of arginine mutations on the

surface. Within these higher ordered structures Lipex is in the open active conformation accounting for the increased Δ SRI observed.

4.3.2 Polymer lipase solutions

As discussed previously lipases can hydrolyse a range of triglycerides, yet upon the introduction of detergents enzymes tend to denature leading to loss of activity.⁵ Numerous techniques have been explored to stabilise proteins in solution through the covalent attachment of polymers to the enzyme.³⁸⁻⁴⁰ The synthesis of protein-polymer conjugates can lead to a reduction in an enzymes turn-over number, it is proposed by Russell and co-workers that this is due to high density of polymers shielding the active site reducing activity.⁴¹ The introduction of polymers to a solution containing Horseradish Peroxidase, Maynard *et al.* have shown that trehalose glycopolymers can stabilise the enzyme after exposure to lyophilisation.⁴² We aim to explore the effects of introducing a variety of polymers on the structure of and activity of Lipex. These polymers were synthesised using nitroxide mediated polymerisation (NMP) as described in Chapter 2, utilising the universal initiator made in Chapter 2 (**2.5**).

4.3.2.1 Synthesis of PBzCl-co-PSt, **P4.1** and **P4.2**

The monomers, vinyl benzyl chloride (BzCl), styrene (St), were polymerised by NMP utilising the universal initiator **2.5**, which was synthesised in Chapter 2. A 20% incorporation of BzCl was targeted. The polymerisation was heated at 125 °C for 4 hours where a conversion of 65% was achieved. The reaction was quenched *via* rapid cooling and precipitated into cool methanol. The white precipitate formed was

dried under vacuum and characterised. The incorporation of BzCl was determined by ^1H NMR spectroscopy (Figure 4.11) 20% incorporation, determined utilising the polymer end group at 3.2 ppm. The molecular weight was determined as 5.1 kDa by size exclusion chromatography (SEC) with a narrow dispersity (Table 4.3) indicating good control over the polymerisation.

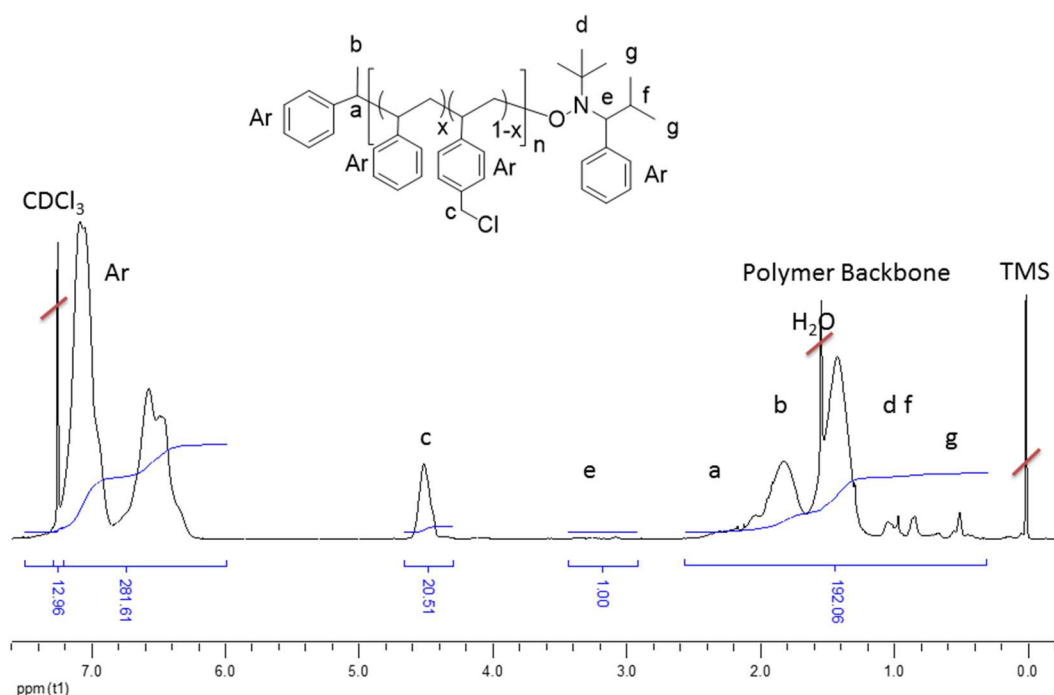


Figure 4.11: Long acquisition ^1H NMR spectrum of P4.1, in CDCl_3 at 400 MHz.

An alternative polymeric scaffold was synthesised with a higher molecular weight, this was done through the free radical polymerisation of St and BzCl with the initiator benzyl peroxide (which forms a radical species upon heating). The polymerisation took place over 4 hours at 70 °C reaching 99% conversion. The incorporation of BzCl was determined by comparing the ratio of the aromatic peaks

in to the pendent methylene signal *via* ^1H NMR spectroscopy to give an incorporation of 18% in **P4.2**.

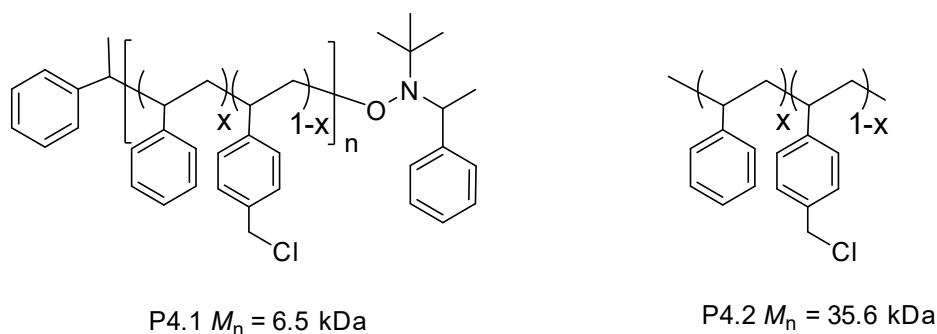


Figure 4.12: Structures of P4.1-P4.2.

Table 4.3 Characteristics of polymers P4.1-4.2, ^adetermined by ^1H NMR spectroscopy (400 MHz, CDCl_3), ^bdetermined by SEC (CHCl_3 , PSt standards).

Name	Polymerisation method	% BzCl incorporation	M_n (kDa) ^a	M_n (kDa) ^b	\bar{D}_M ^b
P4.1	NMP	20	6.5	5.1	1.16
P4.2	Free Radical	18	-	35.6	2.07

4.3.2.2 PBzCl-co-PSt stain tests

Stain tests were initially carried out to investigate the effect of the molecular weight of polymers **P4.1** and **P4.2** (Figure 4.12), on the stain removal of beef fat and lard stains in the presence and absence of Lipex. To each well the Blackbull formulation was added at a concentration of 1.25 mg mL^{-1} at both pH 8.5 and pH 7, with a Lipex concentration of 1 mg L^{-1} . The polymers were initially added at 0.5 mg mL^{-1} giving a final well volume of $200 \mu\text{L}$. Due to the hydrophobicity of these polymers, they were added to the stain test as dispersion in water after five minutes of vortexing followed by five minutes of sonication of the dispersion. Both beef fat and lard stains were

used as work from the Alina group has compared the structural composition of beef fat and lard using gas chromatography flame ionisation detection (GC-FID) differential scanning calorimetry (DSC) analysis.^{43, 44} This work proved that beef fat contained a lower percentage of unsaturated fatty acids in comparison to lard, 74% and 89% respectively, increasing the melting temperature.^{44, 45} Hence beef fat has a higher stability than lard so stain removal is more difficult. The stain test data with the beef fat stain is shown in Figure 4.13. At pH 8.5 the Δ SRI of the **P4.1**-Lipex mixture is within error of the combined polymer **P4.1** and Lipex data. However, a much higher Δ SRI is seen for the combined **P4.2** and Lipex, in comparison to the Lipex and **P4.2** on their own. Decreasing the pH to 7 (non-optimum conditions for the Lipex) a large increase in stain removal is seen for **P4.2**; however, the addition of either polymer to the Lipex has not increased the stain removal, when compared to the free polymer and Lipex combined. This could be attributed to the stain interacting with the higher molecular weight polymer (**P4.2**), hence upon washing the stain (with Prenton water) the stain is removed more readily.

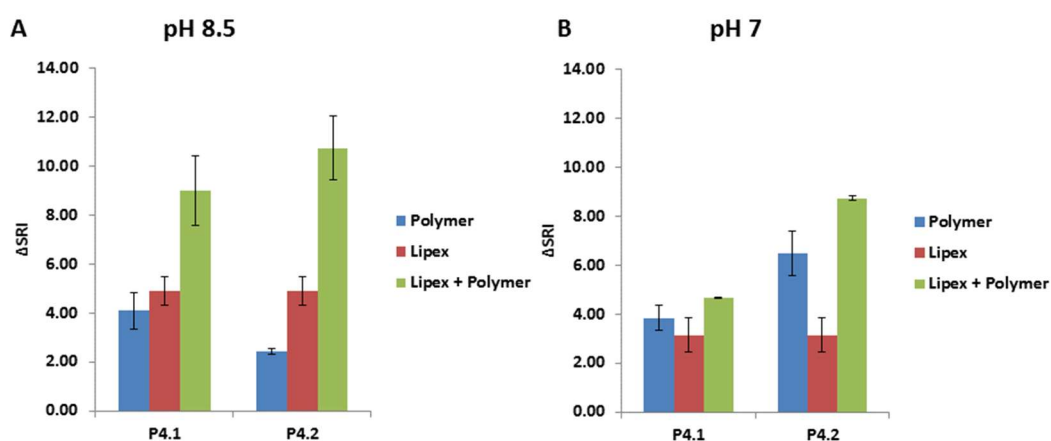


Figure 4.13: Δ SRI at pH 8.5 and pH 7 for P4.1 and P4.2 and Lipex with beef fat stain.

An alternative stain, lard, was also used (Figure 4.14) for which a much lower Δ SRI was seen. Here the stain removal efficiency is again much higher at pH 8.5, the optimum conditions for the Lipex. Interestingly at this pH the polymers alone are removing stain unlike **P4.2** at pH 8.5 with the beef fat stain, the stain removal of the combined polymer and Lipex solution is not greater than the sum of the individual polymer and Lipex solutions. Decreasing the pH results in a significant decrease in the stain removal of the polymer alone. Here, a large increase in stain removal was observed upon the addition of the combined polymer and Lipex solution. Notably negative values were obtained for the polymer solutions at pH 7, this is accounted for by the polymers redepositing onto the stain, decreasing Δ SRI.

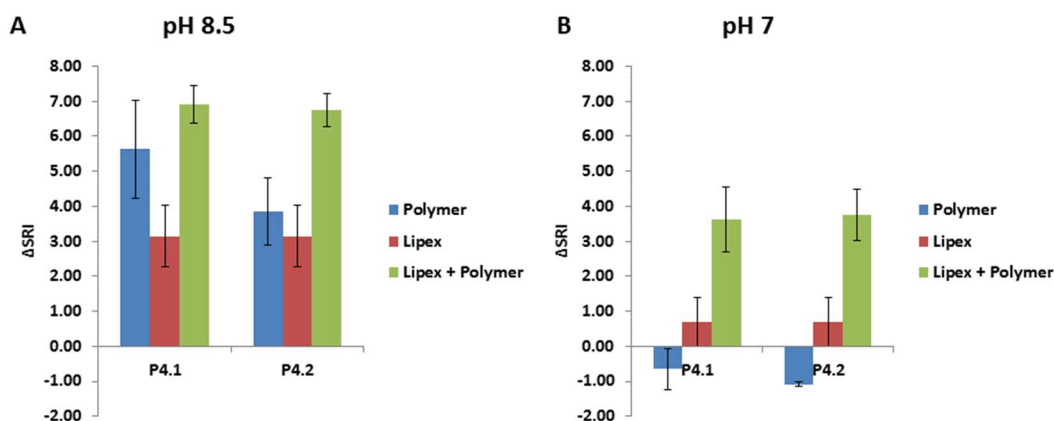
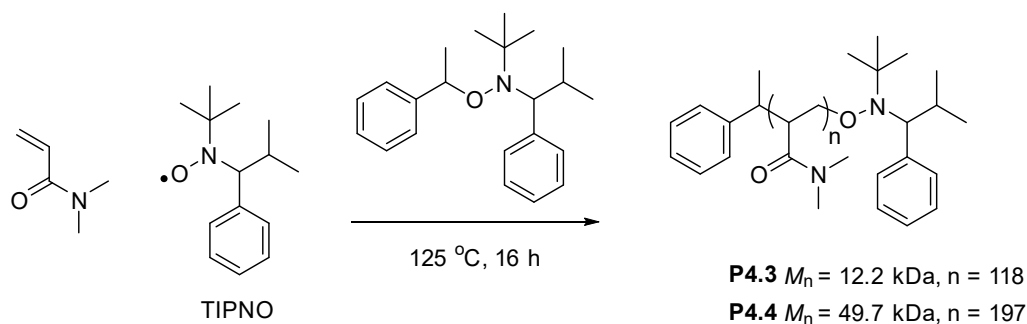


Figure 4.14: Δ SRI at pH 8.5 and pH 7 for P4.1 and P4.2 and Lipex with lard stain.

4.3.2.3 Synthesis of PDMA, **P4.3** and **P4.4**Scheme 4.2: Synthesis of **P4.3** and **P4.4**.

Two water-soluble polymers of different molecular weights were also synthesised to explore (Scheme 4.2) the effects of a hydrophilic polymer and molecular weight on the stain removal. To a dried ampoule the universal initiator **2.5**, the monomer DMA and 2,2,5-Trimethyl-4-phenyl-3-azahexane-3-nitroxide (**2.4**, TIPNO) radical were added. Excess radical was added to account for the persistent radical effect, exerting control over the polymerisation.⁴⁶ The reaction was stirred for 16 h at 125 °C until a conversion of 65% and 80% (**P4.3** and **P4.4**) was achieved to obtain the chosen molecular weight (12 kDa and 50 kDa respectively), at which point the solution was quenched *via* rapid cooling and the polymers were precipitated three times into diethyl ether. The white polymer precipitates were dried under vacuum and analysed utilising ¹H NMR spectroscopy (Figure 4.15) and SEC (Table 4.4). Both polymers **P4.3** and **P4.4** had narrow dispersities ($D_M = 1.17$ and 1.38 respectively) indicating control over the polymerisation, good agreement of the M_n *via* both ¹H NMR spectroscopy and SEC was also demonstrated as shown in (Table 4.4).

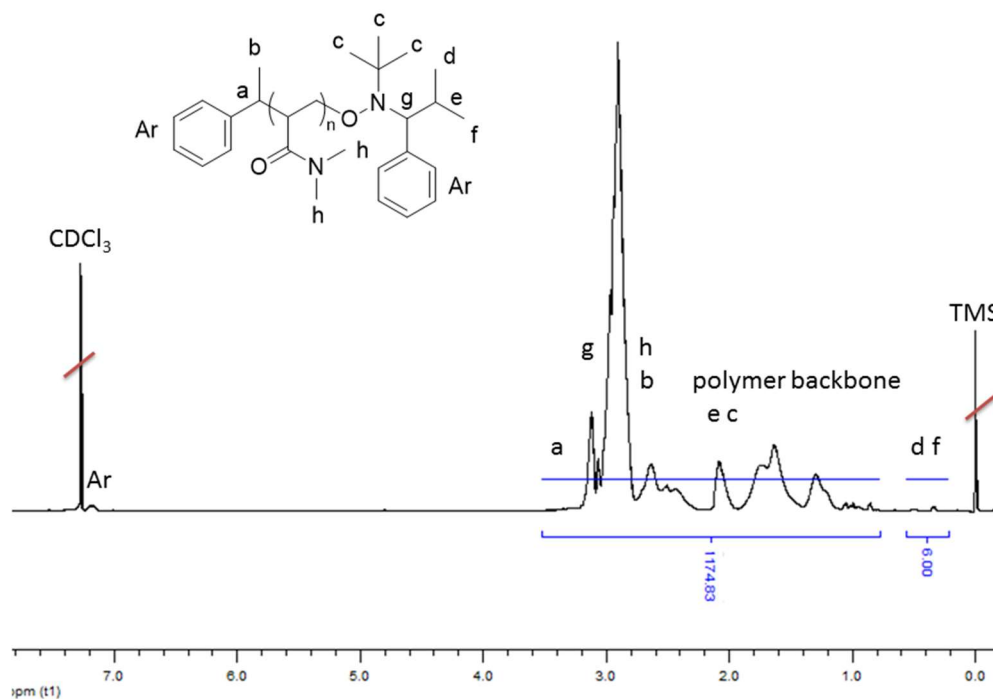


Figure 4.15: Long acquisition ^1H NMR spectrum of P4.3, in CDCl_3 at 400 MHz.

Table 4.4 The properties of polymers P4.3-4.4, ^adetermined by ^1H NMR spectroscopy (400 MHz, CDCl_3), ^bdetermined by SEC (CHCl_3 , PSt standards).

Name	M_n (kDa) ^a	M_n (kDa) ^b	\bar{D}_M ^b
P4.3	12.2	11.1	1.17
P4.4	49.7	33.4	1.38

4.3.2.4 PDMA stain tests

The stain removal efficiency of water-soluble PDMA polymers were screened utilising beef fat and lard stains, following the protocol previously described for **P4.1** and **P4.2**. With the beef fat stains (Figure 4.16) a large difference was observed between the higher and lower molecular weight PDMA. Initially it was apparent that upon the introduction of the higher molecular weight PDMA (**P4.4**) combined with Lipex in solution a significant increase in stain removal is observed at both pH 8.5 and pH7 as shown in Figure 4.16.

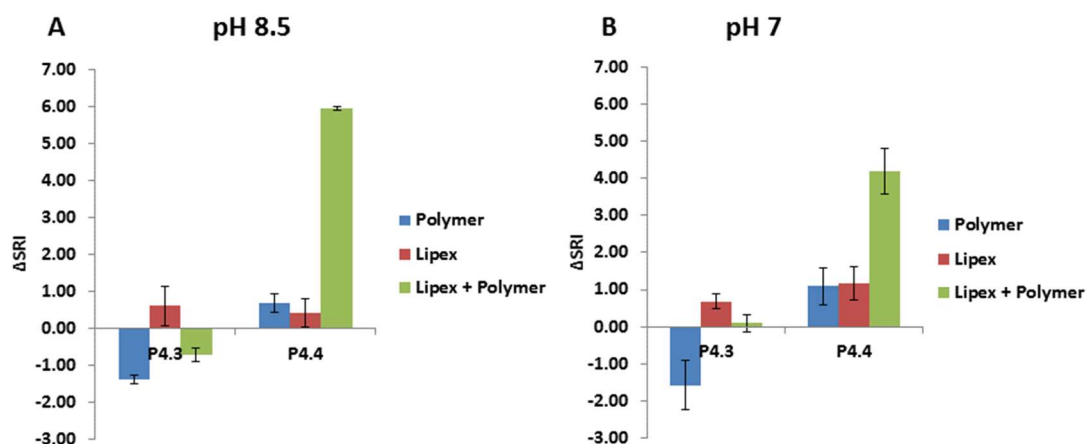


Figure 4.16: Δ SRI at pH 8.5 and pH 7 for P4.3 and P4.4 and Lipex with beef fat stain.

The lard stains (Figure 4.17) showed a lower stain removal with **P4.3** and Lipex than the combined solution of polymer (**P4.3**) and the Lipex, indicating that the lower molecular weight polymer is not cooperatively enhancing the stain removal, with this effect seen at both pH 7 and pH 8.5.

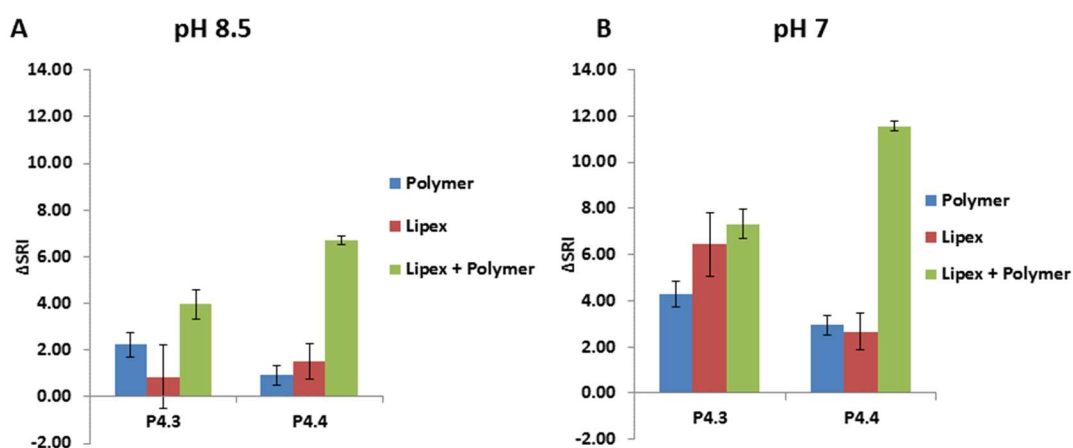


Figure 4.17: Δ SRI at pH 8.5 and pH 7 for P4.3 and P4.4 and Lipex with lard stain.

Initial results showed that increasing the molecular weight of the water-soluble polymers has a positive effect on the Δ SRI (when comparing **P4.3** and **P4.4**) hence these polymers were carried forwards. However, upon repeating a number of these tests, plate-to-plate discrepancies were observed for stain removal with Lipex at the same pH. As a consequence of this, previous test conditions are considered to be void and the new stain test procedure was then adopted. To improve reproducibility of the stain test data, manual high-throughput was utilised with a CyBi[®]-Well 96-channel simultaneous pipettor. A minimum of three plates were run for each set of stain test data with eight repeats on each plate. The stain test was altered to decrease the background SRI observed from the formulation giving more accurate data. This was achieved through increasing the concentration of the Lipex to 10 mg L⁻¹ and decreasing the dose of formulation to 0.8 mg mL⁻¹, with the polymers added in a 10 mol excess to the Lipex. The volume of the solution was decreased from 200 μ L to 150 μ L to prevent the stain from flipping within the solution (ensuring the initial scan correlated to the final scan) and run at 40 °C. It must be noted that only the water-soluble PDMA polymers were taken forward to decrease any effects resulting from re-deposition of insoluble polymers which can affect the stain removal. The data for these polymers is shown in Table 4.5.

Table 4.5: The Δ SRI of P4.3 and P4.4 when compared to a blank standard on stains beef fat and cooking oil with Lipex at pH 8.5.

	Δ SRI Beef Fat	Δ SRI Cooking Oil
Lipex	20.2 \pm 1.2	3.6 \pm 0.7
P4.3	-3.3 \pm 1.0	-1.3 \pm 0.7
P4.3 + Lipex	17.1 \pm 1.2	4.3 \pm 0.7
P4.4	-1.7 \pm 1.3	-1.1 \pm 0.7
P4.4 + Lipex	17.9 \pm 1.8	2.7 \pm 0.8

The largest Δ SRI was seen for Lipex on the beef fat stain. In cooking oil, the presence of **P4.3** with Lipex increased the Δ SRI slightly. With cooking oil and **P4.4** a lower Δ SRI is observed, potentially due to the shielding of the Lipex by the higher molecular weight polymer resulting in a lower Δ SRI. Upon increasing the molecular weight (**P4.4**) similar Δ SRI are seen with beef fat stain, with both decreasing the Δ SRI when combined with Lipex, though these values are still within error of the Δ SRI of Lipex. It has been demonstrated that altering the stain test conditions has significantly increased the Δ SRI for Lipex however the positive effects, of combining with PDMA, previously observed are no longer seen. We attribute this to the position of the polymers on the microtitre plate: previously **P4.4** was positioned in the outer wells; these wells are more susceptible to changes in the surrounding environment hence they are heated much faster, hence in this new method the outer wells are not used.

To determine the effects of scale on these stain tests a larger scale wash study, TERGO testing, utilising a tergotometer was employed. The TERGO tests can be compared to a small scale washing machine. Tested on a 1 L scale, a range of stains

are present (beef fat, lard and cooking oil) in one pot alongside cotton ballasts (cotton fabric with no stain, to ensure a consistent stain to fabric ratio). Cooking oil has a high SRI in the presence of surfactants; therefore a small scale formulation study was carried out prior to the scale up (Figure 4.18) to determine optimal formulation concentrations. A range of Blackbull™ concentrations (0-1.2 mg mL⁻¹) were tested for the stain removal of cooking oil. The greatest Δ SRI for the removal of cooking oil was observed for a formulation concentration of 0.65 mg mL⁻¹. The concentration of formulation used in the TERGO tests was 0.8 mg mL⁻¹, which still gives a relatively good Δ SRI of 11.7 and is compatible with the beef fat and lard stains, indicating good formulation compatibility.

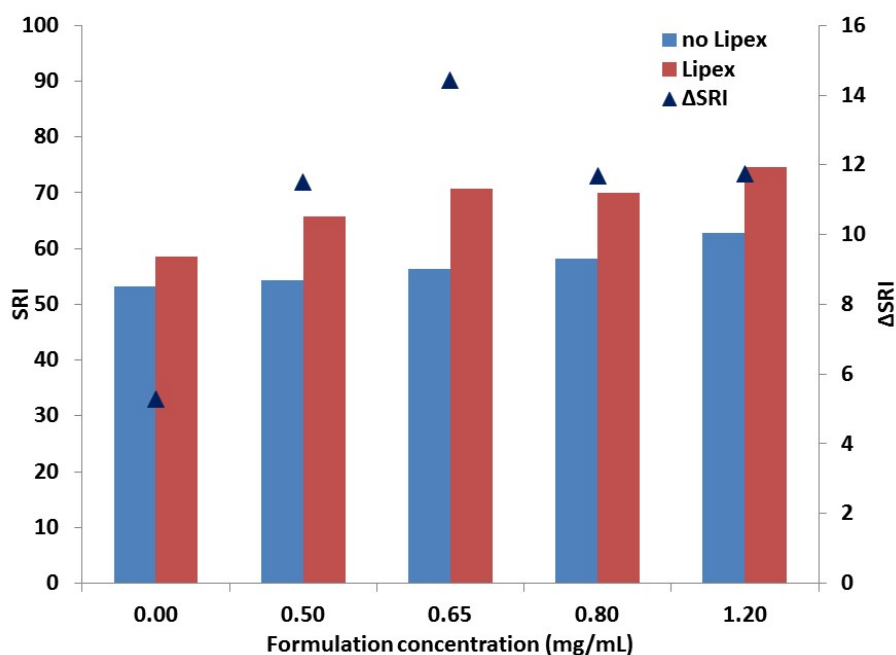


Figure 4.18: Comparison of the SRI observed with cooking oil at 30 °C and 250 rpm with Blackbull formulation (blue) and formulation with Lipex (red) at different concentrations. The calculated Δ SRI for Lipex (triangles).

For the scaled-up study a tergotometer was used, with each stain (beef fat, lard and cooking oil) was repeated five times within the run. The stained fabrics were cut into 7 cm² squares prior to running the study and labelled using a permanent marker. Tests were run at 20 and 40 °C for 1 hour at 100 rpm. Each of the stains was rinsed three times in Prenton water (local tap water with water hardness of 12 FH used as standard) and dried at room temperature overnight. The setup of the study is shown in Figure 4.19.

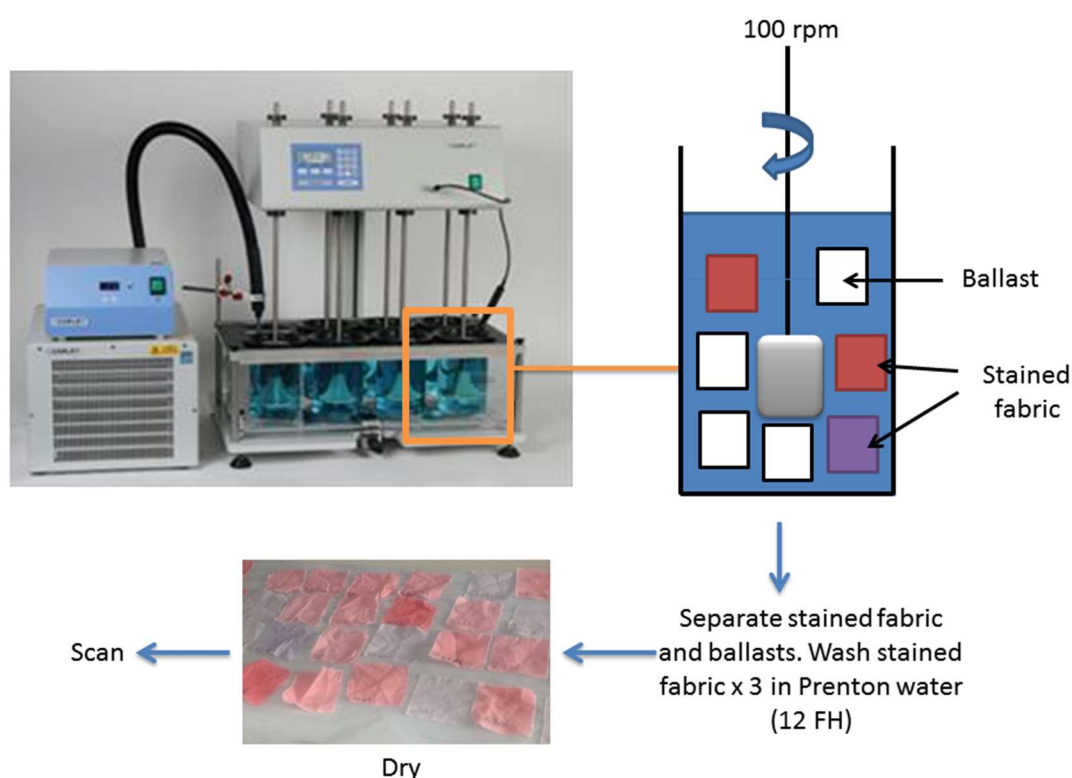


Figure 4.19: Experimental set up for TERGO tests.

The beef fat stain removal data is shown in Table 4.6 . At 20 °C the addition of polymer alone is causing stain removal, likely as a result of the polymers acting as surfactants increasing the stain removal. At 20 °C the stain removal is highest when Lipex and the higher molecular weight PDMA, **P4.4**, were present. Increasing the temperature to 40 °C, the polymers have no effect on the stain removal, attributed to

the higher stain removal seen for the control reaction. At this higher temperature Lipex has a lower Δ SRI again attributed to the increased background stain removal observed for the control reaction.

Table 4.6: The Δ SRI and SRI of P4.3 and P4.4 on beef fat stain with Lipex at pH 8.5, when compared to a white cotton fabric control.

	SRI 20 °C	ΔSRI 20 °C	SRI 40 °C	ΔSRI 40 °C
Control	48.9 \pm 1.8	-	65.7 \pm 0.9	-
Lipex	70.3 \pm 2.1	21.4	73.5 \pm 0.9	7.8
P4.3	54.0 \pm 0.9	5.1	64.0 \pm 2.3	-1.7
Lipex + P4.3	68.7 \pm 0.7	19.8	70.7 \pm 1.3	5.0
P4.4	56.1 \pm 1.5	7.2	64.7 \pm 1.6	-1.0
Lipex + P4.4	72.0 \pm 0.4	23.1	73.0 \pm 1.3	7.3

The Table 4.7 shows the removal of the lard stain at both 20 and 40 °C. Again at 20 °C the presence of **P4.3** with Lipex appears to lower the stain removal compared to Lipex alone. Lipex and Lipex with **P4.4** have similar Δ SRI. Upon increasing the temperature there is no apparent increase in stain removal for Lipex (previous results with beef fat confirm that Lipex is active at 40 °C). This shows that the Lipex is not reacting with lard stain at 40 °C. The presence of the polymers with Lipex at 40 °C has increased stain removal slightly, with **P4.4** showing a larger increase.

Table 4.7: The Δ SRI and SRI of P4.3 and P4.4 on lard stain with Lipex at pH 8.5, when compared to a white cotton fabric control.

		SRI 20 °C	Δ SRI 20 °C	SRI 40 °C	Δ SRI 40 °C
Lard	Control	48.3 \pm 2.0	-	63.5 \pm 1.2	-
	Lipex	63.8 \pm 1.2	15.5	63.7 \pm 0.7	0.2
	P4.3	52.4 \pm 0.7	4.1	66.2 \pm 0.7	2.7
	Lipex + P4.3	61.2 \pm 1.6	12.9	64.7 \pm 1.0	1.2
	P4.4	52.4 \pm 1.0	4.1	65.2 \pm 0.9	1.7
	Lipex + P4.4	65.0 \pm 0.9	16.7	67.1 \pm 1.4	3.6

The final stain analysed was cooking oil, with the Δ SRI results shown in Table 4.8. At 20 °C a similar stain removal for the polymers combined with Lipex and Lipex only is seen. Increasing the temperature has significantly decreased the Δ SRI, notably Lipex with **P4.3** has similar stain removal to **P4.3**.

Table 4.8: The Δ SRI and SRI of P4.3 and P4.4 on cooking oil stain with Lipex at pH 8.5, when compared to a white cotton fabric control.

		SRI 20 °C	Δ SRI 20 °C	SRI 40 °C	Δ SRI 40 °C
Cooking oil	Control	80.2 \pm 0.9	-	88.0 \pm 0.7	-
	Lipex	84.7 \pm 0.6	4.5	90.3 \pm 0.4	2.3
	P4.3	82.7 \pm 0.7	2.5	88.1 \pm 0.8	0.1
	Lipex + P4.3	84.2 \pm 0.4	4.0	88.1 \pm 0.6	0.1
	P4.4	81.6 \pm 0.7	1.4	88.4 \pm 0.4	0.4
	Lipex + P4.4	84.1 \pm 0.5	3.9	90.1 \pm 0.4	2.1

When comparing the small scale studies previously described to the scaled up TERGO studies, the TERGO studies showed an increase in Δ SRI for the free polymers (**P4.3** and **P4.4**) at 20 °C is seen in comparison to Lipex, yet the smaller

scale studies showed no change. We attribute this difference to the longer washing times. Additionally, the fabric content is much higher in the microplate stain tests, the polymer has surfactant like characteristics which may prevent redeposition of the stain onto the fabric during longer washing times. Similarities at the lower temperatures are seen for both Lipex and Lipex with **P4.3** ($M_n = 12.2$ kDa), with the higher molecular weight PDMA (**P4.4**, $M_n = 49.7$ kDa) showing an increase in Δ SRI for both studies. This could be attributed to surfactant effects of the higher molecular weight PDMA in the large scale study. To further study the effects of an increased molecular weight polymer on the stain tests a higher molecular weight PDMA was synthesised.

4.3.2.5 *Synthesis of high molecular weight PDMA*

Given the effects on stain removal seen by increasing the polymer molecular weight in the TERGO studies, a larger molecular weight PDMA was synthesised as previously described, to afford **P4.5** as a white solid. The M_n was determined by ^1H NMR spectroscopy giving a DP of 170 and molecular weight of 171 kDa. SEC (CHCl_3 , PSt calibration) data gave a narrow dispersity of 1.41 with a lower molecular weight than determined by ^1H NMR spectroscopy of $M_n = 136.7$ kDa; this is attributed to the molecular weight of the polymer being out of the limits of the calibration range. A wash study was carried out using this polymer and the small scale stain test (Table 4.9) in a 10 molar excess to the Lipex.

Table 4.9: The Δ SRI of P4.5 with stains beef fat and cooking oil with Lipex at pH 8.5 when compared to a blank standard.

	Δ SRI beef fat	Δ SRI cooking oil
Lipex	17.9 ± 0.6	10.8 ± 1.2
P4.5	0.8 ± 1.1	-1.0 ± 0.8
P4.5 and Lipex	17.0 ± 1.0	7.8 ± 0.7

A much larger decrease in the Δ SRI was observed with the higher molecular weight PDMA. This was attributed to the polymer shielding, and the effect of viscosity of the solution on the microscale generated by the higher molecular weight polymer. It is proposed that this lower SRI is attributed to inaccessibility of the Lipex active site as a consequence of **P4.5**-Lipex interactions. We hypothesise that upon scale-up a larger Δ SRI would be observed for this higher molecular weight polymer.

4.3.3 PDMA Polymers with Lipolase and Lipex

Both Lipolase and Lipex secondary structures were compared in the presence of the polymer solutions **P4.3**, **P4.4** and **P4.5** to determine if any change would be seen. Previously it was hypothesised that PDMA may shield the lipase, reducing stain removal in the small scale wash studies, whereas TERGO tests would show increased Δ SRI. Initially CD spectra were obtained (Figure: 4.20) with **P4.3**, **P4.4** and **P4.5**, which were added in a 10 molar excess to both Lipex and Lipolase.

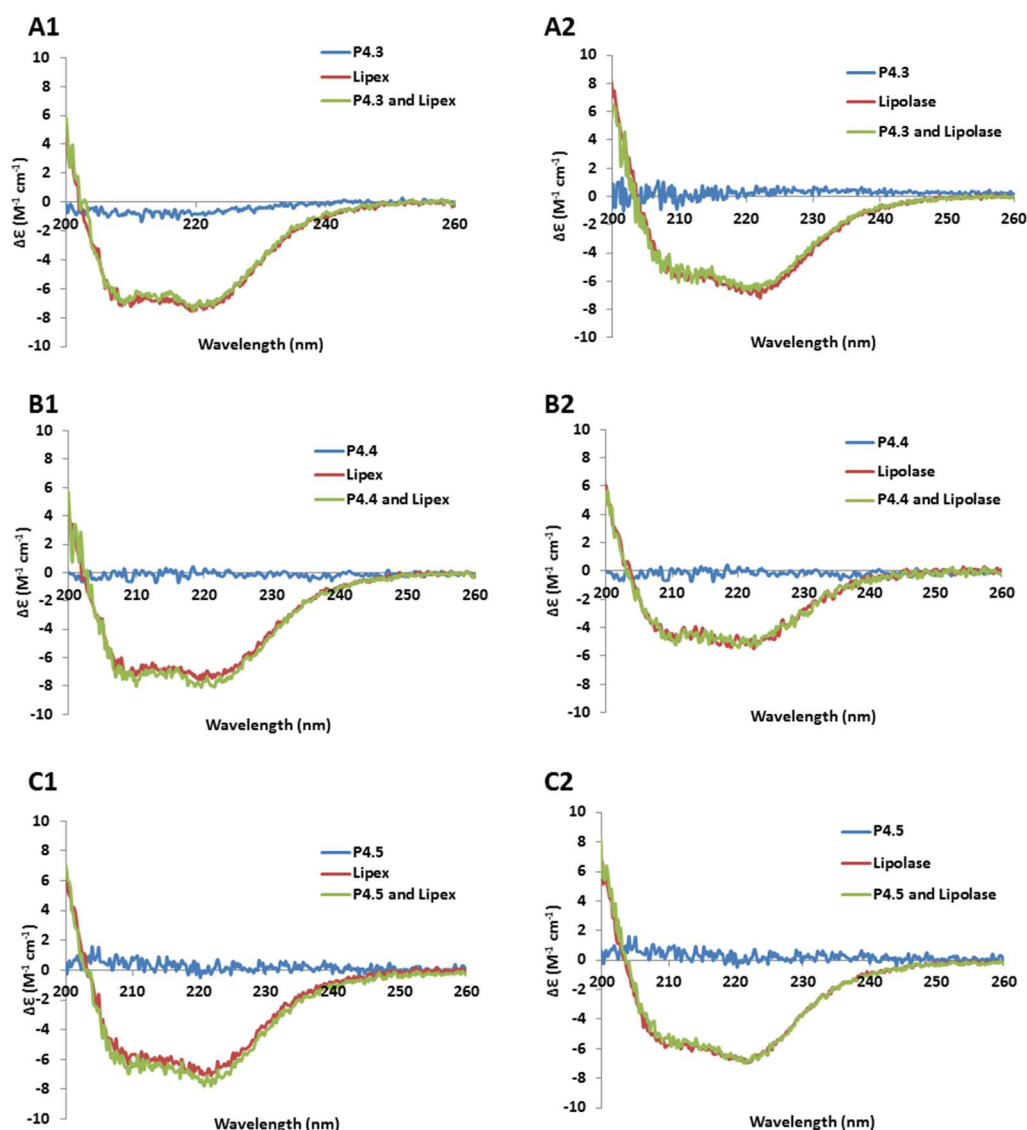


Figure: 4.20 Far-UV CD spectra of P4.3 (A), P4.4 (B), P4.5 (C), Lipex (1) and Lipolase (2) as molar circular dichroism ($\Delta\epsilon$) as a function of wavelength. Run at 20 °C. The spectra were averaged over three runs and three accumulations, buffer was subtracted.

Both lipases showed no change in the presence of these hydrophilic polymers, and are comparable in secondary structure. Two conclusions can be drawn from this data: either (1) the polymer is not interacting with the lipase or (2) the polymer does not affect the secondary structure. Small angle X-ray scattering (SAXS) was used to determine if any change in the globular protein structure of Lipolase is seen in the presence of PDMA (Figure 4.21). Data set A has a much higher concentration of Lipolase (0.6 mg mL^{-1}) in comparison to data set B (0.1 mg mL^{-1}) at the same ratio

of Lipolase ($\times 10$ molar excess). The Guinier-Porod plot shows a good overlap for Lipolase and Lipolase with **P4.4** which indicates the polymer does not disturb the ternary structure of the enzyme. It must be noted that elongated polymer structures are seen for **P4.4**. The plot for Lipolase with **P4.4** shows no difference at medium and high q values, which indicates that Lipolase retains its shape.⁴⁷ The Kratky plots (Iq^2 vs q) demonstrate that no globular structure can be observed for **P4.4** (a linear curve is observed) however in the presence of Lipolase a bell-shaped curve is observed which is characteristic of a globular protein structure. A horizontal asymptote is reached at high q values and the Iq^2 values at the bell-shape curve is symmetrical; indicating that there are almost no unstructured domains.

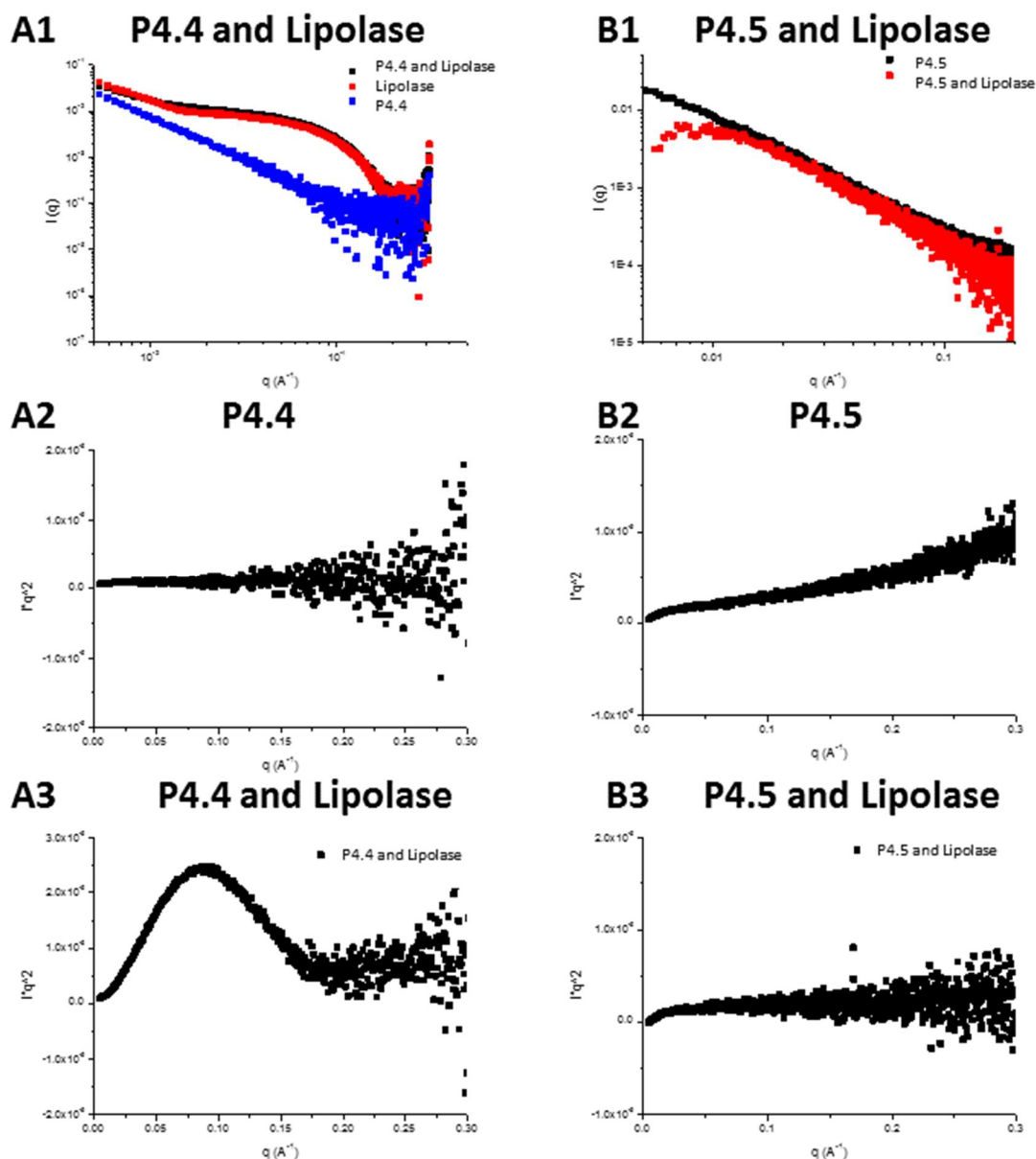


Figure 4.21: Guinier-Porod plots of P4.4 and Lipolase (A1) and P4.5 and Lipolase (B1) of I plotted against q . A Kratky plot of Iq^2 plotted against q for P4.4 (A2) P4.5 (B2) and P4.4 and Lipolase (A3) and P4.457 and Lipolase (B3).

In contrast to this data **P4.5** and Lipolase has a much lower sample concentration and very poor data is observed for lone Lipolase at this concentration due to a low scattering intensity. Again extended polymer structures are seen for **P4.5** alone. Upon the introduction of low concentrations of Lipolase the shape of this curve reveals a change in size at low q values. As only **P4.5** can be detected at these

concentrations this is a good indication that the polymer and Lipolase are interacting within the solution. The curve for the mixture of polymer and Lipolase indicates the presence of a structured assembly in solution, which is more likely to be of spherical shape as the slope of the curve is null at low q values. In the Kratky plot (Figure 4.21 B2), a linear increase is seen for the polymer alone, but upon the introduction of Lipolase discrete changes are observed as the polymer is becoming more globular with less unstructured domains (decrease in the slope of the asymptote at high q values from **P4.5** solution to the solution of **P4.5** and Lipolase).

Interestingly increasing the molecular weight of PDMA has had no effect on the observed CD spectra of Lipolase and Lipex, however upon decreasing the Lipolase concentration SAXS analysis has proven that the Lipolase and PDMA are interacting. The nature of these interactions are discrete due to the non-covalent binding of the polymer, however to rationalise if the action of shielding the protein from external stimuli is maintained over time a stability test is proposed. This would determine if the rate of denaturation of the Lipolase/Lipex can be controlled through the addition of polymer solutions.

Here we have seen that the presence of the homopolymer PDMA has no effect on the secondary structure of the lipases Lipolase and Lipex, although SAXS analysis suggests that PDMA may interact with Lipolase. Due to the insolubility of PSt-*co*-PBzCl in water these polymers were not explored *via* SAXS or CD spectroscopy however promising initial stain test data indicated that the presence of a block copolymer could enhance the stain removal further, hence this will be explored further.

4.3.4 Synthesis of water soluble copolymers

As a result of initial positive effects on stain removal observed in the stain tests for both PSt-*co*-PBzCl and PDMA (in the TERGO studies) a water-soluble copolymer containing PDMA and PBzCl was synthesised. The pendent chlorine was utilised as we could modify this polymer further through the incorporation of the catalyst triazabicyclodec-5-ene (TBD). As discussed previously (Chapter 2) TBD can hydrolyse ester bonds found in fats. Herein we monitor the effects of TBD, when immobilised, on stain removal and the secondary structures of Lipolase and Lipex to explore if lipase and the copolymer, poly(*N,N*-dimethyl acrylamide)-*co*-poly(styrene triazabicyclodec-5-ene) (PDMA-*co*-PStTBD) can work cooperatively in wash formulations and discover if any stabilisation effects are seen.

Initially the copolymer was synthesised by equipping a dried ampoule with BzCl, DMA, and the universal initiator **2.5**. The solution was degassed *via* four freeze pump thaw cycles and placed under a nitrogen atmosphere. The reaction vessel was heated to 125 °C for 6 h to achieve a conversion of 70%. The polymerisation was stopped *via* rapid cooling and precipitated in diethyl ether three times. The white precipitate was then dried under vacuum overnight. This provided **P4.6** which was characterised utilising long acquisition ¹H NMR spectroscopy (Figure 4.22) to give a molecular weight of 11.7 kDa with the SEC data (CHCl₃, PSt calibration) giving a molecular weight of 11.4 kDa with a broad dispersity ($D_M = 1.9$). This high value of dispersity is attributed to a loss of control of the polymerisation with the monomer DMA; introducing the TIPNO radical to the polymerisation will enable good control due to the persistent radical effect.

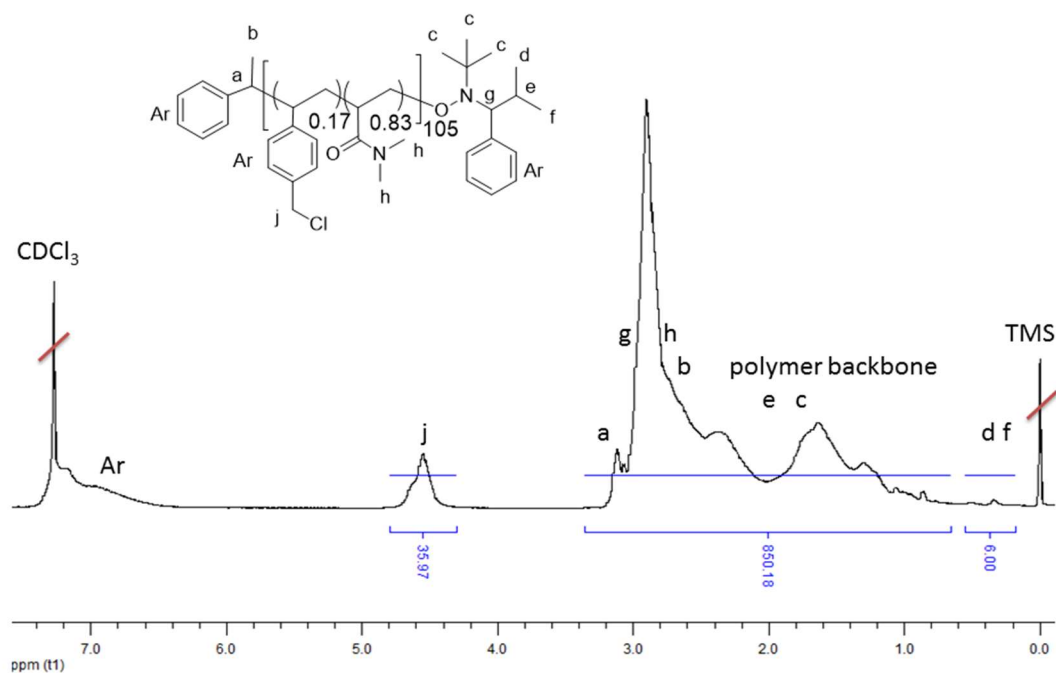
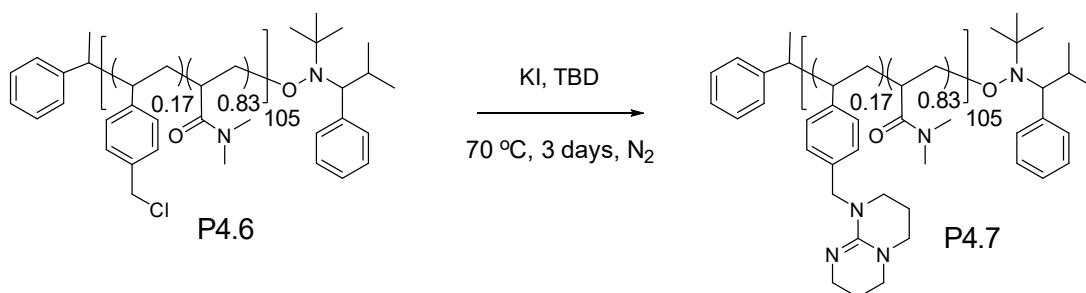


Figure 4.22: Long acquisition ^1H NMR spectrum of P4.6, in CDCl_3 at 400 MHz.



Scheme 4.3: The substitution of TBD onto the polymeric backbone of P4.6 to afford P4.7.

The polymer (**P4.6**) was modified through a post-polymerisation modification (Scheme 4.3): TBD and KI were added to a dried round bottom flask under nitrogen and stirred in dry *N,N*-dimethylformamide (DMF). The polymer **P4.6** was added and the reaction heated to 70 °C for three days. The solvent DMF was subsequently removed under vacuum and the polymer was purified through precipitation into diethyl ether three times. This yielded a yellow solid which was then dried under

vacuum overnight. The resultant polymer **P4.7** was characterised utilising long acquisition ^1H NMR spectroscopy and SEC (Table 4.1). The substitution of TBD was confirmed by the downfield shift in the ^1H NMR spectrum for the methylene group as the TBD substituted the Cl, and appearance of a broad multiplet at 3.0-3.4 ppm. SEC showed an increase in the molecular weight, this is due to the presence of TBD, decreasing the retention time and increasing the molecular weight.

Table 4.10: The properties of the polymers **P4.6** and **4.7**, determined by ^a ^1H NMR spectroscopy, ^bSEC (CHCl_3 , PSt calibration).

Name	% DMA ^a	% St ^a	% loading TBD	M_n (kDa) ^a	M_n (kDa) ^b	\bar{D}_M ^b
P4.6	83	17.0	0	11.7	11.3	1.9
P4.7	83	17.0	17.0	13.6	42.0	1.9

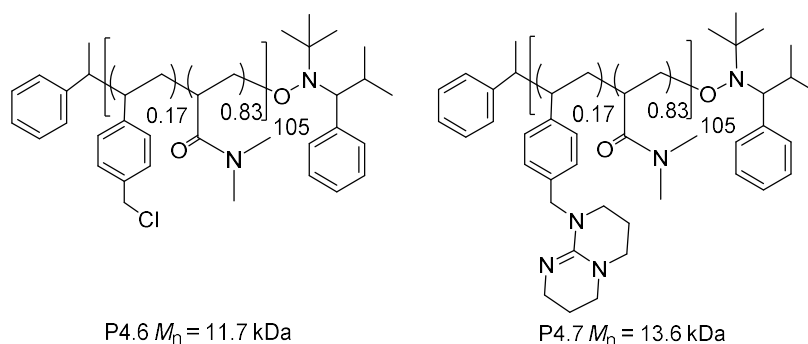


Figure 4.23: Structures of **P4.6** and **P4.7**.

A comparison of the ΔSRI values for **P4.6** and **P4.7** (Figure 4.23) during stain tests with beef fat (Table 4.11) showed a significant decrease in the stain removal especially prevalent in the TBD substituted polymer, indicating that the guanidine functionality had a negative effect on the Lipex. For the cooking oil stain a low ΔSRI was observed, this is due to high stain removal in the control reaction. Here, **P4.6**

and **P4.7** Δ SRI results were within error suggesting no additional stain removal from the TBD catalyst.

Table 4.11: The Δ SRI of P4.6 and P4.7 with Lipex at pH 8.5, when compared to a blank standard on stains beef fat and cooking oil

	Δ SRI Beef Fat	Δ SRI Cooking Oil
Lipex	20.2 \pm 1.2	3.6 \pm 0.7
P4.6	-1.1 \pm 1.0	-1.6 \pm 0.7
P4.6 + Lipex	18.8 \pm 1.2	2.4 \pm 1.3
P4.7	-0.2 \pm 1.8	-1.3 \pm 0.6
P4.7 + Lipex	15.0 \pm 1.0	3.0 \pm 0.9

4.3.5 The effects of immobilised TBD on the structure of Lipolase and Lipex

It is well-documented that guanidine HCl is chaotropic.⁴⁸ This means guanidines can disrupt the order in proteins as they displace water molecules and thus disrupt the complex H-bonding network. To determine the effects of TBD-containing polymers on the secondary structure of lipases, the interactions of polymers **P4.6** and **P4.7** with Lipolase or Lipex were compared by CD spectroscopy and SAXS. As the polymer **P4.6** is the precursor to **P4.7** it was used as a control. From the CD spectra shown in Figure 4.24, both Lipolase and Lipex with **P4.6** have retained similar CD spectra indicating that **P4.6** does not affect the lipases' secondary structure. Upon the introduction of the guanidine functionality onto the polymer backbone, a change in the secondary structure is observed. Both Lipolase and Lipex show an alteration in secondary structure, at 208 nm characteristic of the $\pi \rightarrow \pi^*$ transitions in a α -helix.⁴⁹

This indicates that the immobilised guanidine functionality is interacting with Lipolase and Lipex, changing the secondary structure.

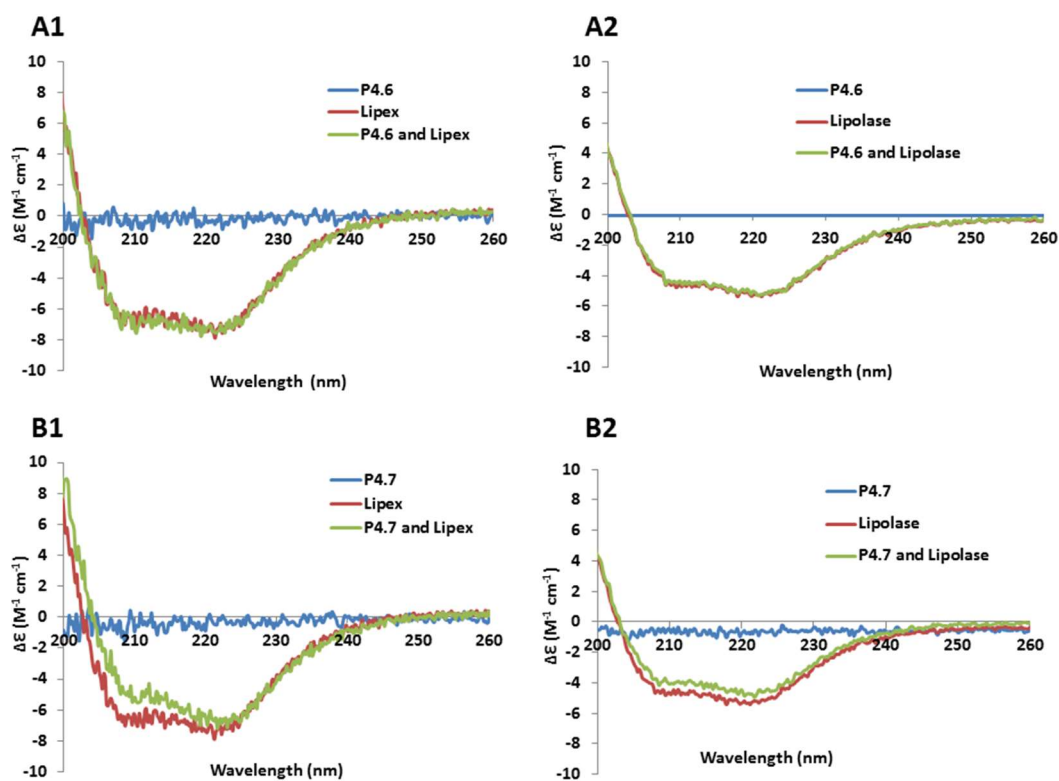


Figure 4.24: Far-UV CD spectra of (A1) P4.6 (no TBD) and Lipex. (A2) P4.6 and Lipolase. (B1) P4.7 (TBD containing polymer) with Lipex. (B2) P4.7 with Lipolase. Plotted as molar circular dichroism ($\Delta\epsilon$) as a function of wavelength. Run at 20 °C. The spectra were averaged over 3 runs and 3 accumulations, buffer was subtracted.

To determine the effects of concentration of **P4.7** on the morphology of Lipolase SAXS analysis was employed. Kratky plots can emphasise a change of shape of different structures. Upon increasing the concentration of **P4.7** from a molar ratio of 50:1 to 2:1 of the Lipolase and **P4.7** respectively, a change in morphology was observed, from a globular structure to a more elongated cylindrical shape. **P4.7** has an elongated morphology in solution; an increase of the concentration of **P4.7** in the enzyme solution leads to a more and more elongated morphology; (Figure 4.25),

indicating a decrease in the globular structure of Lipolase. This supported the observed CD spectroscopy data.

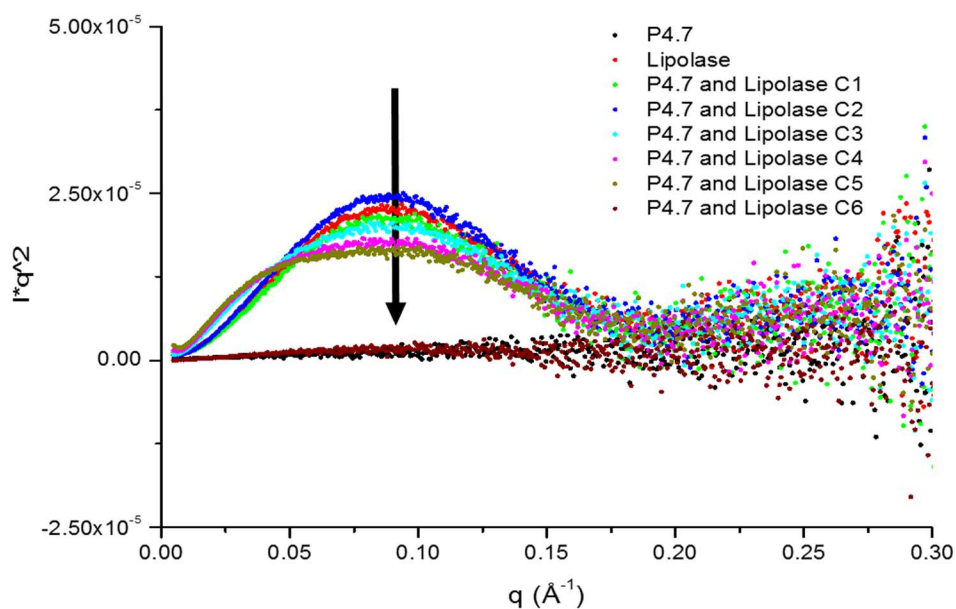


Figure 4.25: Kratky plots of Iq^2 against q for P4.7 and Lipolase at different molar ratios of Lipolase to P4.7 (C1 = 50:1, C2 = 12.5:1, C3 = 4:1, C4 = 3:1, C5 = 2.5:1 and C6 = 2:1)

In addition to this the presence of **P4.7** (a TBD containing polymer) has shown large changes in the secondary structure for Lipolase and Lipex, in comparison to **P4.6** (the pre-polymer) suggesting again that immobilised TBD is detrimental to the stability of the enzyme, hence these TBD functional polymers cannot be used for cooperative hydrolysis within bio-formulations.

4.4 Conclusions

In an attempt to combine the properties of enzymes, polymers, and TBD mixtures of different lipases with polymers were evaluated for their activity. Initially Lipolase and Lipex were compared, Lipex was found to be a more active enzyme than Lipolase, and stain test data and PNP-assays show an improved activity as a result of the genetic modification. This modification has led to small changes in the secondary structure (observed *via* CD spectroscopy). Altering the concentration of surfactants has displayed positive effects on Lipex suggesting the arginine mutations enable positive enzyme-surfactant interactions suggesting Lipex to adopt the “open” active conformation.

Initial polymer screening (PSt-PBzCl and PDMA, of varying molecular weights) showed poor reproducibility. Increasing the enzyme concentration and decreasing the wash volume enabled reproducible data. PDMA, subsequently showed limited enhancement in the stain removal tests. Scaling up this study for TERGO tests showed that lower molecular weight PDMA inhibited the enzymatic activity, this is proposed to be through Polymer-enzyme interactions, inhibiting activity. The presence of Lipolase-PDMA (**P4.5**) interactions have been shown using Kratky plots, as a more globular structure was observed when the polymer was present we propose this is as a consequence of PDMA shielding the lipases from the surrounding environment. The presence of PDMA-lipase interactions opens up further opportunities to explore the stability of lipase within these polymer-protein solutions utilising techniques such as CD spectroscopy SAXS and activity studies. This will be discussed further in the next Chapter.

Immobilisation of guanidine catalysts does not inhibit the chaotropic effects of its small molecule analogue. This was demonstrated by CD spectroscopy were large

changes in the secondary structure were observed with **P4.7**, resembling denaturation of the lipase. This was supported in the stain test studies where a reduction in stain removal is another indication of enzymatic denaturation. It is therefore concluded that the PMA polymers can be mixed with polymers without affecting the secondary structure. Immobilisation of TBD does not inhibit enzyme deactivation hence this polymer cannot be used in synergy with the lipases to improve wash performance. In the next Chapter we will expand on the thermostability of these lipases with PDMA to assess the effects of the PDMA-lipase interactions.

4.5 Materials and Methods

All ^1H NMR spectra were recorded on a Bruker DPX 400 FT-NMR spectrometer using deuterated solvents. The chemical shifts are reported as δ in parts per million. NMR data was analysed using MestRe-C software. Size exclusion chromatography (SEC) analysis was obtained using HPLC grade chloroform (CHCl_3) with 2% triethyl amine (TEA), with a flow rate of 1.0 mL per minute, on two PLgel $5\mu\text{m}$ Mixed-D columns, plus one guard column. The data was analysed using SEC Cirrus software with polystyrene (PSt) standards. Small-angle X-ray scattering (SAXS) measurements were performed on the SAXS/WAXS beamline at the Australian Synchrotron facility at photon energy of 11.0 keV and at Diamond Light Source on the beamline B21 at photon energy of 12.4 keV. All SAXS data was collected by Dr Anaïs Pitto-Barry.

4.5.1 Synthesis of PSt-co-PBzCl

The following procedure is a typical polymerisation *via* NMP. To a dried ampoule, St (5 g, 0.048 mol), BzCl (1.8 g, 0.012 mol) and trimethyl-3-phenylethoxy-4-phenyl-3-azahexane (0.39 g, 1.2 mmol) were added. The ampoule was degassed *via* four freeze pump thaw cycles until a stable vacuum was obtained. The ampoule was then back filled with nitrogen and heated to 125 °C for 3 hours. The polymerisation was stopped by rapid cooling in liquid nitrogen. **P4.1** ^1H NMR (400 MHz, CDCl_3) δ (ppm): 6.2-7.2 ($5\text{H}_{\text{St}} + 4\text{H}_{\text{BzCl}}$, ArH, Ar), 4.4-4.7 (2H_{BzCl} , CH₂, c), 3.2 ($1\text{H}_{\text{end group}}$, CH, e) 2.6-1.5 ($3\text{H}_{\text{backbone}} + 19\text{H}_{\text{end group}}$, CH₂ + CH₃, b, d, f, g). M_n (^1H NMR) = 6.5 kDa, $\text{DP}_{\text{BzCl}} = 10$, $\text{DP}_{\text{St}} = 48$. M_n (SEC, CHCl_3 , PSt calibration) = 5.14 kDa, $D_M = 1.16$. **P4.2** ^1H NMR (400 MHz, CDCl_3) δ (ppm): 6.2-7.2 ($5\text{H}_{\text{St}} + 4\text{H}_{\text{BzCl}}$, ArH), 4.4-4.7

(2H_{BzCl}, CH₂), 2.6-1.5 (3H_{backbone}, CH₂). ¹H NMR spectroscopy gave a conversion of 99%, incorporation of BzCl = 17.6%. *M_n* (SEC, CHCl₃, PSt calibration) = 35.6 kDa, *D_M* = 2.07.

4.5.2 Synthesis of PDMA

The polymers were prepared as described in previous chapters. For instance, the synthesis of **P4.3** was as follows: an ampoule containing a magnetic stirrer bar was dried in the oven. Prior to the addition of the monomers the ampoule was placed under vacuum and back-filled with nitrogen. After the ampoule had cooled the monomer *N,N*-dimethyl acrylamide (10 g, 0.1 mol) was added with *N-tert*-butyl-*N*-(2-methyl-1-phenylpropyl)-*O*-(1-phenylethyl)hydroxylamine (alkoxyamine NMP initiator) (204 mg, 0.63 mmol) and 2,2,5-trimethyl-4-phenyl-3-azahexane-3-nitroxide (TIPNO) (7 mg, 31 μmol). The ampoule was subjected to freeze pump thaw cycles until a stable vacuum was achieved. The ampoule was back-filled with nitrogen and heated at 125 °C. The polymerisation was monitored by ¹H NMR spectroscopy until a conversion of 70% was reached (*ca.* 12 h). The reaction was quenched by rapid cooling in liquid nitrogen, dissolved in THF, and the polymer precipitated three times into 250 mL of diethyl ether. The solid precipitate was filtered and dried in a vacuum oven overnight. **P4.3** ¹H NMR (400 MHz, CDCl₃) δ (ppm): 6.2-7.2 (10H_{end group}, ArH, Ar), 3.2-1.0 (6H_{DMA} + 3H_{backbone} + 14H_{end group}, CH₂ + CH₃, g, h, e, b, c), 0.4-0.2 (6H_{end group}, d, CH₃, d and f). ¹H NMR spectroscopy gave a conversion of 65%. *M_n* (¹H NMR) = 13.1 kDa, DP_{DMA} = 128. *M_n* (SEC, CHCl₃, PSt calibration) = 6.7 kDa, *D_M* = 1.18. **P4.4** ¹H NMR (400 MHz, CDCl₃) δ (ppm): 6.2-7.2 (10H_{end group}, ArH), 3.2-1.0 (6H_{DMA} + 3H_{backbone} + 14H_{end group}, CH₂ + CH₃), 0.4-0.2 (3H_{end group}, d, CH₃). ¹H NMR spectroscopy gave a conversion of 65%.

M_n (^1H NMR) = 49.7 kDa, $\text{DP}_{\text{DMA}} = 498$. M_n (SEC, CHCl_3 , PSt calibration) = 33.4 kDa, $\mathcal{D}_M = 1.38$. **P4.5** ^1H NMR (400 MHz, CDCl_3) δ (ppm): 6.2-7.2 ($10\text{H}_{\text{end group}}$, ArH), 3.2-1.0 ($6\text{H}_{\text{DMA}} + 3\text{H}_{\text{backbone}} + 14\text{H}_{\text{end group}}$, $\text{CH}_2 + \text{CH}_3$), 0.4-0.2 ($3\text{H}_{\text{end group}}$, d , CH_3). ^1H NMR spectroscopy gave a conversion of 65%. M_n (^1H NMR) = 171 kDa, $\text{DP}_{\text{DMA}} = 1700$. M_n (SEC, CHCl_3 , PSt calibration) = 136.6 kDa, $\mathcal{D}_M = 1.41$.

4.5.3 Synthesis of P4.6

The following procedure is a typical polymerisation *via* NMP. To a dried ampoule, BzCl (0.4 g, 0.0025 mol), and DMA (1 g, 0.01 mol), trimethyl-3-phenylethoxy-4-phenyl-3-azahexane (0.04 g, 0.00013 mol) were added. The ampoule was degassed *via* four freeze pump thaw cycles until a stable vacuum was obtained. The ampoule was then back-filled with nitrogen and heated to 125 °C for 3 hours. The polymerisation was stopped by rapid cooling in liquid nitrogen. ^1H NMR (400 MHz, CDCl_3) δ (ppm): 7.2-6.2 (4H_{BzCl} , ArH , Ar), 4.7-4.4 (2H_{BzCl} , CH_2 , j), 3.2-1.0 ($6\text{H}_{\text{DMA}} + 3\text{H}_{\text{backbone}} + 14\text{H}_{\text{end group}}$, $\text{CH}_2 + \text{CH}_3$, g , b , h , e , c), 0.6-0.2 ($6\text{H}_{\text{end group}}$, d , CH_3 , d and f). ^1H NMR spectroscopy gave a conversion of 65%. M_n (^1H NMR) = 11.7 kDa, $\text{DP}_{\text{BzCl}} = 18$, $\text{DP}_{\text{DMA}} = 87$. M_n (SEC, CHCl_3 , PSt calibration) = 11.4 kDa, $\mathcal{D}_M = 1.9$.

4.5.4 Synthesis of P4.7

TBD (0.20 g, 1.5×10^{-3} mol), KI (4.3 mg, 2.6×10^{-5} mol) and dry DMF (5 mL) were added to a dried round bottom flask (RBF) with a magnetic stirrer bar under nitrogen. The polymer (0.5 g, 5.0×10^{-5} mol) was dissolved in dry DMF (5 mL) before being added to the RBF under nitrogen. The RBF was placed in a pre-heated oil bath at 70 °C for 60 hours. The polymer was dialysed extensively against

18.2 M Ω cm water and freeze dried. Yield: 66.5%. ^1H NMR (400 MHz, CDCl_3) δ (ppm): 7.2-6.2 (4H $_{\text{BzCl}}$, ArH, Ar), 4.8-4.5 (2H $_{\text{BzCl}}$, CH $_2$, j), 3.4-1.0 (12H $_{\text{TBD}}$ + 6H $_{\text{DMA}}$ + 3H $_{\text{backbone}}$ + 14H $_{\text{end group}}$, CH $_2$ + CH $_3$, i, g, b, h, e, k, c), 0.6-0.2 (6H $_{\text{end group}}$, d, CH $_3$, d and f). ^1H NMR spectroscopy gave a conversion of 65%. M_n (^1H NMR) = 13.6 kDa, DP_{BzTBD} = 18, DP_{DMA} = 87. M_n (SEC, CHCl_3 , PSt calibration) = 42.2 kDa, D_M = 1.9.

4.5.5 Assays

Fresh stock of PNP-caprylate substrate was prepared in methanol (21 mg, 8 mM) and then subsequently diluted in pH 4 water at several concentrations to give a x 10 stock concentration (1000, 750, 500, 400, 300, 200, 100 and 0 μM). Concentrated stock solutions (10 x) were prepared of Lipex and Lipolase (1 ng mL^{-1}). Tris-HCl buffer (100 μL , 50 mM, pH 8.5) was added to a 96 well plate with 60 μL of 18.2 M Ω cm water, 20 μL of the enzyme stock was added and the solution was equilibrated at 25 $^\circ\text{C}$ for 5 minutes. Finally the PNP-caprylate (10 x) stock solutions were added (20 μL) to give a total well volume of 200 μL . The absorbance was monitored at 405 nm during 1 hour.

4.5.6 Stain Tests

The following procedure is a general procedure for stain testing. To a plate preloaded with the stained fabric, 75 μL of 50 mM buffer solution, 0.8 mg mL^{-1} of BlackbullTM formulation was added with 12 French Hard (FH) (2:1 Ca:Mg) water, and 10 mg L^{-1} Lipex (3.5×10^{-6} mmol) was added along with a 10 fold excess of polymer (3.5×10^{-5} mmol). The total volume was made up with water to 150 μL . A control test was carried out omitting polymer or Lipex. The plates were shaken at 250 rpm

for 30 minutes at 30 °C. The wells are then washed three times with 12 FH water (2:1, Ca:Mg), with a 30 second shake between each wash. The stained fabric was left to dry overnight and scanned using a flatbed scanner.

4.5.7 Tergo Tests

The following procedure is a general procedure for TERGO testing. All of the stained fabrics were cut to a size of 7 cm × 7 cm and pre-scanned and labelled using a black permanent marker pen. To a Tergotometer, 0.9 L of 12 FH water (2:1 Ca:Mg) was added with 0.8 mg mL⁻¹ Blackbull™ formulation, 10 mg L⁻¹ Lipex (3.5 × 10⁻⁶ mmol) with a 10 fold excess of polymer (3.5 × 10⁻⁵ mmol). The solution was made up to a total volume of 2 L and stirred; the solutions were incubated for 10 minutes at 40 °C. The cotton ballasts were separated and added with the stains (× 5 beef fat, × 5 lard and × 5 cooking oil). The solutions were stirred at 100 rpm for 1 hour. After the run the stained fabrics were separated and washed using Prenton water for 15 minutes. Excess water was removed and the stained fabrics were then air dried overnight. Finally the dried stains were analysed using a flatbed scanner.

4.5.8 Circular Dichroism

Circular Dichroism spectroscopy was used to compare the secondary structure of Lipolase (0.05 mg mL⁻¹) and Lipex (0.1 mg mL⁻¹) in the presence of polymer solutions (10 molar excess) after incubation for 10 minutes. All spectra were recorded on a J-720 CD spectrometer (Jasco). All spectra were recorded in 1 mM Tris-HCl buffer (pH 8.5) using a quartz cuvette with a path length of 0.1 cm. All solutions were run three times with three acquisitions and recorded at 20 nm min⁻¹.

These samples were averaged and the background subtracted and normalised to give $\Delta\epsilon$. The CD spectra was further analysed using the online platform DICHROWEB <http://dichroweb.cryst.bbk.ac.uk/html/home.shtml>.²⁸ The data was compared using the CONTIN/LL algorithm and reference set 7 at 190-260 nm.³⁰

4.5.9 SAXS

The samples in solution were run using 1.5 mm diameter quartz capillaries. Capillaries were held in a sample holder with temperature control achieved *via* a water bath. Samples were allowed to equilibrate once at temperature for 10 minutes. The measurements were collected at a sample to detector distance of 3.41 m or 3.34 m to give a q range of 0.005 to 0.3 \AA^{-1} , where q is the scattering vector and is related to the scattering angle (2θ) and the photon wavelength (λ) by the following equation:

$$q = \frac{4\pi\sin(\theta)}{\lambda}$$

All patterns were normalised to fixed transmitted flux using a quantitative beam stop detector. The scattering from a blank was measured in the same location as sample collection and was subtracted for each measurement. The two-dimensional SAXS images were converted into one-dimensional SAXS profiles ($I(q)$ versus q) by circular averaging, where $I(q)$ is the scattering intensity. The functions used for the fitting from the NIST SANS analysis package where “Guinier-Porod”, “Debye”, and “Polydisperse Core with Constant Shell Thickness” models.⁵⁰⁻⁵³ ScatterBrain and Igor software were used to plot and analyse data.^{54, 55} The scattering length density of the solvent, polymer, and enzyme were calculated using the “Scattering Length Density Calculator” provided by NIST Center for Neutron Research.⁵⁶ A Kratky

linear fit was also applied to gain more information on the samples.⁵⁷ All SAXS data was collected and fitted by Dr Anaïs Pitto-Barry.

4.6 References

1. B. A. Cameron, *Fam. Consum. Sci. Res. J.*, 2007, **36**, 151-162.
2. E. Smulders, W. Rähse, W. von Rybinski, J. Steber, E. Sung and F. Wiebel, in *Laundry Detergents*, Wiley-VCH Verlag GmbH & Co. KGaA, 2003, DOI: 10.1002/3527600450.ch1, pp. 1-6.
3. C. Edser, *Focus Surfactants*, 2012, **2012**, 1-2.
4. C. Edser, *Focus Surfactants*, 2007, **2007**, 1-2.
5. Novozymes, *Focus Surfactants*, 2005, **2005**, 4.
6. M. R. Stoner, D. A. Dale, P. J. Gualfetti, T. Becker, M. C. Manning, J. F. Carpenter and T. W. Randolph, *Enzyme Microb. Technol.*, 2004, **34**, 114-125.
7. Jan H. Van Ee, O. Misset and E. J. Baas, *Enzymes in detergency*, Marcel Dekker, New York, 1997.
8. R. Sharma, Y. Chisti and U. C. Banerjee, *Biotechnol. Adv.*, 2001, **19**, 627-662.
9. Y.-Y. Zheng, X.-H. Guo, N.-N. Song and D.-C. Li, *J. Mol. Catal. B: Enzym.*, 2011, **69**, 127-132.
10. A. Salis, M. Monduzzi and V. Solinas, in *Industrial Enzymes*, Springer Netherlands, 2007.
11. G. D. Haki and S. K. Rakshit, *Bioresour. Technol.*, 2003, **89**, 17-34.
12. F. Hasan, A. A. Shah, S. Javed and A. Hameed, *Afr. J. Biotechnol.*, 2010, **9**, 4836-4844.
13. R. D. Schmid and R. Verger, *Angew. Chem. Int. Ed.*, 1998, **37**, 1608-1633.

14. M. Schmidt and U. T. Bornscheuer, *Biomol. Eng.*, 2005, **22**, 51-56.
15. K.-E. Jaeger and T. Eggert, *Curr. Opin. Biotechnol.*, 2002, **13**, 390-397.
16. R. Fernandez-Lafuente, *J. Mol. Catal. B: Enzym.*, 2010, **62**, 197-212.
17. M. Nardini and B. W. Dijkstra, *Curr. Opin. Struct. Biol.*, 1999, **9**, 732-737.
18. A. Jutila, K. Zhu, S. A. Patkar, J. Vind, A. Svendsen and P. K. J. Kinnunen, *Biophys. J.*, 2000, **78**, 1634-1642.
19. L. Brady, A. M. Brzozowski, Z. S. Derewenda, E. Dodson, G. Dodson, S. Tolley, J. P. Turkenburg, L. Christiansen, B. Huge-Jensen, L. Norskov, L. Thim and U. Menge, *Nature*, 1990, **343**, 767-770.
20. Y. Cajal, A. Svendsen, V. Girona, S. A. Patkar and M. A. Alsina, *Biochemistry*, 1999, **39**, 413-423.
21. L. Schrodinger, *Journal*, 2010.
22. U. Derewenda, L. Swenson, Y. Wei, R. Green, P. M. Kobos, R. Joerger, M. J. Haas and Z. S. Derewenda, *J. Lipid Res.*, 1994, **35**, 524-534.
23. A. M. Brzozowski, H. Savage, C. S. Verma, J. P. Turkenburg, D. M. Lawson, A. Svendsen and S. Patkar, *Biochemistry*, 2000, **39**, 15071-15082.
24. J. Skjold-Jørgensen, J. Vind, A. Svendsen and M. J. Bjerrum, *Biochemistry*, 2014, **53**, 4152-4160.
25. I. G. Clausen, E. Gormsen, S. A. Patkar and A. Svendsen, 1992, **WO1992005249 A1**.
26. J. Kyte and R. F. Doolittle, *J. Mol. Biol.*, 1982, **157**, 105-132.

27. S. M. Kelly, T. J. Jess and N. C. Price, *Biochim. Biophys. Acta*, 2005, **1751**, 119-139.
28. L. Whitmore and B. A. Wallace, *Nucleic Acids Res.*, 2004, **32**, W668-W673.
29. N. Sreerama, S. Y. U. Venyaminov and R. W. Woody, *Protein Sci.*, 1999, **8**, 370-380.
30. N. Sreerama and R. W. Woody, *Anal. Biochem.*, 2000, **287**, 252-260.
31. R. Gupta, P. Rathi, N. Gupta and S. Bradoo, *Biotechnol. Appl. Biochem.*, 2003, **37**, 63-71.
32. E. J. Wood, *Biochemical Education*, 1982, **10**, 76-77.
33. P. C. Engel, *Enzyme kinetics : the steady-state approach*, Chapman and Hall ; New York, NY : Chapman and Hall in association with Methuen, London ; New York, 2nd ed edn., 1981.
34. J. Ahmed, U. S. Shivhare and P. Singh, *Food Chem.*, 2004, **84**, 605-611.
35. M. Maskan, *J. Food Eng.*, 2001, **48**, 169-175.
36. D. Otzen, *Colloids Surf., B.*, 2008, **64**, 223-228.
37. G. Fernandez-Lorente, J. M. Palomo, Z. Cabrera, R. Fernandez-Lafuente and J. M. Guisán, *Biotechnol. Bioeng.*, 2007, **97**, 242-250.
38. H. Li, M. Li, X. Yu, A. P. Bapat and B. S. Sumerlin, *Polym. Chem.*, 2011, **2**, 1531-1535.
39. H. Li, A. P. Bapat, M. Li and B. S. Sumerlin, *Polym. Chem.*, 2011, **2**, 323-327.

40. Z. P. Tolstyka and H. D. Maynard, *9.17: Protein–Polymer Conjugates*, Elsevier, Amsterdam, 2012.
41. H. Murata, C. S. Cummings, R. R. Koepsel and A. J. Russell, *Biomacromolecules*, 2014, **15**, 2817-2823.
42. J. Lee, E.-W. Lin, U. Y. Lau, J. L. Hedrick, E. Bat and H. D. Maynard, *Biomacromolecules*, 2013, **14**, 2561-2569.
43. O. Dahimi, M. S. Hassan, A. A. Rahimm, S. M. Abdulkarim and S. M. A., *J. Food Pharm. Sci.*, 2014, **2**, 27-31.
44. O. Dahimi, A. A. Rahim, S. M. Abdulkarim, M. S. Hassan, S. B. T. Z. Hashari, A. Siti Mashitoh and S. Saadi, *Food Chem.*, 2014, **158**, 132-138.
45. A. C. Rustan and C. A. Drevon, in *eLS*, John Wiley & Sons, Ltd, 2001, DOI: 10.1038/npg.els.0003894.
46. H. Fischer, *Macromolecules*, 1997, **30**, 5666-5672.
47. L. L. Hyland, M. B. Taraban and Y. B. Yu, *Soft Matter*, 2013, **9**, 10218-10228.
48. R. C. Rodrigues, J. M. Bolivar, G. Volpato, M. Filice, C. Godoy, R. Fernandez-Lafuente and J. M. Guisan, *J. Biotechnol.*, 2009, **144**, 113-119.
49. L. Whitmore and B. A. Wallace, *Biopolymers*, 2008, **89**, 392-400.
50. A. Guinier and G. Fournet, *Small-angle scattering of X-rays*, Wiley, New York, first edn., 1955.
51. O. Glatter and O. Kratky, *Small angle x-ray scattering*, Academic Press, London, First edn., 1982.

-
52. R. J. Roe, *Methods of X-ray and neutron scattering in polymer science*, Oxford University Press, New York, first edn., 2000.
53. P. Bartlett and R. H. Ottewill, *J. Chem. Phys.*, 1992, **96**, 3306-3318.
54. S. T. Mudie, *Journal*, 2013.
55. S. Kline, *J. Appl. Crystallogr.*, 2006, **39**, 895-900.
56. A. Munter, NIST SLD calculator, <http://www.ncnr.nist.gov/resources/sldcalc.html>, 2014).
57. B. Hammouda, *Probing Nanoscale Structures - The SANS Toolbox*, National Institute of Standards and Technology-Center for Neutron Research, 2010.

5 Stabilisation of Lipases from *Thermomyces lanuginosus*, in Polymer Solutions

5.1 Abstract

Proteins undergo conformational changes upon heating which can be monitored to identify changes in thermostability. Herein we explore the melting temperatures of the thermophilic lipases Lipolase and Lipex. The stability of these proteins was monitored both before and after heating and the results were compared to that of the lipases in the presence of a water-soluble polymer additive. It was observed that an increased thermostability was obtained upon introducing a higher molecular weight polymer through shielding of the enzyme from the surrounding environment.

5.2 Introduction

5.2.1 Mechanism of protein folding and stability

Much research has focused on the mechanism of protein folding. According to Levinthal's paradox, which is a simplified model on protein folding, if a protein was to adopt all conformations it could take up to 10^{77} years to form the native state.^{1, 2} The native structure of an enzyme is particularly important as they specifically fold creating specific active sites. The native protein structure is frequently found when the free enthalpy is at its lowest, hence the enzyme is in its most stable configuration.^{3, 4} Proteins are able to fold into a specific conformation in seconds as a consequence of local interactions which serve as nucleation points.⁵ The driving force behind the folding pathway is namely the release of water molecules, which increases the entropy and thus decreases the free energy of the system, known as nucleation-condensation.⁵ Intramolecular hydrogen bonding, Van der Waals forces and electrostatic interactions further contribute to the stabilisation of the folded conformation and this further contributes to a lowering the enthalpy.³ Cysteine

residues can also play an important part in the stabilisation of the tertiary structure of proteins through the formation of disulfide bridges.⁶

Enzymes have been genetically engineered by Nature over time to accelerate the rate of reaction of particular substrates in a specific environment and are hence often called biocatalysts. One of the main disadvantages of utilising these biocatalysts is their tendency to denature when not within this specific environment. The net stability of an enzyme can be explored by determining the difference in free energy between the unfolded and the folded native state. Circular dichroism (CD) spectroscopy can be used to measure thermodynamic stability, otherwise known as an enzyme's thermal tolerance.⁷ The ellipticity of a protein's secondary structure can steadily change upon heating as the secondary structure is lost and the protein becomes unfolded. As protein folding is not primarily influenced by covalent bonding, the native state stability of an enzyme can be described as a two state model, where a protein is in equilibrium between its folded and unfolded state (depicted in Figure 5.1).

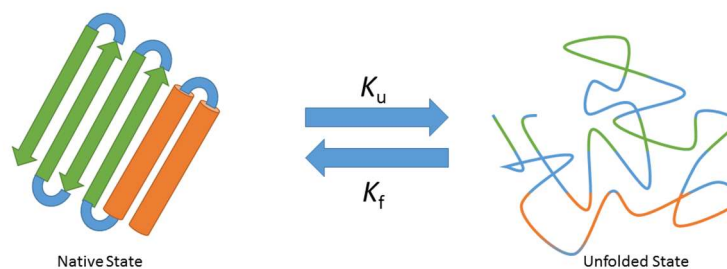


Figure 5.1: A schematic of the equilibrium of a protein in its native and unfolded state, where K_u is the rate of unfolding and K_f is the rate of folding.

The melting temperature (T_m) can be calculated from a thermal unfolding curve, using CD spectroscopy, where T_m is defined as the temperature at which the fractions of folded and unfolded protein are equal to 0.5 (Figure 5.2).^{6, 7} For the lipases Lipex and Lipolase, a strong signal representative of an α -helix occurs at 222 nm in their CD spectra. By monitoring the increase in this signal it is possible to obtain a melting curve. From this signal, the fraction of protein folding can be obtained using Equation 5.1, which allows for the T_m to be determined in the presence of various conditions and additives such as polymer solutions.

Equation 5.1: Calculating the fraction unfolding (f_u) using ellipticity (θ) obtained *via* CD spectroscopy at 222 nm.

$$f_u = \frac{\theta_f - \theta_{220}}{\theta_f - \theta_u}$$

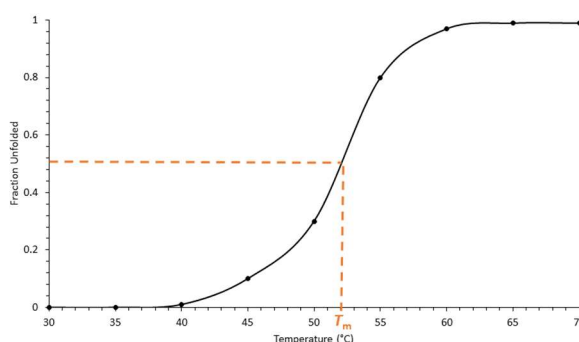


Figure 5.2: Thermal unfolding curve obtained *via* CD spectroscopy.

When proteins are in equilibrium between their folded and unfolded state, the unfolded equilibrium constant (K_u) can be used to calculate the free energy of unfolding (ΔG_{N-U} , Equation 5.2).⁸⁻¹⁰

Equation 5.2: Calculation of the Gibbs free energy for a protein from the folded (native) to the unfolded state.

$$\Delta G_{N-U} = -RT \ln \frac{[U]}{[F]} = -RT \ln K_u$$

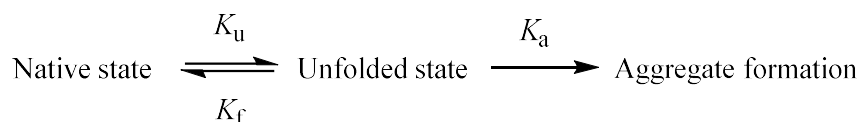
$$K_u = \frac{[U]}{[F]}$$

5.2.2 Protein unfolding

The action of unfolding upon denaturation is a less studied mechanism. Although unfolding of the proteins secondary structures can be monitored, the chemistry behind these pathways has not been widely investigated.^{11, 12} Proteins can unfold due to many environmental factors such as temperature, pH, salt concentration and the introduction of chemical modifiers.¹³⁻¹⁵ The optimised temperature at which an enzyme operates is close to its unfolding temperature. It is hypothesised that this is due to the flexibility of the protein; as more thermophilic proteins have more rigid structures (preventing denaturation) a higher flexibility is necessary to maintain a lower activation energy and allows for diffusion of substrates into the active site.¹⁶

Initial protein unfolding is reversible, however upon prolonged exposure to extreme denaturing conditions (such as high temperatures) irreversible deactivation of the enzyme can occur.^{17, 18} When exposed to higher temperatures (>80 °C) it has been found that asparagine and aspartic acid residues can be chemically modified to form both L- and D-aspartate residues *via* a succinimide intermediate. This process is known to occur at high temperatures when the pH is greater than five due to the presence of hydroxide ions within the solution.¹⁸ L-aspartate also provides a pathway for deamidation *via* the irreversible cleavage of the amide bond at elevated temperatures breaking the primary structure of the protein sequence.¹⁸

Aggregation of proteins into the non-native form can be triggered by many external factors and is problematic as it is an irreversible process. It is well-known that thermal degradation can lead to the onset of irreversible aggregates formation, a process controlled by both conformational and colloidal stability.¹⁵ When a protein unfolds from the native state the hydrophobic regions become exposed, giving rise to aggregate formation through protein-protein interactions of these hydrophobic sites. This aggregation follows the Lumry-Eyring framework in which the initial unfolding is reversible, yet further unfolding of the species results in aggregates which can further associate with other proteins forming a cluster of aggregates (Scheme 5.1).¹⁹



Scheme 5.1: Lumry-Eyring framework describing protein aggregation/inactivation where K_a is the rate of aggregation.

Therefore, through monitoring the thermostability and activity of the lipases, it is possible to determine if any additional stability is afforded to the enzymes when in solution with water-soluble polymers.

5.3 Results and discussion

5.3.1 Lipolase and Lipex temperature stability

In Chapter 4 we compared the structure and activity of two lipases Lipolase and Lipex. These lipases (genetic mutations of *Thermomyces lanuginosus* (TLL)) were found to possess relatively similar structures. To determine the differences in thermal stability CD spectroscopy was again utilised to monitor changes in the secondary structures upon heating. Both Lipolase (0.05 mg mL⁻¹) and Lipex (0.1 mg mL⁻¹) were dissolved in Tris-HCl buffer (pH 8.5, 5 mM) and heated from 10 °C to 80 °C at a rate of 10 °C h⁻¹. The CD spectrum was recorded at 5 °C intervals with three accumulations at a rate of 20 nm min⁻¹. The solution was subsequently incubated at 80 °C for 7 hours and then cooled to 20 °C (1 °C min⁻¹). The solution was then equilibrated at 20 °C for 30 minutes prior to running a final CD spectrum.

By comparing the secondary structures of Lipolase and Lipex after a heating and cooling cycle (Figure 5.3 A1 and B1) a much larger shift is seen in the spectrum of Lipex (B1) in comparison to Lipolase (A1), indicating that Lipex does not refold into its native state after exposure to higher temperatures. A steady increase in $\Delta\epsilon_{222}$ was observed for Lipolase until the temperature reached 60 °C, at which a change in gradient is observed until a plateau is reached at 75 °C (Figure 5.3 A2).¹² This deformation of the Lipolase secondary structure within this temperature range is similar to the melting temperature for TLL (wild-type lipase) which is 72 °C.²⁰ Lipex also has a steady increase at $\Delta\epsilon_{222}$ (Figure 5.3 B2) however a much shallower gradient is observed where the inflection point, the point at which there is a change

in gradient, is lower than previously observed for Lipolase. This suggests Lipex has a lower thermostability than Lipolase.

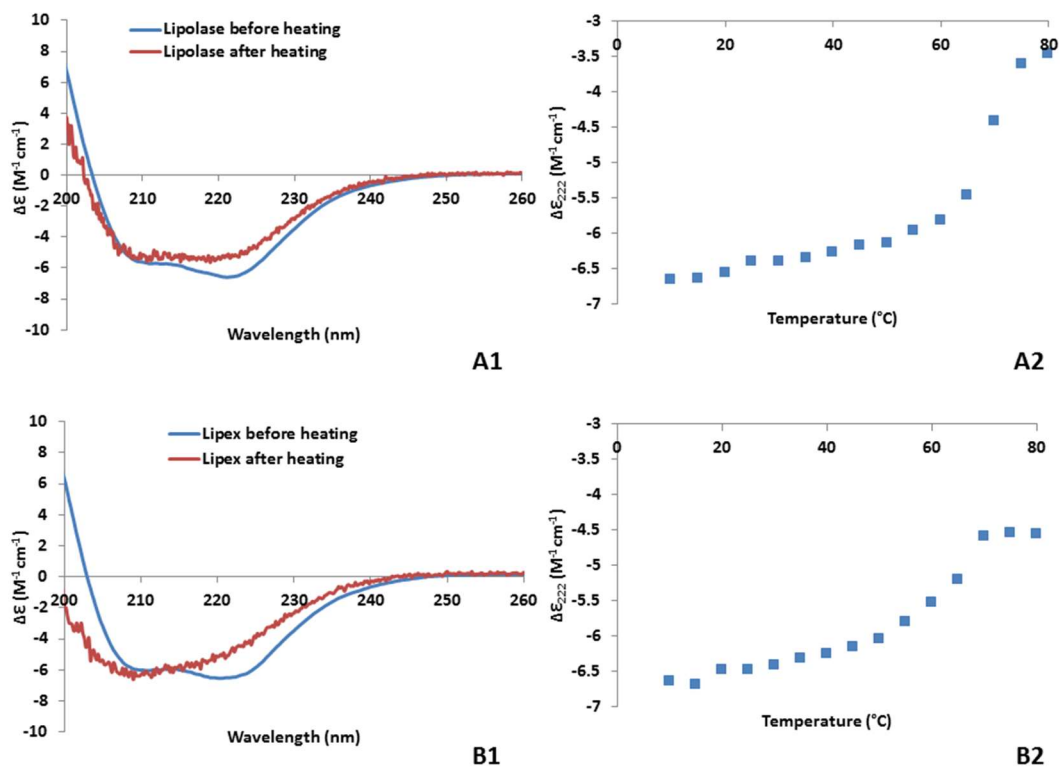


Figure 5.3: Far-UV CD spectra of (A1) Lipolase and (B1) Lipex as molar circular dichroism ($\Delta\epsilon$) as a function of wavelength. Run at 20 $^{\circ}C$ before and after heating. CD analysis at $\Delta\epsilon_{222}$ of Lipolase (A2) and Lipex (B2) as a function of temperature ($^{\circ}C$).

Taking into account the values at $\Delta\epsilon_{222}$, unfolding curves (Figure 5.3 A2, B2) were used to analyse the change in melting temperature, between the Lipolase and Lipex. This was determined by calculating the fraction of the protein in the folded and unfolded state, utilising Equation 5.1. It was assumed that the lipase was in the native state at 10 $^{\circ}C$ and 100% unfolding occurred at 80 $^{\circ}C$. An overlay of the thermal unfolding curves (Figure 5.4) indicates that the melting temperature (T_m , defined as the temperature at which 50% of the protein is unfolded)⁷ was calculated

to be 68 °C for Lipolase and 59 °C for Lipex. Interestingly the thermal stability of the enzymes is found to decrease as the enzyme is increasingly modified *i.e.* the non-modified TLL is most thermally stable, followed by Lipolase then Lipex (containing the greatest number of mutations). This highlights the importance of the primary structure (amino acid sequence) of the lipase on its thermostability.

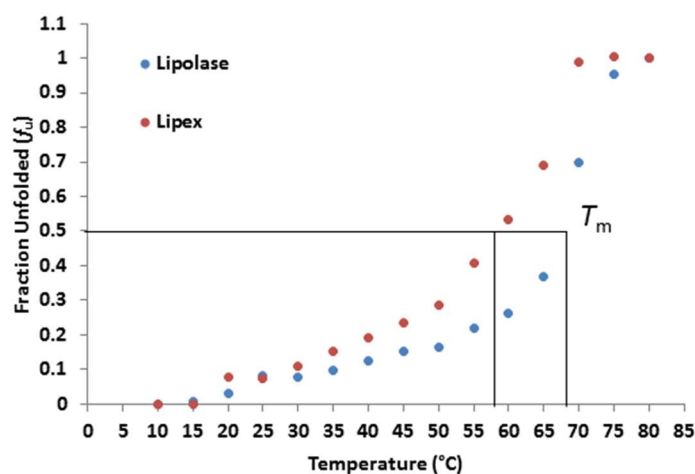


Figure 5.4: A thermal unfolding curve comparing the fraction unfolded against temperature (°C) of Lipolase and Lipex.

An online analysis programme for deconvolution of the secondary structure, DICHROWEB, was used to explore further the changes in CD spectroscopy after heating at 80 °C.^{11, 21} From Table 5.1 it is clear that, for both mutated lipases, after one heating cycle a large increase in the unordered structure is obtained: above the melting temperature the percentage of unordered strands increased and this was maintained after heating. After a heating cycle the overall percentage of β -sheets present has increased for both Lipolase and Lipex, whereas the percentage of α -helix dramatically decreased for both enzymes. This is in accordance with the literature where it is observed that helical secondary structures are less thermally stable than β -

sheets,²² where water molecules more readily disrupt the hydrogen bonding network in the α -helix leading to a loss in order. For both lipases the secondary structures do not return to the native state after heating, indicating this thermal degradation is not reversible for either enzyme. The NRMSD (normalised-root-mean-square-deviation) is used to estimate the difference between the calculated model and the spectra obtained, where low NMMSD values indicate a good fit of the protein to the model used. As the lipases became more disordered this value increased, indicating lower correlation with the model (CONTIN/LL reference set 4).

Table 5.1: The secondary structure content of Lipolase and Lipex determined by CD spectroscopy and interpreted using DICROWEB, using CONTIN/LL analysis programme and reference set 4. Normalised root-mean-square deviation (NRMSD) gives the deviation of the data set from the model used.^{21, 23}

Protein	% α-helix	% β-sheet	% β-turns	% unordered	NRMSD
Lipolase	60.5	7.0	11.6	20.2	0.029
Lipolase at 80 °C	31.6	14.1	23.9	30.4	0.047
Lipolase after heating	44.4	17.2	12.9	26.3	0.087
Lipex	66.4	4.4	13.4	15.8	0.043
Lipex at 80 °C	31.3	16.9	19.8	32.1	0.102
Lipex after heating	34.3	11.3	21.7	32.7	0.146

As the lipases are held at 80 °C for 7 hours prior to cooling, both enzymes irreversibly unfold. To further investigate the thermal stability of Lipolase, its size and shape was evaluated with respect to temperature using SAXS. The commercially available lipase, Lipolase, was further analysed using small-angle X-ray scattering (SAXS). This technique allowed for observations in changes to the globular structure upon heating. Kratky plots (Figure 5.5, left), enable inference of the enzyme folding characteristics, indicated the globular structure for the Lipolase as evidence in the

bell-shaped curve. It should be noted that unfolded structures display a plateau shaped profile in the Kratky plot.^{24, 25}

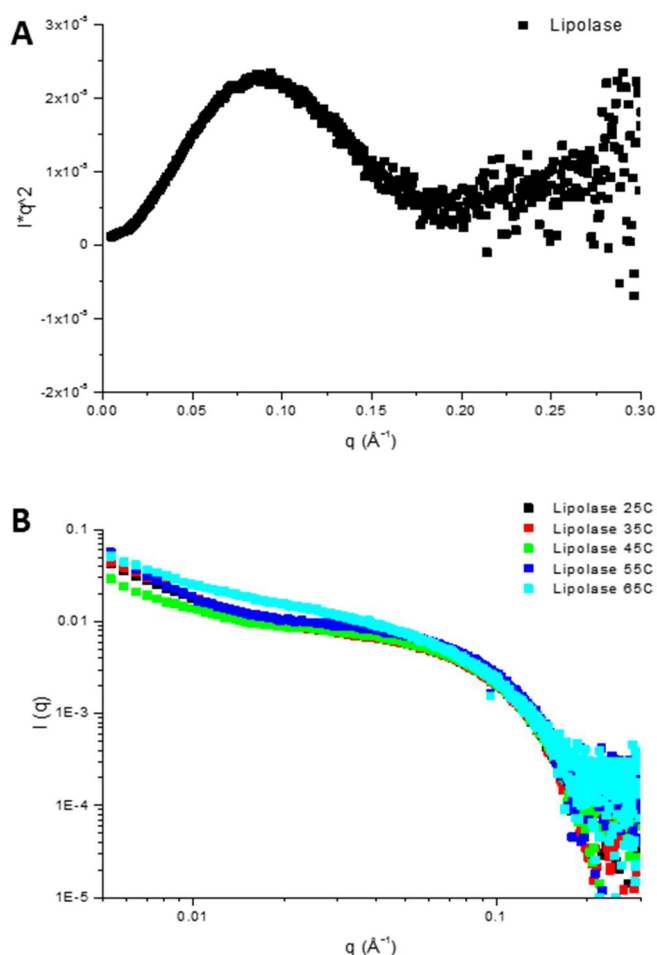


Figure 5.5: A; Kratky plot of Iq^2 plotted against q . B; Porod plot of Lipolase at 25-65 °C as $\ln I$ against $\ln q$ at different temperatures, all SAXS data was collected and fitted by Dr Anaïs Pitto-Barry.

Further analysis of the Kratky plots indicates the Lipolase shows a globular structure containing a network, indicative of the intramolecular bonding taking place within the enzyme. A change in morphology was observed in the Guinier -Porod plot at 65 °C, which is in agreement with the onset of change in the secondary structure observed using CD spectroscopy.²⁶ The Table below shows the Porod exponent (s)

and R_g at 25-65 °C. The s parameter is related to the shape of the structure, and increased from 0.16 to 0.56 after heating indicating a structural reorganisation, and the transition from a spherical structure to a more elongated one ($s = 1$). As a consequence of heating it is apparent that a loss of spherical structure was observed after 55 °C.

Table 5.2: The estimated particle size radius of gyration (R_g) and the dimension parameter (s) for Lipolase at 25-65 °C.

Sample	Guinier-Porod fit	
	R_g (nm)	s
Lipolase 25 °C	1.88 ± 0.01	0.16
Lipolase 35 °C	1.87 ± 0.01	0.17
Lipolase 45 °C	1.91 ± 0.01	0.13
Lipolase 55 °C	1.93 ± 0.01	0.12
Lipolase 65 °C	1.66 ± 0.01	0.56

5.3.2 Polymer lipase stability with PDMA

5.3.2.1 CD spectroscopy studies

In Chapter 4 it was shown that poly(*N,N*-dimethyl acrylamide) (PDMA) interacts with Lipolase and Lipex. It was hypothesised that this interaction was as a result of weak intermolecular bonding of the protein and the synthesised polymer. To determine if an enhancement in thermostability was obtained upon the addition of a PDMA polymer, both **P4.4** and **P4.5** (synthesised in Chapter 4) were incubated, in a ten molar excess to the lipases, with Lipolase (0.05 mg mL⁻¹) and Lipex (0.1 mg mL⁻¹) and subsequently monitored *via* CD spectroscopy. The properties of **P4.4** and **P4.5**

are summarised in Table 5.4, where **P4.5** has a higher molecular weight than **P4.4** (170.0 and 49.7 kDa respectively).

Table 5.3 The properties of polymers P4.4-4.5, ^adetermined by ¹H NMR spectroscopy (400 MHz, CDCl₃), ^bdetermined by SEC analysis (CHCl₃, PSt standards).

Name	M_n (kDa) ^a	M_n (kDa) ^b	D_M ^b
P4.4	49.7	33.4	1.38
P4.5	170.0	136.7	1.41

Initially the higher molecular weight polymer (**P4.5**) was analysed in solution with both Lipolase and Lipex. The polymer, was heated with Lipolase and Lipex in Tris-HCl buffer (pH 8.5, 5 mM) and monitored *via* CD spectroscopy from 10-80 °C at 5 °C intervals, with the temperature increased at a rate of 20 °C h⁻¹, and the solution allowed to equilibrate at each temperature point for 30 minutes prior to analysis. After the temperature ramp the solution was held at 80 °C for 7 hours prior to cooling to 20 °C, where a final CD spectrum was obtained after 20 minutes.

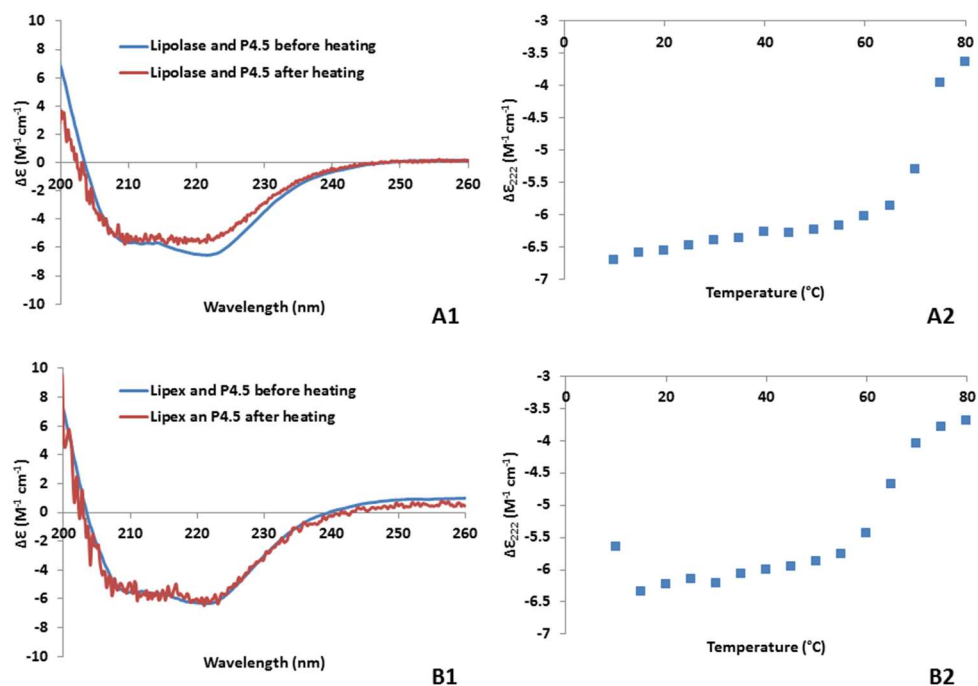


Figure 5.6: Far-UV CD spectra of (A1) P4.5 and Lipolase and (B1) P4.5 and Lipex as molar circular dichroism ($\Delta\epsilon$) as a function of wavelength. Run at 20 °C before and after heating. CD spectroscopy analysis at $\Delta\epsilon_{222}$ of P4.5 and Lipolase (A2) and P4.5 and Lipex (B2) as a function of temperature (°C).

The before and after CD spectra of the **P4.5**-Lipolase solution are similar to the free Lipolase solution CD spectrum (Figure 5.6, A1). Similar changes in the gradients at $\Delta\epsilon_{222}$ were also observed. Interestingly, a much more distinctive change was seen for the **P4.5**-Lipex solution vs the free Lipex. Despite a noisier baseline (attributed to the formation of small aggregates in solution), a good overlap for the pre- and post-heating CD spectrum was observed. It is apparent that in the presence of **P4.5** the majority of the Lipex is able to re-fold into its native state. A large difference was further observed when monitoring $\Delta\epsilon_{222}$ with heating (Figure 5.6, B2); although steeper gradient was observed the onset of the inflection point (unfolding) is at a higher temperature than the free Lipex (55 and 45 °C respectively).

The fraction of unfolding in the presence of **P4.5** was compared for both lipases (Figure 5.7); here a small increase in T_m was shown upon introducing **P4.5** to the

Lipolase solution (68 °C to 71 °C). For the thermostability studies of **P4.5** with Lipex, a change is observed in the unfolding plot where it is apparent that the T_m has increased to 63 °C (from 59 °C) indicating that **P4.5** is able to shield Lipex, increasing its thermal stability. In the previous Chapter, we discussed the favourable interactions of the Lipex with surfactants due to the arginine mutations present on the surface. We propose that these mutations enhance the ability of Lipex to interact with the hydrophobic and hydrophilic segments of the polymer (polymer backbone and functional groups respectively) resulting in an increased thermostability.

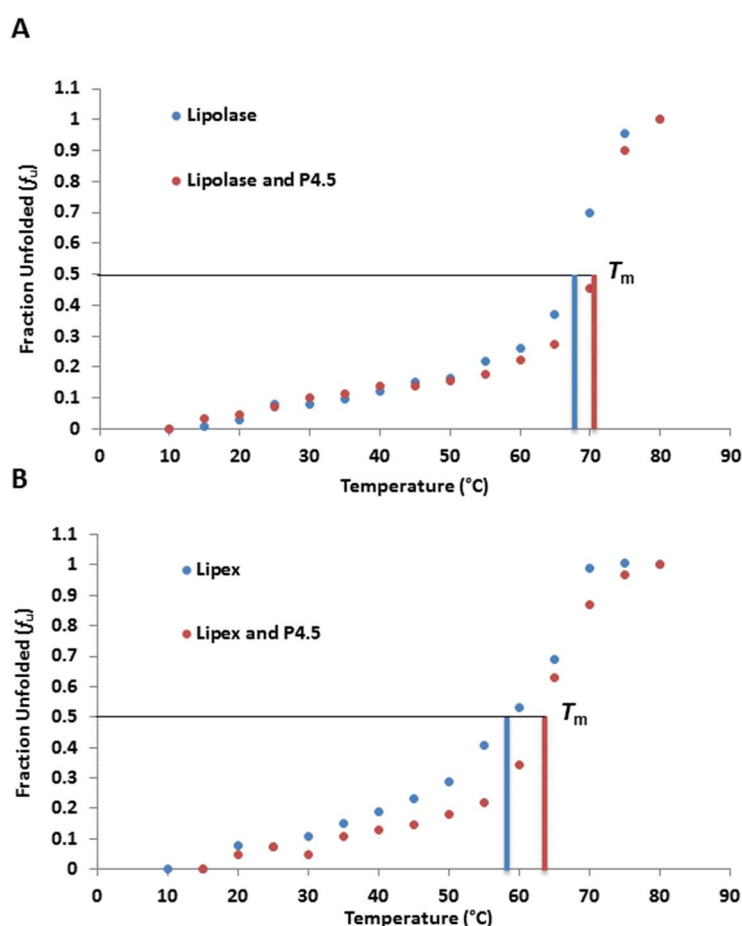


Figure 5.7: A comparison of the fraction unfolded of (A) Lipolase and Lipolase with P4.5, and (B) Lipex and Lipex with P4.5 against temperature (°C).

The CD spectroscopy data for the **P4.5**-lipase solutions was further analysed using DICROWEB (Table 5.4).²¹ A loss in the amount of α -helix and an increase in the percentage of β -sheets were observed for both lipase-**P4.5** solutions, as seen previously for the free lipases. The **P4.5**-Lipolase solutions displayed similar changes in the secondary structure upon heating as the Lipolase without polymer additive. However, the **P4.5**-Lipex solution, which has a large change in structure at 80 °C, showed relatively small changes in the secondary structures after heating with similar fractions of secondary structure towards the native state was observed, this is attributed to the PDMA-protein interactions shielding the protein enabling the protein to refold into its native state.

Table 5.4: The secondary structure content of P4.5 with Lipolase and Lipex determined by CD spectroscopy and interpreted using DICROWEB analysis programme and using CONTIN/LL reference set 4 and 7 (for P4.5 after heating).^{21, 23}

Protein	% α -helix	% β -sheet	% β -turns	% unordered	NMRSD
P4.5 and Lipolase	61.3	4.2	15.6	18.9	0.044
P4.5 and Lipolase at 80 °C	32.1	15.6	23.6	28.9	0.083
P4.5 and Lipolase after heating	43.7	13.0	15.5	27.7	0.114
P4.5 and Lipex	54.8	6.9	14.4	23.9	0.068
P4.5 and Lipex at 80 °C	44.0	15.7	24.1	16.3	0.366
P4.5 and Lipex after heating	51.9	1.8	13.7	32.4	0.211

In both cases, the introduction of **P4.5** has led to a small increase in the melting temperature indicating increased thermostability. To explore this observation further, a second PDMA polymer **P4.4** which has a lower molecular weight than **P4.5**, and was subsequently mixed with both of the lipases to evaluate thermal stability. The polymer was heated to 80 °C in excess (10 times molar excess) to the lipases and the

temperature maintained for 7 hours prior to cooling to 20 °C, to allow for re-folding of the enzyme prior to acquisition of a final CD spectrum. Here a dramatic change in structure was found after heating Lipolase and **P4.4** (Figure 5.8, A1) however a full melting curve could not be observed at $\Delta\epsilon_{222}$ during the temperature ramp study, due to the point of inflection starting at 60 °C, where the instrument cannot heat past 80 °C. After extensive heating of **P4.4**-Lipolase solution it is clear that the enzyme irreversibly denatures, resulting in a poor CD spectrum with little overlap prior to heating and ultimately a denatured Lipolase.

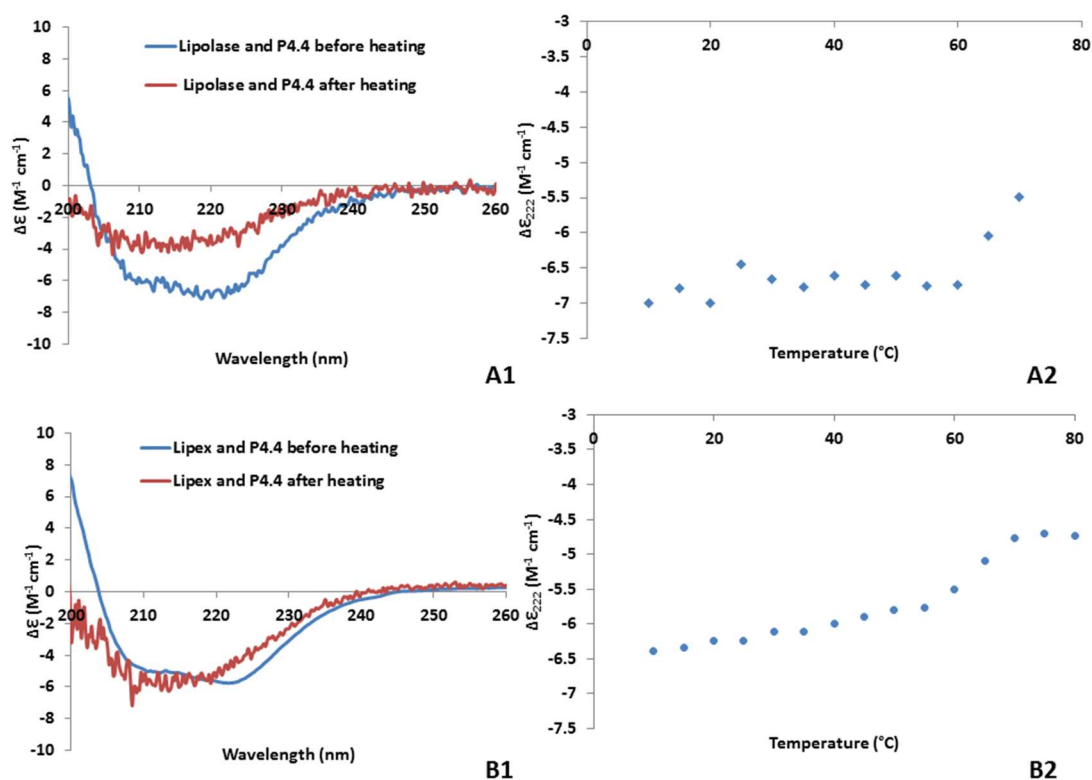


Figure 5.8: Far-UV CD spectra of (A1) P4.4 and Lipolase and (B1) P4.4 and Lipex as molar circular dichroism ($\Delta\epsilon$) as a function of wavelength. Run at 20 °C before and after heating. CD spectroscopic analysis at $\Delta\epsilon_{222}$ of P4.4 and Lipolase (A2) and P4.4 and Lipex (B2) as a function of temperature (°C).

The fraction of unfolded Lipolase could not be determined for the **P4.4**-Lipolase solutions as T_m curve could not be fully obtained, however the CD spectrum below (Figure 5.9, A) provides good overlap of the CD spectrum at higher temperatures, hence prolonged heating leads to denaturation of the Lipolase with **P4.4**, at which the protein irreversibly aggregates. It is plausible that **P4.4** is interacting with the unfolded protein preventing reorganisation to the native state. We hypothesise that the presence of these lower molecular weight polymer chains initially stabilises Lipolase. After prolonged heating the protein is more unfolded hence the smaller, lower molecular weight chains are unable to shield the Lipolase from protein-protein interactions leading to aggregation and subsequently loss in the secondary structure.

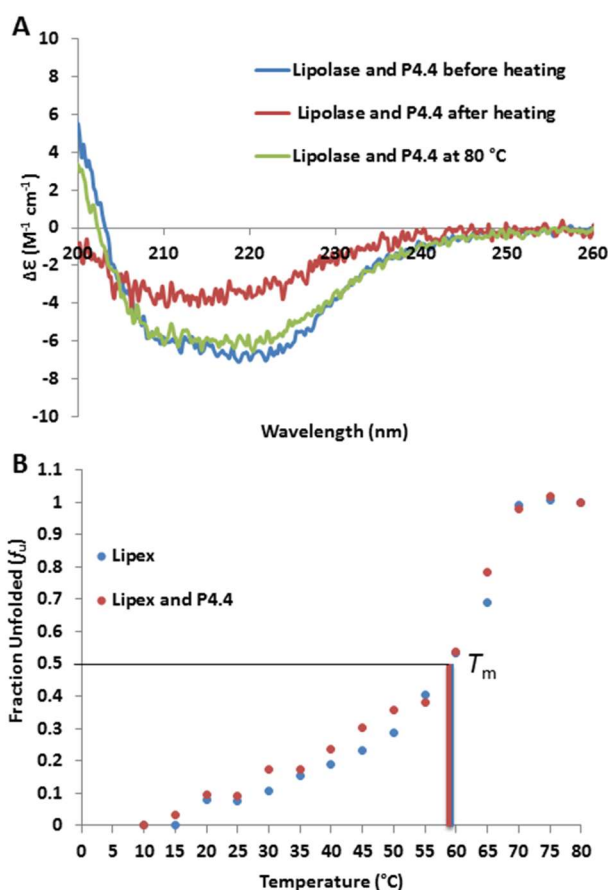


Figure 5.9: (A) An overlay of Lipolase and P4.4 CD spectra before heating, after heating and at 80 °C. (B) A comparison of the fraction unfolded plotted against temperature for Lipex and Lipex with P4.4.

A comparison of the **P4.4**-Lipex solutions after heating provided a less pronounced change in the secondary structure and after heating a very noisy spectrum was obtained. The melting temperature of Lipex has remained unchanged upon heating with **P4.4**. As such the lower molecular weight PDMA provides no additional thermostability with Lipex unlike that which was previously obtained with **P4.5**.

The analysis programme DICHROWEB was again used to predict the percentage of secondary structure present before, during and after heating (Table 5.5). For Lipolase with **P4.4** at 80 °C there is a much higher percentage of α -helix retained in comparison to the free Lipolase, leading to a much smaller increase in the unordered structure, β -sheets and turns, indicating **P4.4** provides stabilisation at higher temperatures with Lipolase. After prolonged heating the secondary structure of Lipolase is unrecognisable to the native state as confirmed by the increased NMRSD value obtained. We hypothesise the presence of **P4.4** inhibits the reformation of intramolecular bonding of Lipolase when refolding into the native state. It is plausible that this leads to intramolecular interactions giving rise to protein-protein aggregation. This can prevent the reformation of intramolecular bonding, critical for the refolding of the protein to its native state. Lipex and **P4.4** show a large increase in NMRSD values at 80 °C, indicating collapse of the secondary structure, similar to previous observations with lone Lipex.

Table 5.5: The secondary structure content of P4.4 with Lipolase and Lipex determined by CD spectroscopy and interpreted using DICROWEB analysis programme and using CONTIN/LL reference set 4.^{21, 23}

Protein	% α -helix	% β -sheet	% β -turns	% unordered	NMRSD
P4.4 and Lipolase	58.5	5.5	16.0	20.0	0.072
P4.4 and Lipolase at 80 °C	49.8	9.1	18.0	23.1	0.075
P4.4 and Lipolase after heating	24.3	23.6	20.6	31.5	0.172
P4.4 and Lipex	54.8	6.9	14.4	23.9	0.068
P4.4 and Lipex at 80 °C	39.3	12.0	31.7	17.0	0.278
P4.4 and Lipex after heating	30.9	23.4	15.5	30.2	0.362

Upon comparing the percentage change of the PDMA-Lipolase solutions to the Lipolase solutions (Table 5.6) no additional stability was observed *via* CD spectroscopy (Figure 5.6) In contrast a much higher retention of secondary structure was observed for Lipex-**P4.5** solutions and a small enhancement was observed with **P4.4**. The increase in thermostability observed with **P4.5** highlights the importance of using higher molecular weight polymers for Lipolase stabilisation. We suggest these polymers are able to shield the enzyme from the external environment. **P4.5** is much larger than the enzyme whereas **P4.4** is twice the molecular weight of the lipases (50 kDa **P4.4** and 26 kDa lipase), hence this polymer only partially stabilises the enzyme.

Table 5.6: The percentage change in secondary structure content of Lipolase and Lipex both with and without P4.5 and P4.4 after heating, determined by CD spectroscopy and interpreted using DICROWEB, using CONTIN/LL analysis programme and reference set 4.^{21, 23} T_m Calculated at $\Delta\epsilon_{222}$.

Protein	$\Delta\%$ α-helix	$\Delta\%$ β-sheet	$\Delta\%$ β-turns	$\Delta\%$ unordered	T_m ($^{\circ}\text{C}$)
Lipolase	-16.1	10.2	1.3	6.1	68
P4.5 and Lipolase	-17.6	8.8	0.1	8.8	71
P4.4 and Lipolase	-34.2	18.1	4.6	11.5	68
Lipex	-32.1	6.9	8.3	16.9	59
P4.5 and Lipex	-2.9	-5.1	0.7	8.5	63
P4.4 and Lipex	-23.9	16.5	1.1	6.3	-

5.3.2.2 SAXS studies

Analysis of **P4.5** and **P4.4** with Lipolase *via* SAXS showed similar results to lone Lipolase when the sample was heated. Due to experimental restrictions of the apparatus, the solutions were heated to a maximum of 60 $^{\circ}\text{C}$ however a change in the globular structure was seen (Figure 5.10). Two conclusions can be drawn from this data: either (1) the protein has denatured at this temperature or (2) the protein no longer interacts with **P4.5** at this temperature. As the polymer is not covalently bound to the protein it is suggested that the protein is interacting with the polymer *via* weak electrostatic interactions. At a certain temperature these bonds are disrupted de-shielding the protein, enabling protein unfolding and exposing hydrophobic residues. For storage at elevated temperatures we suggest more permanent covalently bound polymers will provide higher stabilisation, although such processes may result in decreased enzymatic activity at normal operating temperatures.²⁷

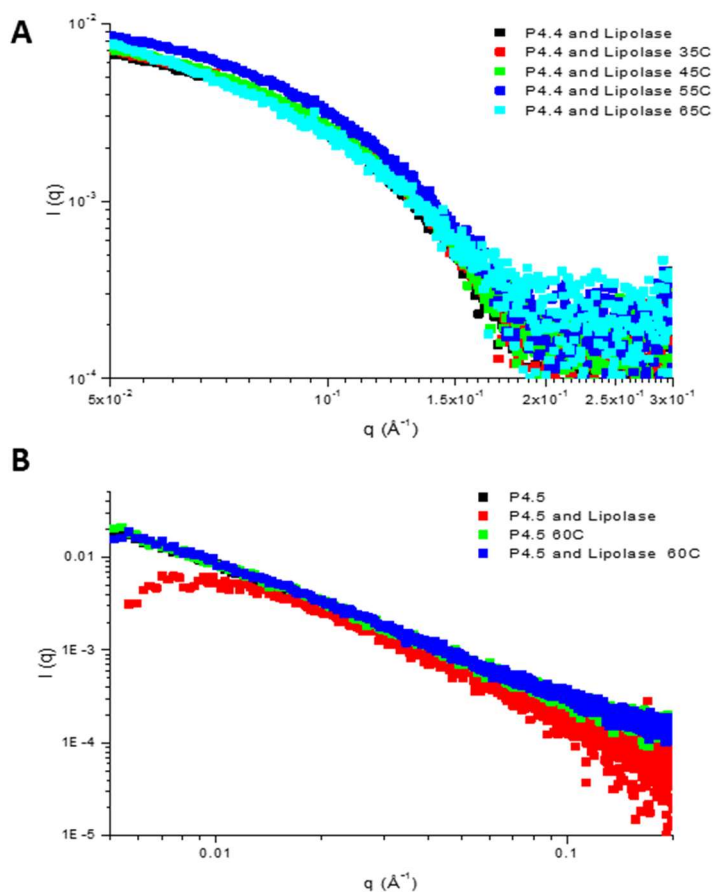


Figure 5.10: A Porod plot at 25-65 °C of $\ln I$ vs $\ln q$ for P4.4 with Lipolase (A) and P4.5 with Lipolase (B).

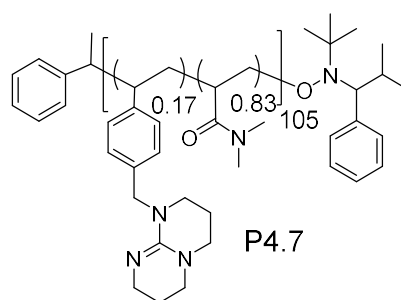
The polymer **P4.4** showed a decrease in globular structure to a more elongated structure after the onset of increasing temperature (Table 5.7). Analysis of the Guinier-Porod fit indicated that at 65 °C the radius of gyration decreases suggesting the width of the elongated structure is smaller than the initial spherical assembly. Following the previous discussion, we can make the assumption that, at this temperature, intramolecular bonds between polymer-protein in solution are disrupted, and as a result the stability of the protein is now reliant on its own molecular weight as higher molecular weight proteins less readily diffuse in the solution resulting in prolonged stabilisation.

Table 5.7: The estimated particle size radius of gyration (R_g) and the dimension parameter (s) for P4.4 and Lipolase at 25-65 °C.

Sample	Guinier-Porod fit	
	R_g (nm)	s
P4.4 and Lipolase 25 °C	1.81 ± 0.01	0.24
P4.4 and Lipolase 35 °C	1.83 ± 0.01	0.21
P4.4 and Lipolase 45 °C	1.90 ± 0.01	0.15
P4.4 and Lipolase 55 °C	1.94 ± 0.01	0.10
P4.4 and Lipolase 65 °C	1.50 ± 0.01	0.70

5.3.3 Polymer lipase stability with P4.7

Previously we have shown that the presence of immobilised TBD is detrimental to the lipases, Lipex and Lipoclean. In order to establish the effects of heating on the partially denatured lipases this polymer (**P4.7**) was used. The polymer **P4.7** (Figure 5.11) was synthesised in the previous Chapter, with a M_n of 13.6 kDa, determined by ^1H NMR spectroscopy.

**Figure 5.11: Structure of P4.7.**

Initially **P4.7** was heated with Lipolase and Lipex in a ten times molar excess in comparison to the lipase and the resultant solution was analysed utilising ramped

temperature CD spectroscopy. Previously it has been demonstrated (Chapter 4) that the immobilised TBD can disrupt the secondary structure of lipase due to the presence of the guanidine functionality. This is reflected in the CD spectrum with a loss in secondary structure prior to heating. A large change in secondary structure was seen for both lipases after heating (Figure 5.12). Here it was not possible to determine the melting temperature due to the initial loss of the secondary structure, with the presence of TBD leading to a loss of structure with time. When monitoring $\Delta\epsilon_{222}$ (Figure 5.12 A2) the onset of melting was not observed for Lipolase, as a consequence of the enzyme being chemically denatured. Lipex displayed a small melting (Figure 5.12 B2) curve however the onset of this is at 10 °C - 30 °C indicating no enhanced thermostability with immobilised TBD.

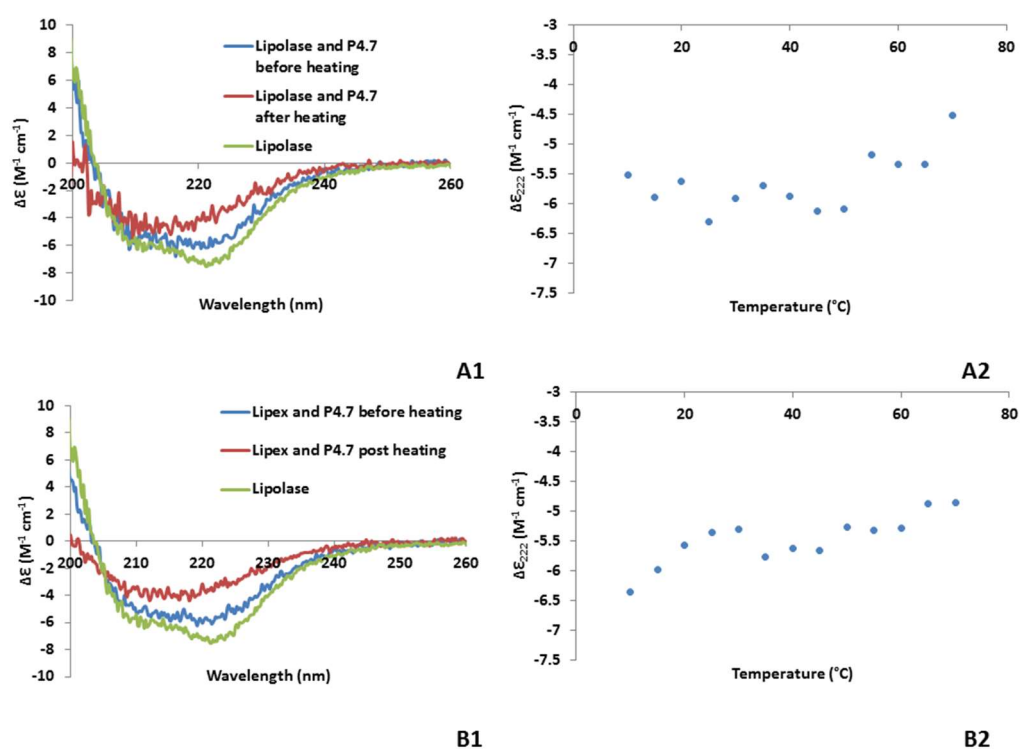


Figure 5.12: Far-UV CD spectra of (A1) P4.7 and Lipolase and (B1) P4.7 and Lipex as molar circular dichroism ($\Delta\epsilon$) as a function of wavelength compared to Lipolase and Lipex (20 °C). Run at 20 °C before and after heating. CD spectroscopy analysis at $\Delta\epsilon_{222}$ of P4.4 and Lipolase (A2) and P4.4 and Lipex (B2) as a function of temperature (°C).

5.3.3.1 SAXS analysis with P4.7

Temperature studies of Lipolase in the presence of **P4.7** again showed a large change in the Guinier-Porod fit (Figure 5.13) once the temperature reached 65 °C.

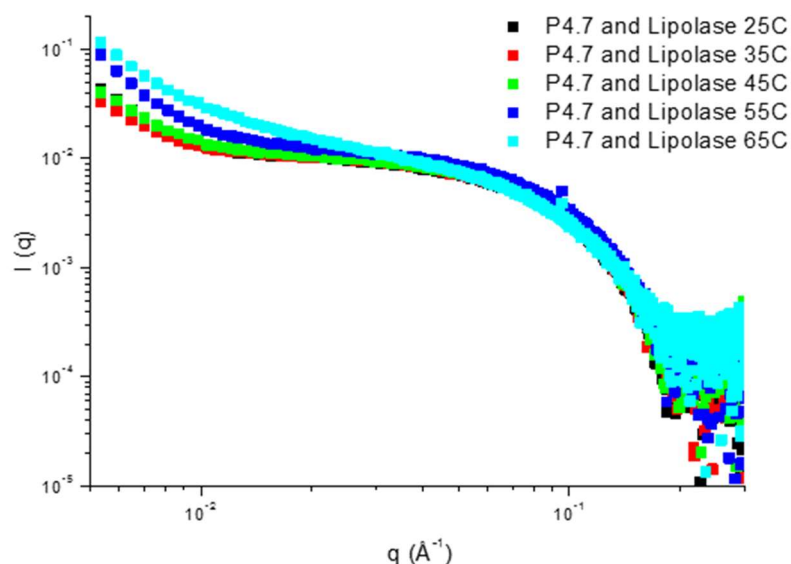


Figure 5.13: A Porod plot at 25-65 °C of $\ln I$ vs $\ln q$ for P4.7 with Lipolase.

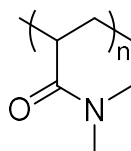
The globular structure of Lipolase at this temperature has changed from a spherical structure to a rod-like structure (Table 5.8), as evidenced by an increase in the dimension parameters (0.1 to 0.5). The width of the elongated structure is smaller than the diameter of the initial spherical structure which is shown by a decrease in R_g (1.94 to 1.58 nm).

Table 5.8: Estimated particle size radius of gyration (R_g) and the dimension parameter (s) for P4.7 and Lipolase at 25-65 °C.

Sample	Guinier-Porod fit	
	R_g (nm)	s
P4.7 and Lipolase 25°C	1.94 ± 0.01	0.12
P4.7 and Lipolase 35°C	1.94 ± 0.01	0.10
P4.7 and Lipolase 45°C	1.91 ± 0.01	0.12
P4.7 and Lipolase 55°C	1.91 ± 0.01	0.11
P4.7 and Lipolase 65°C	1.58 ± 0.01	0.54

5.3.4 Activity studies of the polymer-lipase solutions

The activity of Lipolase was measured using the spectrometric assay of *para*-nitrophenol esters.^{28, 29} Short water-soluble alkyl chains are good models for evaluating esterase activity, while increasing the length of the alkyl chains provides a good model for evaluating lipase activity. Hence the substrate *para*-nitrophenyl-stearate was used to determine lipase activity. In this case, the active site of the lipase is analogous to serine proteases, consisting of the amino acids serine, histidine and aspartate.^{30, 31} Protons are transferred within the active site after activation (*via* “lid” opening) due to the interfacial activation by the hydrophobic fatty acid. Serine acts as a nucleophile, attacking the carbonate group, and the intermediate is then stabilised by the oxyanion hole (as discussed in Chapter 4).^{32, 33} Lipolase in the presence of polymers **P4.3**, **P4.4** and **P4.5** (Figure 5.14) with a 10 times molar excess to the lipase were stored in solution for a week, and the initial lipase activity subsequently monitored, to determine if any additional stability was afforded to the Lipolase.



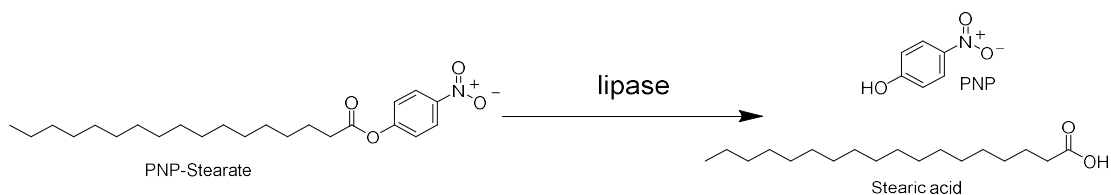
P4.3 $M_n = 11$ kDa

P4.4 $M_n = 58$ kDa

P4.5 $M_n = 170$ kDa

Figure 5.14: PDMA polymers of different molecular weights stored in solution with a 10 times molar excess to Lipolase to monitor their effects on Lipolase stabilisation.

Each polymer-protein solution was sampled at time points $t=0$ hours $t=10$ hours and $t=1$ week and the activity was monitored by UV-Vis spectroscopy using the substrate *para*-nitrophenyl stearate (Scheme 5.2). This is a colourless substrate, however upon hydrolysis the release of *para*-nitrophenol (PNP) results in a colour change which was observed in the visible region at 405 nm.



Scheme 5.2: Formation of PNP and Stearic acid from the hydrolysis of PNP-Stearate in the presence of lipase.

This colour change can be monitored by UV-Vis spectroscopy and enables comparison of the Lipolase activity after storage. As the molar extinction coefficient of PNP can be affected by the pH and temperature of the solution, a standard curve was plotted to determine the molar absorption (ϵ) at 405 nm in Tris-HCl buffer (pH 8.5, 50 mM), which was determined as $14676 \text{ M}^{-1}\text{cm}^{-1}$.

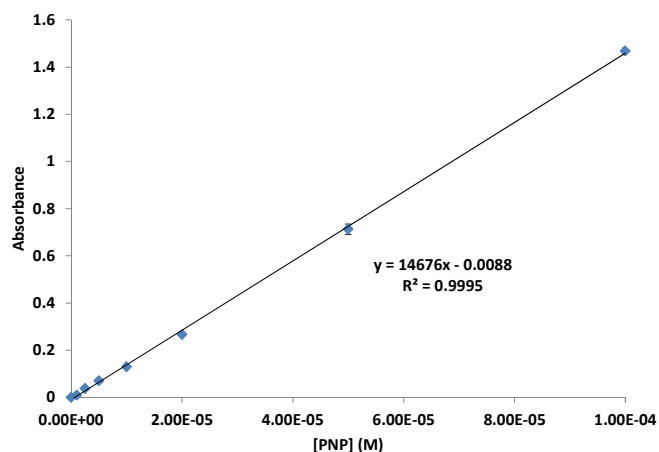


Figure 5.15: A plot of absorbance vs [PNP] (M) to give the extinction coefficient of the substrate PNP of $14676 \text{ M}^{-1}\text{cm}^{-1}$.

To a 96 well plate, the incubated samples containing either Lipolase, Lipolase-Polymer, water or polymer blanks ($20 \mu\text{L}$) were added, with $100 \mu\text{L}$ Tris-HCl buffer (pH 8.5, 50 mM) and water, to make the total volume to $180 \mu\text{L}$, then PNP-Stearate ($20 \mu\text{L}$, 1 mM) was added. Prior to analysis all of the samples were subsequently defrosted and allowed to equilibrate in solution. The activity for ester hydrolysis was obtained for Lipolase solutions after storage for 0 hours, 10 hours and 1 week, with five repeats for each sample, and the initial rate of reaction was monitored using the initial slope of the graph and used to calculate initial velocity (Equation 5.3 and Figure 5.16). The plates were incubated at $20 \text{ }^\circ\text{C}$ prior to the addition of the substrate PNP-stearate (0.1 mM, $20 \mu\text{L}$). The rate at which the PNP is released can be described in terms of rate or velocity (v).^{28, 29} Initially the concentration of product increased linearly with time. As the amount of substrate decreases the product concentration reaches a plateau, therefore the initial rate is calculated and compared for all of the solutions using the following equations.

Equation 5.3: Determination of the initial velocity, where ΔA_{405} is the change in absorbance at 405 nm, Δt is the change in time (s) and ϵ is the extinction coefficient of PNP at 405 nm.

$$\text{slope } (m) = \frac{\Delta A_{405}}{\Delta t}$$

$$\text{velocity } (v) = \frac{m}{\epsilon} \text{ Ms}^{-1}$$

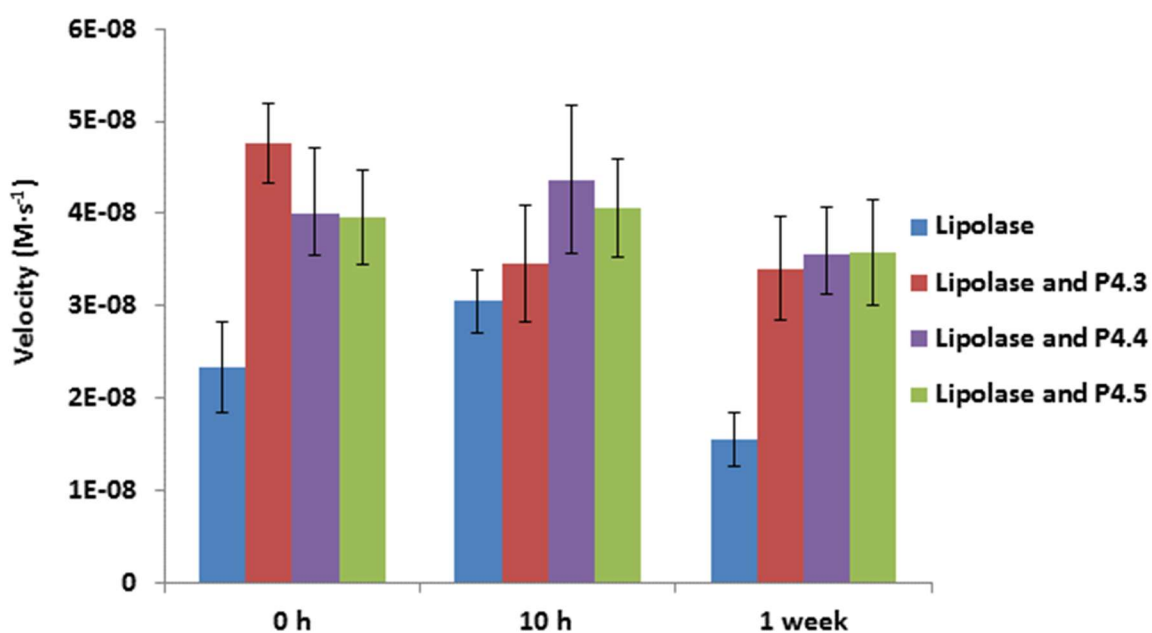


Figure 5.16: Bar chart of the velocity of Lipolase, and Lipolase with P4.3, P4.4 and P4.5 after storage at time intervals 0 h, 10 h and 1 week. Each set of data is shown as an average over five data sets with standard deviation.

It was observed that the addition of the polymer solutions has increased the rate of hydrolysis at 0 hours, however as a consequence of the large error bars no firm conclusions can be made. Notably, after one week the data shows a general decrease in rate is observed for Lipolase, however a much smaller decrease is seen with the polymer-lipase solutions. This suggests that PDMA is conferring additional stability by shielding the Lipolase from the surrounding environment without disturbing the

catalytic activity, however to prove this hypothesis more tests will need to be carried out. When looking at the percentage activity retained (Table 5.9), for Lipolase with the additives **P4.4** and **P4.5**, the activities are still within error of the initial activity. The velocity increases significantly from 0 hours to 10 hours for the Lipolase indicating that longer incubation times are required after dilution prior to analysis for optimised solvation of the Lipolase in solution. After one week Lipolase with **P4.4** and **P4.5** had lost $\sim 10\%$ activity and was still within error for activity at 0 hours. Considering the large difference in polymer molecular weight only a small difference is observed. As a result of the low initial enzyme velocity and little observable effect of polymer molecular weight (all are within standard deviation of one another), we propose that longer incubation times would enable us to determine if there is a plateau point at which molecular weight stability is observed.

Table 5.9: The percentage activity retained for Lipolase and Lipolase with polymers P4.3, P4.4 and P4.5. An average from 5 replicates, and compared to the original activity observed at 0 hour.

	% activity retained	
	10 h	1 week
Lipolase	130 \pm 14	67 \pm 13
Lipolase and P4.3	72 \pm 13	71 \pm 12
Lipolase and P4.4	109 \pm 20	89 \pm 11
Lipolase and P4.5	103 \pm 13	91 \pm 14

To establish if the polymers alone contributed to the hydrolysis a control experiment was run in the absence of Lipolase (Figure 5.17). No hydrolysis was observed indicating negligible effects of polymers on the activity, suggesting any effects arise from polymer-Lipolase interactions.

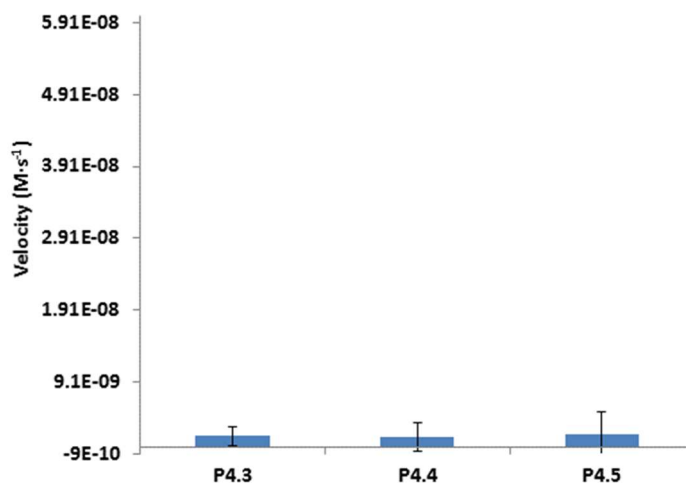


Figure 5.17: The velocity of P4.3, P4.4 and P4.5. Each set of data is shown as an average over 5 data sets with standard deviation as error.

As Lipolase with **P4.5** showed the highest activity after one week, the activity was further probed using the beef fat wash study. These wash studies determine the amount of stain removed after washing, and are compared to non-stained white cotton fabric. After determining the stain removal index (SRI) as previously shown in Chapter 4, the Δ SRI is then determined using the surfactant background as a blank. The wash study used 0.8 g L⁻¹ Blackbull™ formulation, which is incubated with the enzyme (at a concentration of 10 mg L⁻¹), with a total wash volume of 150 μ L. The plate was incubated at 40 °C for 30 minutes and shaken at 250 rpm. Following incubation, the plate was washed three times with water (12 French Hardness, 2:1 Mg: Ca) and left to dry overnight prior to scanning. Initial tests prior to storage showed Lipolase alone to have a large Δ SRI (Figure 5.18) however after one week the Δ SRI had decreased rapidly.

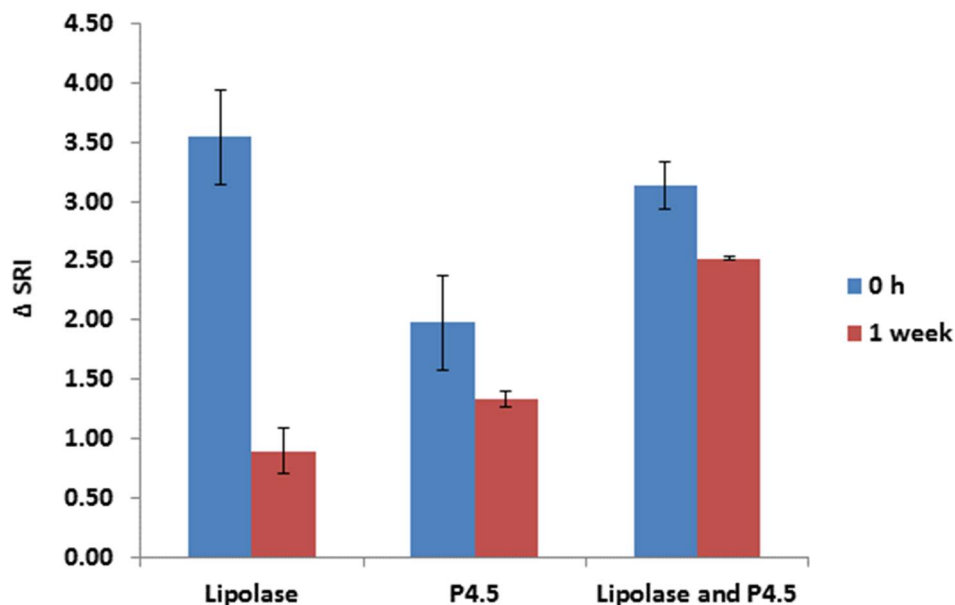


Figure 5.18: The Δ SRI for additive-free Lipolase, and Lipolase with P4.5 after storage at time intervals 0 h and 1 week, in 0.8 g L^{-1} Blackbull formulation. Each set of data is shown as an average over ten data sets with standard deviation as error.

In comparison to the 75% decrease in stain removal observed after one week for Lipolase, the Lipolase with the additive **P4.5** demonstrated a much smaller decrease of 20%. This confirms the presence of the PDMA is able to shield the lipase to provide additional stability without compromising stain removal. These results are in agreement with the percentage activity retained seen earlier for the hydrolysis assays where a higher retention of activity was observed for the polymer solutions.

Previous SAXS data showed interactions between Lipolase and **P4.5**, therefore the sample was also analysed after one-week storage. Due to the low concentrations used the scattering intensity for additive free Lipolase was not high enough for the collection of accurate data. After one week storage the Porod plot remains unchanged (Figure 5.19) suggesting the same interactions exist between **P4.5** and Lipolase with no loss of the globular structure.

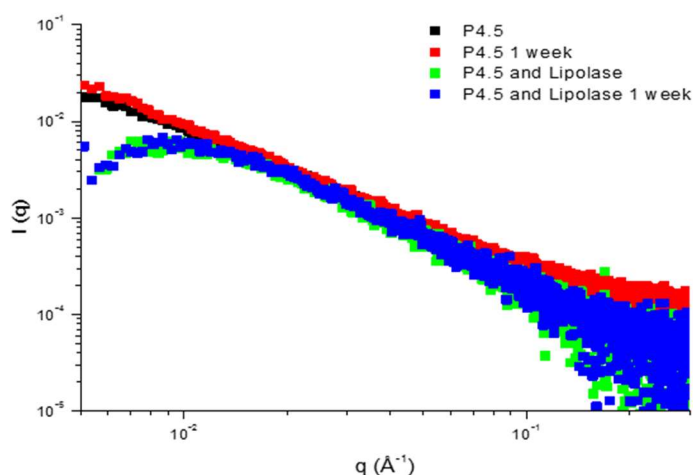


Figure 5.19: A Porod plot before and after one week storage with $\ln I$ plotted vs $\ln q$ for P4.5 and P4.5 with Lipolase.

The addition of **P4.7** (a TBD-containing polymer $M_n = 13.6$ kDa) to Lipolase significantly changed the secondary structure of Lipolase in the CD spectrum. With this in mind **P4.7** was stored in solution at an elevated temperature with Lipolase (75 °C for 12 hours), mimicking an accelerated stability test. This data was compared to the same equivalents of the substituted MTBD (2 mol% MTBD, which accounts for the same TBD loading) with Lipolase to establish if a greater effect is seen in the absence of the polymer chain. The polymer **P4.5** was also run with Lipolase to determine the effect of heating on the residual activity when **P4.5** was present. The activity of Lipolase was determined *via* the PNP-stearate hydrolysis assay before and after 12 hours of heating. The initial velocities before heating (Figure 5.20) were similar for Lipolase and the **P4.5**-Lipolase solutions. The presence of **P4.7** with Lipolase resulted in a much lower activity, attributed to the loss of the secondary structure due to denaturation of the lipase when in the presence of immobilised TBD. No activity was observed when Lipolase was present with MTBD, this smaller molecule similarly being able to disrupt the folding of

Lipolase thus chemically denaturing the lipase. Moreover, the denaturing occurs at a faster rate owing to the faster diffusion of the small molecule *vs* the polymer.

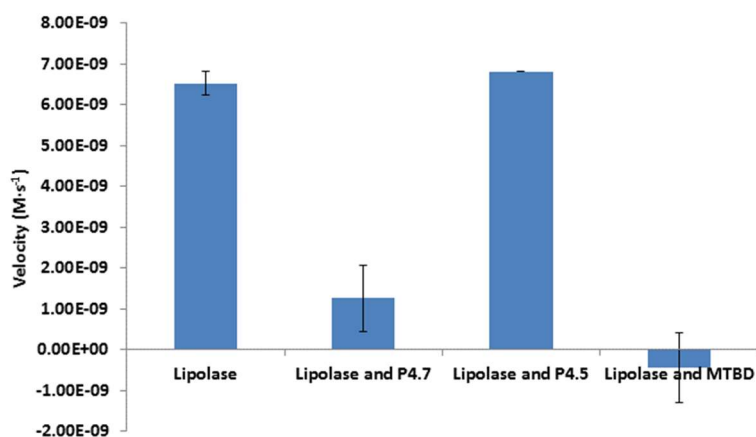


Figure 5.20: The velocity of Lipolase, and Lipolase with P4.7, P4.5 and MTBD. Each set of data is shown as an average over five data sets with standard deviation.

Guanidines are known to accelerate the denaturisation process, hence it is no surprise here that Lipolase with free MTBD shows no activity after accelerated stability studies (Figure 5.21).³⁴ In comparison **P4.7** and Lipolase showed a decrease in activity to 5% of the original velocity, we can conclude that immobilised TBD is still detrimental to protein stability. This data is in agreement with the CD spectroscopy studies shown previously, where a change in the secondary structure was observed on the addition of **P4.7**. In contrast Lipolase with **P4.5** showed 26% residual activity in comparison to Lipolase which has 22% remaining activity. This confirms CD spectroscopy can be used as a tool to determine the negative interactions observed by the addition of polymers.

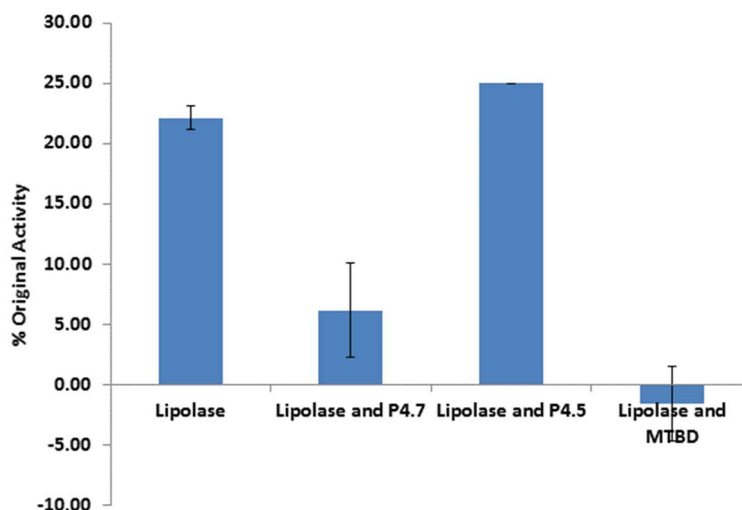


Figure 5.21: The percentage of original activity for Lipolase, and Lipolase with P4.7, P4.5 and MTBD after storage at 75 °C overnight. Each set of data is shown as an average over three data sets with standard deviation as error.

As TBD and MTBD can hydrolyse ester bonds, a control experiment was carried out to determine the background reaction of the polymers (**P4.7** and **P4.5**) and MTBD in the absence of Lipolase and again no hydrolysis was seen (Figure 5.22).³⁵ We speculate that the concentrations of the TBD catalyst is are too low for hydrolysis to take place.

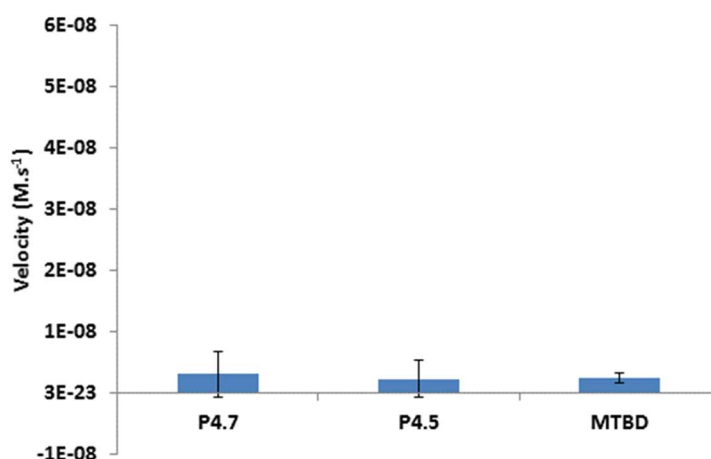


Figure 5.22: The velocity of P4.7, P4.5 and MTBD. Each set of data is shown as an average over three data sets with standard deviation.

We have shown that the presence of PDMA aids the stabilisation of Lipolase, however only a small change in the activity was observed after incubation with varying molecular weight PDMA. It is proposed that molecular weight will play a part in stability however longer stability studies will be required to fully explore this effect and completely monitor the activity. The polymer PDMA is a water-soluble polymer containing a hydrophobic backbone with hydrophilic functional groups suggesting the polymer has surfactant-like characteristics allowing PDMA to shield the lipase preventing unfolding, thus leading to stabilisation of the protein. Analysis of the SAXS has shown that the PDMA polymers retain the same shape and size upon storage with Lipolase, allowing for PDMA to shield the lipase through weak intermolecular forces which can be readily broken upon the application of heat.

5.4 Conclusions

In this Chapter, discrete changes in enzyme behaviour have been observed using simple techniques. CD spectroscopy has provided an excellent tool for the study of the denaturing of both Lipolase and Lipex during heating cycles and these observations have been supported by SAXS analysis. We have demonstrated that the genetic mutations of Lipolase to Lipex have decreased the overall melting temperature from 68 °C to 59 °C respectively.

Moreover, we have offered an insight into the effects of polymer additives and their molecular weight on the enzyme stability. Upon introducing a high molecular weight polymer to the solution an increase in T_m was observed *via* CD spectroscopy. However, upon decreasing the size of the PDMA polymer much smaller stabilisation effects were observed. It is proposed that the reduction in stabilisation is directly related to polymer molecular weight, where the larger polymers can less readily diffuse in the solutions promoting prolonged stabilisation upon heating. The higher molecular weight polymers can also interact more with the enzyme providing more shielding. Although the smaller molecular weight polymers show some stabilisation the data suggests these smaller chains interfere with the refolding of a polymer structure, as a result irreversible protein aggregation occurs in the non-native state.

Monitoring the activity after incubation with the polymer solutions for one week, higher activity was maintained for PDMA-Lipolase solutions, however all data was within the standard error of $t=0$. In order to gain further information on the extent of activity retained we recommend carrying out longer stability studies, where we propose that a greater understanding of the effects of molecular weight on the stability can be gained.

5.5 Outlook

We have found that the lipases, Lipex and Lipoclean, have different thermostabilities where PDMA can reduce the rate of deactivation. For better understanding of the deactivation of the lipases, from an external heat stimulus, we propose further studies examining the unfolding of Lipex and Lipoclean. As mentioned previously it has been reported that asparagine (Asn) residues are labile, undergoing deamidation forming the amino acid aspartate (Asp) in the primary structure denaturing the protein (Figure 5.23).¹⁷

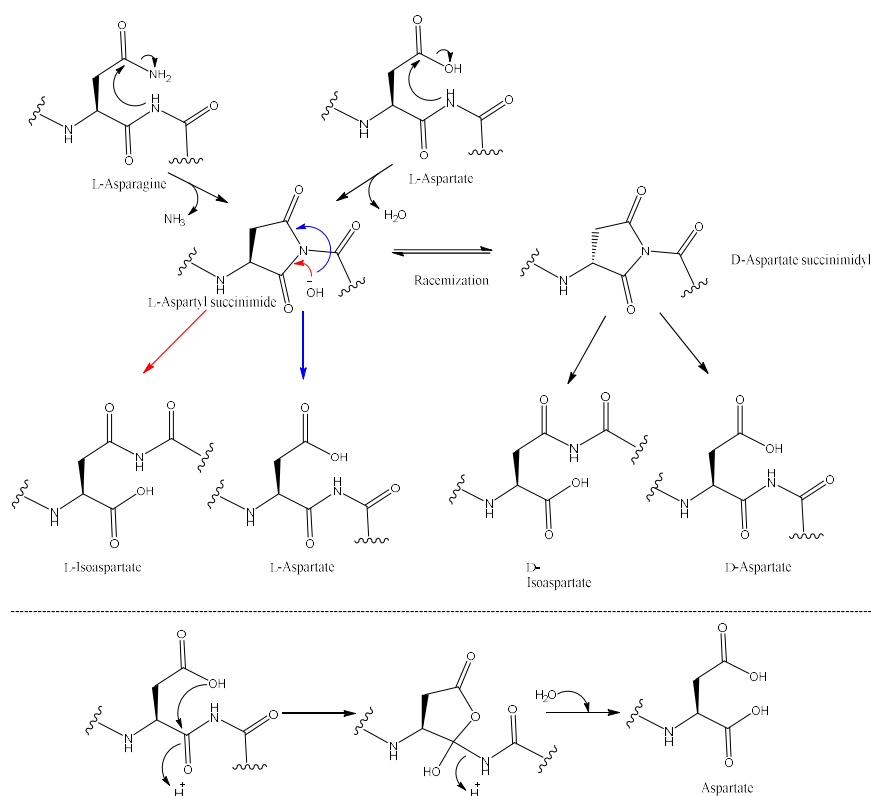


Figure 5.23: Schematic of the deamidation and hydrolysis of Asn and Asp (top) and the hydrolysis of the peptide backbone from an Asp residue (bottom).^{17, 18}

This is *via* a succinimide intermediate and occurs between pH 5-12 and is catalysed by the presence of hydroxide within the solution. The amino acid Asp is also

susceptible to hydrolysis, breaking the peptide chain. Aggregation can also occur as a result of thermo-inactivation, where a protein structure unfolds revealing the hydrophobic core, resulting in irreversible aggregation of the protein, hence a loss in activity is observed.¹⁷ A combination of all of these irreversible processes results in the enzyme failing to return to its native state. In order to determine the mechanism of the deactivation of Lipase and Lipolase, we propose using dynamic light scattering (DLS) to further investigate the temperatures at which aggregation occurs. Matrix-assisted laser desorption/ionisation can also provide information on the peptide sequence hence, the unfolding pathway of Lipex and Lipoclean can be determined.

5.6 Experimental

5.6.1 Circular dichroism

Circular Dichroism was used to compare the secondary structure of Lipolase and Lipex in the presence of polymer solutions before and after heating. Spectra were recorded on a J-720 CD spectrometer (Jasco) in 1 mM Tris-HCl buffer (pH 8.5) using a quartz cuvette with a path length of 0.1 cm. All concentrations were run three times with three acquisitions and recorded at 20 nm min⁻¹. These samples were averaged and the background subtracted. For the thermostability studies the samples were heated at a rate of 10 °C h⁻¹ and equilibrated at the set temperature for 5 minutes prior to analysis. Each temperature point was recorded over three accumulations at a rate of 20 nm min⁻¹ with a band width of 2 nm and a data pitch of 0.2 nm. The sample was subsequently stored at 80 °C for 7 hours, prior to cooling to 20 °C and incubated for 30 minutes before a final CD spectrum was recorded. The CD spectroscopy data was further analysed using the online platform DICHROWEB <http://dichroweb.cryst.bbk.ac.uk/html/home.shtml>.²¹ The data was compared using the CONTIN/LL algorithm and reference set 4 and 7 at 190-260 nm.²³

5.6.2 SAXS

Experiments were run on the SAXS- beamline at the Australian Synchrotron and the B21 beamline at diamond light source. The samples were run in accordance to the experimental procedure described in Chapter 4. All SAXS data was collected and fitted by Dr Anaïs Pitto-Barry.

5.6.3 Stain Testing

The samples were run in accordance to the experimental procedure described in Chapter 4.

5.6.4 Activity studies

All of the stock solutions were prepared at a concentration of 100 ng L⁻¹ of Lipolase. A 10 times molar concentration of the polymer solutions (with respect to the Lipolase, 3×10^{-3} mmol) were prepared in triplicate. The stock solutions were pipetted into Eppendorfs for each time point. The Eppendorfs were stored at room temperature (25 °C) until the pre-determined time point and subsequently removed and frozen until all of the time points had been gained prior to analysis. For the higher temperature studies these solutions were incubated at 75 °C for 12 hours prior to analysis.

5.6.5 Lipase Assay

The incubated samples were allowed to defrost for 30 minutes at 25 °C. The substrate, PNP-stearate, was dissolved in a methanol: hexane solution (95:5) and further diluted in methanol (5 mL, 1 mM, 10 times stock solution). To a 96 well plate Tris-HCl buffer pH 8.5 (100 µL), of the incubated samples (20 µL), and 60 µL water were added to all the experimental wells and incubated at room temperature for 5 minutes. The substrate stock solution (PNP-stearate) was added (20 µL) and the absorbance at 405 nm monitored for 15 minutes and the initial velocity noted, using a FLUROstar OPTIMA plate reader with an absorbance filter of 405 nm.

5.7 References

1. C. Levinthal, *J. Chim. Phys. Phys. Chim. Biol.*, 1968, **65**, 44-45.
2. R. Zwanzig, A. Szabo and B. Bagchi, *Proc. Natl. Acad. Sci. U.S.A.*, 1992, **89**, 20-22.
3. K. A. Dill and H. S. Chan, *Nat. Struct. Biol.*, 1997, **4**, 10-19.
4. V. Daggett and A. R. Fersht, *Trends Biochem. Sci*, 2003, **28**, 18-25.
5. A. R. Fersht, *Curr. Opin. Struct. Biol.*, 1997, **7**, 3-9.
6. R. Horton, L. Moran, G. Scrimgeour, M. Perry and D. Rawn, *Principles of Biochemistry*, Pearson International Edition, New Jersey, Fourth edn., 2006.
7. K. M. Polizzi, A. S. Bommarius, J. M. Broering and J. F. Chaparro-Riggers, *Curr. Opin. Chem. Biol.*, 2007, **11**, 220-225.
8. R. Day, B. J. Bennion, S. Ham and V. Daggett, *J. Mol. Biol.*, 2002, **322**, 189-203.
9. P. L. Privalov and G. I. Makhatadze, *J. Mol. Biol.*, 1993, **232**, 660-679.
10. M. Goyal, T. K. Chaudhuri and K. Kuwajima, *PLOS ONE*, 2014, **9**, e115877.
11. L. Whitmore and B. A. Wallace, *Biopolymers*, 2008, **89**, 392-400.
12. N. J. Greenfield, *Nat. Protoc.*, 2006, **1**, 2527-2535.
13. D. E. Otzen, *Biophys. J.*, 2002, **83**, 2219-2230.
14. M. Oobatake and T. Ooi, *Prog. Biophys. Mol. Biol.*, 1993, **59**, 237-284.
15. E. Chi, S. Krishnan, T. Randolph and J. Carpenter, *Pharm. Res.*, 2003, **20**, 1325-1336.

16. C. Ó'Fágáin, *Enzyme Microb. Technol.*, 2003, **33**, 137-149.
17. R. M. Daniel, M. Dines and H. H. Petach, *Biochem. J.*, 1996, **317**, 1-11.
18. T. Geiger and S. Clarke, *J. Biol. Chem.*, 1987, **262**, 785-794.
19. R. Lumry and H. Eyring, *J. Phys. Chem.*, 1954, **58**, 110-120.
20. J. Skjold-Jørgensen, J. Vind, A. Svendsen and M. J. Bjerrum, *Biochemistry*, 2014, **53**, 4152-4160.
21. L. Whitmore and B. A. Wallace, *Nucleic Acids Res.*, 2004, **32**, W668-W673.
22. S. Vijayakumar, S. Vishveshwara, G. Ravishanker and D. L. Beveridge, *Biophys. J.*, 1993, **65**, 2304-2312.
23. N. Sreerama and R. W. Woody, *Anal. Biochem.*, 2000, **287**, 252-260.
24. S. Doniach, *Chem. Rev.*, 2001, **101**, 1763-1778.
25. O. Glatter and O. Kratky, *Small angle x-ray scattering*, Academic Press, London, First edn., 1982.
26. B. Hammouda, *J. Appl. Crystallogr.*, 2010, **43**, 716-719.
27. H. Murata, C. S. Cummings, R. R. Koepsel and A. J. Russell, *Biomacromolecules*, 2014, **15**, 2817-2823.
28. L. R. Lawin, W. K. Fife and C. X. Tian, *Langmuir*, 2000, **16**, 3583-3587.
29. S. Liu and W. K. Fife, *Macromolecules*, 1996, **29**, 3334-3336.
30. L. Brady, A. M. Brzozowski, Z. S. Derewenda, E. Dodson, G. Dodson, S. Tolley, J. P. Turkenburg, L. Christiansen, B. Huge-Jensen, L. Norskov, L. Thim and U. Menge, *Nature*, 1990, **343**, 767-770.

31. Y. Cajal, A. Svendsen, V. Girona, S. A. Patkar and M. A. Alsina, *Biochemistry*, 1999, **39**, 413-423.
32. D. M. Blow, *Acc. Chem. Res.*, 1976, **9**, 145-152.
33. F. Bordes, S. Barbe, P. Escalier, L. Mourey, I. André, A. Marty and S. Tranier, *Biophys. J.*, 2010, **99**, 2225-2234.
34. R. C. Rodrigues, J. M. Bolivar, G. Volpato, M. Filice, C. Godoy, R. Fernandez-Lafuente and J. M. Guisan, *J. Biotechnol.*, 2009, **144**, 113-119.
35. U. Schuchardt, R. M. Vargas and G. Gelbard, *J. Mol. Catal. A: Chem.*, 1995, **99**, 65-70.

6 Conclusions and future work

This work focused on enzyme mimics, wherein an organic catalyst was immobilised within the core of micelles obtained from an amphiphilic block copolymer, and enzyme stabilisation, where different homopolymers and copolymers were assessed for their ability to enhance the enzyme shelf-life in an aqueous solution.

The catalyst triazabicyclodec-5-ene (TBD) can be immobilised onto an amphiphilic block copolymer. This TBD catalyst proved to be incompatible with RAFT derived polymers and as an alternative NMP synthesised polymers were successfully used. The functionalised amphiphilic polymers effectively assembled forming catalytic nanoreactors embedding TBD within the core, as a model of an enzyme active site. Having demonstrated that NMP is a viable synthetic route for TBD-containing amphiphilic block copolymers, we propose that further exploration would involve optimisation of copolymerisation conditions of the synthesised TBD-monomer with styrene. This would provide an alternative approach towards TBD immobilisation, reducing the number of steps required for polymer synthesis. Moreover, development of the copolymerisation would enable a more facile synthesis of varying block ratios allowing for optimisation of the position of TBD in the final structures.

The incorporation of TBD within a nanoreactor allowed for successful catalysis of Michael addition reaction, with an increased conversion obtained when compared to the free MTBD catalyst in water. This was of particular importance as it enabled

catalysis to take place at room temperature with low catalytic loadings (5 mol%) in aqueous conditions. We found an increase in core loading increased the rate of reaction and, surprisingly, reducing the number of nanoreactors in solution also resulted in increased rates. This is as a result of the accessibility of the catalyst to the substrate. The assembly of blended micelles successfully enhanced activity, as a result of lower aggregation numbers of the micelles. Hence maintaining a low aggregation number allows for more efficient uptake of the substrates into the micellar core. We propose that in future works these polymers can be blended with lower-functionalised polymers providing a range of catalyst loadings, in order to determine the optimum loading for high activity and selectivity. The blended aggregates formed can then be compared for catalysis to their “pure” counterparts. We expect the catalytic behaviour of different systems with equivalent loadings to be similar, thus eliminating the need for specific catalytic loadings of the polymers, hence simplifying the preparation of catalytic nanoreactors. Another potential development of the system would be the introduction of a cross-linker, allowing for recycling experiments of these micelles to determine if these nanoreactors can facilitate recycling experiments making them more environmentally viable as a catalyst.

PDMA was found to interact with the enzyme, lipase, without loss in secondary structure, indicative of retention of activity. The synergetic use of the TBD catalyst and lipase for use in a laundry product was shown to be ineffective. We have found that immobilised TBD greatly distorts the secondary structure of lipases resulting in a loss of activity. In addition to these results, we suggest that enzyme-polymer interactions are dependent on the accessibility of the amide functionality, and

therefore alternative acrylamide polymers can also be explored such as *N-tert*-butyl acrylamide, alkyl acrylamide and diethyl acrylamide. This route would be interesting to explore as it would result in a side chain length dependence profile for polymer-enzyme interactions as determined by SAXS, CD spectroscopy and stability studies.

An increase in the T_m of Lipex was found in the presence of a higher molecular weight PDMA which we proposed was due to PDMA acting as a steric barrier reducing the rate of denaturation. Initial results indicated that PDMA slowed the deactivation of the lipase during storage for one week (however further studies are required to confirm these preliminary results) which we suggest is as a consequence of polymer shielding the lipase from the external environment. To further explore the degradation pathway of these lipases at higher temperatures, we propose MALDI-TOF as a viable technique to monitor deamidation of the proteins upon storage and DLS to monitor aggregation of the protein structures. Running stability studies over a period of months with a range of polymer molecular weights would enable a greater understanding of the dependence of enzymatic deactivation on presence of PDMA polymers.

Within this thesis the importance of higher ordered structures has been highlighted, with regards to synthesis of the nanoparticles, well defined amphiphilic block copolymers allowed for both assembly and catalysis. Enzymatic activity relies heavily on the secondary and tertiary structures, CD spectroscopy and SAXS has shown that PDMA was key to maintaining the enzyme's native structure allowing for increased stabilisation.